From Structure to Thermodynamics with Local Molecular Field Theory

a dissertation presented
by
Richard Charles Remsing III
to
The Chemical Physics Program

in partial fulfillment of the requirements
for the degree of
Doctor of Philosophy
in the subject of
Chemical Physics

The University of Maryland
College Park, Maryland
August 2013

Thesis advisor: John D. Weeks   Richard Charles Remsing III

From Structure to Thermodynamics with Local Molecular Field Theory

Abstract

A fundamental goal of statistical mechanics is to connect a description of the intermolecular interactions and the accompanying microscopic structural details of a molecular system to its macroscopic thermodynamic properties. When the interactions between molecular components are treated with sufficient simplicity, as in an ideal gas or a hard sphere fluid for example, the link between structure and thermodynamics can be apparent. In contrast, when both local and non-local interactions are present in the system, competition between the various short and long ranged forces can lead to surprising thermodynamic behaviors as exemplified by the complexities of liquid water. Local molecular field (LMF) theory provides a physically motivated formalism for systematically decomposing the structure and thermodynamics of molecular systems into portions arising from local and non-local interactions. In this thesis, LMF theory is employed to examine the structure and thermodynamics of molecular systems, with a focus on aqueous solutions.

LMF-motivated truncations of classical water models are first developed as analysis tools to explore the roles of the local hydrogen bond network, dispersion interactions, and long ranged multipolar interactions in the determination of several anomalous thermodynamic properties of bulk water. This type of analysis is then extended to the study the relative importance of hydrogen bonding and interfacial unbalancing potentials in hydrophobic effects. The underlying ideas of LMF theory are then utilized to study local and non-local interactions in ion solvation. Modifications to classical dielectric continuum theories are explored with a focus on determining the electrostatic potentials inside ionic cores. LMF ideas are then used to develop the concept of a Gaussian test charge. We then argue that this type of test charge is the appropriate generalization of a classical point test charge to probe the dielectric response of molecularly detailed systems and develop an accurate formalism for the description of the dielectric response to such probes. Finally, a LMF theoretic foundation for performing free energy calculations is developed and tested before concluding the thesis with a discussion of future work involving LMF theory.

To Amie

Acknowledgements

I must begin by thanking my advisor, Professor John Weeks, for his guidance in my research endeavors over the last five years. His dedication to science, and his unmatched level of insight and clarity is truly inspiring. In my time at Maryland, he has taught me more than I ever could have hoped, and I have truly enjoyed working with him. I look forward to many more stimulating discussions in the future.

I would also like to thank Professors Chris Jarzynski, Dave Thirumalai, Garyk Papoian, and Sergei Sukharev for serving on my committee. Their effort and time is much appreciated. I additionally thank Professors Michael Coplan and Chris Jarzynski for the guidance they have provided as Director and Associate Director of the Chemical Physics graduate program. I am also very grateful for the help Debbie Jenkins and Stacey Bremerman have provided over the years.

It has been a privilege to be a part of the Weeks group, and I would to thank the current and past members for the many scientific discussions in which we have taken part. In particular, Zhonghan Hu helped me get started when I first joined the group, and it has been a pleasure to collaborate with Jocelyn Rodgers on some of the work discussed in this thesis. My time in the group overlapped most with Shule Liu, and I truly enjoyed working with him over the years. I have enjoyed working on several projects with current Weeks group member Ang Gao, and I very much look forward to continuing this work with him. I also thank Natasha Denesyuk and Qiang Liu for stimulating discussions.

I also would like to acknowledge some of the past and present members of the Jarzynski group – Suri Vaikuntanathan, Andy Ballard, Sebastian Deffner, and Zhiyue Lu – with whom I have discussed science on many occasions. The beginning stages of the work discussed in Chapter 4 led to a fruitful

collaboration with Chris Mundy, Marcel Baer, and Greg Schenter which I have enjoyed. In addition, numerous discussions regarding truncated models and LMF theory with Shekhar Garde and the members of his research group are gratefully acknowledged.

I would be remiss if I did not thank my undergraduate advisor, Professor Guillermo Moyna, for allowing me to join his research group as a freshman. He allowed me to explore the wide variety of research being carried out in his group, and without this freedom and his guidance, I may never have pursued chemical physics. For this, I am truly grateful.

Finally, I would like to thank my family. They have always been a strong source of support throughout my life, and their diligence in their own professions has been a constant source of inspiration. Most of all, I would like to thank Amie for her unwavering support, love, and encouragement over the years. Whether urging me to finish this dissertation, or providing a welcome and often much needed diversion, she always seems to know what is best, and I could not imagine my time at Maryland without her. I eagerly anticipate our next adventures as we move forward in our life together.

Contents

3

Listing of figures

4

6

God made the bulk;
Surfaces were invented by the devil.
　　　　　Wolfgang Pauli

1
Introduction

T his dissertation is concerned with the link between microscopic structure and macroscopic thermodynamics. The experimental ability to synthesize and manipulate materials on nano-scopic length-scales has never been greater, and at the heart of this ability is knowledge of the impact that molecular-scale interactions have on bulk properties. As science and technology move forward, theoretical advances are a necessary complement to experimental approaches, and are a necessity when nano-scale properties are of interest. In particular, a combination of statistical physics and computer simulation has proved to be an invaluable tool for such studies. This is the approach employed herein to study the macroscopic thermodynamic consequences of molecular-scale structural details.

Molecular systems can be modeled by prescribing physics-based interaction potentials between atomic groups, which can then be transcribed into formats amenable to computer simulation. While the specific form of these interatomic interactions may vary between systems, most can be separated into a short ranged component responsible for local structure, like the tetrahedral lattice of ice, and a long ranged portion usually arising from Coulomb interactions, which is associated with behavior occurring over much larger than molecular length-scales. The recently developed local molecular field (LMF) theory of nonuniform fluids provides a physical means for optimally dividing such interaction potentials, in addition to a computationally efficient theoretical technique for determining the structural and thermodynamic response to the long ranged component of the interactions [1, 2, 3, 4, 5]. We will exploit the ideas of LMF theory to examine the structure and thermodynamics of complex systems throughout this dissertation.

1.1 Uniform Liquid Structure is Dominated by Short Ranged Forces

The successful development of theories of nonuniform liquids hinges on an understanding of such fluids in the uniform bulk liquid state. Of particular importance for simple liquids, like the Lennard-Jones (LJ) fluid, is understanding the relative roles of repulsive and attractive forces. The fundamental idea of separating the roles of repulsions and attractions has led to monumental breakthroughs in our understanding of the phase behavior of fluids through the work of van der Waals, and later work has substantially influenced our understanding of the liquid state of matter in general [6, 7, 8].

At the core of these developments is the concept of *force cancellation*. To understand these ideas, consider the example of a dense uniform LJ fluid near its triple point, where the LJ potential describing interparticle interactions is

$$u_{\mathrm{LJ}}(r) = 4\varepsilon_{\mathrm{LJ}} \left[\left(\frac{\sigma_{\mathrm{LJ}}}{r} \right)^{12} - \left(\frac{\sigma_{\mathrm{LJ}}}{r} \right)^{6} \right], \tag{1.1}$$

where $-\varepsilon_{\mathrm{LJ}}$ and σ_{LJ} are the energy minimum and inter-particle length scale associated with the fluid. This potential is shown in Figure 4.8a. The LJ potential can be separated into a short ranged purely repulsive portion which is rapidly-varying over molecular length-scales and a long ranged, slowly-varying attractive component. This separation is of the form developed by Weeks, Chandler, and Andersen (WCA) in their seminal work on perturbation theory of uniform liquids [6]. This WCA separation splits the LJ potential $u_{\mathrm{LJ}}(r)$ into its corresponding repulsive and attractive *forces*, such that

$$u_0(r) = \begin{cases} u_{\mathrm{LJ}}(r) + \varepsilon_{\mathrm{LJ}} & r < r_0 \\ 0 & r > r_0 \end{cases} \tag{1.2}$$

and

$$u_1(r) = \begin{cases} -\varepsilon_{\mathrm{LJ}} & r < r_0 \\ u_{\mathrm{LJ}}(r) & r > r_0 \end{cases} \tag{1.3}$$

where $r_0 = 2^{1/6}\sigma_{\mathrm{LJ}}$ is the position of the minimum of the LJ potential [6] and $u_0(r)$ is typically referred to as the WCA potential throughout the literature.

For a single particle in a dense fluid, the *average* vector sum of the attractive forces due to $u_1(r)$ from its surrounding neighbors exactly cancels by symmetry, and this remains true to a good approximation in most typical configurations of a uniform fluid. This force cancellation is schematically illustrated in Figure 4.8b. Therefore, the attractive potential $u_1(r)$ will have a negligible effect on the structure of a dense fluid and merely provides a uniform background energy, which can be accounted for in a simple mean field manner [7]. While the role of the attractive forces is minimal in a dense uniform fluid, the harsh repulsive interactions encompassed by $u_0(r)$ determine the
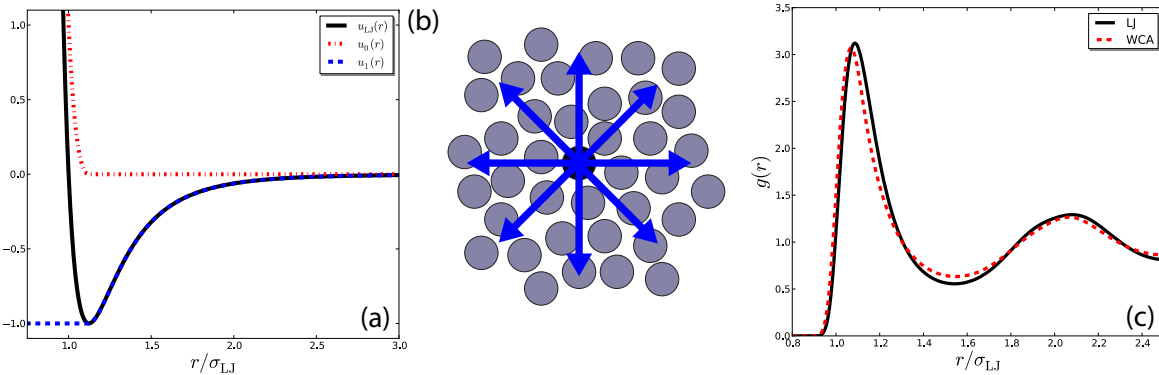
Figure 1.1: (a) Separation of the LJ potential into its rapidly-varying, short ranged and slowly-varying, long ranged components. (b) Schematic illustration of the idea of force cancellation, wherein the vector sum of the force due to $u_1(r)$ (blue arrows) on a tagged particle (black) from its neighbors effectively cancels. (c) Comparison of the pair distribution functions $g(r)$ of the LJ fluid and its corresponding WCA reference system at the state point $T^* = 0.65$ and $\rho^* = 0.85$.

structure of the liquid. Indeed, the pair distribution function $g(r)$ of a LJ fluid is quantitatively captured by its WCA reference system, as shown in Figure 4.8c, where the pair distribution function in a homogenous, isotropic system is given by

$$g(r) = \frac{1}{\rho} \left\langle \frac{1}{N} \sum_{i=1}^{N} \sum_{j=1}^{N}{}' \delta\left(\mathbf{r} - \mathbf{r}_j + \mathbf{r}_i\right) \right\rangle, \tag{1.4}$$

$\rho = N/V$ is the bulk density of a system with N particles in a volume V, $\mathbf{r}_i$ is the position of particle i, $\langle \cdots \rangle$ indicates an ensemble average, $\delta(\mathbf{r})$ is the Dirac delta function, and the prime on the sum over j indicates the omission of terms when $i = j$. The highly accurate description of the LJ fluid by its WCA reference has led to the successful development of perturbation theories of uniform fluids [6]. By assuming equivalence of the pair correlation functions of the LJ and WCA fluids ($g(r) \approx g_0(r)$), one can effectively integrate over the structure of the reference system to obtain thermodynamic properties of the full system. These ideas, in conjunction with theoretical developments to determine the reference fluid $g_0(r)$ [9] with high accuracy, comprise the foundation of the WCA theory of uniform fluids [6].

However, the concept of force cancellation breaks down in the presence of structural inhomogeneities. For example, consider introducing a large hard spherical particle (HS) into a LJ fluid, schematically shown in Figure 1.2a. If one once again considers the vector sum of attractive interactions on a fluid particle, but now for a particle close to the interface between the fluid and the
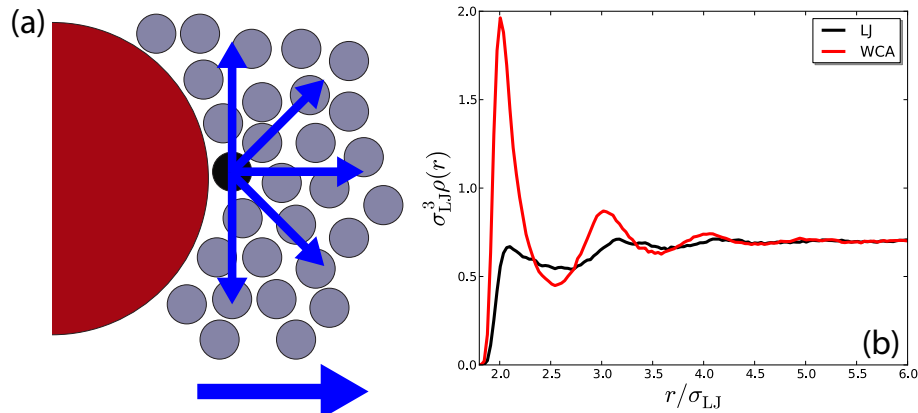
Figure 1.2: (a) Schematic illustration of the unbalanced force (blue) on a particle (black) near the interface of a large hard sphere (red). (b) Comparison of the nonuniform densities of the LJ fluid and its corresponding WCA reference system at the state point $T^* = 0.85$ and $\rho^* = 0.70$.

HS, we see that the slowly-varying long ranged attractions *do not cancel*. Instead, they provide a net *unbalanced force* at the fluid-HS interface that leads to phenomena like drying. The structure of the purely repulsive reference fluid does not approximate that of the corresponding fully interacting LJ fluid, as evidenced by the nonuniform density distributions shown in Figure 1.2b. Accounting for the effects of such unbalanced forces in a short ranged reference fluid requires further theoretical developments, and this is achieved through the use of local molecular field theory for nonuniform fluids.

1.2   Local Molecular Field Theory for Nonuniform Fluids

Local molecular field (LMF) theory utilizes the above-described separation of molecular interactions into short and long ranged components to enable the study of nonuniform systems by simulating short ranged models in the presence of an effective external field that accounts for the averaged effects of any long ranged interactions [1, 2, 3, 4, 5]. LMF theory considers a nonuniform system of particles interacting with a pair potential $u(r) = u_0(r) + u_1(r)$, and in a general external field $\phi(\mathbf{r})$. This external field could be due to hard walls, a fixed solute, or an electric field, for example. LMF theory seeks to map this *full* system onto a *mimic* system, wherein interparticle interactions are described by a short ranged pair potential $u_0(r)$. However, the external field in this mimic system is

now a *renormalized* external field $\phi_R(\mathbf{r})$, such that this LMF mapping is

$$\left\{ \begin{array}{c} u(r) \\ \phi(\mathbf{r}) \end{array} \right\} \Rightarrow \left\{ \begin{array}{c} u_0(r) \\ \phi_R(\mathbf{r}) \end{array} \right\} \tag{1.5}$$

As discussed above, the short ranged interaction potentials are chosen such that $u_0(r)$ contains all the harsh, rapidly-varying portions of the potential. These strong short ranged interactions therefore yield an accurate account of forces between typical nearest neighbors in a liquid. The long ranged component $u_1(r)$ is chosen to be *slowly-varying* over molecular length-scales. The LMF mapping in Equation 1.5, and the renormalized potential $\phi_R(\mathbf{r})$, is chosen in principle such that the singlet density of the full system matches that of the mimic system,

$$\rho^{(1)}\left(\mathbf{r}; [\phi]\right) = \rho_R^{(1)}\left(\mathbf{r}; [\phi_R]\right). \tag{1.6}$$

The short ranged system then "mimics" the structure of the corresponding full system. The functional dependence of the densities on the corresponding external fields will be omitted in the rest of this work unless necessary for clarity.

The effective field, $\phi_R(\mathbf{r})$, is obtained from the self-consistent LMF equation,

$$\phi_R(\mathbf{r}) = \phi(\mathbf{r}) + \int d\mathbf{r}' \rho_R^{(1)}(\mathbf{r}') u_1(|\mathbf{r} - \mathbf{r}'|) + C, \tag{1.7}$$

where C is a constant of integration that sets the zero of the potential, and is typically chosen so that $\phi_R(\mathbf{r})$ is zero in the bulk fluid. Equation 1.7 is obtained from an approximate integration of a combination of the corresponding first equations of the exact Yvon-Born-Green (YBG) hierarchy of equations for the full and mimic systems,

$$k_B T \nabla_{\mathbf{r}} \ln \rho(\mathbf{r}) = -\nabla_{\mathbf{r}} \phi(\mathbf{r}) - \int d\mathbf{r}' \rho(\mathbf{r}|\mathbf{r}') \nabla_{\mathbf{r}} u(|\mathbf{r} - \mathbf{r}'|) \tag{1.8}$$

and

$$k_B T \nabla_{\mathbf{r}} \ln \rho_R(\mathbf{r}) = -\nabla_{\mathbf{r}} \phi_R(\mathbf{r}) - \int d\mathbf{r}' \rho_R(\mathbf{r}|\mathbf{r}') \nabla_{\mathbf{r}} u_0(|\mathbf{r} - \mathbf{r}'|), \tag{1.9}$$

respectively, where

$$\rho(\mathbf{r}|\mathbf{r}') \equiv \frac{\rho^{(2)}(\mathbf{r}, \mathbf{r}')}{\rho(\mathbf{r})} \tag{1.10}$$

is the conditional singlet density: the density at $\mathbf{r}'$ given that a particle is at $\mathbf{r}$, such that $\rho^{(2)}(\mathbf{r}, \mathbf{r}')$ is the nonuniform pair density. These YBG equations relate mean interatomic forces to the structure they induce, such that LMF theory essentially integrates from the "bottom-up" to obtain the structural

11

properties of a molecular system. This contrasts traditional classical density functional theory (DFT) approaches, in which an approximate free energy functional is differentiated to yield structure [10], such that one is working from the "top-down." This distinction between bottom-up and top-down approaches is significant, especially when determining accurate thermodynamic properties, which will be the focus of a later chapter in this thesis.

Subtracting Equation 1.8 from Equation 1.9 when Equation 1.6 holds yields an expression relating $\nabla_{\mathbf{r}}\phi(\mathbf{r})$ to $\nabla_{\mathbf{r}}\phi_R(\mathbf{r})$,

$$
\begin{aligned}
-\nabla_{\mathbf{r}}\phi_R(\mathbf{r}) &= -\nabla_{\mathbf{r}}\phi(\mathbf{r}) - \int d\mathbf{r}' \rho_R(\mathbf{r}'; [\phi_R]) \nabla_{\mathbf{r}} u_1(|\mathbf{r} - \mathbf{r}'|) \\
&\quad - \int d\mathbf{r}' \left[\rho(\mathbf{r}'|\mathbf{r}; [\phi]) - \rho_R(\mathbf{r}'|\mathbf{r}; [\phi_R]) \right] \nabla_{\mathbf{r}} u_0(|\mathbf{r} - \mathbf{r}'|) \\
&\quad - \int d\mathbf{r}' \left[\rho(\mathbf{r}'|\mathbf{r}; [\phi]) - \rho(\mathbf{r}'; [\phi]) \right] \nabla_{\mathbf{r}} u_1(|\mathbf{r} - \mathbf{r}'|).
\end{aligned}
\tag{1.11}
$$

Physically sound approximations are then made to Equation 1.11 to arrive at the LMF equation. These approximations hinge on two crucial ideas. The first is that a good choice of $u_0(r)$ provides an accurate description of nearest neighbor interactions, and therefore higher order correlations as described by the conditional singlet density are also captured by the mimic system on these molecular length scales, in addition to the singlet density which is captured by construction. The second approximation requires that $u_1(r)$ be slowly-varying over nearest neighbor, molecular length-scales, and when these conditions are satisfied, Equation 1.7 can be obtained and is found to be highly accurate. When these conditions hold, the second and third terms in Equation 1.11 vanish. The remaining terms can then be formally integrated to obtain the LMF Equation 1.7.

For LJ interactions, the WCA separation of the potential discussed above typically satisfies the conditions leading to the LMF equation. In systems containing charged particles, experience has shown that it is very useful to separate the $1/r \equiv v(r)$ portion of the Coulomb potential into short ranged rapidly-varying ($v_0(r)$) and long ranged slowly-varying ($v_1(r)$) components as

$$
v(r) = \frac{1}{r} = \frac{\text{erfc}(r/\sigma)}{r} + \frac{\text{erf}(r/\sigma)}{r} \equiv v_0(r) + v_1(r),
\tag{1.12}
$$

where $\text{erf}(r)$ and $\text{erfc}(r) = 1 - \text{erf}(r)$ are the usual error and complementary error functions. This separation is shown in Figure 1.3. The parameter σ is the length-scale on which the potential is separated, typically referred to as the LMF smoothing length. This length-scale is usually chosen on the order of the nearest-neighbor distance between charges. Within an electrostatic context, the
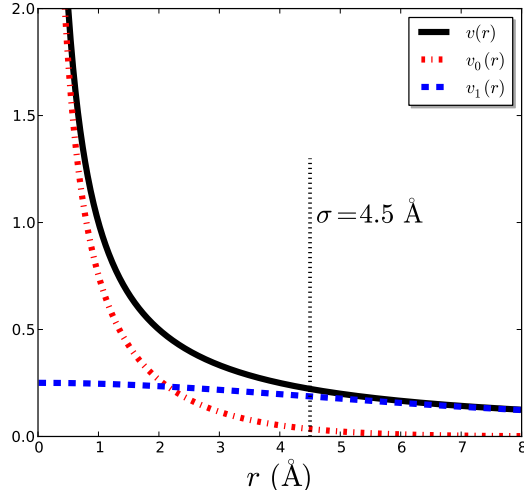
Figure 1.3: Separation of the $1/r$ portion of the Coulomb potential into its short ranged, rapidly-varying and long ranged, slowly-varying components $v_0(r)$ and $v_1(r)$, respectively. The separation shown is for $\sigma = 4.5$ Å, as illustrated.

interaction potential $v_1(r)$ is that due to a unit Gaussian charge distribution of width σ,

$$v_1(r) = \frac{1}{\sigma^3 \pi^{3/2}} \int d\mathbf{r}' \frac{e^{-(\mathbf{r}'/\sigma)^2}}{|\mathbf{r} - \mathbf{r}'|}. \tag{1.13}$$

Analogously, the short ranged potential $v_0(r)$ is that arising from a unit point charge and a neutralizing Gaussian distribution of charge,

$$v_0(r) = \int d\mathbf{r}' \left[\delta(\mathbf{r}') - \frac{e^{-(\mathbf{r}'/\sigma)^2}}{\sigma^3 \pi^{3/2}} \right] \frac{1}{|\mathbf{r} - \mathbf{r}'|}. \tag{1.14}$$

Clearly, $v_1(r)$ is slowly-varying for $r < \sigma$, and reduces to the full $v(r) = 1/r$ for distances larger than the smoothing length, as desired.

A detailed discussion of the derivation of the LMF equation is detailed elsewhere [1, 11]. Therefore, only the results obtained for LJ and Coulomb potentials are quoted when appropriate. However, the self-consistent nature of the LMF equation requires a discussion of the details surrounding its solution, and a detailed account of implementing LMF theory in practical applications is provided in Appendix A. We will use LMF theory and its physically suggestive decomposition of

13

interaction potentials throughout this dissertation to examine the role of local and non-local forces on the structure and thermodynamics of molecular systems, and aqueous media in particular.

1.3 Structure and Thermodynamics of Bulk Water

There may be no better example of structural influence on macroscopic properties than water, and the uniqueness of liquid water will be the focus of much of this dissertation. Water is probably the most far-reaching and important substance studied by science. Without it, life on Earth would not exist, and for this reason it is often called the "matrix of life" [12, 13]. Seemingly uncomplicated when considering its molecular formula alone, liquid H_2O is anything but simple. In fact, water's complexity is what allows it to be such a great medium for biology, and understanding the nature of this liquid is essential to understand processes ranging from protein folding and self-assembly to the design of water repellent materials and cleaning supplies [13, 14].

The structure of bulk water is substantially different from that of typical simple liquids, such as the HS and LJ fluids. Unlike simple liquids, water displays local tetrahedral ordering, due to directional hydrogen bonds (HBs) between neighboring molecules. In classical water potentials like the SPC/E model [15] discussed extensively in the next chapter, hydrogen bonding arises from electrostatic attraction between the positive charge of the hydrogen atomic site and the partial negative charge of an oxygen atom rich in electron density [13]. Although describing the behavior of the electrons of a water molecule in detail requires computationally intense quantum mechanical techniques, a reasonable picture of the liquid structure can be obtained using these simple classical mechanical models, in which the average electron density of a molecule is represented through partial point charges.

Using computer simulations, we first compare the bulk structure of liquid water to that of a simple liquid, namely a LJ fluid with the same LJ parameters as the SPC/E water model. To this end, we first examine the pair distribution functions $g(r)$ in bulk water and the LJ fluid at the same bulk number density. The distributions are shown in Figure 1.4 for correlations between oxygen sites in SPC/E water and between particles in the LJ fluid. Due to H-bonding between water molecules, the first peak in the SPC/E $g(r)$ is found at a much smaller distance than that for the LJ fluid. In fact, the repulsive cores of the LJ potentials of neighboring H-bonded water molecules overlap significantly, something that could be produced in a uniform LJ fluid only at huge pressures, and H-bonding in SPC/E water arises due to frustrated charge-pairing, discussed further in the next chapter.

Another simple measure of the structure of the two liquids is the number of particles within a distance r from the central particle, termed the coordination number, $N(r)$. The coordination

14
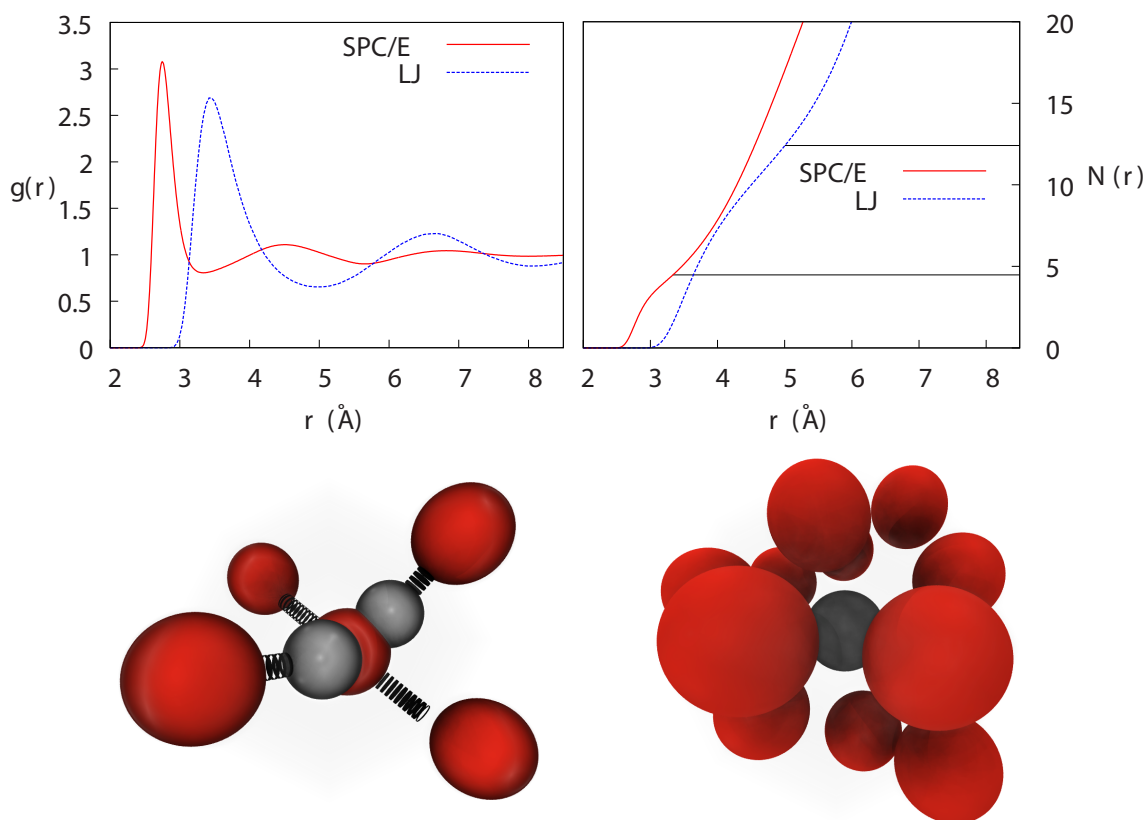
Figure 1.4: (top) Comparison of the pair distribution functions, $g(r)$, and the coordination numbers, $N(r) = 4\pi\rho \int_0^r dr' r'^2 g(r')$, for the SPC/E water model and a LJ fluid with the same bulk density and LJ energy and length-scale parameters. Black solid lines indicate the value of $N(r)$ at the first minimum of the corresponding $g(r)$, which corresponds to the number of nearest neighbors in the first solvation shell. (bottom) Snapshots from MD simulations depicting the first solvation shell of SPC/E water (left) and a LJ fluid (right). In the case of SPC/E water, the central water molecule is shown in its entirety, with oxygen and hydrogen atoms colored red and light grey, respectively, while its nearest neighbors are shown only as oxygen atoms, with hydrogen bonds indicated by dashed black cylinders. For the LJ fluid, the central particle is colored grey, while its nearest neighbors are shown in red.

number is proportional to the integral of $g(r)$,

$$N(r) = 4\pi\rho \int_0^r dr' r'^2 g(r').$$

<div align="right">(1.15)</div>

The coordination numbers of the two systems are shown in Figure 1.4, with the value of $N(r)$ at the first minimum of $g(r)$ indicated by solid lines. The particles located between $r = 0$ and the first minimum of $g(r)$, $r = r_{\min}$, are termed the first coordination shell (FCS), and the number of particles in this region differs significantly between water and simple liquids. The LJ fluid has a coordination number of $N(r_{\min}) \approx 12$ in the FCS, like a simple close-packed structure. Water, on the other hand, has between 4 and 5 nearest-neighbors, much lower than expected from simple close-packing arguments. This value of $N(r_{\min})$ is a direct result of the directional H-bonding present in liquid water, as illustrated by the snapshots of the FCS structures in water and the LJ fluid in Figure 1.4.

While the structure of the LJ fluid at high density is dictated mainly by its repulsive forces (and therefore simple packing arguments) [6], the formation of intermolecular HBs in water, drawn as black dashed cylinders in the figure, leads to a water molecule being tetrahedrally coordinated by its four nearest-neighbors. In an ideal configuration, a molecule of SPC/E water in the bulk will form four hydrogen bonds with its neighbors, two by donation of hydrogen bonds via the explicit hydrogen sites, and two through accepting hydrogen bonds from neighboring molecules at the site of the negative charge. Although lone pairs are not explicitly represented in the SPC/E model, the minimum energy configuration is this tetrahedral H-bonding geometry in which the favorable electrostatic attractions between opposing charges are maximized, while unfavorable, repulsive interactions between like charges are minimized. When combined with the repulsive LJ core energies from neighboring molecules, this leads to an average of only four H-bonding "sites" on each molecule. The insertion of another (fifth) molecule into the FCS without the formation of a H-bond to compensate the large LJ repulsive forces is rather unfavorable, although this does occur, and will be further discussed in the next chapter.

The complex structure of water, dictated by the propensity to form intermolecular hydrogen bonds, gives rise to an incredible number of anomalous thermodynamic properties [16]. Reference [16] lists at least 67 anomalous properties of water, ranging from its high boiling point, melting point, and critical temperature, to maxima and/or minima in the specific heat as a function of temperature (C_V and C_P) and its unusually high surface tension and dynamic anomalies such as a maximum in the diffusion coefficient as a function of temperature at high pressure. A few of the anomalies of bulk water are examined from the perspective of LMF theory in Chapter 2, before turning our attention to nonuniform systems. This chapter is based heavily on R. C. Remsing, J. M. Rodgers, and J. D. Weeks, *J. Stat. Phys.*, 145, 313–334, 2011 [17].

At the heart of many processes occurring in aqueous solution is the hydrophobic effect [13, 14]. A hydrophobic, or "water-fearing" substance is one that is not readily solvated by liquid water, and an attempt at such can often result in phase separation, such as the common phenomena of the

un-mixing of water and oil [13]. It is often noted that the term hydrophobic is actually a misnomer, because the low solubility of nonpolar substances in water results from water having a greater affinity for itself than the hydrophobic substance. The hydrophobic effect, or the propensity for hydrophobic solutes to aggregate in water, has been acknowledged as a major driving force for protein folding, for example [13, 14]. The amino acid units that make up a protein sequence can be classified as hydrophobic or hydrophilic (interacting favorably with water). In order to minimize the free energy of the system, contact between water and the hydrophobic groups should be kept at a minimum. As a means to do so, proteins will tend to fold in such a way that the majority of hydrophobic groups tend to be located in the interior of the protein, while hydrophilic groups are at the surface, in contact with water [13, 14].

It has long been understood that the process of dissolving a small apolar solute in water differs substantially from the hydration of a large hydrophobe, both in structure and thermodynamics. Therefore, a transition between the two regimes occurs as a solute is "grown" from small to large at a crossover radius R_C [18, 19]. While the solvation of solutes with a radius less than R_C is governed by small-scale density fluctuations in the liquid, hydration of an extended solute is dictated by three underlying features: formation of a cavity of the size of the solute, unbalanced dispersion forces that lead to interfacial drying phenomena, and any possible distortions and breaking of the hydrogen bond network in the vicinity of the solute. Cavity formation is a characteristic feature of all solvation processes, whether in a hard-sphere fluid or water, while the existence of unbalanced dispersion forces is observed in both water and simple LJ fluids [3]. Many workers have stressed the underlying similarities of the small and large solute size limits in water and LJ fluids [3, 13, 14, 18, 19], but important details of the length scale dependence of hydrophobic hydration must hinge on the properties of the hydrogen bond network, especially for solute sizes near the crossover radius. Nevertheless, most discussions of the length scale transition in water have not focused on this point, and the precise role of hydrogen bonding, as well as the various other forces present in the system in the vicinity of this crossover in solvation behavior has not been quantified. This task is the subject of Chapter 3, which is heavily based on R. C. Remsing and J. D. Weeks, *J. Phys. Chem. B*, 2013 (in press) [20].

In addition to the solvation of simple hydrophobes, the process of ion hydration is still not fully understood. In particular, the electrostatic nature of charged molecular species renders neutrality and the nature of the boundary conditions of a dielectric system quite important. In addition, the exact representation of the intermolecular interactions of water has a significant influence on both the structure and thermodynamics of ionic solutions, and leads to distinct asymmetries with respect to the sign of the ion charge. We explore the origins of these asymmetries in Chapters 4 and 5, which describes aspects of ongoing collaborative work with researchers at Pacific Northwest National Laboratory. Specifically, Chapter 4 is concerned with the solvation shell around a simple model of an uncharged ionic core, and how the asymmetric intramolecular charge distribution of a water molecule induces asymmetries in the structure and thermodynamics before a charge is even introduced in the

system. The response of dielectric media to the long wavelength component of ion charge is examined in Chapter 5, and a general theoretical formalism for describing this response is developed.

The phrase "from structure to thermodynamics" is embodied by Chapter 6. There, a general framework for performing free energy calculations with LMF theory is developed. The crux of this LMF theoretic formalism is that *good structure begets good thermodynamics*, and accurate structural properties of a molecular system are integrated to obtain the free energy in this "bottom-up" approach to thermodynamics. After demonstrating the accuracy of this formalism for describing numerous processes associated with hydrophobicity, the dissertation is concluded with a summary of its main points and a discussion of future work in Chapter 7.

The central problem in an attempt to understand the nature of a liquid from first principles is that of accounting for its bulk macroscopic properties in terms of the structure, motion, and mutual interactions of the molecules of which it may presumed to be composed.

B. Widom

2

Deconstructing Classical Water Models I: Anomalous Structure and Thermodynamics of Bulk Water [1]

2.1   Introduction

Classical empirical water potentials involving fixed point charges and Lennard-Jones (LJ) interactions were introduced in the first computer simulations of water forty years ago and modern versions are widely used even today in many biomolecular and materials-based simulations. Two recent reviews [21, 22] have focused on this wide class of model potentials and assessed their performance for a broad range of different structural and thermodynamic properties, some of which were used as targets in the initial parameterization of the models. Despite known limitations associated with the lack of molecular flexibility and polarizability, they qualitatively and often quantitatively capture a large number of properties of water and often represent a useful compromise between physical realism and computational tractability.

Given the simple functional forms of the intermolecular potentials it may seem surprising that such good agreement is possible. But recent work has shown that even simpler models where particles interact via isotropic repulsive potentials with two distinct length scales are able to

---

[1]Based in part on R. C. Remsing, J. M. Rodgers, and J. D. Weeks, *J. Stat. Phys.*, 145, 313–334, 2011 [17].

qualitatively reproduce certain characteristic dynamic and thermodynamic anomalies of bulk water [23, 24, 25]. Similarly in dense uniform simple liquids a hard-sphere-like repulsive force reference system can give a good description of the liquid structure, and this in turn permits thermodynamic properties to be determined by a simple perturbation theory [6, 26].

This suggests it should be useful to analyze the construction and predictions of empirical water potentials from the perspective of perturbation theory of uniform fluids and the related Local Molecular Field (LMF) theory [1, 2, 3, 4, 5, 6]. LMF theory provides a more general approach applicable to both uniform and nonuniform fluids and gives strong support to the basic idea of perturbation theory that in a uniform fluid slowly varying long ranged parts of the intermolecular interactions have little effect on the local liquid structure.

To apply these ideas to water we divide the intermolecular interactions in a given water model into appropriately chosen short and long ranged parts. In this context, it is conceptually useful to consider separately the slowly varying long ranged parts of both the LJ interactions and the Coulomb interactions. This deconstruction of the water potential via LMF theory provides a hierarchical framework for assessing separately the contributions of (i) strong short ranged interactions leading to the local hydrogen bonding network, (ii) dispersive attractions between water molecules, and (iii) long ranged dipolar interactions between molecules. Disentangling these contributions without the insight of LMF theory is very difficult due to the *multiple* contributions of the point charges and the LJ interactions in standard molecular water models

In uniform systems, the long ranged forces on a given water molecule from more distant neighbors tend to cancel [6, 7]. The remaining strong short ranged forces between nearest neighbors arise from the interplay between the repulsive LJ core forces and the short ranged attractive Coulomb forces between donor and acceptor charges. These forces determine a minimal reference model that can accurately describe the local liquid structure – the hydrogen-bond network for bulk water. The slowly varying parts of the intermolecular interactions are not important for this local structure and could be varied essentially independently to help in the determination of other properties as is implicitly done in the full model. Based on previous work with LMF theory [2, 11, 27], we examine two basic areas where we expect the different contributions to play varying but important roles – bulk thermodynamics and nonuniform structure. The short ranged interactions responsible for the hydrogen-bonding network are clearly necessary in all cases. LMF theory allows us to determine the relative importance of dispersive attractions and long-ranged dipolar attractions in these applications using simple analytical corrections for thermodynamics and an effective external field for nonuniform structure.

2.2 Local Hydrogen Bonds in Full and Truncated Water Potentials

In this chapter, we will consider one of the simplest and most widely used water models, the extended simple point charge (SPC/E) model [15], but similar ideas and conclusions apply immediately to
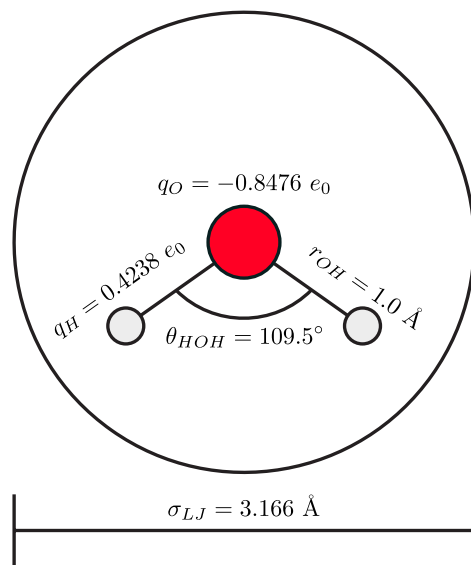
Figure 2.1: Schematic diagram of the SPC/E water model listing its various geometric parameters and interaction parameters. The O-H bond length and H-O-H angle are fixed, such that the molecule is rigid. The LJ well depth is $\epsilon_{LJ} = 0.65$ kJ/mol. The oxygen site is depicted as a large red circle, while the hydrogen atoms are shown as smaller, gray circles.

most other members of this class. As shown in Fig. 2.1, SPC/E water consists of a LJ potential as well as a negative point charge centered at the oxygen site. Positive point charges are fixed at hydrogen sites displaced from the center at a distance of 1 Å with a tetrahedral HOH bond angle. It is a remarkable fact that this simple model can reproduce many structural, thermodynamic, and dielectric properties of bulk water as well as those of water in nonuniform environments around a variety of solutes and at the liquid-vapor interface.

In the following we use the perspective of perturbation and LMF theory to help us see how this comes about. We use these ideas here not to suggest more efficient simulations using short ranged model potentials but rather as a method of analysis that provides physical insight into features of the full model as well. Since a detailed description and justification of LMF theory is given elsewhere [1], we will focus on qualitative arguments and just quote specific results when needed.

Fig. 2.2 gives some insight into why a perturbation picture based on the dominance of strong short ranged forces in uniform environments could be especially accurate for bulk SPC/E and related water models. This shows two adjacent water molecules with a separation of 2.75 Å that form an
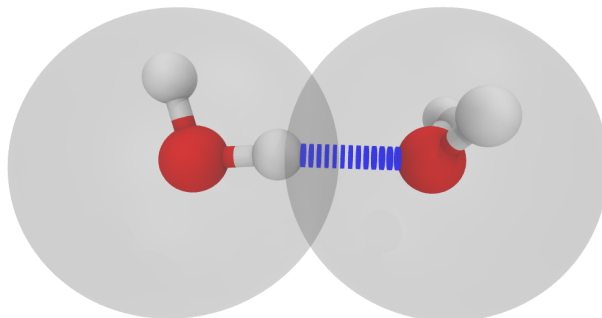
Figure 2.2: Optimal hydrogen bonding configuration of water taken from two molecules in ice Ih. LJ cores are depicted as gray transparent spheres with a diameter $\sigma_{LJ} = 3.16$ Å, while the hydrogen bond between waters with oxygens separated by 2.75 Å is illustrated by a dashed, blue cylinder. Oxygen and hydrogen atoms are colored red and white, respectively.

optimal hydrogen bond as seen in the structure of ice Ih. Hydrogen bonding in this model is driven by the very strong attractive force between opposite charges on the hydrogen and oxygen sites of adjacent properly oriented molecules. Proper orientation permits similar strong bonds to form with other molecules, leading to a tetrahedral network in bulk water. The gray circles drawn to scale depict the repulsive LJ core size as described by the usual parameter $\sigma_{LJ} = 3.16$ Å. The substantial overlap indicates a large repulsive core force opposing the strong electrostatic attraction, finally resulting in a nearest neighbor maximum in the the equilibrium oxygen-oxygen correlation function of 2.75 Å.

It is interesting to note that the first BNS water model introduced in 1970 used a smaller core size $\sigma_{LJ} = 2.82$ Å [28]. However a much larger LJ core with strong core overlap at typical hydrogen-bond distances is a common property of almost every water model introduced since then and seems to be a key feature needed to get generally accurate results from simple classical point charge models. Evidently, the highly fluctuating local hydrogen-bond network in these models arises from geometrically-frustrated "charge pairing", where the strong LJ core repulsions and the presence of other charges on the acceptor water molecule oppose the close approach of the strongly-coupled donor and acceptor charges.

We can test the accuracy of this picture by considering various truncated or "short" water models where slowly varying long ranged parts of the Coulomb and LJ interactions in SPC/E water are completely neglected. We first consider a Gaussian-truncated (GT) water model, already studied by LMF theory [2, 11, 27]. Here the Coulomb potential is separated into short and long ranged parts as

$$v(r) = \frac{1}{r} = \frac{\mathrm{erfc}(r/\sigma)}{r} + \frac{\mathrm{erf}(r/\sigma)}{r} = v_0(r) + v_1(r), \tag{2.1}$$
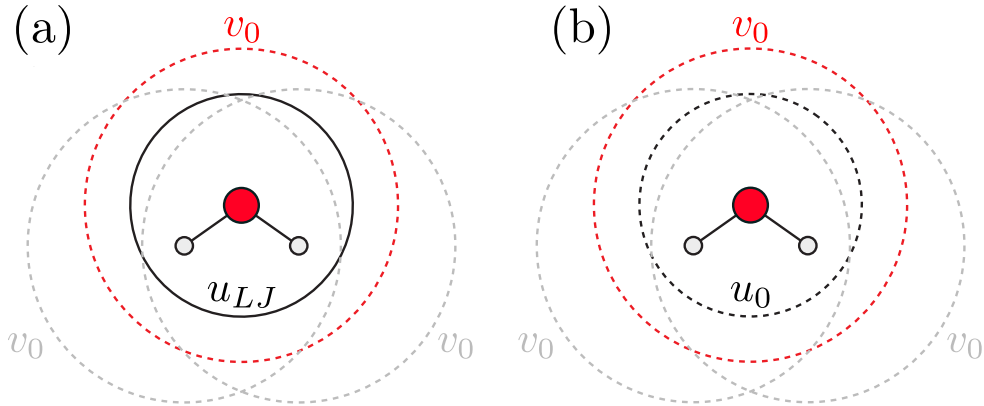
Figure 2.3: Schematic diagrams of (a) GT and (b) GTRC water models. Truncated interactions are indicated by dashed lines, while full interaction potentials are indicated by solid lines. LJ interactions are represented by black lines, while oxygen and hydrogen electrostatic interaction potentials are shown as red and gray lines, respectively.

where erf and erfc are the error function and complementary error function, respectively. The short-ranged $v_0(r)$ is the screened electrostatic potential resulting from a point charge surrounded by a neutralizing Gaussian charge distribution of width σ. Hence $v_0(r)$ vanishes rapidly at distances r much greater than σ while at distances less than σ the force from $v_0(r)$ approaches that of the full $1/r$ potential.

In GT water, depicted in Fig. 2.3a, the Coulomb potential associated with each charged site in SPC/E water is replaced by the short-ranged v_0 with no change in the LJ interaction. As suggested by Fig. 2.2, important features of the local hydrogen-bond network should be well captured by such a truncated model if the cutoff distance controlled by the length parameter σ in Eq. (2.1) is chosen larger than the hydrogen bond distance. Following Refs. [11] and [27], here we make a relatively conservative choice of $\sigma = 4.5$ Å, but values as small as 3 Å give essentially the same results. The circles are drawn to scale with diameters σ and σ_{LJ}.

The basic competition between very strong short ranged repulsive and attractive forces in the hydrogen bond depicted in Fig. 2.2 should be captured nearly as well by an even simpler reference model where the LJ potential is truncated as well, and replaced by the repulsive force reference potential $u_0(r)$ used in the WCA perturbation theory for the LJ fluid [6]. The resulting Gaussian truncated repulsive core (GTRC) model is schematically shown in Fig. 2.3b.

As discussed in perturbation theories of simple liquids [6, 26], a well-chosen reference system should accurately reproduce bulk structure present in the full system at the same fixed density and temperature. As illustrated by the pair distribution functions in Fig. 2.4, bulk GT and GTRC water
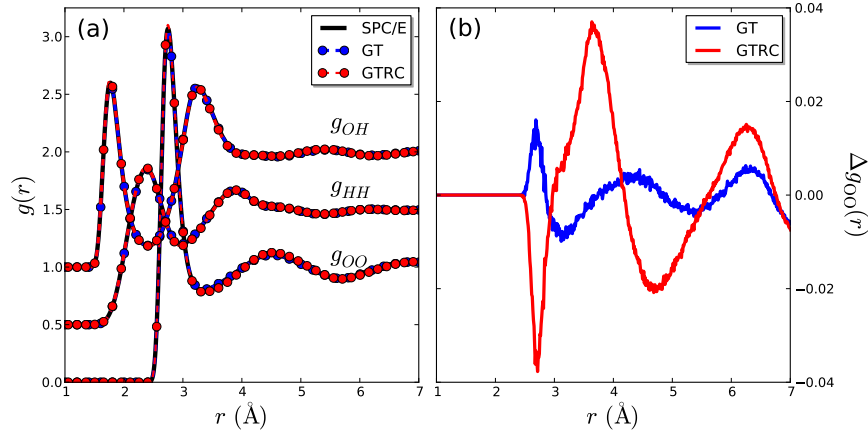
Figure 2.4: (a) Oxygen-oxygen, oxygen-hydrogen, and hydrogen-hydrogen site-site pair distribution functions, $g_{OO}(r)$, $g_{OH}(r)$, and $g_{HH}(r)$, respectively, for the three water models under study at $T = 300$ K and $v = 30.148$ Å^3. g_{HH} and g_{OH} have been shifted by 0.5 and 1 units, respectively, for clarity. (b) Differences between $g_{OO}(r)$ of the full model and that of the designated reference systems, $\Delta g_{OO}(r)$.

models have a liquid state structure virtually identical to that in the full SPC/E model. This very good agreement is also reflected in other properties of the hydrogen-bond network. We directly examined the hydrogen bonding capabilities of GT and GTRC water models through the calculation of the average number of hydrogen bonds per water molecules, $\langle n_{HB} \rangle$, as well as the probability distribution of a water molecule taking part in n_{HB} hydrogen bonds, $P(n_{HB})$, using a standard distance criterion of hydrogen bonds, $R_{OO} < 3.5$ Å and $\theta_{HOO'} < 30°$, where R_{OO} is the oxygen-oxygen distance and $\theta_{HOO'}$ is the angle formed by the H-O bond vector on the hydrogen bond *donating* water molecule and the O-O$'$ vector between the oxygen on the donor water (O) and the acceptor oxygen (O$'$) [29]. For both GT and GTRC water models, $\langle n_{HB} \rangle$ and $P(n_{HB})$ were calculated at temperatures ranging from 220-300 K, and were found to be nearly identical to the analogous quantities in the full SPC/E model. These findings give credence to the idea that these two truncated models reproduce the hydrogen-bond network of the full model to a high degree of accuracy.

These truncated models offer a minimal structural representation of bulk water as a fluctuating network of short ranged bonds determined mainly by the balance between the very strong electrostatic attraction between donor and acceptor charges and the very strong repulsion of the overlapping LJ cores. We can view them as primitive water models in their own right, analogous to other simplified models recently proposed, which capture very well arguably the most important

structural feature of bulk water, the hydrogen bond network, and it is instructive to see what other properties of water such minimal network models can describe. But corrections from neglected parts of the intermolecular interactions are certainly needed for bulk thermodynamic and dielectric properties and for both structure and thermodynamics of water in nonuniform environments. LMF theory provides a more general framework where the truncated models are viewed as useful reference systems that can be systematically corrected to achieve good agreement with full water models. We will use both viewpoints herein.

2.3 Simulation Details

All molecular dynamics simulations were performed using modified versions of the DL_POLY software package [30] and the SPC/E water model [15] or its variants described in Section 2. The equations of motion were integrated using the leapfrog algorithm with a timestep of 1 fs [31] while maintaining constant temperature and pressure conditions through the use of a Berendsen thermostat and barostat respectively [32].

2.3.1 Bulk water simulations

The evaluation of electrostatic interactions in bulk simulations of the full SPC/E water model employed the standard Ewald summation method using a real space cutoff of 9.5 Å, unless this was larger than half of the box length, in which case the cutoff was set to half of the box length [31]. Short-ranged electrostatic interactions in the GT and GTRC reference systems, as well as LJ interactions in all systems, were truncated at the real space cutoff length used in the analogous full system. Simulations of bulk water were performed with $N = 1000$ molecules in the isothermal-isobaric (NPT) ensemble to determine the density maximum and with $N = 256$ molecules in the canonical (NVT) ensemble to determine $P(T)$, the internal pressure, and the cascade of anomalies described below. The internal pressure in Eq. (2.8) was calculated by evaluating $\varepsilon(v)$ for numerous values of v at each T. The function $\varepsilon(v)$ was then fit to a polynomial, which was differentiated at the desired v to yield the internal pressure.

2.3.2 Simulation of nonuniform systems

In order to generate starting configurations for the LV and LS interfacial systems discussed in Section 5, we first equilibrated N water molecules in a cubic geometry, where N is listed in Table 1. The z-dimension of the system was then elongated to more than three times the x- and y-dimensions, and in the case of the LS interface, a wall potential of the form

$$U_w(z) = \frac{A}{|z - z_w|^9} - \frac{B}{|z - z_w|^3} \tag{2.2}$$

25

was added at $z_w = 0$ and the parameters A and B are given in Ref. [33]. In order to ensure water molecules did not approach the wall from $z < 0$, a repulsive wall was added at large z to constrain the water molecules to the desired region of the simulation cell while still allowing a large vacuum region for the formation of a vapor phase. Electrostatic interactions were handled using the corrected Ewald summation method for slab geometries [34] with a real space cutoff of 11.0 Å, which was also the cutoff distance for LJ and short-ranged electrostatic interactions.

2.4   Thermodynamic Anomalies

The complex structure of water, dictated by the propensity to form intermolecular hydrogen bonds, gives rise to an incredible number of anomalous thermodynamic properties [16]. Reference [16] lists at least 67 anomalous properties of water, ranging from its high boiling point, melting point, and critical temperature, to maxima and/or minima in the specific heat as a function of temperature (C_V and C_P) and its unusually high surface tension and dynamic anomalies such as a maximum in the diffusion coefficient as a function of temperature at high pressure. Herein, we utilize the above-described short ranged variants of the SPC/E water model to elucidate the molecular origins of several anomalous thermodynamic properties of liquid water. In particular, the density maximum, as well as the anomalous temperature and density dependences of the internal pressure of water are examined.

2.4.1   Density Maximum

Now we turn our attention to the thermodynamics of bulk water. For a fixed volume V, temperature T, and number of molecules N, the pressure and other thermodynamic properties of the GT and GTRC systems will not generally equal those of the full system. However, because of the accurate reference structure, we can correct the thermodynamics using simple mean-field (MF) arguments. Thus we can define the pressure in the full system to be the sum of the short-ranged reference pressure and a long-ranged correction, $P = P_0 + P_1$.

Simple corrections to the energy and pressure of the GT model from this perspective were recently derived [27]. With $\sigma = 4.5$ Å, these corrections are relatively small and were ignored in most earlier work using truncated water models but they are conceptually important in revealing the connections between truncated models and perturbation theory and are required for quantitative agreement. The pressure correction $P_1 = P_1^q$ for the GT model arises only from long-ranged Coulomb interactions and is given as

$$P_1^q = -\frac{k_B T}{2\pi^{3/2}\sigma^3}\frac{\epsilon - 1}{\epsilon},\tag{2.3}$$

where ϵ is the dielectric constant.

In the case of the GTRC model, the need for a thermodynamic correction is much more obvious since we have to correct for the absence of LJ attractions as well. Here we adopt the simple analytic correction used in the van der Waals (vdW) equation derived from WCA theory for the LJ fluid, as discussed in Ref. [3]. Thus $P_1 = P_1^q - a\rho^2$ for the GTRC potential, where

$$a \equiv -\frac{1}{2} \int d\mathbf{r}_2 \, u_1(r_{12}) \tag{2.4}$$

and u_1 is attractive part of the LJ potential. This simple approximation does not give quantitative results but does capture the main qualitative features and we use it here to emphasize the point that both the long ranged Coulomb and dispersion force corrections to bulk GTRC water can be treated by simple perturbation methods.

We can test the accuracy of these corrections by using them to help determine the temperature T_{MD} at which the density maximum of the full SPC/E water model at a constant pressure of 1 atm should occur. This can alternatively be defined as the temperature at which the thermal expansion coefficient, α_P, is zero. Accordingly, we seek to evaluate α_P using the relation

$$\alpha_P \equiv \frac{1}{v} \left(\frac{\partial v}{\partial T} \right)_P = -\frac{1}{v} \left(\frac{\partial P}{\partial T} \right)_v \left(\frac{\partial v}{\partial P} \right)_T, \tag{2.5}$$

where $v = V/N$ is the volume per particle. Using the last expression we can determine where the quantity $(\partial P/\partial T)_v = 0$ by monitoring the corrected pressure of the reference systems while changing the temperature at a fixed density. This can be done by simulation in the canonical ensemble. The fixed density ensures that the structure of the reference and full systems are very similar, as assumed in the derivation of the corrections in Eqs. (2.3) and (2.4). We can also determine T_{MD} through the first equality in Eq. (2.5) by finding where $(\partial v/\partial T)_P = 0$. Thus we simulate GT and GTRC water at constant pressures of $P_0 = P - P_1$, where $P = 1.0$ atm is the pressure in the full system. Note that the correction $P_1^q \equiv P_1^q(T; \epsilon(T))$ is temperature-dependent, as is the dielectric constant ϵ, so that we are not moving along an isobar in P_0, but an isobar in P. The temperature-dependent values of ϵ were taken to be the experimental values [35].

Figs. 2.5a and 2.5b give the density and pressure of full SPC/E water and the corrected reference models as a function of temperature. As expected, the inclusion of P_1^q in the pressure of GT water quantitatively corrects the density and pressure of this system. However, the MF correction applied to GTRC water, $P_0 = P - P_1^q + a\rho^2$, is not as accurate, although the dependence of ρ on T is qualitatively well captured. These remaining errors arise from our use of the simple van der Waals $a\rho^2$ correction for the long ranged part of the LJ potential. This level of agreement is typical when this correction is used in pure LJ fluids [3] and a full WCA perturbative treatment of the attractive portion of the LJ potential in GTRC water would likely lead to quantitatively accurate results [6].

27
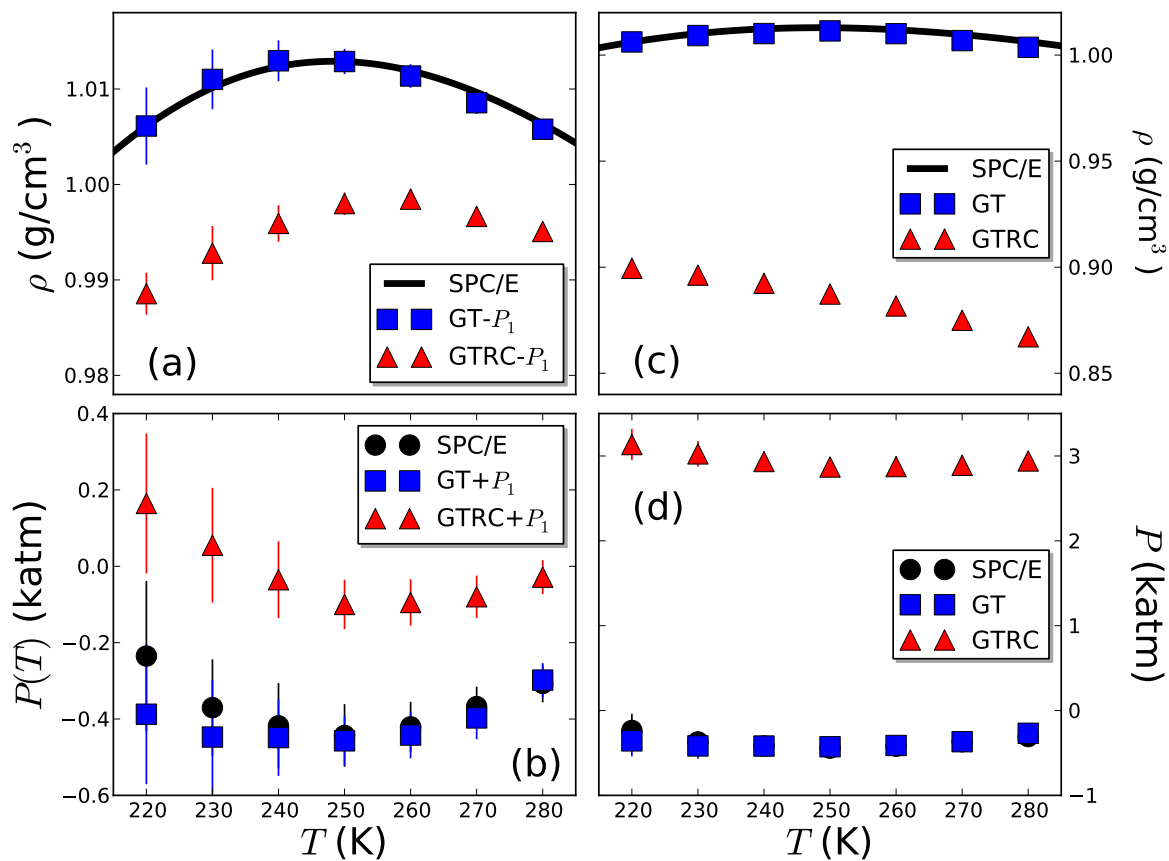
Figure 2.5: The dependence of (a) density and (b) pressure for the corrected reference models as a function of temperature. The analogous quantities for the models without MF corrections are shown in (c) and (d), respectively. $\rho(T)$ is calculated at a constant pressure of 1.0 atm and $P(T)$ is calculated at a fixed volume of $v = 30.148$ Å^3. Full SPC/E data for $\rho(T)$ at constant P was taken from the work of Ashbaugh *et al.* [36].
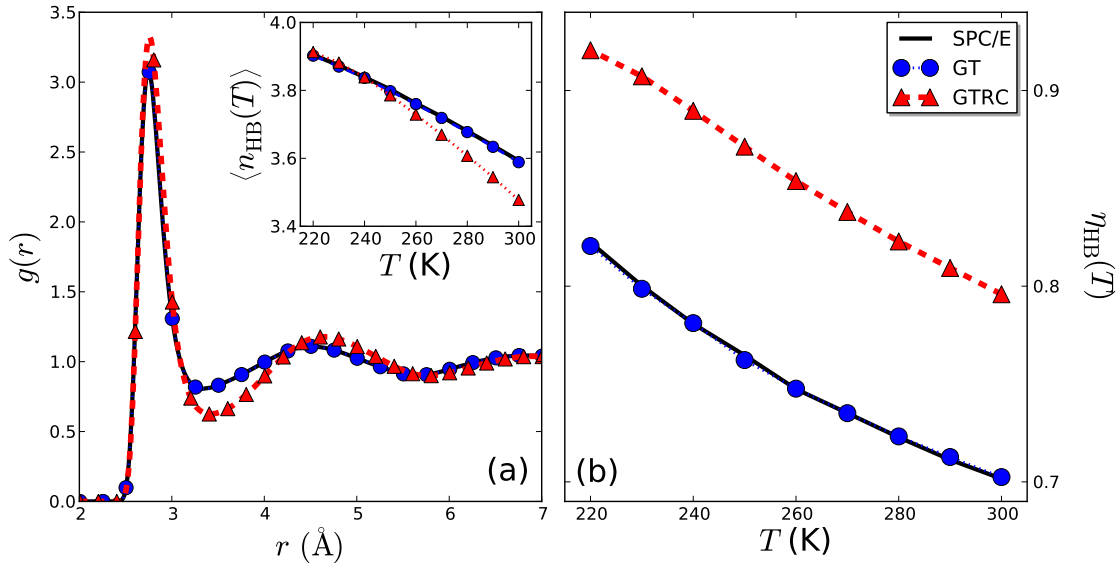
Figure 2.6: (a) The oxygen-oxygen pair distribution function, $g_{OO}(r)$, for the three water models at $T = 300$ K. *Inset*: The average number of hydrogen bonds per water molecule as a function of temperature, $\langle n_{HB}(T) \rangle$, for full and truncated water models. (b) Hydrogen bonding efficiency η_{HB} as a function of temperature. All results were obtained at a constant uncorrected pressure of 1 atm.

We now turn to the alternate and less accurate interpretation of the GT and GTRC models as primitive water models in their own right. Do these models at an uncorrected pressure of 1 atm have a density maximum and how well does it compare to that of the full model? To that end, we find where $(\partial v/\partial T)_P = 0$ in each model by varying the temperature along an isobar using MD simulations in the isothermal-isobaric ensemble at a constant pressure of 1 atm. By requiring the same pressure in the full and reference models, we probe structurally different state points in general and there is no guarantee that the density and temperature of the reference systems at a density maxima (if present) will be similar to that in the full system. Nevertheless Fig. 2.5c shows that the GT model does have a density maximum very similar to that of the full model. This is because the pressure correction to the density from the long-ranged Coulomb interactions in Eq. (2.3) is very small on the scale of the graph. In contrast, the uncorrected GTRC model does not exhibit a density maximum at $P = 1.0$ atm, even upon cooling to 50 K.

These results should be compared to earlier work where the TIP4P water potential was approximated by a simpler "primitive model" [37]. In that work, the repulsive LJ core was mapped onto a hard-sphere potential, hydrogen bonding was captured by a square-well potential, and

29

long-ranged dipole-dipole interactions were represented with a dipolar potential. The equation of state was found using a perturbative approach, and thermodynamic quantities were analyzed. The authors of Ref. [37] found that the inclusion of dispersion forces does not lead to a density maximum, and only when both dispersive interactions and long-ranged dipole-dipole interactions were taken into account did a density maximum appear.

To provide some understanding of these differing results, we analyze the structure of the uncorrected GT and GTRC reference models in comparison to the full model at the common pressure of one atmosphere. The oxygen-oxygen radial distribution functions, $g_{OO}(r)$, for each of the three water models at $T = 300$ K are depicted in Fig. 2.6a. The GT model is in good agreement with the full model, consistent with its accurate description of the bulk water density and the density maximum. In contrast, as shown later in Fig. 2.11, the coexisting liquid density of GTRC water is about about 15% lower than that of the full water model. Nevertheless the first peak of $g_{OO}(r)$ in GTRC water is *higher* than that of the full water model due to better formation of local hydrogen bonds. As shown in the inset, a molecule of GTRC water has slightly fewer hydrogen bonds on average than full and GT water models for temperatures higher than 240 K. However the hydrogen bond efficiency shown in Fig. 2.6b,

$$\eta_{HB} = \frac{\langle n_{HB} \rangle}{\langle n_{NN} \rangle}, \tag{2.6}$$

where $\langle n_{NN} \rangle$ is the average number of nearest-neighbors satisfying $R_{OO} < 3.5$ Å, indicates that GTRC water is about 10 percent more efficiently hydrogen bonded to its available neighbors at all temperatures. In this sense the low density GTRC water at $P = 1.0$ atm is structurally more ice-like than the full water model.

These results provide some insight into earlier first principles simulations of liquid water using density functional theory [38, 39, 40]. The standard exchange-correlation functionals used there can give a good description of local hydrogen bonding, but do not include effects of van der Waals interactions. These simulations produced a decrease in the bulk density of water accompanied by increased local structural order very similar to that seen here for GTRC water. Moreover, when dispersive interactions were crudely accounted for, they observed much better agreement with experiment, in complete agreement with our findings for perturbation-corrected GTRC water.

Our results indicate that van der Waals attractions play the role of a cohesive energy needed to achieve the high density present in SPC/E water at low pressure, as demonstrated by the qualitative accuracy of Eq. (2.4) and the good agreement of the GT model. Evidentially a density maximum can arise only when additional somewhat less favorably bonded molecules are incorporated into the GTRC network to produce the full water density. If the local hydrogen bond network of water at the correct bulk density is properly described, long ranged dipolar forces are not needed to obtain the correct behavior of $\rho(T)$. Indeed, LJ attractions are not needed either provided that the proper bulk density is prescribed by some other means. Thus we found that if GTRC water is kept at a high constant pressure of 3 katm, where its bulk density is close to that of the full water model at ambient

conditions, a density maximum is also observed.

2.4.2 Internal Pressure

We further employ the reference water models to explain the anomalous "internal pressure" of water [41]. For a typical van der Waals liquid, the internal pressure is given by $P_i = (\partial \varepsilon / \partial v)_T \approx a\rho^2$ for low to moderate densities, where $\varepsilon = E/N$ is the energy per molecule. In fact, it was recently shown by computer simulation that the portion of the internal pressure due to the attractions in a LJ fluid displays this $a\rho^2$ dependence even at high densities [42]. Water, on the other hand, displays a negative dependence of P_i on density. It is this anomalous behavior that we seek to explain.

We begin by partitioning the internal energy of the system as

$$\varepsilon = \varepsilon^{LJ} + \varepsilon^q, \tag{2.7}$$

where ε^{LJ} is the Lennard-Jones contribution to the energy and ε^q is the energy due to charge-charge interactions (note that the change in kinetic energy when perturbing the volume at constant T is zero, so we only consider the potential energy). We can then write the internal pressure as

$$P_i = \left(\frac{\partial \varepsilon}{\partial v} \right)_T = P_i^{LJ} + P_i^q. \tag{2.8}$$

This decomposition of P_i will allow us to determine which molecular interactions are responsible for the strange dependence of this quantity on ρ.

Fig. 2.2 suggests the following qualitative picture. At a given temperature and density the dominant hydrogen bond contribution to the energy ε is determined from the balance between strong repulsive forces from the LJ cores and strong attractions from the more slowly varying Coulomb interactions between donor and acceptor charges. The Coulomb contribution P_i^q to the internal pressure $P_i(T, \rho)$ is positive since a small positive change in volume reduces the negative Coulomb energy and similarly the LJ core contribution to P_i^{LJ} is negative. If the density is now varied at constant temperature we would expect the changes in $P_i(T, \rho)$ to be dominated by the rapidly varying LJ core forces.

Conversely, to the extent that the repulsive LJ cores are like hard spheres, they would contribute no temperature dependence to the internal pressure at fixed density. Thus we expect the more slowly varying Coulomb forces to largely determine how the internal pressure varies with temperature at fixed density. The results given below are in complete agreement with these expectations.

We evaluated Eq. (2.8) by performing MD simulations of water in the canonical ensemble for various volumes at $T = 300$ K. The dependence of the internal pressure on density at $T = 300$ K is shown in Fig. 2.7. Note that the total internal pressure, P_i, becomes increasingly negative as ρ is increased, in direct opposition to the $a\rho^2$ dependence given by the vdW equation of state. However,

31
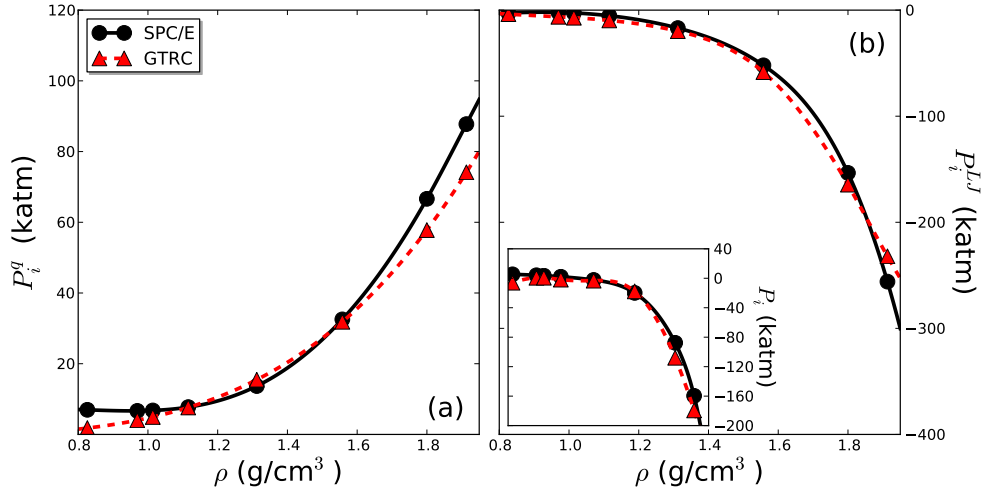
Figure 2.7: (a) The electrostatic contribution to the internal pressure, P_i^q, and (b) the analogous contribution from LJ interactions, P_i^{LJ}. The total internal pressure as a function of density is shown in the inset. Lines are guides to the eye.

it is known that as the density of a LJ fluid is increased to high values so that neighboring repulsive cores begin to overlap, the total P_i exhibits a maximum, after which the internal pressure becomes increasingly negative from the dominant contribution of the repulsive interactions [42].

As shown in Fig. 2.2 there is substantial overlap of the repulsive LJ cores between nearest neighbors in SPC/E water. The repulsive interactions from these LJ cores dominate the density dependence of both ε and P_i for SPC/E and related water models, as evidenced by the similarity of the internal pressures of both the full and GTRC water models in Fig. 2.7. Although $\varepsilon^q > \varepsilon^{LJ}$ for all density, ε^q does not exhibit very large changes upon increasing density, a direct consequence of the ability of water to maintain its hydrogen bond network under the conditions studied. Thus the density dependence of the internal pressure of SPC/E water is actually similar to that of a LJ fluid but one at a very high effective density with substantial overlap of neighboring cores.

In addition to the anomalous density dependence of P_i, the temperature dependence of the internal pressure of water has also been called an anomaly [41]. For most organic liquids (and vdW fluids), the internal pressure decreases with increasing temperature, but that of water increases when the temperature is increased, as shown in Fig. 2.8. Using the concepts presented above, we can rationalize this behavior in terms of molecular interactions. By decomposing P_i into its electrostatic and LJ components, we find that P_i^q dominates the temperature dependence of the internal pressure, increasing with increasing temperature, while P_i^{LJ} is dominated by repulsive interactions at all
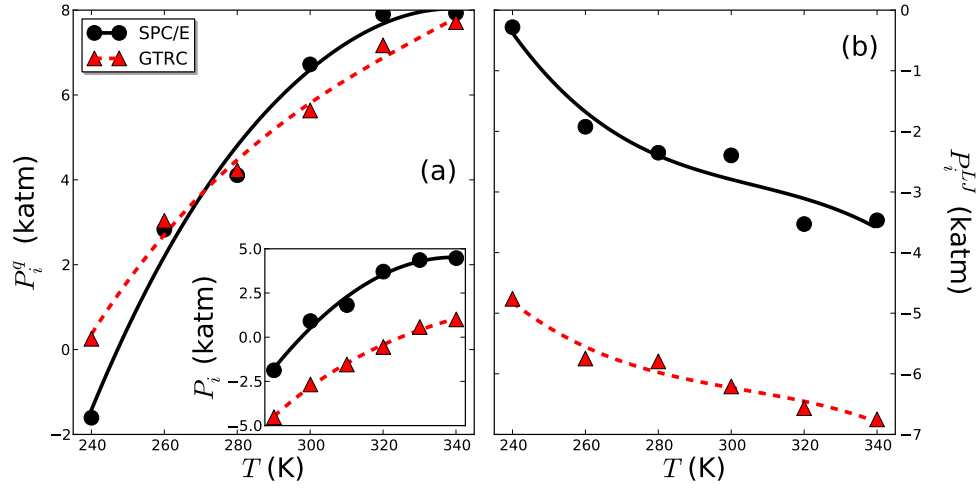
Figure 2.8: (a) The electrostatic contribution to the internal pressure, P_i^q, and (b) the analogous contribution from LJ interactions, P_i^{LJ}, both as a function of temperature at a fixed volume of $v = 29.9$ Å^3. The total internal pressure as a function of temperature is shown in the inset. Lines are guides to the eye.

temperatures studied, as evidenced by its negative value for all T. As the temperature of the system is increased, the number of ideally tetrahedrally coordinated water molecules decreases, and the hydrogen bond network becomes increasingly "flexible". Therefore, if one increases the volume of the system at high T, water will more readily expand to fill that volume. But an increase in the electrostatic energy will also occur due to a slight decrease in the number of (favorable) hydrogen bonding interactions. This will happen to a lesser extent at low temperatures, when the hydrogen bond network is more rigid and the thermal expansivity of water is lower.

2.5   The Cascade of Anomalies

In the previous sections, short-ranged water models were used to provide insight into the anomalous temperature dependence of the density, as well as the anomalous temperature and density dependence of the internal pressure of bulk water [17]. In addition, the pair structure as measured through site-site correlation functions was found to be captured by both GT and GTRC water [17]. In this section, we examine the extent to which the GT and GTRC models reproduce more complex measures of the orientational and translational ordering, as well as the dynamics of bulk SPC/E water as described by the diffusion coefficient.

33
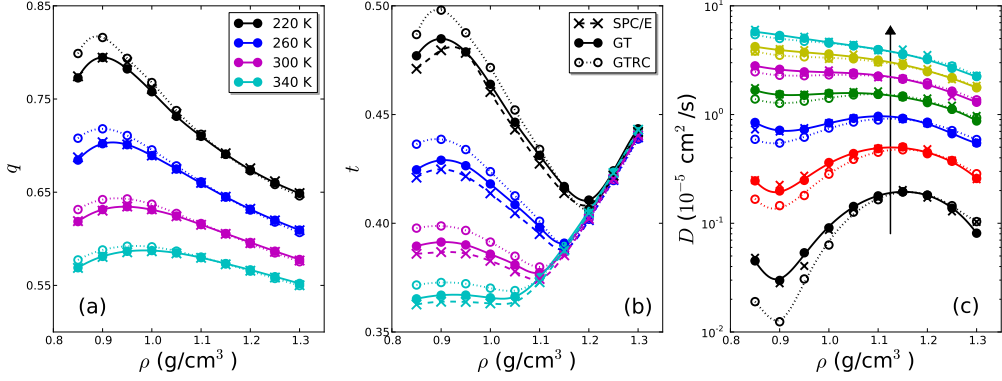
Figure 2.9: Density dependence of (a) the tetrahedral order parameter q, (b) the translational order parameter t, and (c) the diffusion coefficient D for the SPC/E, GT, and GTRC models at temperatures in the range of 220 K to 340 K. The arrow in (c) indicates the direction of increasing temperature, for $T=220$ K to $T=340$ K in steps of 20 K.

In order to quantify orientational and translational order in the various models, we utilize the order parameters defined by Errington and Debenedetti [43], q and t, respectively. The tetrahedral order parameter q is defined as

$$q = 1 - \frac{3}{8} \sum_{j=1}^{3} \sum_{k=j+1}^{4} \left(\cos \psi_{jk} + \frac{1}{3} \right)^2, \tag{2.9}$$

where ψ_{jk} is the angle formed by the vectors connected the oxygen atom of a water molecule with those if its nearest-neighbors j and k, and $0 \leq q \leq 1$, such that the lower and upper bounds on q correspond to an ideal gas and a perfect tetrahedral network, respectively.

The translational order parameter t is

$$t = \frac{1}{\xi_c} \int_0^{\xi_c} d\xi \, |h(\xi)|, \tag{2.10}$$

where $\xi = r\rho^{1/3}$ is the oxygen-oxygen distance between molecules scaled by the average separation between molecules. The cutoff distance is chosen to be $\xi_c = 2.843$, following previous work. The oxygen-oxygen pair correlation function is $h(r) = g(r) - 1$, such that $g(r)$ is the usual pair distribution function. The order parameter t quantifies the extent to which translational ordering in the fluid of interest deviates from ideal gas behavior, since $g(r) = 1$ in an ideal gas.

At high density and temperature, the order parameters q and t are in agreement for all three

models, SPC/E, GT, and GTRC. This is consistent with the idea that long-ranged forces cancel in dense fluids at high temperatures, and therefore play a negligible role in the determination of liquid structure at these state points. As the density and/or temperature is decreased, the GTRC model is more orientationally and translationally ordered than SPC/E, as evidenced by its larger values of q and t in Figures 2.9a and 2.9b. This is consistent with the above-drawn conclusion that GTRC water has a more "ice-like" H-bond network that SPC/E water, even at the same density.

The orientational ordering of GT water, on the other hand, agrees with SPC/E water for all T and ρ studied. Orientational structure in bulk water is achieved through delicate balance of short-ranged electrostatics and dispersion forces. The former leads to tetrahedral H-bonding between a water and its four nearest-neighbors, while the latter disrupts the tetrahedrality of this network by "pulling" a fifth neighbor into the coordination shell. Because GT water has both local charge-charge interactions and LJ attractions, the local, orientation structure of water is accurately captured in this model.

However, the removal of long-ranged electrostatic interactions leads to increased translational ordering at low T and ρ with respect to that of the SPC/E model. This increased translational ordering at low temperatures is due to the inability of GT water to screen dipoles at a distance much greater than σ. At these low temperatures, dipolar ordering akin to that observed between hydrophobic walls [2] but to a much lesser extent increases the translational order in the system. However, at high T, any slight long ranged dipolar ordering is disrupted by thermal fluctuations, and the translational ordering of GT water as measured by t agrees with that of the full SPC/E model at the same temperature and density.

The diffusion coefficients presented in Figure 2.9c were obtained through linear fitting of the long-time behavior of the mean-squared displacement, $\mathrm{MSD}(t) = \langle \mathbf{r}^2(t) \rangle$, and use of the Einstein relation, $6D = d\mathrm{MSD}(t)/dt$. It is found that the self-diffusivity of liquid water is intimately related to its orientational structuring, with GTRC water diffusing slower than SPC/E and GT water at state points where it has larger values of the order parameter q. The D-values obtained for SPC/E and GT water, however, are in accord for all T and ρ studied, illustrating that the subtle differences observed in longer-ranged translational order, as measured by t, have little effect on the self-diffusivity. This is consistent with the classic view of diffusion processes in liquids; a molecule "rattles" within its coordination shell on short-timescales, then, when this shell is disrupted, the molecule "hops" out of this shell and becomes part of another coordination shell. From this view, diffusion rates are a direct consequence of local ordering in the nearest-neighbor shell of a tagged water molecule, as supported by the data presented here.

We now turn our attention to the "cascade of anomalies" of each model, as defined by Errington and Debenedetti. This cascade is constructed from the locations of the minima and maxima of various order parameters as a function of ρ and T. The locations of these extrema in the $\rho - T$ plane indicate illustrate that the region of thermodynamic anomalies, as measured by the temperature of

35
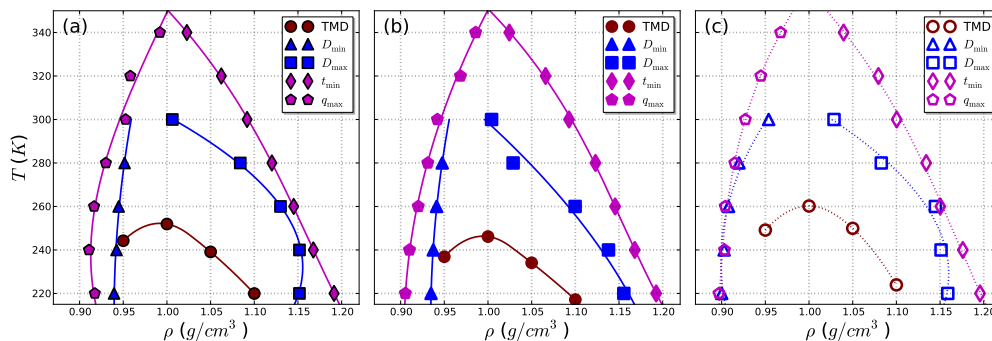
Figure 2.10: The cascade of anomalies for the (a) SPC/E, (b) GT, and (c) GTRC water models.

maximum density (TMD), is located within the region of dynamic anomalies, which, in turn is contained within the structurally anomalous region. The dynamically anomalous region is defined as that in which the diffusion coefficient increases with increasing density (or pressure), which is therefore bound by diffusion minima and maxima. The region of structural anomalies is bound from below by maxima in the orientational order parameter q (though can be equivalently obtained from maxima in t), and is bound from above by minima in the translational order parameter t, such that within the bounds, structural order decreases upon compression.

This general ordering of anomalous regions is found to be true for all three models. SPC/E and GT water have nearly identical cascades of anomalies, but the shape and width of the boundaries differ in the GTRC model. The TMD occurs at higher T for GTRC water, but the general shape is the same as the TMD boundary in SPC/E and GT water. The dynamically anomalous region is significantly wider for the GTRC water model than that in the other two models. Nevertheless, this boundary is still contained within the structurally anomalous region, which is nearly equivalent to that of the other two models.

2.6 Unbalanced forces in nonuniform aqueous media from the viewpoint of LMF theory

In contrast to uniform systems, a net cancellation of long ranged forces does not occur in nonuniform environments, and these unbalanced forces can cause significant changes in the structure and thermodynamics of the system [2, 3]. As shown above, the bulk structure of both the GT and GTRC models are very similar to that of the full water model at a given temperature and density. But interfacial structure and coexistence thermodynamic properties of the uncorrected reference models can be very different. For example, GTRC water still has a self-maintained liquid-vapor (LV)

36
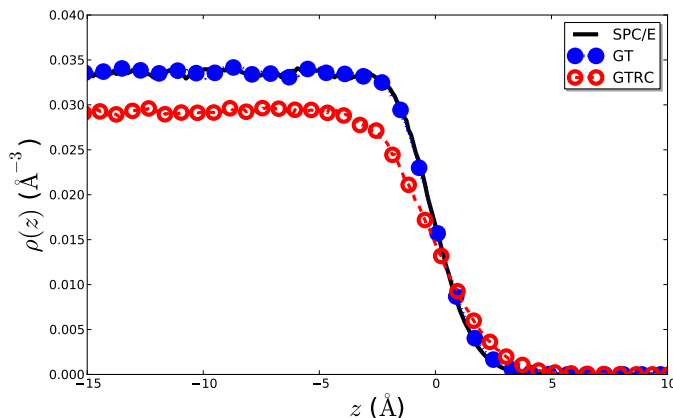
Figure 2.11: Density profiles of oxygen sites at the liquid-vapor interface of SPC/E, GT, and GTRC water models. The Gibbs dividing surface of each interface is located at $z = 0$.

interface at T = 300 K as illustrated in Fig. 2.11, even though the LJ attractions are ignored, because of the strong charge pairing leading to hydrogen bond formation. However its 90-10% interfacial width increases to $w \approx 4.9$ Å from the $w \approx 3.5$ Å seen in both GT water and the full water model, and the coexisting liquid density of GTRC water is about about 15% lower. In contrast, the density profile of the GT model with LJ interactions fully accounted for is in very good qualitative agreement with that of the full model. This strongly suggests that if local hydrogen bonding is properly taken into account, the equilibrium structure of the LV interface of water is governed mainly by long ranged LJ attractions, with long ranged dipole-dipole interactions playing a much smaller role. It is the exact balance of these long ranged interactions we seek to examine in this section.

LMF theory provides a framework in which the averaged effects of long ranged forces are accounted for by an effective external field [1]. It has previously been used mainly as a computational tool to permit very accurate determination of properties of the full nonuniform system while using a numerical simulation of the short ranged reference system in the presence of the effective field [2, 5, 44]. But the effective or renormalized field also gives a convenient and natural measure of the importance of long ranged forces in different environments. In this section we use the renormalized external fields determined directly from simulations of interfaces in the full SPC/E water model along with simulations of truncated water models to quantitatively examine the relative influence of the local hydrogen bond network and unbalanced long-ranged Coulomb and van der Waals forces.

We first consider the LV interfaces of the SPC/E, GT, and GTRC water models shown in Fig. 2.11. The removal of long-ranged electrostatics in the GT model leaves the density distribution

virtually unchanged, whereas removal of the LJ attractions in GTRC water has a substantial impact on $\rho(z)$. To understand this behavior, we focus our attention on the impact of the averaged unbalanced forces from the long-ranged electrostatic and LJ interactions, as determined in LMF theory from the effective external fields $\mathcal{V}_{\text{R1}}$ and $\phi_{\text{R1}}^{\text{LJ}}$, respectively and defined below. The unbalanced force $\mathcal{F}$ acting on an oxygen site from the LMF potentials is given by

$$\mathcal{F}_{\text{O}}(\mathbf{r}) = -\nabla_{\mathbf{r}}\phi_{\text{R1}}^{\text{LJ}}(\mathbf{r}) - q_{\text{O}}\nabla_{\mathbf{r}}\mathcal{V}_{\text{R1}}(\mathbf{r}). \tag{2.11}$$

Here q_{O} is the partial charge on the oxygen site and $\mathcal{V}_{\text{R1}}(\mathbf{r})$ is the slowly-varying part of the effective electrostatic field, given by

$$\mathcal{V}_{\text{R1}}(\mathbf{r}) = \frac{1}{\epsilon} \int d\mathbf{r}' \rho^q(\mathbf{r}') v_1 \left(|\mathbf{r} - \mathbf{r}'| \right), \tag{2.12}$$

where $\rho^q(\mathbf{r})$ is the total charge density of the system. The other contribution $\phi_{\text{R1}}^{\text{LJ}}(\mathbf{r})$ is the field arising from the unbalanced LJ attractions on the oxygen site (where the LJ core is centered), given by

$$\phi_{\text{R1}}^{\text{LJ}}(\mathbf{r}) = \int d\mathbf{r}' \left[\rho(\mathbf{r}') - \rho_{\text{B}}\right] u_1 \left(|\mathbf{r} - \mathbf{r}'| \right), \tag{2.13}$$

with $\rho(\mathbf{r})$ indicating the nonuniform singlet density distribution of oxygen sites and ρ_{B} defined as the bulk density of oxygen sites at the state point of interest [1, 3]. Since the hydrogen sites lack LJ interactions, the unbalanced LMF force acting on a hydrogen site is due exclusively to electrostatics,

$$\mathcal{F}_{\text{H}}(\mathbf{r}) = -q_{\text{H}}\nabla_{\mathbf{r}}\mathcal{V}_{\text{R1}}(\mathbf{r}). \tag{2.14}$$

Given its importance in the density distribution of water, it may seem natural to examine the components of the LMF force on the oxygen sites, $\mathcal{F}_O(z)$, shown in the inset of Fig. 2.12a. Naive examination of the relative magnitude of these force functions would lead to the conclusion that long-ranged electrostatics are the dominant unbalanced force at the LV interface. However, $\mathcal{V}_{\text{R1}}$ also interacts with hydrogen sites and one should instead consider the net forces from long ranged Coulomb and LJ interaction felt by an entire water *molecule* at these interfaces.

This ensemble averaged net molecular force $\langle \mathcal{F} \rangle$ (Fig. 2.12b) clearly indicates that the net unbalanced force at an interface is almost entirely due to long-ranged LJ attractions from the bulk, which pull water molecules away from the interface. The long-ranged Coulomb contributions to the average force on a water molecule are essentially negligible in comparison. This is not surprising since water molecules are neutral, and it has previously been shown that the small net interfacial electrostatic force simply provides a slight torque on water molecules in this region [2]. This torque has little effect on the oxygen density distribution, as illustrated by the good agreement of the GT model density profile with that of the full water model in Fig. 2.11. However, it plays a key role in

38
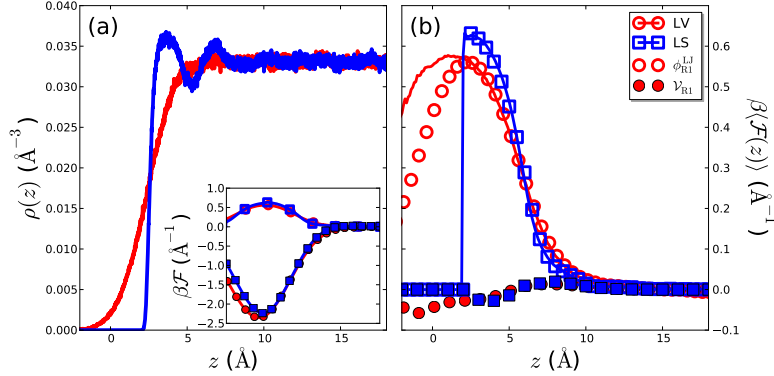
Figure 2.12: (a) Density distributions as a function of the z-coordinate for the hydrophobic LS interface and the LV interface of water. (b) Ensemble averaged net force on a water *molecule* due to $\mathcal{V}_{R1}$ (open symbols) and ϕ_{R1}^{LJ} (closed symbols) at the LV (circles) and LS (squares) interfaces. Solid lines indicate the net force due to u_1. The black dashed line at $z = 0$ Å indicates the position of the hydrophobic wall. The Gibbs dividing interface of the LV system is located at $z = 2.34$ Å, in order to make comparison with the water-wall interface. *Inset*: Forces on oxygen sites only, determined by evaluating the gradient of the corresponding LMF potentials.

determining electrostatic and dielectric properties, which are strongly affected by the behavior of the total charge density, and here the uncorrected GT model gives very poor results [1, 2].

It is also instructive to compare the unbalanced long ranged forces at the LV interface to those at the liquid-solid (LS) interface between water and a model hydrophobic 9-3 LJ wall introduced by Rossky and coworkers [45], as shown in Fig. 2.12b. Despite the large differences in the density profiles shown in Fig. 2.12a, the net unbalanced forces on molecules at the LV and LS interfaces are remarkably similar for all z until molecules encounter the harsh repulsion of the wall and an accurate sampling of $\langle \mathcal{F}(z) \rangle$ by simulation cannot be made. Water molecules can sample all regions in the liquid-vapor interface, leading to a smooth $\langle \mathcal{F}(z) \rangle$ at smaller z.

Indeed, the net molecular force due explicitly to a configurational average of the attractive $u_1(r)$ acting on molecules present at each z-position is in outstanding quantitative agreement with that arising from $\phi_{R1}^{LJ}(z)$ for all adequately sampled regions in the liquid, as illustrated by the solid lines in Fig. 2.12b. This serves largely as confirmation of the validity of the mean-field treatment inherent in LMF theory within the liquid slabs. Deviations between the two quantities for distances less than the Gibbs dividing surface are a reflection of the increasing effect of larger force fluctuations due to long-wavelength capillary waves not well described by mean field theory. The relative magnitudes of the components of $\langle \mathcal{F} \rangle$ for the LV and LS interfaces are strikingly similar, with the net unbalanced LJ force $\left\langle \mathcal{F}\left(z; \phi_{R1}^{LJ}\right) \right\rangle$ reaching its maximum value of slightly less than $k_B T/\text{Å}$ near the Gibbs dividing

interface and the repulsive boundary of the wall, respectively.

The similarities of the unbalanced forces at the LV and the hydrophobic LS interfaces of water and the dominance of the LJ attractions are completely consistent with the analogies commonly drawn between these two systems [14, 18, 46] and used in the LCW theory of hydrophobicity [3, 19, 47]. A common criticism of LCW theory is its apparent neglect of the hydrogen bond network of water and the use of a van der Waals like expression for the unbalanced force at an interface. Although some features of the network are implicitly captured by using the experimental surface tension and radial distribution function of water as input to the theory, electrostatic effects at the interface, including dipole-dipole interactions, are ignored. However, this assumption is justified since the averaged effects of long-ranged dipole-dipole interactions, accounted for by $\mathcal{V}_{R1}$, are shown to indeed be negligible at a hydrophobic interface (Fig. 2.12). LCW theory correctly describes the unbalanced LJ attractions from the bulk, which dominates the behavior at both the liquid-vapor and extended hydrophobic interfaces.

2.7   Conclusions

In this work, we have examined the different roles of short and long ranged forces in the determination of the structure and thermodynamics of uniform and nonuniform aqueous systems, using concepts inherent in classical perturbation and LMF theory. In particular, we have evaluated individually for SPC/E water the contributions of (i) all the strong short ranged repulsive and attractive interactions that lead to the local hydrogen-bonding network, (ii) longer ranged dispersive LJ attractions between molecules, and (iii) long ranged dipole-dipole interactions, and demonstrated a hierarchical ordering of their importance in determining several properties of water in uniform and nonuniform systems.

All of our truncated models accurately describe the local hydrogen bonding network, and as expected, this network alone is sufficient to match bulk structure as well as solvent structure around small hydrophobic solutes provided that the bulk density and temperature are accurately prescribed. Furthermore, the anomalous temperature and density dependence of the "internal pressure" of water is found to be dominated by the competing short-ranged repulsive and attractive forces determining the local hydrogen bonding network as well.

But local network concepts alone cannot capture all the complexities of even the simple SPC/E water model. While the dispersive LJ attractions between water molecules primarily provide a uniform cohesive energy in bulk systems, they strongly influence the structure and density profile of large scale hydrophobic interfaces. Their importance provides further support for analogies between water at extended hydrophobic interfaces and the liquid-vapor interface, and the unbalanced LJ force can be used to quantify the transition between small and large scale hydrophobicity for simple solutes.

Although the long-ranged dipolar interactions between molecules have only small effects on most of the interfacial density properties considered here, we have shown elsewhere that they are crucial in

determining dielectric properties of both bulk and nonuniform water. Indeed, as will be discussed elsewhere, we have found that electrostatic quantities may in fact be a sensitive structural probe of hydrophobicity in general environments [48].

This interaction hierarchy, wherein strong short-ranged local interactions alone determine structure in uniform environments while the longer ranged forces are needed as well to capture other properties could prove quite useful in refining simple site-site water models. Current water models incorporate a vast amount of clever engineering and empirical fine-tuning and manage to reproduce a variety of different properties through a complex balance of competing interactions with simple functional forms. Changes in the potential that improve one property generally speaking produce poorer results for several others.

One promising route to a more systematic procedure may be sensitivity analysis, in which small perturbations of potential parameters are made and the correlated response of a variety of physical observables is quantified. By perturbing the relative magnitudes of short and long ranged interactions, Iordanov *et al.* found that thermodynamic properties of bulk water are most sensitive to small changes in the LJ repulsions and the short ranged electrostatic interactions [49], in agreement with our findings. A new water model was then proposed by optimizing parameters to reproduce a specific bulk thermodynamic quantity (the internal energy) in an attempt to correct the deficiencies present in a previously developed water potential.

However, the theoretical scheme of splitting the potential described in this paper may provide a more concrete and physically suggestive path to incrementally match various known physical quantities for water without ruining the fitting of previous quantities, and one could combine an approach like sensitivity analysis with the conceptual framework presented herein to systematically optimize a specific water model.

In particular, it has recently been suggested that the accuracy with which a water model can predict the experimental T_{MD} correlates well with the accuracy that the same model displays in predicting the thermodynamics of small-scale hydrophobic hydration [36]. Arguably, the least justified feature of current simple water models like SPC/E is the functional form of the core LJ potential $u_0(r)$, especially at the very short separations relevant for describing local hydrogen bonding as illustrated in Fig. 2.2. One could try to fine-tune a GTRC-type model through alteration of the local hydrogen bond network by varying the form of the repulsive core in order to match the experimental density maximum, as well as other bulk properties like the internal pressure, in order to obtain a short-ranged system that yields accurate bulk properties. Although a detailed discussion of this process is beyond the scope of this chapter, one could try to use some type of optimization procedure to determine such potentials [49, 50, 51]. Perhaps first principles DFT simulations [38, 39] could be used to provide a more fundamental description of the local network. Subsequently, the structure and thermodynamics of nonuniform systems, which require dispersions and long ranged Coulomb interactions, could be used to parametrize the long-ranged interactions.

In a sense, hydrophobic bonds also represent a kind of hydrogen bond (or 'anti-hydrogen bond') because they arise by being unable to participate in the strong hydrogen bonding of water molecules; that is, they are stabilized by the rather strong hydrogen bonds of water.

Walter Kauzmann

3

Deconstructing Classical Water Models II: The Length Scale Dependence of Hydrophobic Hydration and Association [1]

3.1 Introduction

Hydrophobic interactions play a key role in phenomena ranging from biological processes like protein folding and membrane formation to the design of water-repellent materials [13, 14, 46]. Thus, significant effort has been devoted to studying the behavior of apolar moieties in water. In pioneering work, Stillinger argued that hard sphere solutes smaller than a critical radius R_C can be inserted into liquid water while maintaining the hydrogen bond network, but for solutes with a radius larger than R_C bonds must be broken, generating a molecular scale interface with properties resembling that of the liquid-vapor interface in water [18]. More recent work has confirmed the basic features of this idea and put the arguments on a firmer statistical mechanical foundation [3, 14, 19, 46].

While this qualitative description of the length scale dependence of hydrophobic hydration seems physically very reasonable, it focuses only on the hydrogen bond network of water and makes no mention of the van der Waals (VDW) attractions and long ranged multipolar interactions between

---

[1]Based heavily on R. C. Remsing and J. D. Weeks, *J. Phys. Chem. B*, 2013 (in press) [20].

water molecules or of the VDW attractions that would be present between a more realistic solute and the solvent. Moreover, a qualitatively similar length scale transition is seen in a dense Lennard-Jones (LJ) fluid near the triple point, with the formation of a "dry" vapor-like interface around a large hard sphere solute [3]. In that case clearly there are no hydrogen bonds and the transition is generated solely by unbalanced VDW attractive forces arising from solvent molecules far from the solute.

Consideration of such unbalanced forces is an essential ingredient in the Lum-Chandler-Weeks (LCW) theory of hydrophobicity [19], which uses the same basic framework to describe hard sphere solvation in simple liquids and in water, differing only in the thermodynamic parameters needed as input to the theory [19, 52, 53]. Indeed LCW theory has been criticized for not treating hydrogen bonds and other distinctive features of water more explicitly and there has also been considerable debate about possible effects of solute-solvent LJ attractions on the proposed length scale transition in water [46]. Thus it seems useful to explore in more detail the varying roles hydrogen bonds, VDW interactions, and long ranged multipolar interactions play in hydrophobic solvation, and to determine what analogies exist to solvation in simple, non-associating fluids.

To that end, we build on our previous work [17] using truncated water models, and exploit the underlying ideas of perturbation [6, 7] and local molecular field [1, 3] (LMF) theories of uniform and nonuniform fluids, respectively, to study hydrophobic solvation and association from small to large length scales. We employ short ranged variants of the SPC/E water model to show that small scale solvation and association in water is governed by the energetics of the hydrogen bond network alone. However when the solute is large and the hydrogen bond network is broken at the hydrophobic interface, water behaves in a manner qualitatively similar to a simple fluid, with unbalanced LJ attractions dominating the solvation behavior.

In the next section, the truncated water models are briefly introduced and our simulation methods are detailed. Section III examines the roles of unbalanced dispersion and electrostatic forces in determining the equilibrium solvation structure around small and large apolar solutes. The strength of the hydrogen bond network around small solutes is then analyzed by perturbing the hydration shell in Section IV. The role of this network in setting the length-scale for the crossover in solvation thermodynamics is then studied in Section V. The origin of entropy convergence is briefly discussed in Section VI. Finally, the hydrophobic association of model methane and fullerene molecules is studied in Section VII. Our conclusions and a discussion of the implications of this work are given in Section VIII.

3.2   Models and Simulation Details

Hydrogen bonds in most classical water models arise from "frustrated charge pairing", where an effective positive charge on a hydrogen site of one molecule tries to get close to a negatively charged acceptor site on a neighboring molecule, as discussed in the previous chapter [17]. This strong attractive interaction is opposed by the overlap of the repulsive LJ cores and the presence of other

hydrogen sites in the acceptor molecule. As a result, short ranged versions of the full water model where Coulomb interactions are truncated at distances larger than the hydrogen bond length and with only truncated LJ core interactions if desired can still give a very accurate description of the hydrogen bond network and pair correlation functions in bulk water [2, 17].

In this chapter, we use the extended simple point charge (SPC/E) model of water [15] and the short ranged variants of this model discussed in the previous chapter [17] to examine hydrophobic hydration and association as the solute perturbs the hydrogen bond network. The truncated models provide a hierarchical framework for disentangling in such classical models the separate contributions of (i) strong short ranged interactions leading to the hydrogen bond network, (ii) longer-ranged VDW attractions between water molecules and with the solute, and (iii) long ranged dipolar interactions between water molecules.

In order to compare the SPC/E water model at a pressure of $P = 1$ atm with the short ranged GT and GTRC models in the work presented below, the latter two models were simulated at corrected pressures yielding the same density using the pressure corrections described earlier [17, 27]. In the preceding chapter, it was shown that simple analytical corrections to the pressure can bring the bulk densities of these three models into quantitative agreement. All data presented in this work were obtained from molecular dynamics simulations performed in the isothermal-isobaric ensemble (constant NPT) using a modified version of the DL_POLY2.18 software package [30]. Constant temperature and pressure conditions were maintained through the use of a Berendsen thermostat and barostat, respectively [32]. The evaluation of electrostatic interactions in simulations of the full SPC/E water model employed the Ewald summation method [31].

It is instructive to compare the solvation behavior of water to that of a simple LJ fluid at an analogous state point throughout this work. Therefore, following the work of Huang and Chandler [52], we also study a LJ fluid at a state point near the triple point, where the potential is truncated and shifted at 2.5σ. This LJ fluid is studied at a reduced temperature and pressure of $T^* = k_B T/\epsilon = 0.85$ and $P^* = P\sigma^3/\epsilon = 0.022$, respectively, corresponding to a reduced density of $\rho^* = \rho\sigma^3 = 0.70$. In order to study the analogous short ranged reference fluid, we use the same repulsive force truncation of the LJ potential as was used for the GTRC water model, and study the model at a mean-field corrected pressure that accounts for the lack of LJ attractions [17].

We should emphasize that the above-mentioned short ranged GT and GTRC models are *not* being used in this paper as replacements for standard long-ranged models such as SPC/E or to give accurate representations of most properties of real water. Rather, we utilize these models as *analysis tools* to examine the different roles the hydrogen bond network as described by the GT or GTRC models, long ranged dispersions, and dipolar interactions play in determining the properties of systems containing liquid water.

However, the GT model describes very well pair correlation functions and hydrogen bond statistics in bulk water, and as we discuss further below, it also captures many features of the water density in nonuniform environments including the basic length scale transition for hydrophobic solutes [17].

But thermodynamic and particularly electrostatic properties depend sensitively on the long ranged Coulomb interactions and GT results need corrections for quantitative accuracy. Acharya and Garde [54] have recently carried out a detailed study of the strengths and weaknesses of the GT model as a simple water model in a variety of settings, including both hydrophobic and ionic solvation.

3.3 The Influence of Long Ranged Interactions on Interfacial Structure

In this section, we examine the role of the various unbalanced forces in determining the interfacial structure of water near a hydrophobic solute. The solute is considered to be a uniform density of LJ particles, such that its interaction with water can be represented by an integration of the LJ potential over the volume of the solute, resulting in the integrated "$9 - 3$" potential of Huang and Chandler [55]

$$
\begin{aligned}
U_{\text{sw}}\left(r; R_S\right) \;=\; & \pi \varepsilon_{sw} \rho \sigma_{\text{sw}}^3 \left[\frac{4}{5} \sigma_{\text{sw}}^9 \left(\frac{1}{8rr_+^8} - \frac{1}{9r_+^9} - \frac{1}{8rr_-^8} + \frac{1}{9r_-^9} \right) \right. \\
& \left. - \; 2\sigma_{\text{sw}}^3 \left(\frac{1}{2rr_+^2} - \frac{1}{3r_+^3} - \frac{1}{2rr_-^2} + \frac{1}{3r_-^3} \right) \right],
\end{aligned}
\tag{3.1}
$$

where $r_\pm = r \pm R_S$. The parameters of the potential are chosen to mimic paraffin, such that the density of LJ sites, energy, and length scale are given by $\rho = 0.0240$ Å^{-3}, $\varepsilon_{sw} = 0.882$ kJ/mol, and $\sigma_{\text{sw}} = 3.468$ Å, respectively [55]. Furthermore, in order to make this particle as hydrophobic as possible, only the repulsive part of the potential is used, such that the solute-water interaction potential used in the MD simulations is given by

$$
U_{0,\text{sw}}(r) = \begin{cases} U_{\text{sw}}(r) - U_{\text{sw}}\left(r_0\right), & r \leq r_0 \\ 0, & r > r_0 \end{cases}
\tag{3.2}
$$

where r_0 is the location of the minimum of the potential. Finally, we should note that the size of the particles is better represented through an effective hard-sphere radius, R_{HS}, rather than the size parameter R_S found in the potential. This effective radius can be estimated as [9]

$$
R_{\text{HS}} \approx \int_0^\infty dr \left\{ 1 - \exp\left[-\beta U_{0,\text{sw}}(r) \right] \right\},
\tag{3.3}
$$

where $\beta = \left(k_{\text{B}}T\right)^{-1}$, and will be reported as R_{HS} herein.

The hydration structure around small solutes has been postulated to be a direct consequence of the need for water to maintain its hydrogen bond network. A small solute can be "inserted" into bulk

45
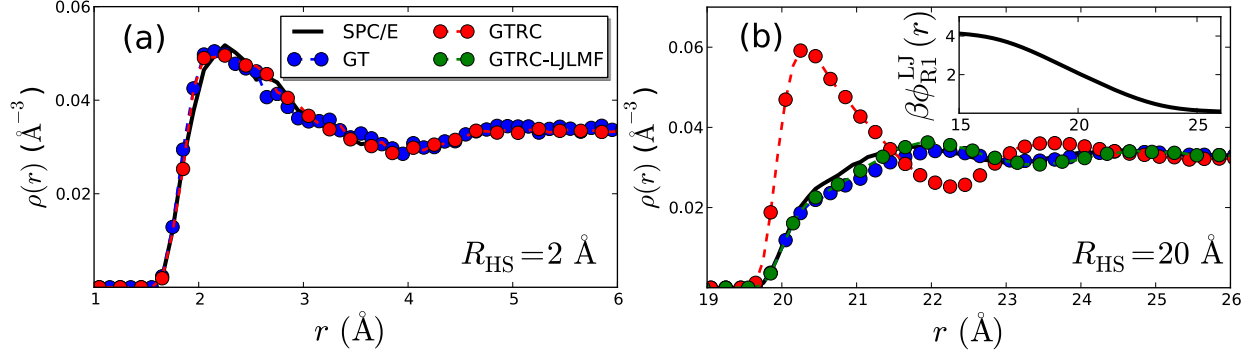
Figure 3.1: Density distributions around solutes of radii $R_{\mathrm{HS}} \approx 2$ Å (a) and $R_{\mathrm{HS}} \approx 20$ Å (b). The inset in (b) depicts the renormalized portion of the LJ LMF for GTRC water in units of $k_{\mathrm{B}}T$.

water with the network continuing around the solute without breaking hydrogen bonds. Indeed, in the small solute regime we find that the nonuniform densities of GT and GTRC models around an apolar particle are nearly identical to that of the full SPC/E water, dramatically confirming that local hydrogen bonding dictates the hydration structure in this limit (Figure 3.1a).

In the large solute limit, Figure 3.1b, the density profiles of SPC/E and GT water are still very similar, demonstrating that long ranged electrostatic interactions have an almost negligible influence on this measure of interfacial structure. GTRC water, on the other hand, has a $\rho(r)$ markedly different from that of SPC/E water.

Removal of the LJ attractions from the bulk liquid in GTRC water eliminates the phenomena of drying, and it evidentially wets the surface of the solute. According to LMF theory [1], we can account for the averaged effects of the neglected LJ forces by using a renormalized solute field

$$\phi_{\mathrm{R}}^{\mathrm{LJ}}(\mathbf{r}) = U_{0,\mathrm{sw}}(r) + \int d\mathbf{r}' \left[\rho_{\mathrm{R}}(\mathbf{r}') - \rho_{\mathrm{B}}\right] u_1 \left(|\mathbf{r} - \mathbf{r}'|\right), \tag{3.4}$$

where quantities obtained in the presence of the effective field are indicated by the subscript 'R' throughout this work, ρ_{B} is the bulk density of the fluid, and $u_1(r)$ is the attractive portion of the LJ potential. The use of this renormalized field recovers drying behavior and brings the density profile of GTRC water into qualitative agreement with that of the SPC/E and GT models, as illustrated by the curve labeled 'GTRC-LJLMF' in Figure 3.1b. The renormalized portion of the LMF, $\phi_{\mathrm{R}1}^{\mathrm{LJ}}(\mathbf{r}) \equiv \phi_{\mathrm{R}}^{\mathrm{LJ}}(\mathbf{r}) - U_{0,\mathrm{sw}}(r)$, provides an effective force that pushes solvent molecules away from the solute, as shown in the inset of Figure 3.1b.

From the data presented in Figure 3.1, we can conclude that the unbalanced forces arising from LJ attractions are the driving force for drying at extended hydrophobic interfaces. Indeed, we have

46

previously shown that the net force on a water molecule at an extended hydrophobic interface from long ranged electrostatics is much smaller than that from LJ attractions [17]. Nevertheless, long ranged electrostatics play a subtle but important role in determining the orientational preferences of water and properties dependent upon this orientational structure. One such quantity is the electrostatic or polarization potential $\Phi(r)$ felt by a test charge

$$\Phi(r) = -\int_0^r dr' \mathcal{E}(r') = -\int_0^r \frac{dr'}{r'^2} \int_0^{r'} dr'' r''^2 \rho^q(r''), \tag{3.5}$$

where $\rho^q(\mathbf{r}) \equiv \langle \sum_i q_i \delta(\mathbf{r} - \mathbf{r}_i) \rangle$ is the ensemble averaged charge density of the system and $\mathcal{E}(r)$ is the electric field due to the polarization of water molecules induced by the presence of the solute.

The polarization potential of SPC/E water, shown in Figure 3.2a, reaches a constant value of approximately 500 mV in the bulk region, consistent with previous determinations of interface potentials at extended hydrophobic interfaces for this water model [2]. Removal of the long ranged electrostatic interactions in GT water leads to an approximate charge density that does not predict this plateau in the bulk region, Figure 3.2a. Thus there is a net electric field $\mathcal{E}(r)$ in this system, even far from the solute surface as shown in Figure 3.2b. The appearance of a non-vanishing electric field in the bulk of GT water is associated with an over-orientation of interfacial OH bonds toward the solute surface. This is evidenced by a larger peak at $\theta_{\mathrm{OH}} \approx 0°$ in the probability distribution $P(\theta_{\mathrm{OH}})$ for interfacial GT water molecules in comparison to that observed for SPC/E water, shown in Figure 3.2c, where θ_{OH} is the angle formed by the OH bond vector and the oxygen-solute vector

The increase in the number of OH groups pointing toward the interface in GT water is driven by the tendency to maintain the hydrogen bond network alone. This results in the formation of an overly ordered dipole layer at the interface, demonstrated by the peak at $\theta_\mu \approx 60°$ in $P(\theta_\mu)$, shown in Figure 3.2d, where θ_μ is the angle formed by the dipole vector of water and the oxygen-solute vector. Without long ranged dipole-dipole interactions, water far from the surface does not respond to the presence of this dipole layer, and $\mathcal{E}(r)$ remains non-zero well into the bulk region. However, we can compensate for the averaged effects of the long ranged electrostatics through the introduction of the electrostatic LMF for an uncharged solute [1]

$$\mathcal{V}_{\mathrm{R}}(\mathbf{r}) = \int d\mathbf{r}' \rho_{\mathrm{R}}^q(\mathbf{r}') v_1(|\mathbf{r} - \mathbf{r}'|), \tag{3.6}$$

where $v_1(r) = \mathrm{erf}(r/\sigma)/r$ is the long ranged, slowly varying component of $1/r$, separated with a smoothing length $\sigma = 4.5$ Å [17] herein, and in general σ should be chosen to be greater than the nearest-neighbor distance in a fluid [1]. Inclusion of this renormalized solute potential in the GT water system leads to quantitative accuracy of both the electrostatic and orientational structure of interfacial water, evidenced by the curves labeled GT-LMF in Figure 3.2.

47
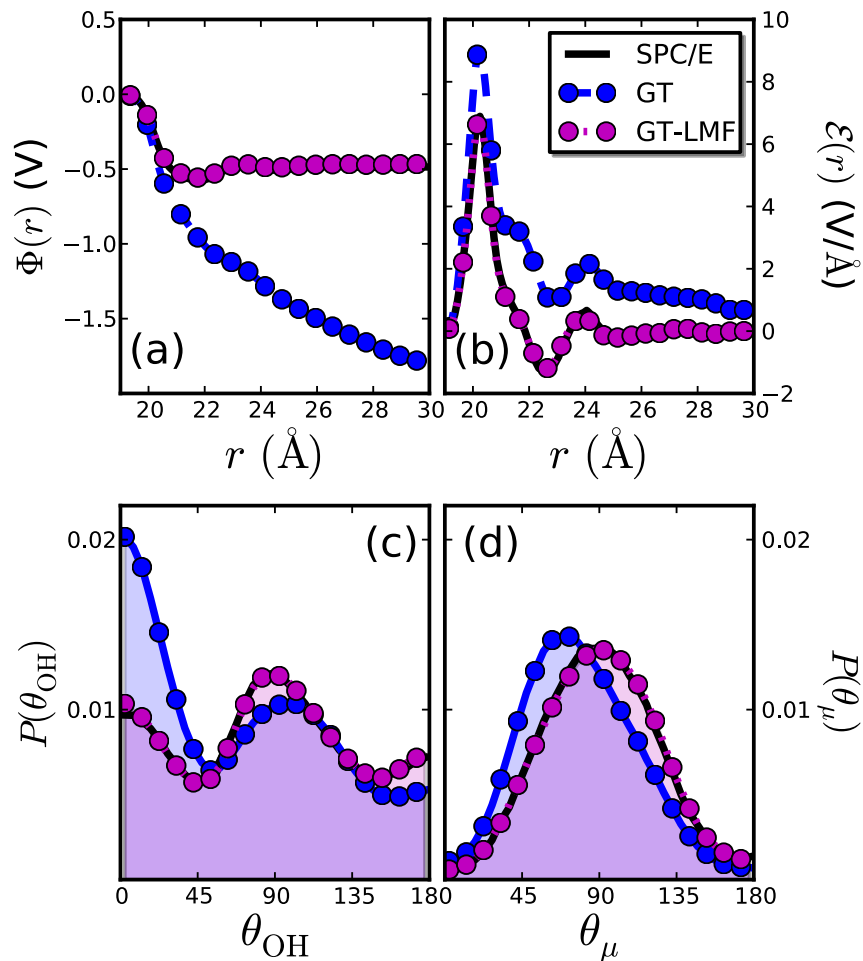
Figure 3.2: (a) Polarization potential $\Phi(r)$ and (b) the corresponding electric fields $\mathcal{E}(r)$ obtained for a solute of $R_{\mathrm{HS}} \approx 20$ Å in SPC/E and GT water, as well as for GT water in the presence of the electrostatic LMF (GT-LMF). (c) Probability distributions of the angle formed by the OH bond vector and the vector connecting the oxygen site with the center of the solute (θ_{OH}), for molecules within 1 Å of the solute surface for the three systems shown in (a). The analogous distributions for the dipolar angle θ_μ are shown in (d).

In his seminal work on nonpolar solutes in aqueous solutions, Stillinger deduced that orienting an OH bond toward the interface provides the least energetic detriment to the hydrogen bond network of water [18]. In GT water there are no opposing long ranged electrostatic interactions and the energetics of the hydrogen bond network alone determines the orientational preferences of water at the interface. However, this results in too high a probability of pointing an OH bond toward the interface, illustrating that while hydrogen bonding is a major driving force in determining the structure of water around large apolar solutes, it is not the sole determinant of the observed orientational preferences of interfacial water.

In an earlier contribution, Stillinger and Ben-Naim initially postulated that the dipole and quadrupole moments of water lead to a mean torque on a molecule at the interface with its vapor that orients the dipole moment of an interfacial water molecule toward the bulk liquid [56]. This behavior is reflected in the change of $P(\theta_\mu)$ upon the inclusion of long ranged interactions through $\mathcal{V}_\mathrm{R}$, which provides the slowly-varying torque necessary to slightly turn the molecular dipoles of interfacial water in the direction of the bulk and obtain the desired orientational structure, evidenced by the distributions $P(\theta_\mu)$ shown in Figure 3.2d. Therefore, the orientational structure of water at extended hydrophobic surfaces is a result of a delicate balance of the energetics of the hydrogen bond network *and* the mutipolar interactions arising from the electrical asymmetry of a water molecule, with the former dominating.

3.4 The Response of Interfacial Water to Unbalanced Forces

In this section, we examine the response of short ranged reference systems around solutes of varying sizes to the presence of very strong unbalanced forces like those seen in reality only for very large solutes. This provides a stringent test of the stability of the hydrogen bond network around small solutes even when subjected to strong perturbations. In order to accomplish this task, we scale the long ranged LJ LMF determined for a large solute of radius $R_\mathrm{HS} \approx 20$ Å by its radius, and then rescale the field to the desired solute size, $\tilde{R}_\mathrm{HS}$,

$$\tilde{\phi}_\mathrm{R1}\left(r; \lambda, \tilde{R}_\mathrm{HS}\right) = \lambda\phi_\mathrm{R1}^\mathrm{LJ}\left(\frac{\tilde{R}_\mathrm{HS}}{R_\mathrm{HS}}r; R_\mathrm{HS}\right). \tag{3.7}$$

where $\phi_\mathrm{R1}^\mathrm{LJ}(\mathbf{r})$ is the slowly-varying renormalized portion of the LMF shown in the inset of Figure 3.1b. Here the notation $\phi_\mathrm{R1}^\mathrm{LJ}(r; R_\mathrm{HS})$ indicates that the field $\phi_\mathrm{R1}^\mathrm{LJ}$ is a function of r and that it was determined when a solute of radius R_HS is fixed at the origin. The fictitious, rescaled LMF is indicated by $\tilde{\phi}_\mathrm{R1}$, and the coupling parameter λ is used to further adjust the magnitude of this field. In effect we have taken the large unbalanced LJ force around a large solute, which Figure 3.1b shows is strong enough to significantly perturb the large scale density profile of GTRC water when corrected with LMF theory, and artificially applied it to a small scale system like that in Figure 3.1a

with an intact local hydrogen bond network. This provides insight into the very different response interfaces around small and large hydrophobic solutes have to repulsive forces over a wide range of magnitude as λ is varied, including exceptionally large unbalanced forces seen in reality only near large hydrophobic solutes.

In order to quantify the response of water to strong unbalanced forces, we focus on the λ-dependence of the average number of water molecules in the solute solvation shell, $\langle N(\lambda) \rangle_{\tilde{\phi}_{R1}}$, as well as the corresponding response function

$$\chi(\lambda) = -\frac{1}{\langle N(0) \rangle_{\tilde{\phi}_{R1}}} \left(\frac{\partial \langle N(\lambda) \rangle_{\tilde{\phi}_{R1}}}{\partial \lambda} \right), \tag{3.8}$$

where $\langle \cdots \rangle_{\tilde{\phi}_{R1}}$ indicates that the ensemble average is performed in the presence of the field $\tilde{\phi}_{R1}\left(r; \lambda, \tilde{R}_{HS}\right)$. The function $\langle N(\lambda) \rangle_{\tilde{\phi}_{R1}}$ is calculated for distances $r < r_{\min}$, where $r_{\min}$ is defined as the distance at which the density distribution in the absence of the field reaches its first minimum.

In the large scale hydration regime the broken hydrogen bonds in the interfacial region effectively permit the interface to detach from the solute and the interface is "soft" and fluctuating. We expect water to have a response qualitatively similar to that of simple liquids where drying occurs with increasing strength of $\tilde{\phi}_{R1}$. However, in the small length scale limit, while network fluctuations certainly occur, the hydrogen bond network is basically maintained around the solute. We thus expect that the small scale solute-water interface is "stiff" and highly resistant to perturbations unless they are strong enough to break hydrogen bonds. This should lead to behavior that is fundamentally different from that of a simple LJ fluid, which lacks such strong, local interactions.

As postulated above, in the large solute regime, the behavior of $\langle N(\lambda) \rangle_{\tilde{\phi}_{R1}}$ and $\chi(\lambda)$ are qualitatively similar for both GTRC water and the WCA fluid (Figures 3.3b and 3.3d). Gradual dewetting is observed with increasing field strength, until no molecules are present in the solvation shell region at high values of the coupling parameter. In fact, as λ is increased, a peak in the response function χ is observed, indicative of a drying transition in the hydration shell of the solute; the details of the transition differ between GTRC water and the WCA fluid due to differences in state points and interaction potentials.

In the small solute regime, the WCA fluid displays signatures of a drying transition completely analogous to those seen in the large solute case with a simple shift in λ. GTRC water, on the other hand, does not display characteristics of such nanoscale dewetting (Figures 3.3a and 3.3c); $\langle N(\lambda) \rangle_{\tilde{\phi}_{R1}}$ stays roughly constant and the response function fluctuates about zero. Using a typical geometric definition of a hydrogen bond [17, 29], we find that the average number of hydrogen bonds per molecule, for waters located between the solute and the position of the first maximum in the corresponding $\rho(r)$, fluctuates around 3.5 for all $\lambda \geq 0$, very close to the bulk value of 3.6 hydrogen bonds per water molecule. Therefore, the hydrogen bond network is maintained around the small
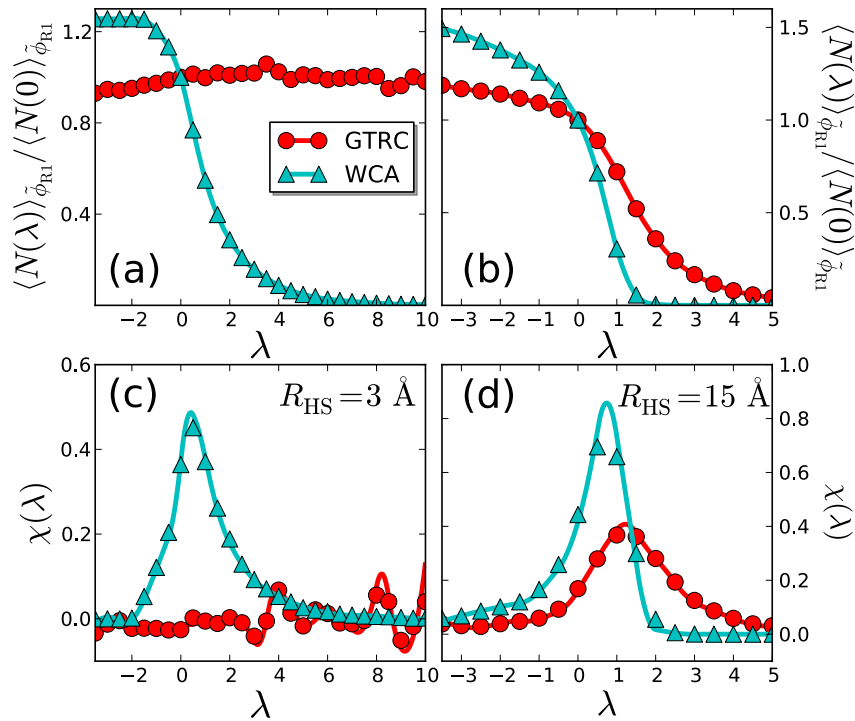
Figure 3.3: Average number of truncated water and LJ molecules in the first solvation shell as a function of the coupling parameter λ for solutes of radii $R_{\mathrm{HS}} \approx 3$ Å (a) and $R_{\mathrm{HS}} \approx 15$ Å (b). Results are shown for both GTRC water and the WCA fluid (with the LJ parameters of SPC/E water), and $\langle N(\lambda) \rangle_{\tilde{\phi}_{\mathrm{R1}}}$ has been normalized by its value in the case of zero field in order to make comparisons between the two fluids. The corresponding response functions are shown in (c) and (d), respectively. Solid lines in (a) and (b) are spline fits to $\langle N(\lambda) \rangle_{\tilde{\phi}_{\mathrm{R1}}}$ and those in (c) and (d) are the negative derivatives of the corresponding fits.

solute for all studied values of λ, and the strong local interactions of the hydrogen bond network prohibit drying at the solute surface, even in the presence of the extremely large external fields considered herein.

The above-described results indicate that the underlying physics behind the solvation behavior in a LJ fluid is qualitatively similar in the small and large length scale regimes, dependent only on the magnitude of the unbalancing potential arising from the bulk, while that of water qualitatively differs in the two regimes. In the large length scale regime, water behaves in a manner similar to a LJ fluid, with the unbalanced LJ attractions having a substantial impact on the solvation structure. For solutes smaller than the crossover radius, however, water wets the surface of the solute even in the presence of extremely large (though fictitious) unbalancing potentials; the hydration shell remains intact due to the great strength of the local hydrogen bond network. Therefore, interfacial fluctuations and the physics dictating where the length scale transition occurs is different for water than for simple, non-hydrogen bonding fluids.

3.5   Hydrogen bonding sets the scale for the crossover in hydration thermodynamics

The above-described physical balance between hydrogen bonding and interfacial unbalancing potentials also plays a key role in the solvation thermodynamics of apolar solutes. Gibbs free energies of solvation, ΔG, were calculated by performing equilibrium simulations of solutes with effective hard sphere radii $R_{\mathrm{HS}} \leq 13$ Å in increments of $\Delta R_{\mathrm{HS}} \approx 0.5$ Å. Due to poor phase space overlap between neighboring windows, ΔR_{HS} was decreased to 0.25 Å to determine ΔG for solutes with $R_{\mathrm{HS}} > 7$ Å solvated by GTRC water. The solvation free energies presented herein were calculated using the Bennett acceptance ratio or BAR [57, 58] method. To emphasize the crossover in the scaling behavior of the solvation free energies, we normalize ΔG by the surface area of the apolar solute (Figure 3.4), $\Delta \tilde{G} = \Delta G / 4 \pi R_{\mathrm{HS}}^2$.

In the small solute regime, $R_{\mathrm{HS}} \leq R_C \approx 5.0$ Å, the hydration free energies are in agreement for all three models. This illustrates that the hydration thermodynamics of small, nonpolar solutes are dictated by the local structure of water alone, as would be expected from the conclusions drawn above regarding solvation in the SPC/E, GT, and GTRC models. Indeed, the dominant role of local structure in the small solute regime is not restricted to water, as indicated by the agreement of the solvation free energies for LJ and WCA fluids for small solute sizes shown in Figure 3.4b.

The free energy for large solutes scales with surface area in both SPC/E water and the LJ fluid, and here long ranged interactions become increasingly important. Only small differences in ΔG are observed between SPC/E and GT water, reflecting the relatively small role of long ranged electrostatics in hydrophobic hydration [17]. LJ attractions, on the other hand, make a substantial contribution to the hydration free energy. Indeed because of the absence of these attractions, GTRC water completely lacks the plateau in $\Delta \tilde{G}$ for large solute sizes.

The behavior of the GTRC water model can be explained by noting that in the large solute regime,
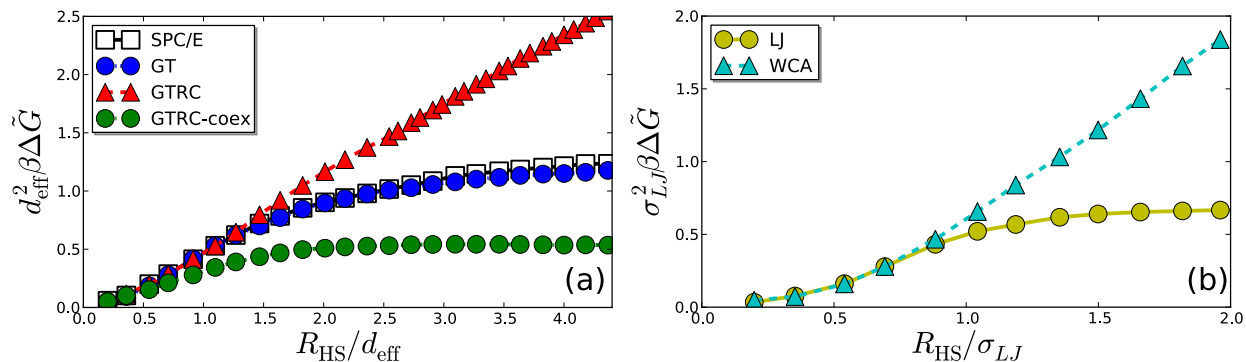
Figure 3.4: Solvation free energies of apolar spheres per unit solute area as a function of solute radius, scaled by the effective diameter of a corresponding solvent molecule ($d_{\mathrm{eff}} = 2.75$ Å for water), for (a) SPC/E, GT, and GTRC water models, as well as (b) a LJ fluid and its corresponding WCA reference system. Error bars are smaller than the symbols shown.

$\Delta G \sim PV_S + \gamma A_S$, where V_S and A_S are the volume and surface area of the solute, respectively, P is the pressure of the system, and γ is the solute-water surface tension. In order to obtain the same bulk density as SPC/E water at a pressure of 1 atm, the GTRC model must be maintained at a pressure of roughly 3 katm. At this state the GTRC water model is far from liquid-vapor coexistence, and the pressure is large enough to make the PV_S term dominate the behavior of ΔG for large solutes.

However we have previously shown that GTRC water can indeed have a self-maintained liquid-vapor interface, but at a lower bulk density close to that of ice. The interface is maintained by the strong short ranged Coulomb attractive forces between donor and acceptor sites and the need to preserve as many hydrogen bonds as possible [17]. However, because there are no unbalanced forces from LJ attractions, the surface tension is much smaller than that of the full SPC/E model.

As shown in the curve labeled "GTRC-coex" in Figure 3.4a, the solvation free energies in GTRC water near coexistence in both the small and large solute regimes are smaller in magnitude than those in SPC/E water. However it exhibits essentially the same crossover radius as the full SPC/E model and scales with solute surface area for large solutes. The behavior of ΔG below the crossover radius can be understood from our previous results for the bulk structure of the GTRC model near coexistence [17]. The bulk coexistence density is close to that of ice and the hydrogen bond network has a more ordered tetrahedral structure that can more readily accommodate the formation of a cavity than is the case for SPC/E water.

Although the solvation free energies of apolar solutes in water and in the LJ fluid exhibit qualitatively similar crossover behavior, they differ in one important respect: the length scale at which

the crossover in solvation behavior occurs. For the LJ fluid, the crossover radius is approximately equal to the diameter of a solvent particle. At this solute size, the unbalanced forces from the LJ attractions of the bulk region become large enough to "pull" particles away from the solute surface, leading to drying.

Although unbalanced LJ forces also exist when apolar particles of similar size are solvated by water, the possible disruption of strong local hydrogen bonds between interfacial water molecules dominates the energetics, and the crossover occurs only when water is not able to maintain this network. This leads to an estimate for the crossover radius, $R_C \approx 5$ Å, almost twice the diameter of a water molecule (2.75 Å) and significantly larger than that found in a LJ fluid. As shown above, hydrophobic solvation in GTRC water near coexistence also displays a crossover in its scaling behavior at a value of R_C essentially the same as that of the full SPC/E model. Because GTRC water accounts only for the hydrogen bond network, we can conclusively say that the crossover in solvation behavior is determined by the hydrogen bond network of water alone, occurring when the solute size is increased to a point beyond which it is impossible for this network to remain intact, consistent with the original arguments of Stillinger [18].

Given the importance of the hydrogen bond network for small scale solvation in water, how can we rationalize the success of the LCW theory [19] and related lattice models incorporating similar physics [47, 59], which lack an explicit description of hydrogen bonds? These theories correctly describe the small scale physics driven by Gaussian density fluctuations in the bulk solvent and the large scale physics dominated by the formation of a vapor-like interface around a large repulsive solute. Effective parameters controlling the transition between the two regimes are fit to experimental data for each particular solvent.

The key experimental parameters determining the transition length scale in the LCW theory are the liquid-vapor surface tension, and the bulk density and compressibility. The small compressibility and large surface tension of water compared to a LJ fluid implicitly accounts for the strength of the hydrogen bond network in bulk water and the difficulty of disrupting it by interface formation for large solutes. This allows the LCW theory to qualitatively describe the different transition length scales in both water and a LJ fluid [52] using the same basic framework. But LCW theory uses mean field ideas and square gradient and other approximations, and errors are seen in its detailed predictions for certain other properties like the interface width [52]. More detailed approaches describing structure and fluctuations in both small and large length scale regimes are needed for quantitative calculations.

More recent work by Rajamani, Truskett, and Garde [60] has clarified the relation between bulk thermodynamics and the crossover radius. They suggested that the crossover radius is proportional to the Egelstaff-Widom length scale $l_{\text{EW}} = \gamma \kappa_T$, the product of the liquid-vapor surface tension γ and the isothermal compressibility κ_T [61]. Quantitative agreement can be achieved by using a microscopic compressibility that depends on the solute volume rather than the long wavelength bulk compressibility in conjunction with the solute-water interfacial tension to estimate the crossover

radius R_C.

A simple but stringent test of this idea is to compare the Egelstaff-Widom length scale of GTRC water near liquid-vapor coexistence to that of SPC/E water. As discussed above, the crossover radius in GTRC water is essentially the same as in SPC/E water. This is easily rationalized from our microscopic understanding of the very similar behavior of the hydrogen bond network around the solute in GTRC and SPC/E water. If this simple physics is reflected in the Egelstaff-Widom length scale, this too should be nearly the same although both the surface tension and bulk compressibility differ considerably in the two models.

Indeed, the compressibility κ_T^{GTRC} of GTRC water at $T = 300$ K and a pressure of 1 atm is 0.087 katm^{-1}, roughly a factor of two larger than that of SPC/E at the same state point, 0.045 katm^{-1}, while the surface tension of the GTRC model $\gamma^{\text{GTRC}} \approx 27$ mN/m, is about half of that of the SPC/E model $\gamma^{\text{SPC/E}} \approx 54.7$ mN/m. Here the value for SPC/E water was taken from the work of Sedlmeier and Netz [62] and the surface tension of GTRC water was estimated by extrapolating the solvation free energies $\Delta \tilde{G}(R_{\text{HS}})$ presented in Section V to the limit $R_{\text{HS}} \to \infty$. Thus, the Egelstaff-Widom length scales of SPC/E and GTRC water are nearly equal, $l_{\text{EW}}^{\text{SPC/E}} = 0.24$ Å and $l_{\text{EW}}^{\text{GTRC}} = 0.23$ Å, respectively, as expected.

3.6 Entropy convergence is a consequence of the hydrogen bond network

The temperature dependence of hydrophobic hydration also displays features distinct from solvation in typical van der Waals liquids. Specifically, hydration free energies ΔG of small apolar particles increase with increasing temperature along a significant portion of the coexistence curve until a maximum is reached. Above this temperature, free energies of solvation decrease with increasing temperature, a behavior typical of most fluids. Associated with this region of anomalous solvation is the phenomenon of *entropy convergence*, in which the hydration entropies, $\Delta S = -(\partial \Delta G / \partial T)_P$, intersect near a temperature of 400 K for a large range of solute sizes, although the location of the hydration free energy maximum varies somewhat with solute size. Analogous to the discussion of the crossover length scale, the explanation of entropy convergence typically uses thermodynamic arguments, citing the small and nearly constant compressibility of water along the liquid-vapor coexistence line, relative to organic solvents [63, 64, 65], although explanations exist that do not hinge on the relative incompressibility of bulk water [66].

In this section, we show that entropy convergence in water arises from the hydrogen bond network through its impact on bulk thermodynamics by studying the temperature dependence of hard sphere solvation in the SPC/E and GTRC water models near liquid-vapor coexistence. Simulations of bulk SPC/E and GTRC water were carried out at a pressure of 1 atm and temperatures ranging from 275K–500K and 225K–425K, respectively. Hard sphere solvation free energies in the small solute
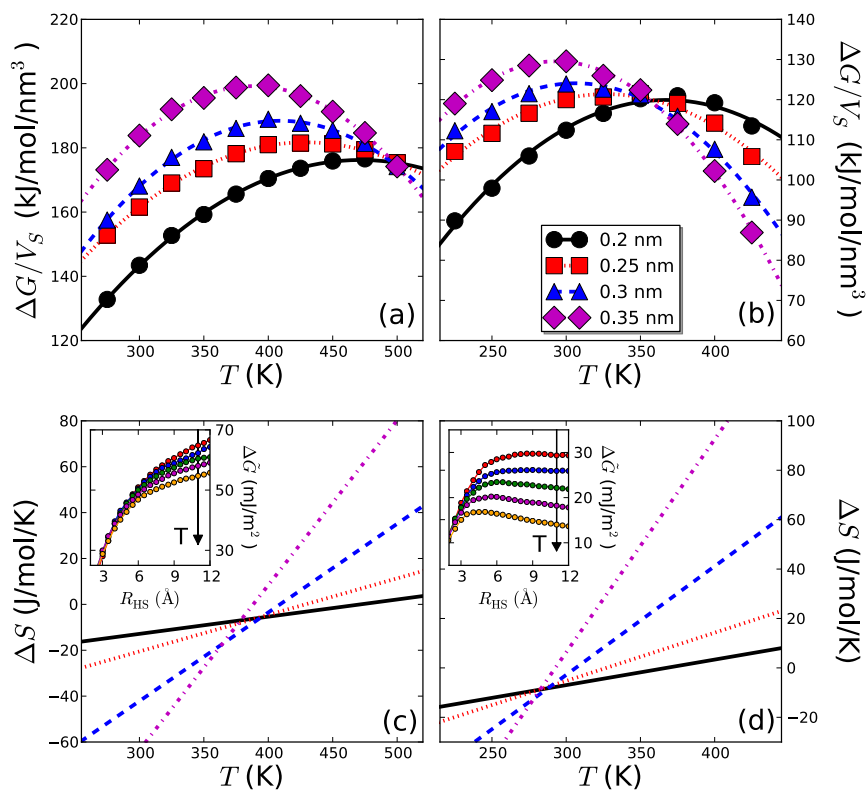
Figure 3.5: Hard sphere solvation free energy ΔG per unit solute volume V_S as a function of temperature in (a) SPC/E and (b) GTRC water. The corresponding entropies of solvation ΔS as a function of T are shown in (c) and (d), respectively. Hard sphere radii are indicated in the legend. Solvation free energies as a function of solute size for $T = 300$ K, 325 K, 350 K, 375 K, and 400 K are shown in the insets of (c) and (d) for the SPC/E and GTRC models, respectively. The arrows point in the direction of increasing temperature.

regime were determined by assuming Gaussian bulk density fluctuations [63, 64, 67],

$$\Delta G \approx \frac{k_{\mathrm{B}} T \rho_{\mathrm{B}}^2(T) V_S^2}{2\sigma_{V_S}(T)} + \frac{k_{\mathrm{B}} T}{2} \ln\left[2\pi\sigma_{V_S}(T)\right], \tag{3.9}$$

where $\sigma_{V_S} = \langle(\delta N)^2\rangle_{V_S}$ is the mean squared fluctuation in the number of molecules N in a solute-sized probe volume V_S, with $\delta N = N - \langle N\rangle_{V_S}$, and we consider the volume $V_S = 4\pi R_{\mathrm{HS}}^3/3$ of a spherical solute of radius R_{HS} herein. These solvation free energies were then fit to $\Delta G(T) = a + bT - cT^2$, and are plotted as lines in Figures 3.5a and 3.5b. Solvation entropies were determined from the negative derivative of these fits, and are shown in Figures 3.5c and 3.5d.

The temperature dependence of hard sphere solvation is qualitatively similar in both SPC/E and GTRC water. In fact, entropy convergence is observed in the GTRC model, albeit at a convergence temperature $\tilde{T}$ approximately 100 K less than the convergence temperature in SPC/E water; $\tilde{T}_{\mathrm{SPC/E}} = 387 \pm 8$ K and $\tilde{T}_{\mathrm{GTRC}} = 291 \pm 7$ K, obtained from linear fitting of ΔS as a function of the heat capacity of solvation, $\Delta C_P(T) = T(\partial\Delta S/\partial T)_P$, for several temperatures [65]. Despite this quantitative distinction, the fact that the minimal reference network of GTRC water captures the phenomena of entropy convergence explicitly demonstrates that this signature of hydrophobic hydration is directly related to the energetics of the hydrogen bond network over a wide range of temperatures.

Previous work has shown that the logarithmic term in Equation 3.9 has merely a secondary effect on entropy convergence, shifting $\tilde{T}$ to somewhat lower values and $\Delta S(\tilde{T})$ from zero to negative values [63]. Therefore, in order to obtain a qualitative, microscopic explanation for entropy convergence, we can neglect this term in the Gaussian approximation for the free energy, and write the solvation entropy as

$$\Delta S \approx -\left(\frac{k_B V_S^2}{2\sigma_{V_S}}\right) \rho_{\mathrm{B}}^2(T)\left[1 - 2T\alpha_P(T)\right], \tag{3.10}$$

where $\alpha_P = -(\partial\ln\rho_{\mathrm{B}}/\partial T)_P$ is the thermal expansion coefficient at constant pressure, which was determined by fitting the bulk densities to Laurent polynomials [36]. Here we have also assumed that the temperature dependence of the variance σ_{V_S} can be neglected, as has been previously established [63]. Thus within the accuracy of Equation 3.10, entropy convergence is seen for $\Delta S(\tilde{T}) = 0$, and an estimate of the convergence temperature can be obtained from the intersection of $\alpha_P(T)$ and $(2T)^{-1}$. The convergence temperatures obtained for the SPC/E and GTRC models from Equation 3.10 are roughly 420 K and 330 K, respectively, in reasonably good agreement with the results presented above, although $\tilde{T}$ will always be overestimated in this approximation. Nonetheless, the difference between the convergence temperatures of the two models is quantitatively captured by this estimation, indicating that additional T-dependences arising in ΔG are
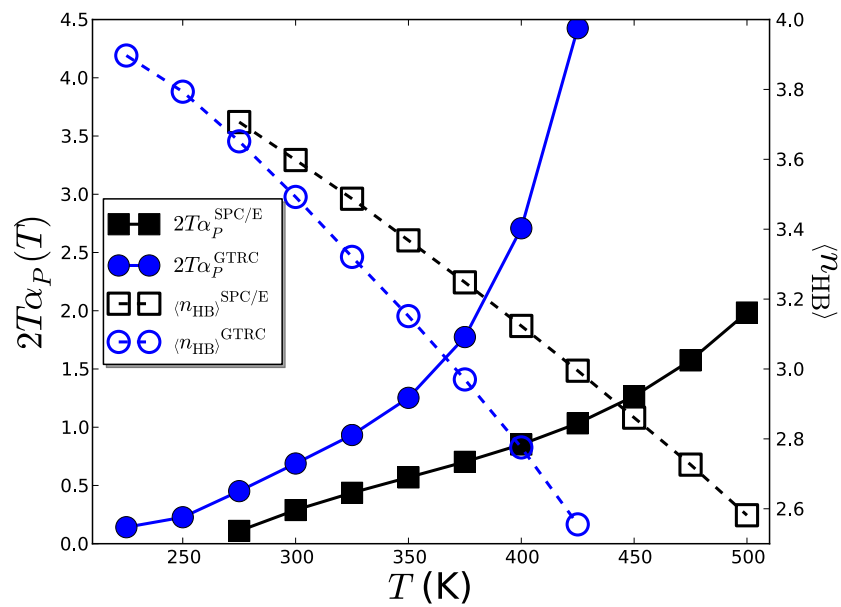
Figure 3.6: Thermal expansion coefficient multiplied by twice the temperature (left axis, closed symbols) and average number of hydrogen bonds per water molecule (right axis, open symbols) for SPC/E and GTRC water.

similar in the two models, and these have been discussed in detail elsewhere [63, 65].

In this simplified Gaussian framework the behavior of $\alpha_P(T)$ plays a key role in entropy convergence. In the case of SPC/E water, the thermal expansion coefficient vanishes at the temperature of maximum density near 248 K [17, 36]. As shown in Figure 3.6, $2T\alpha_P(T)$ then increases with increasing temperature but remains less than one until about 420 K, where entropy convergence is predicted to occur. The thermal expansion coefficient of GTRC water behaves in a qualitatively similar manner with $2T\alpha_P(T)$ remaining less than one until about 330K, although $\alpha_P(T)$ is never negative, because this model lacks a density maximum near liquid-vapor coexistence [17]. The behavior of the thermal expansion coefficient is a direct consequence of the energetics of the H-bond network in both models. At ambient temperatures, the average number of hydrogen bonds per molecule approaches four in both SPC/E and GTRC water [17]. With increasing temperature, thermal fluctuations increasingly disrupt the entropically unfavorable hydrogen bond network in both models (Figure 3.6), which leads to an increase in the thermal expansion coefficient. However, the lower density of GTRC water permits more fluctuations as the temperature is increased, consistent with its larger compressibility and a more rapid increase in $\alpha_P(T)$, leading to a lower convergence temperature.

We also determined the temperature dependence of large solute solvation free energies following the description in the previous section. After the length scale transition, solvation is dominated by interfacial physics. As evidenced by the insets in Figure 3.5, hard sphere solvation free energies in this regime decrease with increasing temperature for both models, following the T-dependence of the surface tension, just as is the case for LJ solvation.

3.7   Long ranged interactions and the size dependence of hydrophobic association

In this section, we examine the role of the various short and long ranged forces in the thermodynamics of hydrophobic association. In order to accomplish this task, we consider the association of pairs of spherical solutes, one pair in which both solutes are in the small-scale regime, while the other pair consists of two large solutes. We first examine the free energy as a function of solute-solute distance, R,

$$\beta W(R) = -\ln P(R), \tag{3.11}$$

where $P(R)$ was obtained by umbrella sampling with the harmonic biasing potential

$$U_{\text{bias}}(R) = \frac{\kappa}{2} \left(R - R^* \right)^2, \tag{3.12}$$

R^* is the desired value of R, and κ is a force constant tuned to achieve adequate overlap between neighboring windows. The probability distribution $P(R)$ was then constructed from the set of biased simulations using the multistate Bennet acceptance ratio method (MBAR) [68].
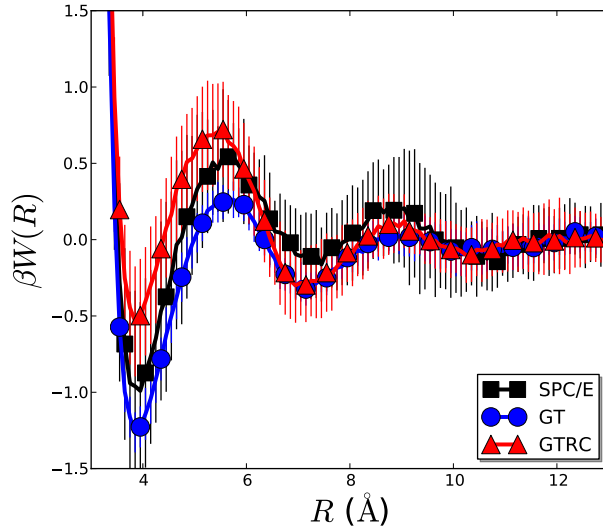
Figure 3.7: Potential of mean force, $W(r)$, between two UA methane particles in SPC/E, GT, and GTRC water.

We first focus on hydrophobic association in the small scale regime, and consider the association of two united atom (UA) methane models, which are simply LJ particles with length and energy parameters of $\sigma_{\text{Me}-\text{Me}} = 3.73$ Å and $\epsilon_{\text{Me}-\text{Me}} = 1.234$ kJ/mol, respectively [69]. Methane-water interactions were obtained from Lorentz-Berthelot mixing rules.

The potentials of mean force, $W(R)$, shown in Figure 3.7 for the association of two UA methanes are nearly identical for all water models under consideration. Therefore, not only does the hydrogen bond network dictate the solvation structure around individual small solutes, but also the association of solutes in this length scale regime, as expected from the results presented in the previous sections.

We now consider the association of two large C60 fullerene molecules in the various models of water. Each C60 is represented as a single site using the coarse-graining procedure prescribed by Girifalco [70, 71], such that the fullerene-fullerene interaction is given by

$$U_{\text{FF}}(R) = -\alpha \left[\frac{1}{s(s-1)^3} + \frac{1}{s(s+1)^3} - \frac{2}{s^4} \right] + \zeta \left[\frac{1}{s(s-1)^9} + \frac{1}{s(s+1)^9} - \frac{2}{s^{10}} \right], \quad (3.13)$$

where $\alpha = 4.4775$ kJ/mol, $\zeta = 0.0081$ kJ/mol, $s = R/2\eta$, and $\eta = 3.55$ Å. The C60-water
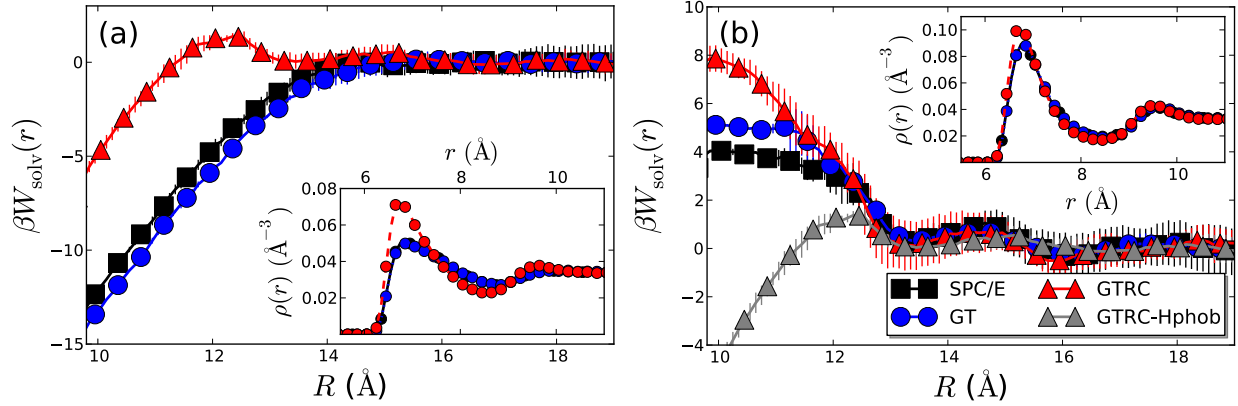
Figure 3.8: Solvent-induced potential of mean force, $W_{\text{solv}}(R)$, between two (a) purely repulsive and (b) attractive coarse-grained C60 particles in SPC/E, GT, and GTRC water. Insets in (a) and (b) show the corresponding nonuniform densities around a single coarse-grained C60 immersed in each water model. The gray curve in (b) is the GTRC PMF from panel (a).

interaction potential is

$$U_{\text{wF}}(r) = 4N\epsilon_{\text{wF}}\frac{\sigma_{\text{wF}}^2}{r\eta}\left\{\frac{1}{20}\left[\left(\frac{\sigma_{\text{wF}}}{\eta-r}\right)^{10} - \left(\frac{\sigma_{\text{wF}}}{\eta+r}\right)^{10}\right] - \frac{1}{8}\left[\left(\frac{\sigma_{\text{wF}}}{\eta-r}\right)^4 - \left(\frac{\sigma_{\text{wF}}}{\eta+r}\right)^4\right]\right\}, (3.14)$$

where $N = 60$, $\sigma_{\text{wF}} = 3.19$ Å, and $\epsilon_{\text{wF}} = 0.392$ kJ/mol. Previous work has shown that this coarse-grained water-C60 interaction provides a very good representation of the solvation structure in the corresponding atomically-detailed water-C60 system [71].

The water-C60 interaction potential $U_{\text{wF}}(r)$ leads to a hydrophilic particle due to the high density of carbon sites on the surface of the C60 molecule. Therefore, we also consider a hydrophobic particle obtained by using only the repulsive water-C60 and C60-C60 forces. This is obtained by performing a WCA-like separation of the potentials U_{FF} and U_{wF} to obtain the corresponding purely repulsive potentials $U_{0,\text{FF}}$ and $U_{0,\text{wF}}$, as detailed above for U_{sw}.

We further separate the potential of mean force as $W(R) = W_{\text{vac}}(R) + W_{\text{solv}}(R)$, where $W_{\text{vac}}(R)$ and $W_{\text{solv}}(R)$ are the vacuum and solvent-induced portions of the PMF, respectively, focusing on the latter contribution herein. The solvent-induced PMFs between purely repulsive C60 particles in the SPC/E and GT water models, shown in Figure 3.8a, are indicative of the hydrophobic effect; the association of two large apolar particles in water is barrierless, although the free energy of association is slightly lower in GT water due to its lower surface tension. Previous work has shown that the

collapse of two extended hydrophobic surfaces proceeds by the formation of a vapor tube [72, 73], in which solvent molecules are evacuated from a cylindrical region between the two hydrophobes, and we will show below that the association of two repulsive fullerenes also occurs by this mechanism.

In GTRC water, however, the PMF $W_{\text{solv}}(R)$ displays a slight barrier at $R \approx 15$ Å, and another significantly higher barrier at $R \approx 12$ Å, as shown in Figure 3.8a. Because the C60-C60 distance does not explicitly account for changes in the behavior of the aqueous solvent, it is not a good reaction coordinate to study the association of two large hydrophobes on its own [72, 73] and $W(R)$ cannot provide an explanation for the appearance of this barrier in $W_{\text{solv}}(R)$.

To understand hydrophobic association in GT and GTRC water, we calculate the free energy as a function of the C60-C60 distance R and the density ρ_v of water in a cylindrical volume of radius 3.75 Å between the particles. This two-dimensional free energy landscape is given by $\beta W(R, \rho_v) = -\ln P(R, \rho_v)$, where $P(R, \rho_v)$ was calculated using the indirect umbrella sampling method [74] to bias the number of particles in the volume v. The harmonic potential in Equation 3.12 was used to bias R. Again MBAR was used to reconstruct the probability distribution from these biased simulations [68].

The free energy surface shown in the top panel of Figure 3.9 indicates that hydrophobic collapse in GT water (or SPC/E water) is indeed driven by the barrier-less formation of a vapor tube [72, 73] at a C60-C60 distance between 14 and 15 Å. Hydrophobic collapse in GTRC water, on the other hand, does not follow this mechanism because capillary evaporation in the inter-fullerene region has been suppressed by the removal of LJ attractions in the solvent. This is consistent with the lack of drying at the interface of a single repulsive solute, as evidenced by the nonuniform densities shown in the inset of Figure 3.8a and would be anticipated from the results presented in Section IV.

Instead, the free energy minimum in GTRC water (for a specific value of R) remains at liquid-like densities as the C60-C60 distance is decreased, until the water molecules cannot physically remain between the fullerene particles due to repulsive core overlap near $R \approx 12$ Å. Only at this point are the solvation shell water molecules in the inter-fullerene region expelled. This expulsion of water molecules in the observation volume causes the large free energy barrier observed at the same inter-fullerene distance in the one-dimensional $W_{\text{solv}}(R)$ for GTRC water shown in Figure 3.8a.

Instead of artificially suppressing capillary evaporation between large hydrophobes by removal of solvent LJ attractions as in GTRC water, we can directly counteract the unbalanced LJ interfacial forces leading to evaporation in the GT or full water models by making the solutes sufficiently hydrophilic. LMF theory would predict very similar behavior for these two systems. This is accomplished by using the full U_{FF} and U_{wF} potentials to describe fullerene-fullerene and water-fullerene interactions, respectively. Inclusion of the water-C60 attractive interactions leads to an almost perfect cancellation of these unbalanced forces, as evidenced by the good agreement of the SPC/E and GT nonuniform densities with that of the GTRC model, shown in the inset of Figure 3.8b.
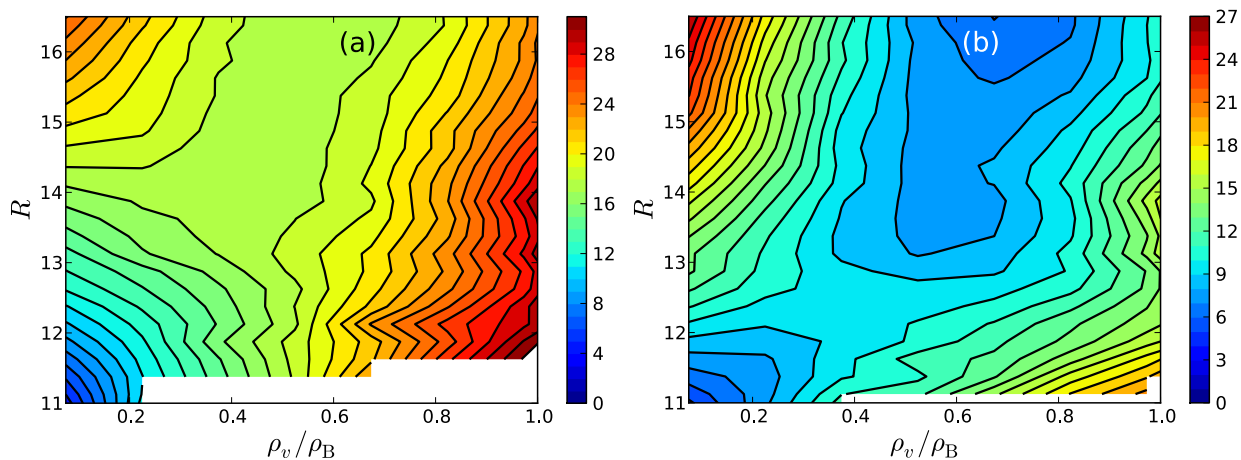
Figure 3.9: Free energy as a function of C60-C60 distance, R, and density of water in the observation volume v with respect to that in the bulk, ρ_v/ρ_B, for the association of two hydrophobic fullerene particles in (a) GT and (b) GTRC water models. Contour lines are spaced in increments of $k_B T$.

These strong solute-water attractions, arising from the high surface density of carbon atoms, render the C60 molecule hydrophilic, and the associated solvent-induced PMFs are repulsive for all distances. This indicates that water opposes the association of two such particles, in accord with previous results [75]. Because of the effective hydrophilicity of the particles, capillary evaporation between the particles does not occur, and $W_{\mathrm{solv}}(R)$ is the same for all three models for $R \geq 12$ Å. At smaller separations water is forcibly expelled from the inter-fullerene region due to overlap with the repulsive cores of the solutes and then differences arise due to the differing pressure of the systems.

The two-dimensional PMF $W(R, \rho_v)$ was also calculated for the case of hydrophilic fullerene particles in GT water, and is shown in Figure 3.10. This PMF is qualitatively very similar to that shown for hydrophobic collapse in GTRC water in Figure 3.9b as expected. As R is decreased, the free energy minimum as a function of ρ_v remains in regions of liquid-like densities. It is not until very small R, less than 12 Å, that $W(R, \rho_v)$ develops a minimum at low ρ_v, indicating a global free energy minimum at the contact state. In fact, the solvent induced PMF $W_{\mathrm{solv}}(R)$ between hydrophobic solutes in GTRC water is nearly identical to the PMFs obtained between hydrophilic solutes in all models until water is expelled from the inter-fullerene region, $R < 12$ Å, as illustrated by the curve labeled 'GTRC-Hphob' in Figure 3.8b. In contrast to what is found for the association of large hydrophobic particles, the solvent opposes association and the contact state is stabilized by the large solute-solute attractions between hydrophilic fullerenes.
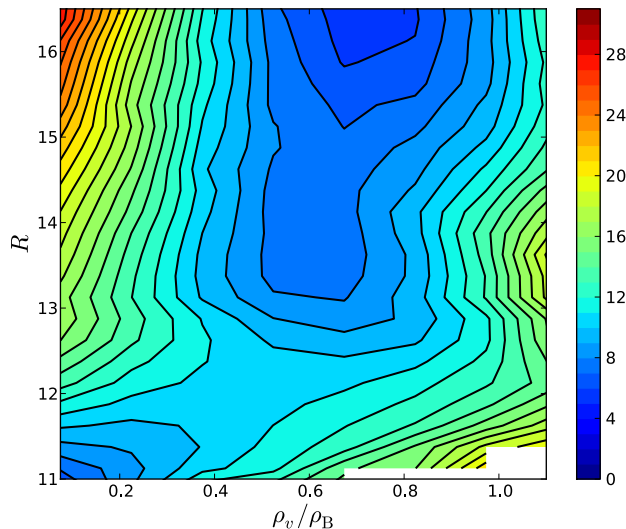
Figure 3.10: Free energy as a function of C60-C60 distance, R, and density density of water in the observation volume v with respect to that in the bulk, ρ_v/ρ_B, for the association of two hydrophilic fullerene particles in GT water. Contour lines are spaced in increments of $k_B T$.

3.8 Conclusions

We have used short ranged variants of the SPC/E water model [17] in conjunction with LMF theory to examine the crossover in the behavior of hydrophobic hydration with increasing solute size. While small scale solvation is determined exclusively by the local structure of water, *i.e.* the hydrogen bond network, long ranged interactions are important for the accurate description of the hydration of large apolar solutes. Dispersion interactions lead to the phenomena of drying at extended hydrophobic interfaces, while long ranged dipolar interactions are essential for the description of the orientational ordering of water in the vicinity of a large solute, as well as for interfacial electrostatic properties.

The truncated GT and GTRC water models also provide insight into hydrophobic interactions between solutes in the small and large length scale regimes. The local structure of water, dictated by the hydrogen bond network, is found to govern the association of two small scale solutes, a concept which has been successfully exploited to provide a theoretical framework for describing hydrophobic hydration and association at small length scales [67]. Moreover, previous work has shown that coarse-grained models, whereby water molecules interact via a single spherically symmetric pairwise potential, can reproduce the thermodynamics of association of two methanes [76, 77]. From the results presented here, it is not surprising that such coarse-grained models can capture features of small scale hydrophobicity, since these models also describe the bulk structure of water with near

quantitative accuracy.

The association of two large scale hydrophobes involves the formation of an inter-solute vapor tube, and the unbalanced forces arising from water-water LJ attractions are found to be of the utmost importance for this mechanism of hydrophobic association. In this regime the coarse-grained water models will fail completely. Cancellation of the effects of interfacial unbalanced forces, either by explicit removal of solvent-solvent LJ attractions (as in GTRC water) or by addition of large solute-water attractions that counterbalance these forces, suppresses capillary evaporation between two large solutes. As a result the solute surface is wet by the aqueous solvent, and free energy barriers to the association of two large hydrophilic solutes exist. In all these cases comparison of results in the full model with those from the short-ranged GT and GTRC water models provides a simple and physically suggestive way to disentangle the effects of longer ranged dispersive and Coulomb interactions from properties of the local hydrogen bond network.

Lo, all in silicence, all in order stand
And mighty folios first, a lordly band;
Then quartos, their well-order'd ranks maintain,
And light octavos fill a spacious plain:
See yonder, ranged in more frequent rows,
A humbler band of duodecimos;

George Crabbe

4

On Molecular Interactions and the Response to Nanoscale Broken Symmetries I: Cavity Solvation

4.1 Introduction

The solvation of ions in water presents many conceptual and computational challenges to current models of ion and water interactions. The solvation free energy is usually described using a two step process [78, 79, 80, 81, 82]: i) the formation of a cavity in water that accommodates the neutral ion core along with its associated ion-water dispersion interactions and ii) the additional free energy resulting from charging the core to the full charge of the ion. The simplest Born model treats water outside the cavity as a continuum dielectric that responds linearly to the inserted charge, and predicts that the resulting electrostatic free energy contribution is independent of the sign of the charge.

This disagrees with experiment and workers have long recognized that nonlinear electrostatic effects induced by the initial insertion of the ion core must be taken into account. These nonlinearities arise from the molecular nature of the system, since steric effects from inserting even a neutral ion core can strongly perturb the number and arrangements of local hydrogen bonds and orientations of molecular dipoles and other multipoles.

The fixed cavity or ion core itself breaks the translational symmetry of the bulk solvent and induces molecular scale interfaces between the solute and solvent. The nonuniform charge density

induced by a neutral solute can be generally characterized as a locally broken charge symmetry, and will typically generate an electrostatic potential difference between the region near the solute and in the bulk solvent. Accounting for this potential difference as the solute itself is further charged represents an important correction to the Born theory. Broken charge symmetry is quite general and can be seen in many other charged systems with local correlations on the scale of the solute size, exemplified by the insertion of a hard sphere solute into a size asymmetric primitive model of an ionic solvent, as we will discuss later.

But water and other molecular solvents can also exhibit broken angular symmetry from non-spherical molecular cores and the asymmetric intramolecular charge distribution. Using quantum chemistry results, Agmon has suggested that regions with a net effective positive charge in a water molecule are localized near the distinct hydrogen sites, while the associated negative charge is smeared nearly uniformly along a "negativity track" between the classical lone pair sites [83]. Broken angular symmetry from any source would give rise to differences between donor and acceptor hydrogen bonds even in bulk water, and would be expected to have more dramatic effects on the molecular interfaces involved in solvation of neutral solutes, with further important consequences for charged solutes.

In this chapter we study the structural and electrostatic consequences of the various broken symmetries that arise from inserting the simplest model of an uncharged ion core, a hard sphere solute of varying radius R_{HS}, into water as described by two classical water models, SPC/E and TIP5P, and by state-of the art quantum density functional calculations [1]. As we will show, the broken symmetries from hard sphere solvation generate special configurations that are particularly sensitive to small differences between donor and acceptor hydrogen bonds and to local variations in the induced charge density. This system thus provides a stringent test of classical water models in a physically important application where accurate quantum calculations can be carried out to assess their predictions.

4.2   The Negativity Track

The SPC/E and TIP5P models differ qualitatively in their description of donor and acceptor hydrogen bonds. Hydrogen bonds in almost all classical water models arise from "frustrated charge pairing", where an effective positive charge on a donor hydrogen site of one molecule tries to get close to a negatively charged acceptor site on a neighboring molecule, as illustrated in Figure 2.2 of Chapter 2. This strong electrostatic attractive force is opposed by overlap of the repulsive Lennard-Jones (LJ) cores centered on the oxygen sites and the presence of other hydrogen sites in the

---

[1]All quantum simulations and subsequent analysis of their output were performed by Christopher Mundy, Marcel Baer, and Gregory Schenter at Pacific Northwest National Laboratory (PNNL).
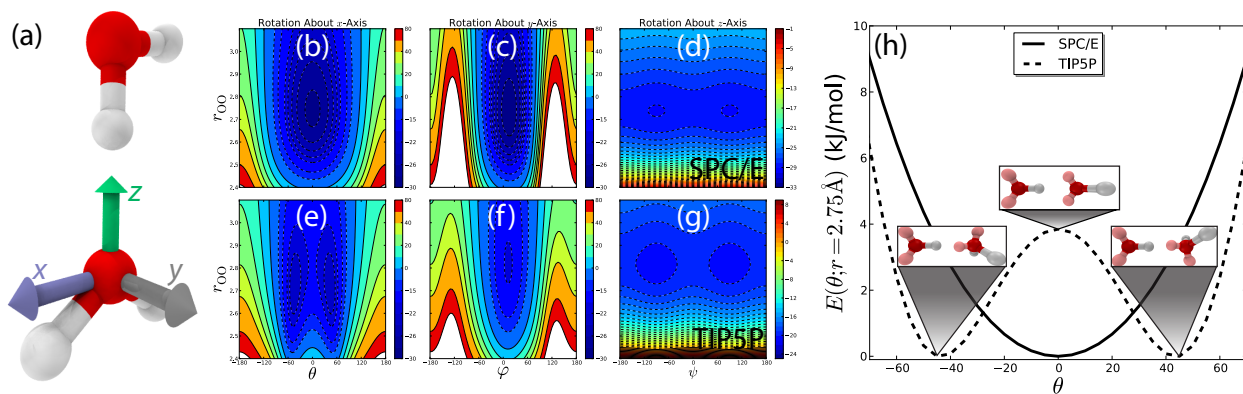
Figure 4.1: (a) Local coordinate system used to compute water dimer interaction energies as a function of oxygen-oxygen distance r_{OO} along the z-axis and as the water at the origin is rotated by an angle θ, φ, or ψ around the x-, y-, or z-axis, respectively. Rotation about the x-axis by the angle θ corresponds moving along the proposed 'negativity track' of Agmon [83]. Dimer interaction energies for are shown for both (b-d) SPC/E and (e-g) TIP5P water models. Note that the contours are not equally spaced in (b), (c), (e), and (f), but spaced by smaller increments near the energy minima. (h) The energy as a function of the angle of rotation about the x-axis (*i.e.* along the 'negativity track') for the H-bond distance $r_{OO} = 2.75$ Å is also shown for both models, where the energies have been shifted such that the minimum is located at $E = 0$. TIP5P dimer configurations at the relevant extrema are also shown. All energies are in kJ/mol.

68

acceptor molecule. In the SPC/E model all the negative charge is placed on the central oxygen site while in TIP5P negative point charges are placed on explicit "lone-pair" sites displaced tetrahedrally outward from the oxygen site.

Because of the more symmetric treatment of positive and negative charges, we would expect much smaller differences in properties of donor and acceptor hydrogen bonds for a typical molecule in bulk TIP5P water as compared to SPC/E water. In this sense TIP5P is reminiscent of the early BNS water model, with its completely symmetric treatment of tetrahedral charge sites [28], or of the purely tetrahedral mW model [84], which makes no distinction between donor and acceptor bonds. Charge pairing to distinct negative sites in TIP5P should also yield hydrogen bonds with reduced angular fluctuations when compared to those in SPC/E and related three and four site water models, where all the negative charge is placed on a single site located much further inside the LJ core. This permits greater flexibility in accepting hydrogen bonds from neighboring molecules in the SPC/E model, effectively generating a classical version of the "negativity track" discussed by Agmon [83].

A simple demonstration of this effect is to compute the H-bonding energy $E(r, \Omega)$ of a classical water dimer as a function of the water-water distance r and orientation Ω. We consider the oxygen-oxygen distance as one reaction coordinate along which we compute the energy. The orientational dependence of the H-bonding energy is described by rotating one water about the local x-, y-, and z-axes illustrated in Figure 4.1a by the angles of rotation θ, φ, and ψ, respectively, such that $\Omega = (\theta, \varphi, \psi)$. In Chapters 2 and 3, we discuss the use of GTRC truncations of classical models, and how these truncated models define a minimal reference system that describes the H-bond network. Therefore, the interaction energies for the SPC/E and TIP5P dimers shown in Figures 4.1b and 4.1c are those of the GTRC variants of each model, such that the local interactions leading to H-bond formation are disentangled from long ranged dispersion and multipolar forces.

Although the classical representation of lone pair electron density influences all energy landscapes in Figure 4.1, the effects of the negativity track are most prevelant in $E(r, \theta)$. At the H-bond distance, $r = 2.75$ Å, the SPC/E dimer energy displays a single energy minimum, located at a rotation angle of $\theta = 0°$, as shown in Figures 4.1b and 4.1h. This orientation corresponds to H-bond formation at the virtual *trigonal* site of the acceptor oxygen, and this orientation is also shown in Figure 4.1a. Of particular importance is the lack of an energetic barrier in $E(r, \theta)$ as θ is changed in the SPC/E dimer, indicating that the donor hydrogen can readily 'slide' along the classical negativity track of the acceptor oxygen site.

The dimer H-bond energies $E(r, \Omega)$ obtained for the TIP5P model strongly contrast those of the SPC/E model. As shown in Figures 4.1e and 4.1h, the TIP5P dimer energy (evaluated using the GTRC truncation scheme) has a barrier of roughly 4 kcal/mol (6.7 $k_B T$ at $T = 300$ K) located at $r = 2.75$ Å and $\theta = 0°$, due to the absence of any negative charge at the trigonal site. Instead, energetic minima are located at $\theta \approx \pm 45°$, in accord with the location of the lone pair sites. Therefore, the donor hydrogen cannot move freely from one lone pair site to another in the TIP5P
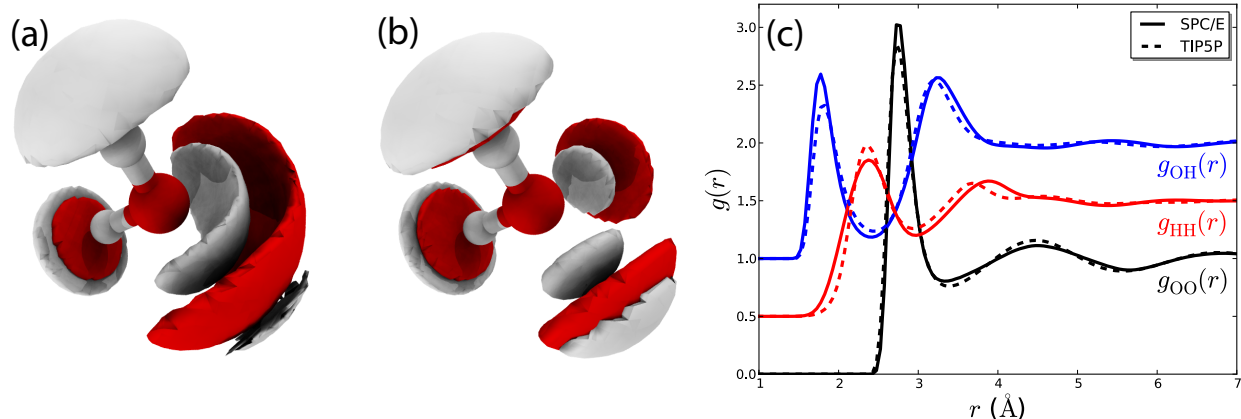
Figure 4.2: Isosurfaces of the three dimensional oxygen (red) and hydrogen (white) densities around a central water in the (a) SPC/E and (b) TIP5P models at $T = 300$ K and $P = 1$ atm. Isosurfaces are drawn at twice the bulk density of each species and TIP5P lone pair sites are not shown for ease of comparison to SPC/E. (c) Spherically symmetric site-site pair distribution functions $g(r)$ in both water models. Hydrogen-hydrogen and oxygen-hydrogen distributions are shifted vertically by 0.5 and 1, respectively.

model, but must overcome the energetic barrier at $\theta = 0°$ through thermal fluctuations[2] , and TIP5P water is not considered to have a classical negativity track.

In addition, the presence of such energetic barriers to rotation will influence local H-bond dynamics [83], but this is not our focus. In this work, we concentrate on the consequences of the proposed negativity track on the structure and thermodynamics of aqueous solutions. In the bulk, the influence of the negativity track can be observed in the three dimensional density distribution of oxygen and hydrogen sites around a central water, and isosurfaces of these $\rho(\mathbf{r})$ distributions are shown in Figure 4.2 for both SPC/E and TIP5P water. In SPC/E water, a continuous lobe of hydrogen density and an accompanying lobe of oxygen density are found around the oxygen atom of the central water, consistent with the ability of the H-bond donating water to move freely along the acceptor site in this model. On the other hand, TIP5P shows two distinct regions of high density at the location of the lone pair sites and a lack of density at the trigonal site. The location of this density deficiency is also consistent with that of the energetic barrier to rotation discussed above, illustrating that the form of $E(r, \theta)$ can have subtle effects on the bulk structure.

---

[2]In the bulk, cooperative effects from neighboring water molecules should reduce the size of the barrier. Nonetheless, a barrier to rotation is still expected to exist, as supported by the results presented in Figure 4.2 and the discussion in the text.

However, the differences in the behavior of $\rho(\mathbf{r})$ between SPC/E and TIP5P water have little influence on other structural and thermodynamic properties of the liquids. Indeed, the spherically symmetric pair distribution functions $g(r)$ of each model shown in Figure 4.2c agree quite well. The bulk dynamic and thermodynamic properties of SPC/E and TIP5P are also in relatively good agreement with each other and with other water models, especially after appropriate scaling is performed [85].

Unlike what is found in the bulk, the subsequent sections of this chapter demonstrate that the way in which lone pairs are modeled does have a significant influence on the structure and thermodynamics of *nonuniform systems*. In particular, the solvation of model spherical solutes is significantly affected by the presence or absence of the donor-acceptor asymmetries that lead to the concept of a classical negativity track.

4.3 Structural Response to Cavities

The various effective representations of physical lone pair electrons in classical water models lead to qualitatively different results for hard sphere solvation and the thermodynamics of charging these model ionic cores, as we now show in this section. The donor/acceptor asymmetries that appear are not readily apparent in common measures of interfacial structure like the nonuniform densities shown in Figure 4.3, which are remarkably similar when water is modeled with the SPC/E or TIP5P potential for all cavity sizes under study. The only differences arise in the large solute regime and are due to larger unbalanced LJ forces in the TIP5P model than those in SPC/E because of a deeper attractive well in the TIP5P LJ potential.

However, donor/acceptor asymmetries are manifested in the orientational structure of water around solutes, and therefore the manner in which the hydrogen bond network is maintained in the interfacial region. The orientation of a water molecule relative to the solute can be uniquely defined by two angular coordinates [86], θ_μ and ϕ. The first of which is the angle formed by the vector between the water oxygen and the center of the solute, $\vec{r}_{OS}$, and the dipole moment vector of the water molecule, $\vec{\mu}$, where $\vec{r}_{OS}$ points in the direction of the solute. The angle ϕ is obtained by first defining a local coordinate frame in which $\vec{\mu}$ is the z-axis and the normal to the H-O-H plane is the x-axis, such that the y-axis will point in the direction of the H-H vector. The oxygen-solute vector $\vec{r}_{OS}$ is then projected onto the xy-plane of the local frame, and ϕ is defined as the angle between this projection and the x-axis of the local frame. Due to the symmetry of the water molecule, ϕ can be made to satisfy $0 \leq \phi \leq 90°$.

Joint probability distributions $P(\theta_\mu, \phi)$ for the classical SPC/E and TIP5P models, as well as DFT results obtained with both the PBE and BLYP functionals are shown in Figure 4.4 for water molecules within 1 Å of the surface of a hard sphere with a radius of $R_{HS} = 4$ Å, which is close to

71
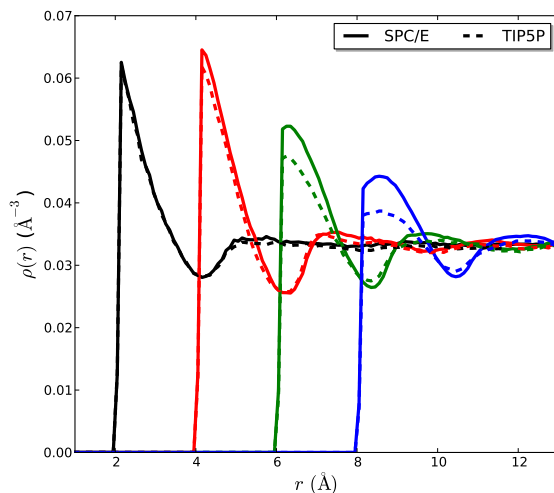
Figure 4.3: Nonuniform singlet densities for SPC/E and TIP5P water around cavities with radii $R_{\mathrm{HS}} = 2$, 4, 6, and 8 Å.

the crossover radius R_C but still in the small scale regime. The two dominant orientations both correspond to a water molecule pointing one H-bonding group directly toward the bulk, while the other three H-bonds continue around the solute. In the case of SPC/E water, Figure 4.4a, pointing the donor hydrogen sites around the solute is preferred, such that an acceptor group is pointed into the bulk, indicated by the large peak at low ϕ labeled B. However, the orientation obtained upon interchange of donor/acceptor groups, orientation $\tilde{B}$, is much less populated. In this entropy-dominated, small solute regime, differences in the flexibility of the H-bond networks of SPC/E and TIP5P water become apparent as the solvation entropy is maximized. The tendency of SPC/E water to point acceptor sites toward the bulk is a direct result of this maximization, and leads to an increased flexibility in the H-bond network formed between the first and second solvation shells.

Angular asymmetry is virtually absent in the TIP5P model, and may even be expected, to the extent that H-bond acceptors are represented in nearly the same fashion as donors in this potential. Interestingly, the results obtained from both sets of DFT simulations are also consistent with a nearly symmetric representation of donor and acceptor moieties, in stark contrast to what is expected from previous *ab initio* studies that support the negativity track picture discussed by Agmon and others [83]. Further work is needed to discern the validity of the negativity track picture, although our results do not support this concept for hard sphere solvation.

Hydrogen bond configurations and the associated nonuniform charge density near the inserted
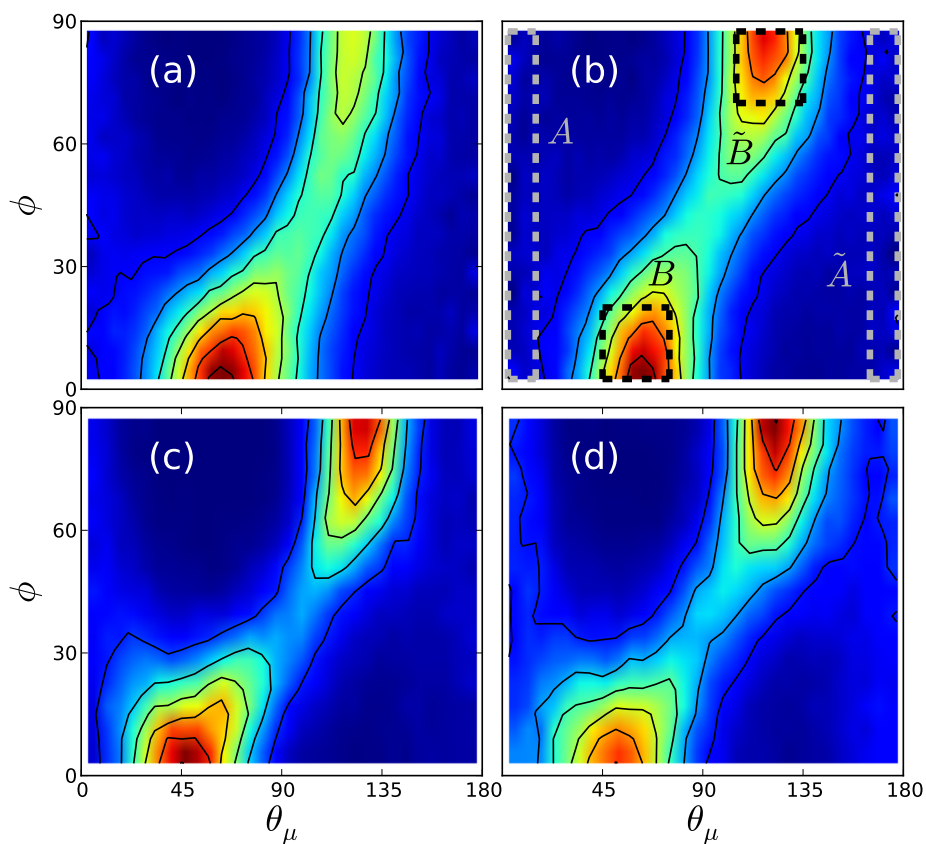
Figure 4.4: Joint probability distributions $P(\theta_\mu, \phi)$ calculated for molecules within 1 Å of the surface of the solute with $R_{\mathrm{HS}} = 4$ Å for the classical (a) SPC/E and (b) TIP5P water models, as well as the corresponding distributions obtained from DFT-based simulations using the (c) BLYP and (d) PBE functionals. Red indicates high probability, while blue corresponds to low probability. The specific orientations discussed in the text and in Figure 4.5 are indicated in (b) by the dashed regions.
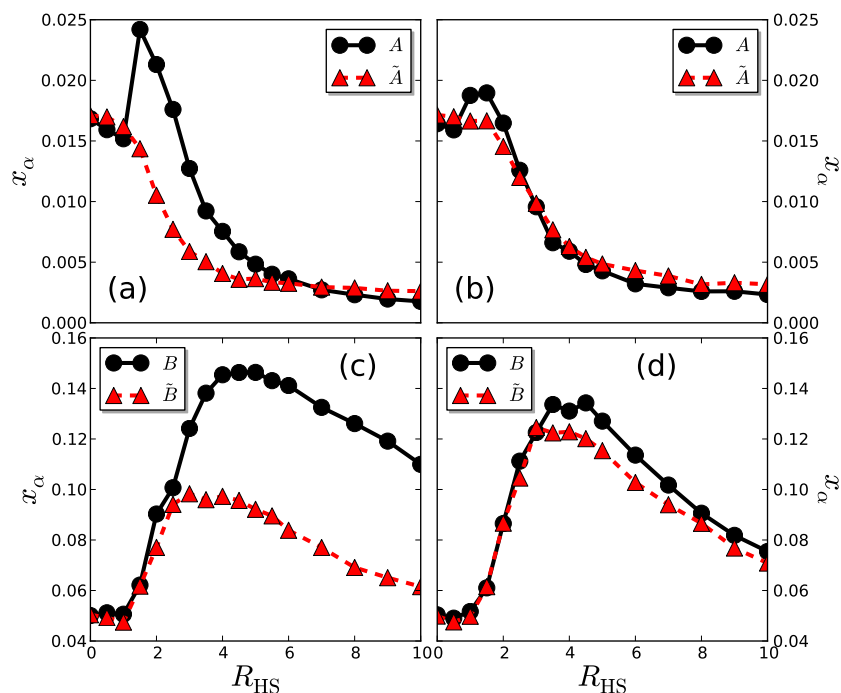
Figure 4.5: Solute size dependence of the fractions of orientations α and $\tilde{\alpha}$ in (a,c) SPC/E and (b,d) TIP5P water models for (a,b) $\alpha = A$ and (c,d) $\alpha = B$.

solute also have very interesting behavior as the solute radius is varied, with the most dramatic change occurring at a crossover radius of $R_C \approx 0.5$ nm. Hydrogen bonds must be broken to accommodate larger solutes, and the resulting molecular interface resembles the liquid-vapor interface of water. Both SPC/E and TIP5P give qualitatively similar descriptions of the enthalpically driven length scale transition and the interfacial properties of large solutes, but smaller solutes can be accommodated into the bulk hydrogen bond network with mainly an entropic penalty from constrained fluctuations near the solute. Here subtle differences in the arrangements of donor and acceptor bonds can play a key role, especially near the length-scale transition.

The solute size-dependent orientational structure of interfacial water is first examined by classifying molecules according to their angular preferences, as indicated in Figure 4.4b. We focus on the behavior of each orientation α, as well as the corresponding orientations obtained by interchanging the lone pair and hydrogen sites, $\tilde{\alpha}$. The fraction $x_\alpha(R_{HS})$ of hydration shell waters of

type α as a function of solute size shown in Figure 4.5 reveals that distinct donor/acceptor asymmetries emerge for solute sizes near R_C in the case of SPC/E water. In particular, a prominent peak appears in $x_A(R_{HS})$ prior to the crossover radius, while $x_{\tilde{A}}(R_{HS})$ monotonically decays with R_{HS}. Similar asymmetries are observed for populations B and $\tilde{B}$, respectively, but with the respective fractions peaking in the vicinity of R_C.

The TIP5P potential, on the other hand, is much more symmetric with regard to interchange of donor and acceptor sites (α and $\tilde{\alpha}$) for all R_{HS}; any small asymmetries are commensurate with the slight differences between the lone pair and hydrogen sites. Transitions in the populations of $A/\tilde{A}$ and $B/\tilde{B}$ in TIP5P water occur at nearly the same solute radius as the analogous quantities in SPC/E water, supporting the idea that the qualitative features of the length-scale transition are captured by both potentials, while the specific details surrounding the crossover differ.

4.4   Thermodynamic Consequences: Ion Solvation and the Cavity Potential

An immediate consequence of the donor/acceptor angular asymmetries and the corresponding broken charge symmetries found here is the nature of the electrostatic potential in the vicinity of the water-solute interface. Subtle differences in orientational structure can lead to drastic changes in the value of the mean electrostatic potential at the center of the cavity, termed the cavity potential herein. This quantity is crucial to theoretical estimates of the charging free energy of a neutral core, traditionally the second step in obtaining ion solvation free energies. However, there is still no consensus as to exactly what electrostatic potential is appropriate for predicting ion solvation free energies.

Previous work from Ashbaugh [87] sought to modify the classical expressions for the charging free energy $\Delta\mu_Q$ by a term linear in the ionic charge Q in order to account for the experimentally observed asymmetries in ion solvation free energies, wherein anions and cations are solvated more and less readily, respectively, than predicted by the symmetric Born model. This work implied a modification of the Born model for ionic charging in a dielectric medium with permittivity ϵ of the form

$$\Delta\mu_Q = Q \left\langle \phi_A(0; \overline{\mathbf{R}}) \right\rangle_0 - \frac{Q^2}{2R_B} \left(1 - \frac{1}{\epsilon} \right),$$ (4.1)

where R_B is termed the Born radius and $\left\langle \phi_A(0; \overline{\mathbf{R}}) \right\rangle_0$ is the value of the electrostatic potential at the center of an uncharged core evaluated as an ensemble average over configurations $\overline{\mathbf{R}}$ from a simulation with periodic boundary conditions (PBCs) in all directions, as indicated by $\langle \cdots \rangle_0$. It is important to note that in this framework, the electrostatic potential is evaluated such that its value is zero in the bulk liquid, and this convention is designated by the subscript "A."

The classical Born equation is recovered when $\left\langle \phi_A(0; \overline{\mathbf{R}}) \right\rangle_0 = 0$ in Equation 4.1. This modification, which still treats R_B as a free parameter, was able to account for the asymmetric nature

of $\Delta\mu_Q$ for large solutes with radii larger than 5–6 Å [3], but not completely for small core sizes. The asymmetries observed for small ions were explained by Garde and coworkers [78], and later by Bardhan *et al.* [79]. Because the harsh repulsive core of the ion only excludes the oxygen site of a water molecule, hydrogen sites can get closer to the ion charge than the oxygen atom of the same molecule. Therefore, by adjusting R_B independently for positive and negative ions, both works were able to account for this type of asymmetry, arising from the intramolecular charge asymmetries of a water molecule.

However, these advances were still unable to provide an adequate description of solvation processes involving ions. In particular, cavity potentials obtained from *ab initio* DFT simulations are opposite in sign and roughly seven times larger in magnitude than those obtained from the classical SPC/E model (+3.5 V versus -0.5 V). Therefore, quantum mechanics based models would predict ion solvation free energies in qualitative disagreement with those from experiment and classical simulations.

This was seemingly resolved by the two interface model of Harder and Roux, which suggested that the cavity potential should be referenced to the electrostatic potential of the vapor phase by performing a simulation with a liquid-vapor interface present [88]. In this case, the modified Born model becomes

$$\Delta\mu_Q = Q \left\langle \phi(0; \overline{\mathbf{R}}) - \Phi_{\mathrm{LV}} \right\rangle_0 - \frac{Q^2}{2R_B} \left(1 - \frac{1}{\epsilon} \right), \qquad (4.2)$$

where Φ_{LV} is the electrostatic potential difference across a planar liquid-vapor (LV) interface, often referred to as the surface potential. By subtracting Φ_{LV} from $\left\langle \phi(0; \overline{\mathbf{R}}) \right\rangle_0$, simulation results obtained in the presence and absence of a LV interface were brought into agreement, and reasonable results could be obtained from DFT simulations [89, 90]. In addition, dielectric continuum theory predictions for the free energy of moving an ion from the bulk to a LV interface by Baer *et al.* [91], which are consistent with simulation data for the same process, produce a cavity potential that is consistent with the two interface model. While these results seem to resolve the paradoxical asymmetry associated with ion solvation, there are numerous problems associated with this approach. Not the least of which is that solvation calculations cannot be performed away from liquid-vapor coexistence, indicating that ion solvation in general from the persepective of the cavity potential is still not completely understood. We seek to resolve this conundrum herein.

4.4.1 The Role of the Bethe Potential

In order to fully understand the process of charging an ionic core in a dielectric medium, we must first begin with the uniform solvent itself. Previous approaches, from the Born model to the two

---

[3]It will be shown later in this chapter that this length scale corresponds to a transition from short ranged local interactions dominating the cavity potential to long ranged electrostatics being paramount.

interface model, assume that the electrostatic potential of the bulk liquid is arbitrary, and often taken to be zero. At first glance this may seem reasonable, because the *average* charge density of a uniform dielectric is zero, and the electric field in the bulk also vanishes. However, this does not imply that the average potential is zero; a constant potential will also produce a zero electric field. Accounting for the effects of this constant potential of a bulk phase, termed the Bethe potential, is the key ingredient to understanding ion solvation.

The Bethe potential is derived in Appendix B and is given by [92, 93]

$$\phi_{\text{Bethe}} = -\frac{4\pi}{3}T = -\frac{2\pi}{3}\left\langle \frac{1}{V}\int d\mathbf{r}r^2\rho^q(\mathbf{r};\overline{\mathbf{R}})\right\rangle_B, \tag{4.3}$$

such that the integration is over the volume V of the simulation cell,

$$T = \frac{1}{2}\left\langle \frac{1}{V}\int d\mathbf{r}r^2\rho^q(\mathbf{r};\overline{\mathbf{R}})\right\rangle_B \tag{4.4}$$

is the trace of the second moment tensor (also referred to as the primitive quadrupole moment tensor) arising from the solvent charge density

$$\rho^q(\mathbf{r};\overline{\mathbf{R}}) = \sum_{i=1}^{N_C} q_i\delta(\mathbf{r} - \mathbf{r}_i(\overline{\mathbf{R}})) \tag{4.5}$$

in configuration $\overline{\mathbf{R}}$ for the N_C solvent charges, and $\langle\cdots\rangle_B$ indicates an ensemble average over configurations $\overline{\mathbf{R}}$ in the uniform, bulk system. Note that T, and therefore ϕ_{Bethe}, is constant throughout space and is a property of the bulk. The Bethe potential can vary significantly between different models of the same molecule. In the case of rigid, classical models, the trace of the second moment tensor T, and therefore ϕ_{Bethe}, is proportional to the trace of the primitive quadrupole moment tensor of a single molecule:

$$\phi_{\text{Bethe}} = -\frac{4\pi}{3}\rho_{\text{B}}\,\text{Tr}\left\{\mathcal{Q}_{\text{mol}}\right\}, \tag{4.6}$$

where ρ_{B} is the bulk density and $\text{Tr}\left\{\mathcal{Q}_{\text{mol}}\right\}$ is the trace of the primitive quadrupole tensor of a single molecule, $\mathcal{Q}_{\text{mol}}$. Equation 4.6 is derived in Appendix D. The quadrupole moments of classical water potentials are typically not parameterized when developing such models, and therefore they differ

significantly between the planar SPC/E model and the near tetrahedral TIP5P model [4], for example, resulting in different values of ϕ_{Bethe} for the two models. We can also expect that the ϕ_{Bethe} of quantum mechanics-based models, which include some representation of nuclear and electronic charges, will differ significantly from classical models, as supported by the large positive electrostatic potential difference across a liquid vapor interface [94]. However, since solvation energies probe changes induced by the solute, we may expect on very general grounds, and will see below, that ion solvation energies do not depend on ϕ_{Bethe}.

We now focus on the solvation free energy of a single ion in a bulk fluid, as is typically estimated in simulations. The system consists of a cubic box with PBCs, and the model ion, composed of a hard core or cavity with a point charge at its center, fixed at the origin of the simulation cell. As discussed above, the free energy of solvation can be written as $\Delta\mu = \Delta\mu_{\text{cav}} + \Delta\mu_Q$, where $\Delta\mu_{\text{cav}}$ is the free energy of inserting a cavity corresponding to the size of the ion into the solvent and $\Delta\mu_Q$ is the free energy of charging the cavity from zero to a charge Q. We concern ourselves with the latter quantity herein.

In general, we cannot perform a simulation of a non-neutral system, especially when using Ewald summation [31] to handle the electrostatics in the periodic environment. In this case, when we charge the ion from zero to Q, we must also turn on a neutralizing uniform background charge density from zero to $-Q$, canceling the ion charge and maintaining neutrality at every step. The uniform background penetrates the cavity and exerts no force on the ion. This seems to be the least intrusive way to maintain neutrality in a finite system with PBCs while focusing mainly on properties of the ion. However, there are significant finite size effects due to the use of Ewald summation with PBCs that must also be taken into account [78, 80, 81, 95].

In order to obtain an expression for the free energy of charging $\Delta\mu_Q$, we first define the interaction energy $\Psi(\overline{\mathbf{R}})$ in configuration $\overline{\mathbf{R}}$ between the point charge and the solvent, with the preexisting cavity present, as

$$\Psi(\overline{\mathbf{R}}) = \int d\mathbf{r}\, Q\delta(\mathbf{r})\phi(\mathbf{r};\overline{\mathbf{R}}) + \int d\mathbf{r}\left(-\frac{Q}{V}\right)\phi(\mathbf{r};\overline{\mathbf{R}}) = Q\phi(0;\overline{\mathbf{R}}) - \frac{Q}{V}\int d\mathbf{r}\,\phi(\mathbf{r};\overline{\mathbf{R}}), \qquad (4.7)$$

where V is the volume of the central simulation cell and the charge densities of the ion and the background are $Q\delta(\mathbf{r})$ and $-Q/V$, respectively. The quantity

$$\phi(\mathbf{r};\overline{\mathbf{R}}) = \int d\mathbf{r}'\frac{\rho^q(\mathbf{r}';\overline{\mathbf{R}})}{|\mathbf{r} - \mathbf{r}'|} \qquad (4.8)$$

---

[4]For SPC/E water, $\mathrm{Tr}\left\{\mathcal{Q}_{\text{mol}}^{\text{SPC/E}}\right\} = r_{\text{OH}}^2 q_{\text{H}}$, where r_{OH} is the oxygen-hydrogen bond length and q_{H} is the charge on a hydrogen site. The analogous expressions for TIP5P water is $\mathrm{Tr}\left\{\mathcal{Q}_{\text{mol}}^{\text{TIP5P}}\right\} = (r_{\text{OH}}^2 - r_{\text{OL}}^2)q_{\text{H}}$, where r_{OL} is the oxygen-lone pair site bond length. Note that the bond lengths and charges are also not equivalent in the two models and quadrupoles are obtained using the oxygen site as the origin of the local coordinate system.

is the electrostatic potential arising from the solvent, such that $\phi(0; \overline{\mathbf{R}})$ is the value of the electrostatic potential at the origin (the location of the point charge) in configuration $\overline{\mathbf{R}}$.

In general, the average electrostatic potential $\left\langle \phi(\mathbf{r}; \overline{\mathbf{R}}) \right\rangle$ can be written as the sum of a constant potential of the uniform phase (with no cavity present), *i.e.* the Bethe potential [92], and an electrostatic potential induced by inhomogeneities, which can be thought of as the change in the electrostatic potential induced by the nanoscale broken charge symmetries that arise at the solute-solvent interface, even in the absence of solute charge. Therefore, we can write the electrostatic potential from the solvent as

$$\left\langle \phi(\mathbf{r}; \overline{\mathbf{R}}) \right\rangle = \phi_{\text{Bethe}} + \left\langle \Delta\phi(\mathbf{r}; \overline{\mathbf{R}}) \right\rangle. \tag{4.9}$$

The nonuniform potential $\left\langle \Delta\phi(\mathbf{r}; \overline{\mathbf{R}}) \right\rangle$ is the change in the solvent electrostatic potential induced by the presence of the solute relative to the bulk solvent, and is nonzero even when the solute charge is zero and only an uncharged cavity is present in solution.

We now proceed to derive an expression for the free energy $\Delta\mu_Q$ by a straightforward coupling parameter integration, but alternate forms of $\Delta\mu_Q$ obtained from potential distribution theory are presented in Appendix C. In order to obtain the desired change in free energy from a system with a cavity and no charge to one with a cavity and a charge with its associated neutralizing background, the interaction energy is linearly coupled to a parameter λ, such that

$$\Psi_\lambda(\overline{\mathbf{R}}) = \lambda Q \phi(0; \overline{\mathbf{R}}) - \lambda \frac{Q}{V} \int d\mathbf{r} \phi(\mathbf{r}; \overline{\mathbf{R}}) \tag{4.10}$$

is the interaction energy at state λ. Note that this fashion of coupling λ to the interaction energy $\Psi_\lambda(\overline{\mathbf{R}})$ turns on the point charge and the neutralizing uniform background charge density in a manner that maintains neutrality for all values of the coupling parameter λ. The free energy of state λ is given by

$$\beta\mu_Q(\lambda) \propto -\ln \int d\overline{\mathbf{R}} e^{-\beta\mathcal{H}_0(\overline{\mathbf{R}})} e^{-\beta\Psi_\lambda(\overline{\mathbf{R}})}, \tag{4.11}$$

where $\mathcal{H}_0(\overline{\mathbf{R}})$ is the portion of the Hamiltonian describing solvent-solvent interactions. Differentiating this free energy with respect to λ yields the average

$$\frac{\partial\beta\mu_Q}{\partial\lambda} = \left\langle \frac{\partial\beta\Psi_\lambda(\overline{\mathbf{R}})}{\partial\lambda} \right\rangle_\lambda, \tag{4.12}$$

where $\left\langle \cdots \right\rangle_\lambda$ indicates an ensemble average over the system described by a coupling parameter of λ, in which there is a cavity already present in the system. We can now integrate over λ to obtain the

free energy of charging,

$$\Delta\mu_Q = Q \int_0^1 d\lambda \left\langle \phi(0; \overline{\mathbf{R}}) \right\rangle_\lambda - \frac{Q}{V} \int_0^1 d\lambda \left\langle \int d\mathbf{r} \phi(\mathbf{r}; \overline{\mathbf{R}}) \right\rangle_\lambda. \tag{4.13}$$

Using Equation 4.9, the first term in Equation 4.13 can be expressed as

$$Q \int_0^1 d\lambda \left\langle \phi(0; \overline{\mathbf{R}}) \right\rangle_\lambda = Q\phi_{\text{Bethe}} + Q \int_0^1 d\lambda \left\langle \Delta\phi(0; \overline{\mathbf{R}}) \right\rangle_\lambda. \tag{4.14}$$

The second term in Equation 4.13, arising from the background charge density, can be rewritten using Equation 4.9 as

$$-\frac{Q}{V} \int_0^1 d\lambda \left\langle \int d\mathbf{r} \phi(\mathbf{r}; \overline{\mathbf{R}}) \right\rangle_\lambda = -Q\phi_{\text{Bethe}} - \frac{Q}{V} \int_0^1 d\lambda \left\langle \int d\mathbf{r} \Delta\phi(\mathbf{r}; \overline{\mathbf{R}}) \right\rangle_\lambda. \tag{4.15}$$

Harris has shown the electrostatic potential $\phi^{\text{EW}}(\mathbf{r})$ obtained from conventional Ewald summation is that of a system with no net charge, zero dipole, and zero primitive quadrupole (or equivalently, zero traceless quadrupole and zero second moment tensor) [93]. Therefore, even if the system has a non-zero second moment tensor, specifically its trace T, this will be absent from the potential as evaluated by the Ewald method. Therefore, the Ewald potential is equivalent to the electrostatic potential of the system with the Bethe potential removed, *i.e.* $\Delta\phi(\mathbf{r}; \overline{\mathbf{R}}) = \phi^{\text{EW}}(\mathbf{r}; \overline{\mathbf{R}})$. One well-known feature of the Ewald potential is that its average must be zero over the simulation cell,

$$\frac{1}{V} \int d\mathbf{r} \phi^{\text{EW}}(\mathbf{r}; \overline{\mathbf{R}}) = \frac{1}{V} \int d\mathbf{r} \Delta\phi(\mathbf{r}; \overline{\mathbf{R}}) = 0, \tag{4.16}$$

such that the second term in Equation 4.15 vanishes. Therefore, the contribution to the free energy from turning on the background charge is

$$-\frac{Q}{V} \int_0^1 d\lambda \left\langle \int d\mathbf{r} \phi(\mathbf{r}; \overline{\mathbf{R}}) \right\rangle_\lambda = -Q\phi_{\text{Bethe}}, \tag{4.17}$$

as would be expected.

Finally, combining Equations 4.13, 4.14, and 4.17, the total free energy of charging is [5]

$$\Delta \mu_Q = Q \int_0^1 d\lambda \left\langle \Delta \phi(0; \overline{\mathbf{R}}) \right\rangle_\lambda . \tag{4.18}$$

The contributions from the constant bulk potential ϕ_{Bethe} have canceled, and will do so for any neutral combination of charges. The expression for the free energy given in Equation 4.18 is a direct result of structural perturbations of the solvent *induced by the solute*, and does not contain any contributions from the bulk. Therefore, ion solvation probes *changes* in the electrostatic potential induced by the presence of the solute and there is no contribution from the absolute potential of the bulk phase.

We may now ask why approaches like the two interface model have had success in describing ion solvation for a vast array of forms of the solvent interaction potential. The surface potential [96, 97] that arises at a planar liquid-vapor (LV) interface can be written using Equation 4.6 in the following form,

$$\Phi_{\text{LV}} = 4\pi \int_{z_{\text{V}}}^{z_{\text{L}}} P_z(z) dz + \left[\phi_{\text{Bethe}}^{\text{L}} - \phi_{\text{Bethe}}^{\text{V}} \right], \tag{4.19}$$

where the first term in the expression for Φ_{LV} is an integration of the z-component of the molecular dipole moment density $P_z(z)$ from a point in the bulk vapor phase z_{V} to a point in the bulk liquid phase z_{L}. The second term is a difference of the Bethe potentials in the bulk liquid (L) and vapor (V) phases, and the latter is typically taken to be zero in the case of water at ambient conditions due to a negligible solvent density in the vapor phase. The first term in Equation 4.19 is the portion of the electrostatic potential difference that arises from the structural changes induced by a planar liquid-vapor interface, while the term involving the Bethe potentials is a bulk contribution.

In the absence of solute charge, including the neutralizing background, the two interface model defines the electrostatic potential at the center of a cavity in the presence of a LV interface as $\left\langle \phi(0; \overline{\mathbf{R}}) \right\rangle_{0,\text{LV}} = \left\langle \phi(0; \overline{\mathbf{R}}) \right\rangle_0 - \Phi_{\text{LV}}$. By making the reasonable assumption that because of the low vapor density $\phi_{\text{Bethe}}^{\text{V}} \approx 0$, and using Equations 4.9 and 4.19, the cavity potential in the presence of a LV interface is

$$\left\langle \phi(0; \overline{\mathbf{R}}) \right\rangle_{0,\text{LV}} = \left\langle \Delta \phi(0; \overline{\mathbf{R}}) \right\rangle_0 - 4\pi \int_{z_{\text{V}}}^{z_{\text{L}}} P_z(z) dz, \tag{4.20}$$

which does not depend on the Bethe potential! Therefore, by neglecting free energy changes from the neutralizing background, but including Φ_{LV}, the two interface model removes the contribution from ϕ_{Bethe}, albeit at the cost of including the additional dipolar potential from solvent reorganization at the LV interface. Note that this dipolar potential is absent in purely quadrupolar fluids like methane [88],

---

[5]Note that when the system is not neutral, for example, if the neutralizing background is not included, the contribution from the Bethe potential does not vanish. In this case, the free energy of charging the cavity is given by $\Delta \mu_Q = Q \int_0^1 d\lambda \left\langle \phi(0; \overline{\mathbf{R}}) \right\rangle_\lambda$.

81

and the two interface model yields the desired value of the potential needed for Equation 4.18 exactly in this case, although one is still constrained to state points along the LV coexistence curve.

Also note, however, that the two interface model is still not physically correct. In essence, using the potential given by Equation 4.20 in expressions for the charging free energy would seem to indicate that an interface infinitely far away from an ion will have a significant influence on the solvation thermodynamics of the solute. This cannot be the case, because interfacial electric fields vanish rapidly away from the location of the LV interface, and the potential in Equation 4.18 should be used regardless of the geometry of the simulation cell. In addition, it is only for the special case of negligible vapor density that it is appropriate to make the approximation that the potential of this phase is zero, and the solvent will not generally have a vanishing bulk potential in the vapor.

4.4.2 Calculation of Bulk and Nonuniform Electrostatic Potentials

The determination of the electrostatic potential has been a source of confusion in itself, especially when concerning that of the uniform bulk liquid phase. Therefore, we devote this subsection to discussing the calculation of such potentials. The original development of the Bethe potential was concerned with finding the mean inner potential at the center of an infinite crystal lattice. More recent work on this same issue has led to the insight that the potential of a bulk phase is arbitrary *until boundary conditions are defined* [92]. If no boundaries are defined, so that the bulk phase extends to infinity, the potential of the bulk phase is zero. This is the approach taken by the Ewald summation and what is typically done in simulations determining the cavity potential [78, 87], wherein one simply integrates Poisson's equation from $r = 0$ to $r = L/2$, where L is the length of the cubic simulation cell.

However, as discussed above, this approach of considering an infinite bulk is not correct, and in general the bulk phase will have a non-zero potential relative to the vacuum, which should be taken as zero. Indeed, the bulk electrostatic potential can be obtained from Equation 4.3. Boundaries are introduced in this expression by bounding the integration volume by that of the cubic simulation cell. Although Equation 4.3 does provide accurate numerical results for the potential of the bulk phase relative to the vacuum in the absence of any macroscopic interfaces (like a liquid-vapor interface), a method for determining the bulk potential that makes the effect of boundaries clear is still desired.

The bulk potential of uniform fluid can be obtained from a simulation using PBCs introducing the concept of a hypothetical droplet, similar to what is often imagined in classical electrostatic discussions of dielectric media. This process is illustrated in Figure 4.6. At each configuration $\overline{\mathbf{R}}$ in a simulation, a cutoff radius r_c is defined. Then, a droplet of radius r_c is "carved out" of the bulk, forming an imaginary interface to which the liquid is not allowed to respond. It is important to note that this droplet must contain *neutral* molecular charge distributions, since the presence of net charge will render the medium a conductor with zero bulk potential. There is a direct analogy to the concept of a Gibbs dividing surface in interfacial physics where a uniform bulk is supposed to extend

82
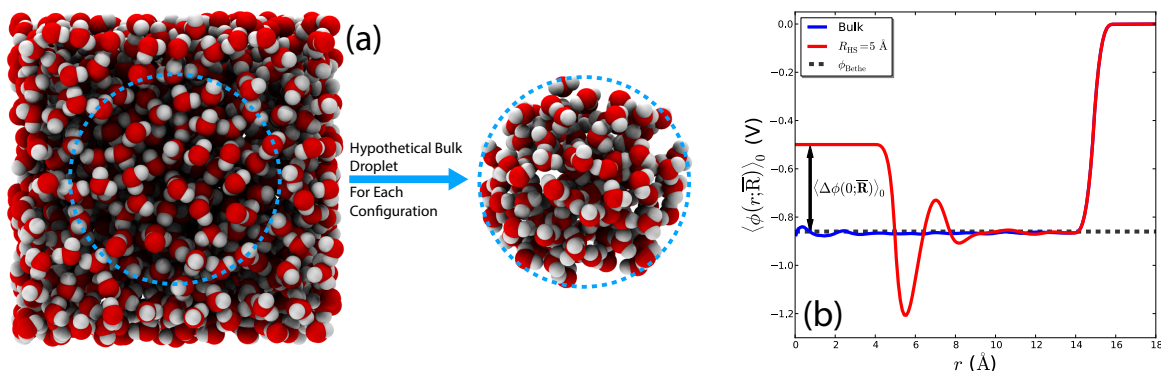
Figure 4.6: (a) Schematic depiction of carving a hypothetical droplet of neutral molecular charge densities out of a configuration of bulk water. (b) Electrostatic potentials determined by integrating Poisson's equation the hypothetical droplets with and without a cavity present in the bulk phase. The change in the electrostatic potential induced by the presence of the cavity is referred to as the cavity potential, $\langle\Delta\phi(0;\overline{\mathbf{R}})\rangle_0$, and is depicted in the figure. The potential ϕ_{Bethe} obtained from Equation 4.3 is also shown.

unchanged up to the dividing surface [8].

Once this droplet is defined, Poisson's equation is integrated to yield the electrostatic potential in configuration $\overline{\mathbf{R}}$ with respect to the vacuum for a system with spherical symmetry,

$$\phi(r;\overline{\mathbf{R}}) = -\int_0^r \frac{dr'}{r'^2}\int_0^{r'} dr''r''^2\rho^q(r;\overline{\mathbf{R}}) + \int_0^\infty \frac{dr'}{r'^2}\int_0^{r'} dr''r''^2\rho^q(r;\overline{\mathbf{R}}), \tag{4.21}$$

where the second constant term references the configurational potential to the vacuum phase located at $r \gg r_c$. The average electrostatic potential is simply obtained as the ensemble average in each configuration, $\langle\phi(r;\overline{\mathbf{R}})\rangle_B$. For a uniform bulk, $\langle\phi(r \ll r_c;\overline{\mathbf{R}})\rangle_B = \phi_{\text{Bethe}}$ and $\langle\phi(r \gg r_c;\overline{\mathbf{R}})\rangle_B = 0$, which allows for the determination of ϕ_{Bethe} as the difference in the electrostatic potential between these two limits. This is demonstrated in Figure 4.6.

We conclude this subsection by emphasizing that this method of determining $\langle\phi(r;\overline{\mathbf{R}})\rangle$ explicitly references the average electrostatic potential to its value in the vacuum but does not require the presence of a macroscopic phase boundary in a simulation. This approach is not restricted to uniform media, and can readily be extended to determine electrostatic potentials in nonuniform systems. Indeed, the potential determined in the presence of a cavity, shown in Figure 4.6b, yields ϕ_{Bethe} as the potential in the bulk phase and also allows for the estimation of $\langle\Delta\phi(0;\overline{\mathbf{R}})\rangle_0$. This allows for the determination of the cavity potential and therefore the study of ion hydration away from liquid-vapor coexistence. In addition, it is also important to note that the introduction of a
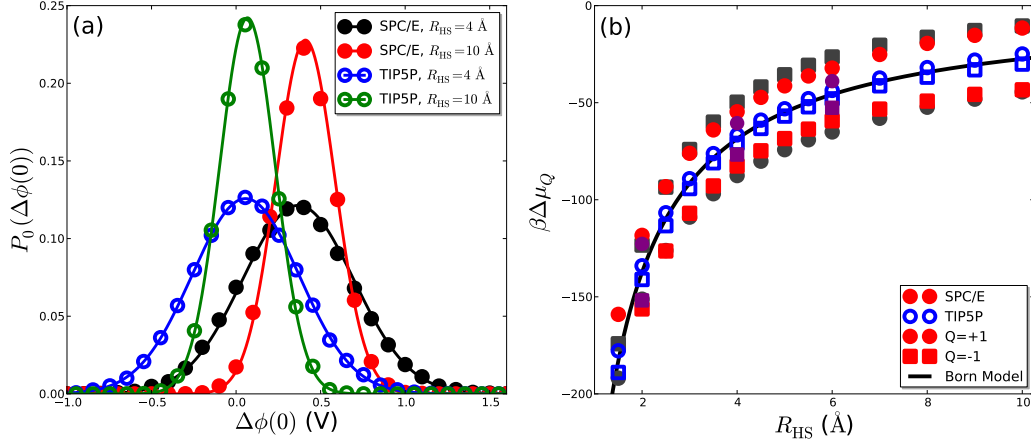
Figure 4.7: (a) Probability distributions $P_0(\Delta\phi(0))$ of the cavity potential $\Delta\phi(0)$ in the absence of any solute charge. Distributions are shown for $R_{\mathrm{HS}} = 4$ Å and $R_{\mathrm{HS}} = 10$ Å for both the SPC/E and TIP5P models. Note that as the solute size is increased, the distributions narrow, in accord with Equation 4.25. Solid lines are Gaussian distributions with the same mean and variance as the simulation results, drawn as data points. (b) Free energies of charging a hard core of radius R_{HS} predicted by Equation 4.26 for the SPC/E and TIP5P models. Gray and purple symbols indicate the SPC/E and PBE-DFT free energy predictions for a *non-neutral* system as discussed in the text. The solid line is the charge-symmetric prediction of the Born model.

macroscopic liquid-vapor interface modifies the bulk potential by $4\pi \int_{z_V}^{z_L} P_z(z)dz$, but the change in the potential induced by the presence of a cavity, $\left\langle \Delta\phi(0;\overline{\mathbf{R}}) \right\rangle_0$, is unchanged by the presence of an interface far away.

4.4.3 Nanoscale Influences on Dielectric Continuum Theory

The above discussion has lead us to the idea that ion solvation probes changes in the electrostatic potential that are induced by the presence of the solute relative to the bulk phase, as exemplified by Equation 4.18. However, the results presented there make no connections to classical dielectric continuum theories. In order to accomplish this task, we can use the form of $\Delta\mu_Q$ obtained from PDT in Appendix C,

$$\Delta\mu_Q = -k_{\mathrm{B}}T \ln \left\langle e^{-\beta Q \Delta\phi(0;\overline{\mathbf{R}})} \right\rangle_0. \tag{4.22}$$

84

As further discussed in the next chapter, DCTs like the Born model for ion solvation assume that linear response theory is accurate, which is equivalent to stating that the probability distribution of the cavity potential $P_0(\Delta\phi(0)) = \left\langle \delta_{\mathrm{D}}\left(\Delta\phi(0) - \Delta\phi(0; \overline{\mathbf{R}})\right)\right\rangle_0$ is Gaussian, where $\delta_{\mathrm{D}}(x)$ refers to the Dirac delta function. When this is the case, a second-order cumulant expansion of Equation 4.22 can be performed, yielding

$$\Delta\mu_Q \approx Q\left\langle\Delta\phi(0; \overline{\mathbf{R}})\right\rangle_0 - \frac{\beta Q^2}{2}\left\langle\left(\delta\Delta\phi(0; \overline{\mathbf{R}})\right)^2\right\rangle_0, \tag{4.23}$$

where

$$\left\langle\left(\delta\Delta\phi(0; \overline{\mathbf{R}})\right)^2\right\rangle_0 = \left\langle\left(\Delta\phi(0; \overline{\mathbf{R}}) - \left\langle\Delta\phi(0; \overline{\mathbf{R}})\right\rangle_0\right)^2\right\rangle_0 = \left\langle\left(\delta\phi(0; \overline{\mathbf{R}})\right)^2\right\rangle_0, \tag{4.24}$$

because the contribution to $\phi(\mathbf{r}; \overline{\mathbf{R}})$ from ϕ_{Bethe} is a constant that does not depend on $\overline{\mathbf{R}}$.

Previous work [87, 98, 99] has shown that the fluctuations of the cavity potential can be related to the macroscopic Born theory via

$$\frac{\beta Q^2}{2}\left\langle\left(\delta\Delta\phi(0; \overline{\mathbf{R}})\right)^2\right\rangle_0 = \frac{Q^2}{2R_B}\left(1 - \frac{1}{\epsilon}\right). \tag{4.25}$$

Therefore, the linear response approximation to the charging free energy can be written as the following modified Born model,

$$\Delta\mu_Q \approx Q\left\langle\Delta\phi(0; \overline{\mathbf{R}})\right\rangle_0 - \frac{Q^2}{2R_B}\left(1 - \frac{1}{\epsilon}\right), \tag{4.26}$$

which differs from Equations 4.1 and 4.2 by the form of the term linear in the ionic charge, which in this case is proportional to the electrostatic potential at the center of the cavity *induced by the presence of the solute*.

Probability distributions of the cavity potential, shown in Figure 4.7a, are well approximated by Gaussian distributions of the same mean and variance (shown as solid lines), giving credence to the cumulant expansion performed to arrive at Equation 4.26. The variances of the distributions in SPC/E and TIP5P water are similar for solutes of the same size, as may be expected from Equation 4.25 and the fact that they have similar dielectric constants. However, the mean of the distributions differ between water models. This differing average cavity potential is a direct result of the subtle structural differences at the cavity-water interface described above. SPC/E has a higher preference to point hydrogen sites toward the cavity, resulting in a more negative cavity potential than TIP5P water. The high symmetry of the TIP5P model results in a cavity potential closer to zero, and the cavity potential would vanish in the case of a water model with perfect tetrahedral symmetry, like the BNS model of Ben-Naim and Stillinger [28].

The smaller magnitude of the TIP5P cavity potential leads to smaller solvation asymmetries with

85

respect to the sign of the ion charge than is expected from SPC/E. Indeed, the predicted free energies of charging in SPC/E and TIP5P water, compared with the classical Born model in Figure 4.7b, supports this idea. The magnitude of the deviations from the Born model are also in good agreement with previous results [78], with anions being more favorably solvated than cations of the equivalent size.

In the framework presented here, $\left\langle \Delta\phi(0;\overline{\mathbf{R}}) \right\rangle_0 = \left\langle \phi_A(0;\overline{\mathbf{R}}) \right\rangle_0$. However, previous work has used $\left\langle \phi_A(0;\overline{\mathbf{R}}) \right\rangle_0$ to predict charging free energies of a *non-neutral* system in the absence of a neutralizing background charge density [78, 87]. Coincidentally, this subtle misinterpretation recovers the expected charge asymmetry observed in experiment. If one utilizes the form of Equation 4.26 appropriate to a system with a net charge,

$$\Delta\mu_Q \approx Q \left\langle \phi(0;\overline{\mathbf{R}}) \right\rangle_0 - \frac{Q^2}{2R_B}\left(1 - \frac{1}{\epsilon}\right), \tag{4.27}$$

charging free energies predicted for classical water models display the opposite asymmetry. These predictions for the SPC/E model are shown as gray data points in Figure 4.7b.

In contrast, the predicted charging free energies obtained using cavity potentials from quantum mechanical DFT simulations shown as the purple data points in Figure 4.7b display the experimentally observed asymmetry for a *non-neutral* system. The absolute cavity potentials obtained from DFT simulations are opposite in sign to the corresponding classical potentials, leading to charging free energies of the expected asymmetry with respect to the sign of the ion charge. It was shown above that these DFT calculations resulted in an interfacial structure similar to that of the TIP5P cavity-water interface, which would lead one to believe that the resultant cavity potentials should be similar. However, unlike classical point-charge models, the nuclear and electron densities of water are explicitly represented in such quantum models. Therefore, electron density can "spill" somewhat into the cavity, effectively allowing negative charge density to penetrate further into the solute than any positive charge. This is in stark contrast to what occurs in classical models, where a positive point charge can penetrate further than negative charges. Due to the closeness of negative charge density to the center of the solute, we can expect the resultant DFT cavity potentials to be positive, as is observed. However, $\left\langle \Delta\phi(0;\overline{\mathbf{R}}) \right\rangle_0$ is opposite in sign and much larger than that of classical models, as discussed above. Thus, the predicted free energies of charging in a neutral system significantly differ between classical and quantum representations of the molecular interactions in water, despite the promising predictions obtained for systems with a net charge. Ongoing work is being undertaken to resolve this issue. Therefore, we focus our attention on $\left\langle \Delta\phi(0;\overline{\mathbf{R}}) \right\rangle_0$ obtained for classical water models in the remainder of this chapter, but the results found qualitatively apply to $\left\langle \phi(0;\overline{\mathbf{R}}) \right\rangle_0$ as well.

4.5 Length-scales of Ion Solvation

Originating with the work of Ashbaugh [87], it has been appreciated that after a core radius of roughly 5–6 Å, the cavity potential is relatively insensitive to the ion size. In order to understand this phenomenon, we further extend our analysis by decomposing the cavity potential into short-ranged (SR) and long-ranged (LR) components, also termed near- and far-field, respectively. Following the treatment of electrostatics in local molecular field (LMF) theory, we can write the electrostatic potential as

$$
\begin{aligned}
\phi(\mathbf{r}; \overline{\mathbf{R}}) &= \int d\mathbf{r}' \frac{\rho^q(\mathbf{r}'; \overline{\mathbf{R}})}{|\mathbf{r} - \mathbf{r}'|} \\
&= \int d\mathbf{r}' \frac{\rho^{qc}(\mathbf{r}'; \overline{\mathbf{R}})}{\epsilon |\mathbf{r} - \mathbf{r}'|} + \int d\mathbf{r}' \frac{\rho^{q\sigma}(\mathbf{r}'; \overline{\mathbf{R}})}{\epsilon |\mathbf{r} - \mathbf{r}'|} \\
&\equiv \phi_{\mathrm{SR}}(\mathbf{r}; \overline{\mathbf{R}}) + \phi_{\mathrm{LR}}(\mathbf{r}; \overline{\mathbf{R}}),
\end{aligned}
\tag{4.28}
$$

where $\phi_{\mathrm{SR}}(\mathbf{r}; \overline{\mathbf{R}})$ is the near-field portion of the electrostatic potential, while $\phi_{\mathrm{LR}}(\mathbf{r}; \overline{\mathbf{R}})$ is the corresponding far-field component, such that

$$
\rho^{qc}(\mathbf{r}; \overline{\mathbf{R}}) = \int d\mathbf{r}' \rho^q(\mathbf{r}'; \overline{\mathbf{R}}) \left[\delta(|\mathbf{r} - \mathbf{r}'|) - \frac{\exp(-|\mathbf{r} - \mathbf{r}'|^2 / \sigma^2)}{\sigma^3 \pi^{3/2}} \right]
\tag{4.29}
$$

is the short ranged "core" component of the charge density, and

$$
\rho^{q\sigma}(\mathbf{r}) = \int d\mathbf{r}' \rho^q(\mathbf{r}'; \overline{\mathbf{R}}) \frac{\exp(-|\mathbf{r} - \mathbf{r}'|^2 / \sigma^2)}{\sigma^3 \pi^{3/2}}
\tag{4.30}
$$

is the *Gaussian-smoothed*, LR portion of the charge density, which naturally arises in LMF theory.

As detailed in Appendices E.1 and E.2, the far-field component of the potential completely contains the contributions from the first non-vanishing multipole moment of the charge density $\rho^q(\mathbf{r})$, as well as the next higher order moment. Therefore, the splitting of the potential in Equation 4.28 effectively isolates the longest-wavelength modes of the electrostatic response to the presence of the solute within $\phi_{\mathrm{LR}}(\mathbf{r}; \overline{\mathbf{R}})$. This far-field component will also contain non-trivial modifications to the higher moments in terms of the lower moments, and these modifications in turn make up the multipole contributions to $\phi_{\mathrm{SR}}(\mathbf{r}; \overline{\mathbf{R}})$. In the case of water, the electrostatic potential $\phi_{\mathrm{LR}}(\mathbf{r}; \overline{\mathbf{R}})$ will have the exact same dipole and quadrupole terms as $\phi(\mathbf{r}; \overline{\mathbf{R}})$, while $\phi_{\mathrm{SR}}(\mathbf{r}; \overline{\mathbf{R}})$ will contain only multipole contributions of order greater than the quadrupole. Therefore, $\phi_{\mathrm{SR}}(\mathbf{r}; \overline{\mathbf{R}})$ will also lack any contribution from the Bethe potential, which will be considered part of the far field
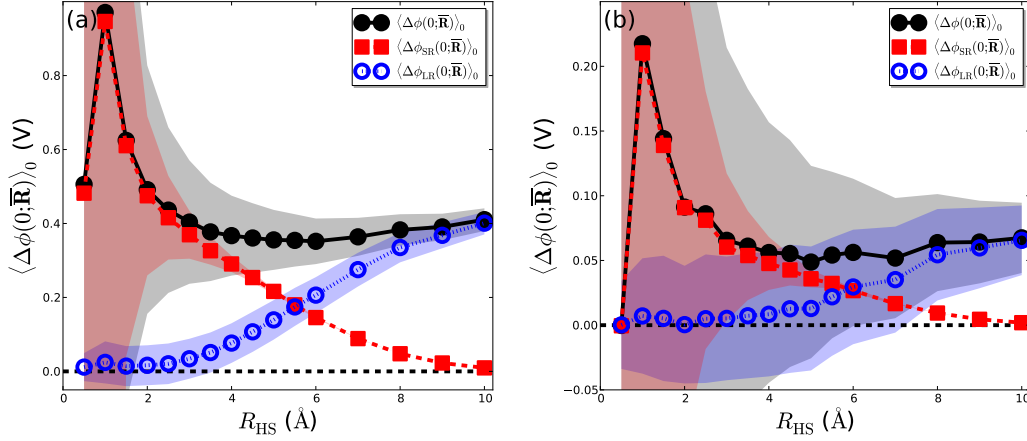
Figure 4.8: Decomposition of the cavity potential into near- and far-field components, $\langle\Delta\phi_{\text{SR}}(0;\overline{\mathbf{R}})\rangle_0$ and $\langle\Delta\phi_{\text{LR}}(0;\overline{\mathbf{R}})\rangle_0$, respectively, for (a) SPC/E and (b) TIP5P water as a function of solute size. Shaded regions indicate the variance of the corresponding distributions of each component of the cavity potential, shown in Figure 4.9. Note the different scales of the vertical axes in (a) and (b).

response. The cavity potential can then be written as

$$
\begin{aligned}
\left\langle\Delta\phi(0;\overline{\mathbf{R}})\right\rangle_0 &= \left\langle\phi(0;\overline{\mathbf{R}})\right\rangle_0 - \phi_{\text{Bethe}} = \left\langle\phi_{\text{SR}}(0;\overline{\mathbf{R}})\right\rangle_0 + \left\langle\phi_{\text{LR}}(0;\overline{\mathbf{R}})\right\rangle_0 - \phi_{\text{Bethe}} \\
&= \left\langle\Delta\phi_{\text{SR}}(0;\overline{\mathbf{R}})\right\rangle_0 + \left\langle\Delta\phi_{\text{LR}}(0;\overline{\mathbf{R}})\right\rangle_0 ,
\end{aligned}
\tag{4.31}
$$

such that the far-field component of the cavity potential is

$$
\left\langle\Delta\phi_{\text{LR}}(0;\overline{\mathbf{R}})\right\rangle_0 = \left\langle\phi_{\text{LR}}(0;\overline{\mathbf{R}})\right\rangle_0 - \phi_{\text{Bethe}}
\tag{4.32}
$$

and the near-field component is simply $\left\langle\Delta\phi_{\text{SR}}(0;\overline{\mathbf{R}})\right\rangle_0 = \left\langle\phi_{\text{SR}}(0;\overline{\mathbf{R}})\right\rangle_0$.

For a planar interface, the electrostatic potential difference across the phase boundary, given by Equation 4.19, is a sum of a long ranged dipolar component and the Bethe potential. In this limit, the surface potential is exclusively due to far field contributions. Therefore, we can expect that $\left\langle\Delta\phi_{\text{LR}}(0;\overline{\mathbf{R}})\right\rangle_0$ will dominate the cavity potential in the large solute limit. This is indeed the case, evidenced by the data shown in Figure 4.8. In contrast, we find that for small solutes ($R_{\text{HS}} < 1$ nm), the cavity potential has a significant component that is due to near-field electrostatics, which do not contain dipole and quadrupole contributions. Therefore, by separating the electrostatics into near- and far-field components, we can readily see that in the small cavity limit higher order multipoles will
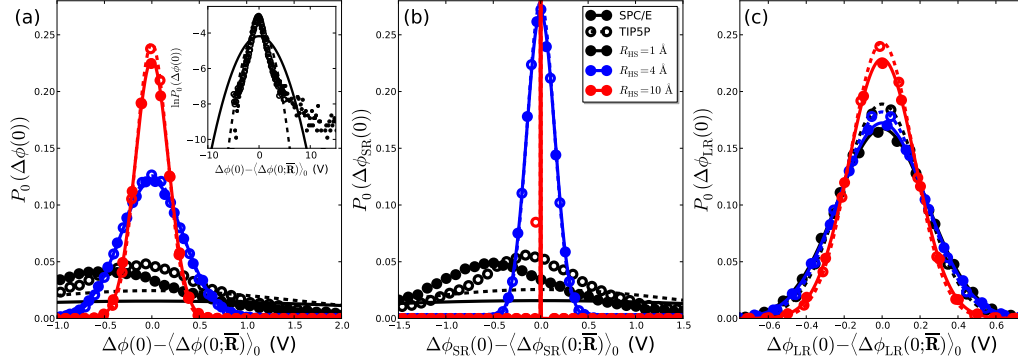
Figure 4.9: Probability distributions of (a) the total cavity potential, (b) its near-field component, and (c) its far-field for cavities of radii R_{HS} =1, 4, and 10 Å in SPC/E and TIP5P water. Solid and dashed lines are Gaussian distributions with the same mean and variance as the corresponding simulation data points for the SPC/E and TIP5P models, respectively. The inset in (a) displays $\ln P_0(\delta\phi(0))$ and the corresponding Gaussian distributions with the same mean and variance for $R_{HS} = 1$ Å for SPC/E and TIP5P water. Note that for small cavity sizes the distributions do not follow Gaussian statistics.

make a nontrivial contribution to the cavity potential, in agreement with explicit multipole expansions of the potential [100, 101].

In the small solute regime, when the near-field electrostatics contribute substantially to $\left\langle\Delta\phi(0;\overline{\mathbf{R}})\right\rangle_0$, the cavity potential is very sensitive to local structure, and therefore the manner in which the H-bond network is maintained around the solute. Due to the donor/acceptor angular asymmetries detailed above, $\left\langle\Delta\phi_{SR}(0;\overline{\mathbf{R}})\right\rangle_0$ displays a significant dependence on the specific form of the water-water interaction potential; cavity potentials generated by SPC/E water are roughly 4–5 times larger in magnitude than those for the TIP5P model for all R_{HS}. However, the qualitative features of the solute size-dependence of all portions of the cavity potential are independent of the choice of water model. The near-field component of the cavity potential is significant for $R_{HS} < R_C$, a crossover occurs at a solute radius near R_C, after which $\left\langle\Delta\phi_{LR}(0;\overline{\mathbf{R}})\right\rangle_0$ dominates the behavior of the cavity potential.

The variances of the corresponding distributions of the components of the cavity potential are depicted as shaded regions in Figure 4.8. The variance of the near-field portion has a significant dependence on solute size, decreasing with increasing cavity radii, and it will reach a δ-function distribution for $R_{HS} \gg \sigma$, as evidenced by the probability distributions of the near-field component of the cavity potential shown in Figure 4.9b. In contrast, the variance of the far-field portion of the

cavity potential changes very little as the solute is changed from a point solute to $R_{HS} = 10$ Å, and the distributions of $\Delta\phi_{LR}(0)$ are remarkably Gaussian for all solute sizes, Figure 4.9c. Therefore, deviations from a Gaussian in distributions of the total cavity potential, shown in Figure 4.9a, arise solely from the non-Gaussian nature of the near-field component. This may not be surprising, since near-field interactions involve local reorientations of charge on the scale of a water molecule, and significant non-linearities due to structural rearrangements can be expected when charging a neutral core. On the other hand, long ranged electrostatic interactions are slowly-varying over such small distances, and the corresponding far-field response is a collective behavior involving length-scales on the order of several molecules, exemplified by the formation of dipole layers at the interface of a large cavity, for example. As such, we can expect far-field components of electrostatic quantities to follow Gaussian behavior with a variance described by linear-response relations akin to Equation 4.25, which treat the solvent as a dielectric continuum. These ideas are discussed in further detail in the next chapter.

4.6   Conclusions

In this chapter, we have demonstrated that subtle differences in the representation of molecular interaction are manifested in the structure and thermodynamics of ion hydration. In particular, the proposed negativity track of Agmon [83], arising from a delocalization of electron density about the oxygen atom of a water molecule, was not substantiated by quantum mechanical DFT calculations of hard sphere solutes in water. Instead, the manner in which the hydrogen bond network is maintained around solutes near the length scale transition was found to be consistent with the explicit representation of lone pair electrons in the classical TIP5P water model, and contrasts the structure of SPC/E water around the solute, which displays significant donor/acceptor asymmetries.

These subtle asymmetries in nanoscale interfacial structure have significant consequences on the thermodynamics of solvation; in this case, ion hydration is influenced by structure through the cavity potential. In our quest to illustrate this point, we have also shed light on the paradoxical hydration asymmetry with respect to the sign of the ion charge. In particular, the symmetric portion of the charging free energy, originally described by Born, should be modified by an additional term consisting of the product of the ion charge and the portion of the electrostatic potential at the center of the cavity that is induced by the solute, and not the total electrostatic potential as initially postulated. This component of the cavity potential is obtained by removing the constant potential of the bulk dielectric, termed the Bethe potential, and several methods of calculating this potential were explored. The approach developed herein also allows for the study of ion solvation away from liquid-vapor coexistence, something that is not possible when employing the two-interface model discussed throughout the text.

In addition, by separating this cavity potential into near- and far-field components, it was shown that near-field electrostatics, and therefore higher order multipole interactions, are important when

solvating small ions. However, a crossover occurs in the range $5\text{ Å} < R_{\text{HS}} < 10\text{ Å}$, in which the contribution from the near-field electrostatics diminishes, and after which the cavity potential is exclusively due to far-field electrostatics. It has been suggested that after this length scale ion specific effects vanish [102], and consequently, our results imply that such ion specificity arises from near-field electrostatics. In addition, long ranged components of dielectric response are found to be Gaussian in nature for all solute sizes, and continuum descriptions of far-field electrostatics are expected to be accurate. We will describe some aspects of such DCTs in the next chapter.

We conclude by noting that our findings are not restricted to aqueous solutions. Two particularly interesting and important limits are illustrated by considering ion solvation in methane and a size-asymmetric primitive model (SAPM) electrolyte. As mentioned above, methane, at least in the tetrahedral site-site classical model typically used, is a purely quadrupolar molecule; it has no dipole or net charge. For such a fluid, $\left\langle \phi(0; \overline{\mathbf{R}}) \right\rangle_0^{\text{Me}} = 0$, such that $\left\langle \Delta\phi(0; \overline{\mathbf{R}}) \right\rangle_0^{\text{Me}} = \phi_{\text{Bethe}}^{\text{Me}}$. In this case, there is no structural component to the cavity potential, and the symmetry with respect to the sign of the ion charge depends only on the sign of $\phi_{\text{Bethe}}^{\text{Me}}$. In addition, for solvation of a single ion in the *absence* of a neutralizing background, the charging process is completely symmetric with respect to the sign of the ion charge, because $\left\langle \phi(0; \overline{\mathbf{R}}) \right\rangle_0^{\text{Me}} = 0$.

The SAPM electrolyte represents the opposite limit, wherein the cavity potential is completely determined by the response of the solvent to the solute. The bulk potential vanishes in any conductor, therefore $\phi_{\text{Bethe}}^{\text{SAPM}} = 0$. It immediately follows that the cavity potential $\left\langle \Delta\phi(0; \overline{\mathbf{R}}) \right\rangle_0^{\text{SAPM}} = \left\langle \phi(0; \overline{\mathbf{R}}) \right\rangle_0^{\text{SAPM}}$ is solely due to the structure induced by the solute, which in this case is simply a consequence of the size asymmetry between the positive and negative ions of the SAPM. Indeed, in the limit that the solvent ions are the same size, leading to the symmetric primitive model (SPM), the cavity potential vanishes.

If we develop only a macroscopic description of matter in an electric field, we shall find it hard to answer some rather obvious sounding questions.

Edward M. Purcell

5

On Molecular Interactions and the Response to Nanoscale Broken Symmetries II: Dielectric Response

5.1 Ion Solvation from the LMF Perspective

The theoretical and computational treatment of ion solvation typically begins by dividing the solvation process into electrostatic and non-electrostatic steps, such that one begins with a uniform bulk solvent and ends with a single ion of charge Q in solution. The traditional approach, illustrated in Figure 5.1 and considered even by Born [103], separates an ion into a hard core, which excludes solvent charge from a spherical volume of radius R, and a point charge at the center of this cavity. Instead of inserting an ion directly into the solvent, first a cavity is created by inserting the hard spherical core of the ion into the fluid. This first step is typically considered non-electrostatic in nature, because the free energy of core insertion does not depend on the ion charge. However, as discussed in detail in the preceding chapter, significant asymmetries in the structural response of the solvent to such cavities can develop. This asymmetric structure of the solvation shell can induce a non-zero electrostatic response to cavity formation, exemplified by the cavity potential. Therefore, significant electrostatic asymmetries already exist when a spherical cavity is formed in a dielectric.

The asymmetric solvation structure around a cavity additionally complicates the classical concept of a test charge in molecular simulation. Dielectric response cannot be probed directly with a point

test charge because it can overlap with charged molecular sites, giving rise to singularities. Therefore, point charges must be placed inside cavities already existing in a fluid. But standard dielectric continuum arguments no longer hold due to the asymmetries and nonlinearities associated with the solvent response to a cavity. To overcome such issues, we will utilize LMF theory to introduce the concept of a *Gaussian test charge*. We will show that Gaussian charge distributions are the appropriate entity to use as a test charge in order to probe dielectric response in molecular simulations.

The non-zero electrostatic response of the solvent to the ion core will make the next step of the solvation process, placing a point charge of magnitude Q at the center of the spherical cavity, asymmetric with respect to the sign of Q. Further asymmetries develop when one considers the additional polarization of the solvent, in this case water, in response to the presence of the ion charge. This polarization asymmetry will depend on the nature of the water-water intermolecular potential, and, to a lesser extent, the ion-water interaction potential. If the ionic charge is negative, classical water models like SPC/E and TIP5P will tend to orient a positively charged hydrogen site toward the ion. Indeed, when the joint probability distributions $P(\theta_\mu, \phi)$ discussed in the previous chapter are calculated for water molecules in the hydration shell of an anion, we find similar structures for both models, Figures 5.2a and 5.2b. However, if one considers turning on a positive charge at the center of the ion core, the different representations of the lone pair electrons will lead to significantly different solvation structures. Indeed, the distributions in Figure 5.2c indicate that SPC/E tends to point its dipole moment away from a cation, and can readily adopt configurations along its "classical negativity track." In contrast, the cationic hydration shell structure of TIP5P water is nearly symmetric with respect to the anionic shell upon interchange of lone pair and hydrogen sites, Figure 5.2d. The high symmetry of the TIP5P solvation shell may be expected from our results in the previous chapter.

An alternative view of ion solvation can be obtained through the perspective of LMF theory, as depicted in Figure 5.3. We can divide the final step of the traditional process, charging the ionic core, into near- and far-field components. The near-field portion of the point charge, with potential $Qv_0(r)$, is short ranged, rapidly varying over molecular length scales, and will contain the divergence of the Coulomb potential as r goes to zero. Therefore, the insertion of this truncated point charge into the fluid cannot be performed without a cavity present, and this step must follow insertion of the ion core. Consequently, asymmetric solvation behavior associated with the presence of a cavity in the fluid, as well as the polarization asymmetry discussed above, will be associated with this near-field charging process.

The far-field component of the point charge corresponds to a Gaussian charge distribution of magnitude Q and width l, where l is the LMF length scale used to separate the point charge. Insertion of this Gaussian charge distribution into the solvent can be accomplished with or without an excluded volume present in the liquid, because the potential due to this charge distribution is finite at $r = 0$. Therefore, we can rearrange the steps in the ion solvation process as depicted in Figure 5.3:
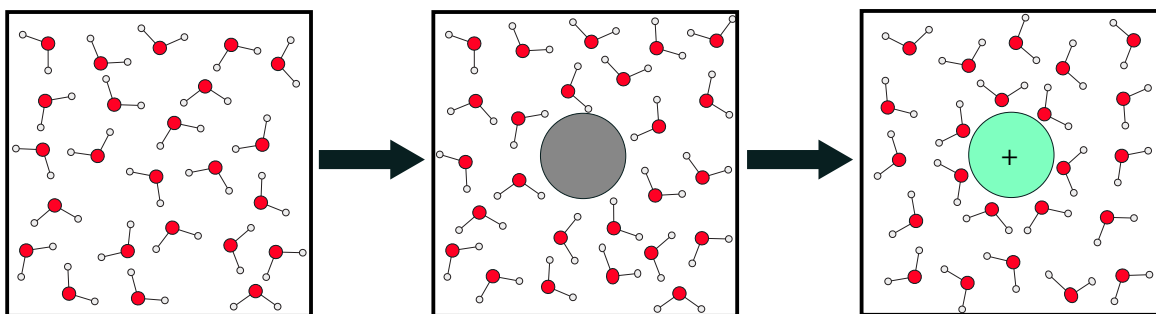
Figure 5.1: Illustration of the classical view on ion solvation in aqueous solution. The first step consists of inserting a hard core into the solvent, depicted as a grey sphere, and the free energy of this process is considered non-electrostatic in nature. This first step already exhibits non-linear response and asymmetries in the solvation shell of the cavity. This asymmetric structure leads to further asymmetries in the rest of the solvation process. The electrostatic portion of the ion solvation free energy is due to charging of the hard sphere to yield the fully charged ion, indicated by the green sphere with a "+" at the center, and this makes up the second step of the ion solvation process. Note that this latter step can be further split into two processes from an LMF perspective: turning on the short ranged ion charge $Qv_0(r)$, and turning on the far field contribution, $v_Q(r) = Qv_1(r)$.

(i) introduce a Gaussian charge distribution into the bulk fluid, (ii) insert a spherical cavity into the solvent at the center of the Gaussian charge, and (iii) turn on the near-field portion of the charge. The free energy change associated with this process is identical to that of Figure 5.1, yet the alternative rearrangement better illustrates where asymmetries and non-linearities arise.

Modification of strong, local interactions, like the insertion of a hard core in the presence or absence of a Gaussian test charge, or turning on near-field charges, will typically induce a non-linear and asymmetric solvent response [1], as discussed above and in detail in the previous chapter. In contrast, we expect the insertion of an appropriately chosen Gaussian charge distribution into the solvent to be a small perturbation, such that the first step in the LMF-based ion solvation process in Figure 5.3 follows linear response theory and therefore will be symmetric with respect to the sign of Q. Therefore, the LMF approach to ion solvation isolates linear and symmetric responses in the first step, while moving all asymmetries and non-linear responses to steps (ii) and (iii). These latter steps involve strong short ranged interactions more dependent on details of the particular molecular models used and are not amenable to general theoretical treatment. This chapter focuses on step (i),

---

[1]If the cavity radius is much larger than the truncation length of the charge, $R \gg l$, the surrounding fluid will not interact with the near-field component of the charge. In this special case, the solvent will not exhibit a response to this portion of the charging process. However, there will still exist a large non-linear response to the insertion of such a large cavity and an associated asymmetric hydration structure and cavity potential.
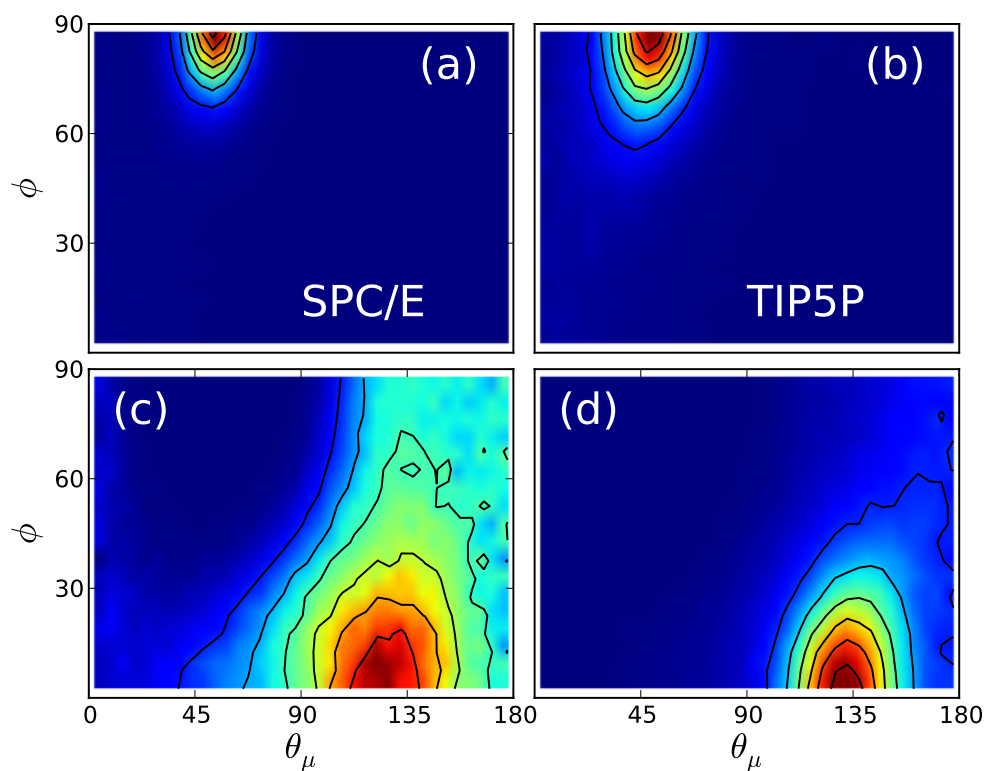
Figure 5.2: Joint probability distributions $P(\theta_\mu, \phi)$ calculated for molecules in the first hydration shell of an anionic (a,b) or cationic (c,d) LJ particle of unit charge in SPC/E (a,c) or TIP5P (b,d) water. Red indicates high probability, while blue corresponds to low probability. The water-ion LJ interaction parameters are $\sigma_{\mathrm{LJ}} = 3.44778$ Å and $\varepsilon_{\mathrm{LJ}} = 0.893228$ kJ/mol, and correspond to a united atom representation of methane [80]. For consistency, the same ion-water LJ parameters were used for both SPC/E and TIP5P water systems.
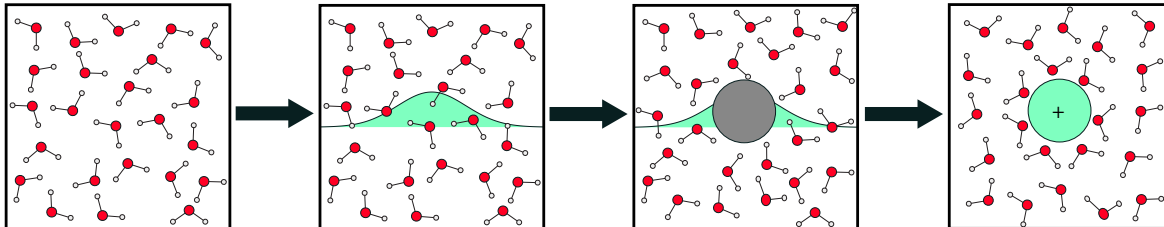
Figure 5.3: Illustration of the LMF-based reordering of the ion solvation process as discussed in the text. The first step in this process corresponds to inserting a Gaussian charge distribution of width l and magnitude Q into the uniform bulk fluid, and this distribution is schematically indicated by the green region in the second panel from the left. This first step is expected to be symmetric with respect to the sign of Q and in the linear response regime, as detailed in the text. The next step in the process consists of inserting the uncharged ion core at the location of the Gaussian test charge, yielding a solute with far-field electrostatics and strong, short ranged, non-electrostatic core interactions. This step in the solvation process will introduce asymmetries with respect to Q due to the asymmetric nature of the water molecule and the H-bond network around the solute. The response of the solvent to the introduction of such a cavity is also expected to be non-linear, due to harsh repulsive core interactions. The third and final step of the process is to turn on the near-field portion of the ion charge, $Qv_0(r)$, effectively turning the Gaussian charge into a point charge. This step will be asymmetric with respect to the sign of Q if the water model used is not perfectly tetrahedral. Whether or not the solvent response to this charging process is in linear regime will depend on both the magnitude and sign of Q, as well as the exact form of the water-water and water-ion interaction potentials, and general statements regarding this type of charging cannot be made.

inserting a Gaussian charge distribution into a fluid of interest. We develop accurate analytic approximations to the structural and thermodynamic response of dielectric and conducting fluids to such Gaussian charges, and find that such distributions are an interesting probe of dielectric response in their own right. Indeed we argue they play the role of the classical test charge but can be consistently used in molecular simulations.

5.2 Regularizing point charge singularities: Probing the dielectric response of bulk fluids with Gaussian charges

Inserting a test charge into a fluid continuum to probe its dielectric response is commonplace in classical electrostatics [104, 105, 106]. Nevertheless, complications arise when this is performed in a molecular detailed system. For example, a point charge can be readily inserted into the space between molecules, which is free of nuclear charge or effective point charges in classical models. However, if

the probe is placed close to a charged atomic site, singularities arise and the associated energetics and response cannot be calculated. This *classical Coulomb collapse* singularity is often avoided through the introduction of a hard spherical volume surrounding the probe charge where even intramolecular point charge sites are not allowed to penetrate [106], and appears in the commonly used scheme depicted in Figure 5.1 to calculate ion solvation free energies [80, 81].

An alternative route to this type of regularization is to smear the probe with a Gaussian distribution, resulting in a Gaussian test charge, which, with smearing over large enough scales (a few Angstroms for water), can be inserted even near intramolecular point charged sites without large singular energies arising. This type of charge distribution arises when using LMF theory ideas to reorganize the steps involved in calculating ion solvation free energies, as illustrated in Figure 5.3. We derive accurate analytic approximations to the structural and thermodynamic response of dielectric fluids to a Gaussian test charge herein.

We first consider the free energy change upon insertion of a Gaussian charge distribution of width l centered at the origin, such that the electrostatic potential is

$$v_Q(r) = \frac{Q \operatorname{erf}(r/l)}{r} = Q v_1(r). \tag{5.1}$$

One formally exact way to determine the free energy of inserting this distribution, ΔG_l, is to use PDT,

$$e^{-\beta \Delta G_l} = \left\langle e^{-\beta \Psi(\overline{\mathbf{R}})} \right\rangle_0 = \left\langle e^{\beta \Psi(\overline{\mathbf{R}})} \right\rangle_Q^{-1}, \tag{5.2}$$

where $\langle \cdots \rangle_Q$ and $\langle \cdots \rangle_0$ indicate ensemble averages over configurations of the system where the Gaussian charge distribution is present or absent, respectively,

$$\Psi(\overline{\mathbf{R}}) = \sum_{i=1}^{N} q_i v_Q(r_i) = \int d\mathbf{r} \rho^q(\mathbf{r}; \overline{\mathbf{R}}) v_Q(r) \tag{5.3}$$

is the total energy of interaction with the Gaussian charge distribution for a single point in phase space $\overline{\mathbf{R}}$, and

$$\rho^q(\mathbf{r}; \overline{\mathbf{R}}) = \sum_{i=1}^{N_C} q_i \delta(\mathbf{r} - \mathbf{r}_i(\overline{\mathbf{R}})) \tag{5.4}$$

is the singlet charge density of the system of N_C charges, where $\mathbf{r}_i(\overline{\mathbf{R}})$ and q_i, respectively, are the position and charge of site i in configuration $\overline{\mathbf{R}}$, such that the average charge density in the presence

of $v_Q(r)$ is given by

$$\rho_Q^q(\mathbf{r}) = \left\langle \rho^q(\mathbf{r};\overline{\mathbf{R}}) \right\rangle_Q = \left\langle \sum_{i=1}^{N_C} q_i \delta(\mathbf{r} - \mathbf{r}_i(\overline{\mathbf{R}})) \right\rangle_Q. \tag{5.5}$$

A formally equivalent but alternative route to the free energy ΔG_l that avoids averaging over exponentials is to proceed by coupling parameter integration, and this is detailed in Appendix F.

The Gaussian charge distribution can be considered a small perturbation with appropriately chosen Q and l, and so we expect the system to respond in a manner consistent with linear response theory. In this regime, the free energy of turning on $v_Q(r)$ is given by the Gaussian or linear response approximation to Equation 5.2,

$$\Delta G_l \approx \frac{1}{2} \left[\left\langle \Psi(\overline{\mathbf{R}}) \right\rangle_0 + \left\langle \Psi(\overline{\mathbf{R}}) \right\rangle_Q \right]. \tag{5.6}$$

Note that in the bulk, uniform fluid, the average charge density is $\rho_0^q(\mathbf{r}) = 0$, and therefore $\left\langle \Psi(\overline{\mathbf{R}}) \right\rangle_0 = 0$. The free energy of turning on the Gaussian distribution of charge can now be written as

$$\Delta G_l = \frac{1}{2} \left\langle \Psi(\overline{\mathbf{R}}) \right\rangle_Q = \frac{1}{2} \int d\mathbf{r} \rho_Q^q(\mathbf{r}) v_Q(r) = \frac{1}{2} \frac{1}{(2\pi)^3} \int d\mathbf{k} \hat{\rho}_Q^q(\mathbf{k}) \hat{v}_Q(k), \tag{5.7}$$

where we have used Parseval's theorem to rewrite the free energy in terms of an integral in Fourier space, and $\hat{v}_Q(k) = \frac{4\pi Q}{k^2} e^{-k^2 l^2/4}$. Further consequences of Equation 5.7 are discussed in Appendix G. We proceed by finding an analytic expression for the structural response $\rho_Q^q(\mathbf{r})$ to the Gaussian test charge in the next subsection.

5.2.1 Nonuniform Charge Densities from Linear Response Theory

A functional expansion of $\rho_Q^q(\mathbf{r})$ about the uniform system to linear order in $v_Q(r)$ allows us to rewrite the charge density of the nonuniform system in terms of the charge-charge linear response function of the uniform system;

$$\rho_Q^q(\mathbf{r}) \approx \rho_0^q(\mathbf{r}) + \int d\mathbf{r}' \frac{\delta \rho_0^q(\mathbf{r})}{\delta \left[-\beta v_Q(\mathbf{r}') \right]} \left[-\beta v_Q(\mathbf{r}') \right] = -\beta \int d\mathbf{r}' \chi_0^{qq}(|\mathbf{r} - \mathbf{r}'|) v_Q(\mathbf{r}'), \tag{5.8}$$

where $\chi_0^{qq}(\mathbf{r}, \mathbf{r}') = \left\langle \delta \rho_0^q(\mathbf{r};\overline{\mathbf{R}}) \delta \rho_0^q(\mathbf{r}';\overline{\mathbf{R}}) \right\rangle_0$ is the charge-charge linear response function and $\delta \rho_0^q(\mathbf{r};\overline{\mathbf{R}}) \equiv \rho^q(\mathbf{r};\overline{\mathbf{R}}) - \rho_0^q(\mathbf{r}) = \rho^q(\mathbf{r};\overline{\mathbf{R}})$. The resulting expression for the density in k-space is then given by

$$\hat{\rho}_Q^q(\mathbf{k}) \approx -\beta \hat{\chi}_0^{qq}(\mathbf{k}) \hat{v}_Q(\mathbf{k}). \tag{5.9}$$

98

The Gaussian in $\hat{v}_Q(\mathbf{k})$ cuts off large k components in $\hat{\rho}_Q^q(\mathbf{k})$. For large enough l, we can thus expand the charge-charge linear response function to second order as

$$\hat{\chi}_0^{qq}(\mathbf{k}) \sim \hat{\chi}_0^{(0)qq} + k^2 \hat{\chi}_0^{(2)qq} = k^2 \hat{\chi}_0^{(2)qq}, \tag{5.10}$$

where $\hat{\chi}_0^{(0)qq} = 0$ due to neutrality, and $\hat{\chi}_0^{(2)qq} = -\frac{1}{6} \int d\mathbf{r} r^2 \chi_0^{qq}(r)$. The expression for the charge density then becomes

$$\hat{\rho}_Q^q(\mathbf{k}) \approx -4\pi\beta Q \hat{\chi}_0^{(2)qq} e^{-k^2 l^2/4} \tag{5.11}$$

The second moment of the charge-charge linear response function is exactly related to the dielectric constant by a generalization of the Stillinger-Lovett moment conditions [27, 106, 107, 108, 109],

$$4\pi\beta\hat{\chi}_0^{(2)qq} = 1 - \frac{1}{\epsilon}. \tag{5.12}$$

Therefore, the expression for the charge density in Equation 5.11 becomes

$$\hat{\rho}_Q^q(\mathbf{k}) = -Q\left(1 - \frac{1}{\epsilon}\right) e^{-k^2 l^2/4}, \tag{5.13}$$

or, equivalently in real space,

$$\rho_Q^q(\mathbf{r}) = -Q\left(1 - \frac{1}{\epsilon}\right) \frac{1}{l^3 \pi^{3/2}} e^{-r^2/l^2}. \tag{5.14}$$

Thus, in this approximation the charge density induced by a Gaussian test charge with potential $v_G(r)$ is a Gaussian with the same width as the test distribution and with magnitude $-Q\left(1 - \frac{1}{\epsilon}\right)$. This illustrates the classical concept of incomplete charge screening in a dielectric, where the magnitude of a charge immersed in a dielectric that is felt by a test charge very far away is reduced by a factor of $1/\epsilon$. In the case of a conducting medium, $\epsilon = \infty$, and complete screening is recovered, $\hat{\rho}_Q^q(0) = -Q$.

In addition to the bare charge density, we can also readily obtain an approximate expression for the Gaussian smoothed charge density $\rho_Q^{q\sigma}(\mathbf{r}) = \int d\mathbf{r}' \rho^q(\mathbf{r}') \rho_G(|\mathbf{r} - \mathbf{r}'|; \sigma)$, where $\rho_G(\mathbf{r}; \sigma) \equiv \exp(-r^2/\sigma^2)/\sigma^3 \pi^{3/2}$. Using Equation 5.14 for the charge density, $\rho_Q^{q\sigma}(\mathbf{r})$ is given by

$$\rho_Q^{q\sigma}(\mathbf{r}) = -Q\left(1 - \frac{1}{\epsilon}\right) \frac{1}{\gamma^3 \pi^{3/2}} e^{-r^2/\gamma^2}, \tag{5.15}$$

where $\gamma \equiv \sqrt{l^2 + \sigma^2}$. We can anticipate that approximation 5.15 for the smoothed charge density will be accurate even for circumstances where Equation 5.14 fails, because the smoothed charge

density is a description of the long-wavelength response of a charged system [1].

At this point, I should mention that the charge density in the presence of $v_Q(r)$ can also be obtained from configurations of the bulk fluid using the configuration-based linear response formulation of Hu and Weeks [110],

$$\rho_Q^q(\mathbf{r}) = \frac{\left\langle \rho_0^q(\mathbf{r}; \overline{\mathbf{R}}) e^{-\beta \Psi(\overline{\mathbf{R}})} \right\rangle_0}{\left\langle e^{-\beta \Psi(\overline{\mathbf{R}})} \right\rangle_0} \approx -\beta \left\langle \delta\rho_0^q(\mathbf{r}; \overline{\mathbf{R}}) \delta\Psi_0(\overline{\mathbf{R}}) \right\rangle_0,$$ (5.16)

where the approximation is valid in the linear regime and $\delta\Psi_0(\overline{\mathbf{R}}) \equiv \Psi(\overline{\mathbf{R}}) - \left\langle \Psi(\overline{\mathbf{R}}) \right\rangle_0 = \Psi(\overline{\mathbf{R}})$. Hu and Weeks discuss the more general case, where the 0 system is nonuniform, and in general

$$\left\langle \delta\rho_0^q(\mathbf{r}; \overline{\mathbf{R}}) \delta\Psi_0(\overline{\mathbf{R}}) \right\rangle_0 = \int d\mathbf{r}' \chi_0^{qq}(\mathbf{r}, \mathbf{r}') v_Q(\mathbf{r}')$$ (5.17)

for any particular choice of the reference system. For the specific case where the reference state is a uniform fluid, as considered here, we can readily evaluate both the left and right sides of Equation 5.17, as both will depend only on the scalar distance r. However, if we consider turning on a test charge distribution in a nonuniform environment, the charge-charge linear response function $\chi_0^{qq}(\mathbf{r}, \mathbf{r}')$ is six-dimensional, while the fluctuation term on the LHS of Equation 5.17 is at most three-dimensional, and can easily be evaluated in both uniform and nonuniform systems.

5.2.2 The Continuum Free Energy

When the above approximations for the induced charge density are valid, we can readily obtain an analytic expression for the free energy ΔG_l by inserting Equation 5.14 into Equation 5.7, yielding

$$\Delta G_l = -\frac{Q^2}{l\sqrt{2\pi}} \left(1 - \frac{1}{\epsilon}\right).$$ (5.18)

This approximation for ΔG_l can be used to analytically evaluate the first step in the LMF-based ion solvation process of Figure 5.1. It is also interesting to note that Equation 5.18 has the same form as the classical Born charging free energy, with $2R_B \to l\sqrt{2\pi}$.

Regularizing the electrostatic interactions by consideration of a Gaussian charge distribution and not a point charge is essential, as it eliminates any divergences at large k. Indeed, if one tries to carry out the above with a point charge, the integration over k in Equation 5.7, and therefore the free energy, will diverge (analogously, the point charge limit of Equation 5.18, $\lim_{l\to 0} \Delta G_l$, also diverges). This divergence occurs as k approaches infinity, or equivalently as r approaches zero. This classical Coulomb collapse singularity occurs at small scales, contrasting the other common divergence of the Coulomb potential when $r \to \infty$, for example, when analytically evaluating the electrostatic energy

of a system in classical statistical mechanics, $\lim_{R \to \infty} \int_{r_c}^{R} d\mathbf{r} \frac{1}{r} = \infty$, where the cutoff $r_c > 0$ regularizes the potential at short distances. While Gaussian charges still have the latter, long-ranged divergences, the short-ranged, $r \to 0$ singularity is tamed, allowing us to consider processes like inserting a test distribution in a molecular system.

The free energy in Equation 5.18 can be readily generalized in terms of a k-dependent dielectric constant, arising from the higher order terms neglected in the small-k expansion of the charge-charge linear response function in Equation 5.10. In this case,

$$\frac{4\pi\beta}{k^2} \hat{\chi}_0^{qq}(k) = 1 - \frac{1}{\epsilon(k)}, \tag{5.19}$$

and the linear response expression for the free energy becomes

$$\Delta G_l = -\frac{Q^2}{l\sqrt{2\pi}} \left[1 - \frac{l\sqrt{2\pi}}{\pi} \int_0^\infty dk \frac{e^{-k^2 l^2/2}}{\epsilon(k)} \right], \tag{5.20}$$

which can be readily evaluated if $\epsilon(k)$ is known, or at least a good representation of the small k-behavior of $\epsilon(k)$ should provide a reasonable approximation to ΔG_l. Simulations results for $\chi_0^{qq}(r)$ will provide such data, and can be used to verify the approximations used above. We also expect that linear response theory will be quite accurate for a Gaussian charge distribution with $l \geq 4$ Å in all classical water models, but there may, and most likely will be small differences in $\epsilon(k)$ depending on the particular interaction potential for water.

5.2.3 Gaussian Fluctuations of the Interaction Energy

The accuracy of the linear response approximations in the derivation of ΔG_l imply that the distribution of the interaction energy $\Psi(\overline{\mathbf{R}})$ is Gaussian. The distribution is then completely defined by its first two cumulants, and we determine analytic expressions for these quantities in this subsection.

In the uniform system, the first cumulant is trivially zero, $\left\langle \Psi(\overline{\mathbf{R}}) \right\rangle_0 = 0$. From Equations 5.7 and 5.18, the mean evaluated over configurations in the system with the charge present is

$$\left\langle \Psi(\overline{\mathbf{R}}) \right\rangle_Q = 2\Delta G_l = -\frac{2Q^2}{l\sqrt{2\pi}} \left(1 - \frac{1}{\epsilon} \right). \tag{5.21}$$

In Appendix G, we demonstrate that the variances in the systems with and without the Gaussian charge present are equal, $\left\langle (\delta\Psi(\overline{\mathbf{R}}))^2 \right\rangle_0 = \left\langle (\delta\Psi(\overline{\mathbf{R}}))^2 \right\rangle_Q$. The variance can be evaluated by first noting that $\left\langle (\delta\Psi(\overline{\mathbf{R}}))^2 \right\rangle_0 = \left\langle \Psi^2(\overline{\mathbf{R}}) \right\rangle_0$, because the mean interaction energy is zero in the uniform

101

fluid. The square of the energy can be rewritten as

$$
\begin{aligned}
\left\langle \Psi^2(\overline{\mathbf{R}}) \right\rangle_0 &= \left\langle \int d\mathbf{r} \int d\mathbf{r}' \rho^q(\mathbf{r}; \overline{\mathbf{R}}) \rho^q(\mathbf{r}'; \overline{\mathbf{R}}) v_Q(\mathbf{r}) v_Q(\mathbf{r}') \right\rangle_0 \\
&= \int d\mathbf{r} \int d\mathbf{r}' \left\langle \rho^q(\mathbf{r}; \overline{\mathbf{R}}) \rho^q(\mathbf{r}'; \overline{\mathbf{R}}) \right\rangle_0 v_Q(\mathbf{r}) v_Q(\mathbf{r}') \\
&= \int d\mathbf{r} \int d\mathbf{r}' \chi_0^{qq}(|\mathbf{r} - \mathbf{r}'|) v_Q(\mathbf{r}) v_Q(\mathbf{r}') \\
&= \frac{1}{(2\pi)^3} \int d\mathbf{k} \hat{\chi}_0^{qq}(\mathbf{k}) \hat{v}_Q(\mathbf{k}) \hat{v}_Q(-\mathbf{k}),
\end{aligned} \tag{5.22}
$$

using Parseval's theorem and the convolution theorem to arrive at the last equality. By expanding the linear response function $\hat{\chi}_0^{qq}(\mathbf{k})$ to second order and using the Stillinger-Lovett second moment condition, as done above for the free energy, we obtain

$$
\left\langle (\delta\Psi(\overline{\mathbf{R}}))^2 \right\rangle_0 = \left\langle (\delta\Psi(\overline{\mathbf{R}}))^2 \right\rangle_Q = \frac{2k_{\mathrm{B}}TQ^2}{l\sqrt{2\pi}} \left(1 - \frac{1}{\epsilon} \right) = -2k_{\mathrm{B}}T\Delta G_l. \tag{5.23}
$$

The probability distribution of the interaction energy can then be described by the Gaussian distribution

$$
P_{0/Q}(\Psi) = \left[2\pi \left\langle (\delta\Psi(\overline{\mathbf{R}}))^2 \right\rangle_{0/Q} \right]^{-1/2} \exp\left[-\frac{\left(\Psi - \left\langle \Psi(\overline{\mathbf{R}}) \right\rangle_{0/Q} \right)^2}{2 \left\langle (\delta\Psi(\overline{\mathbf{R}}))^2 \right\rangle_{0/Q}} \right], \tag{5.24}
$$

such that sampling in the presence of the Gaussian charge simply shifts the mean of the distribution.

5.3 Long-Wavelength Dielectric Response is Insensitive to Molecular-Scale Details

We can now test the above ideas by probing the response of dielectric fluids to a Gaussian charge distribution with simulation. In this section, we focus on the response of SPC/E and TIP5P water to this type of regularized test charge. We can take several approaches to handle the electrostatics in the simulation of these systems. The results presented in this section were obtained by using the Ewald summation method to calculate electrostatic interactions between water molecules, while the interactions between the Gaussian distribution and water was performed by simple summation using the minimum image convention. This manner of treating electrostatics leads to artifacts at the edges of the box due to discontinuities in the force from the Gaussian test charge, and we therefore omit water molecules within five Angstroms of the box edge in our results. We will see later that when
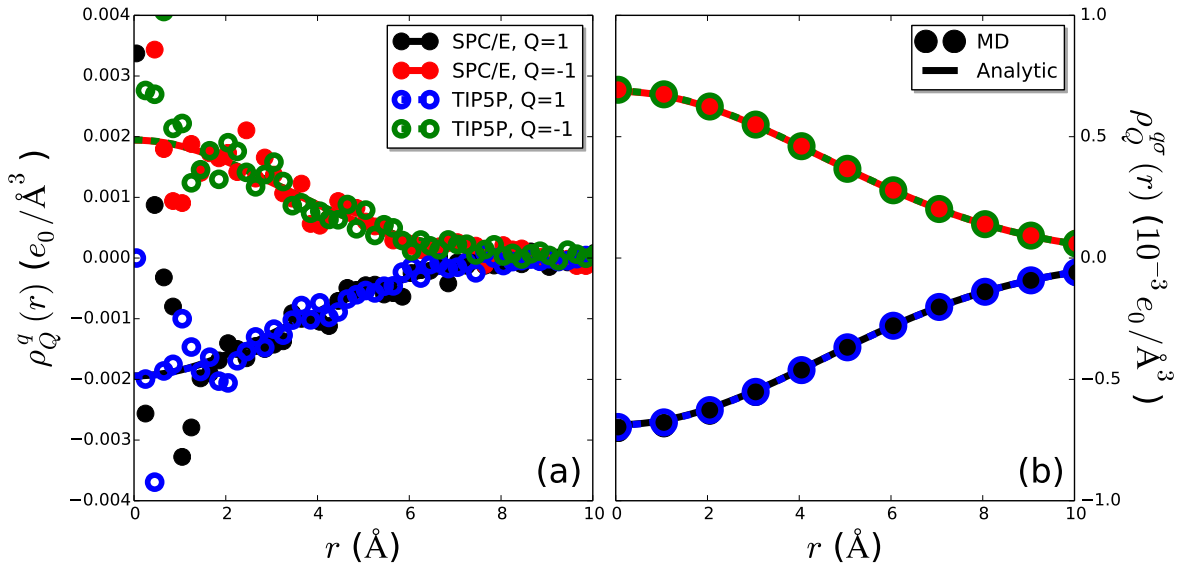
Figure 5.4: (a) Bare and (b) Gaussian smoothed charge densities for SPC/E and TIP5P water obtained in the presence of Gaussian test charge of magnitude $Q = \pm 1$ and width $l = 4.5$ Å. Data points are simulation results while lines in (a) and (b) are the analytic approximations of Equations 5.14 and 5.15, respectively. Smoothed charge densities were calculated using a smoothing length of $\sigma = l$.

Ewald summation is used to evaluate all electrostatic interactions in the system, including those between the Gaussian charge and water, significant finite size effects arise due to the periodicity of the Ewald method and need to be taken into account in our formalism.

In the previous chapter, it was demonstrated that small differences in the interaction potentials of SPC/E and TIP5P lead to significant differences in the structural response to a spherical cavity and, therefore, ion solvation thermodynamics. However, the bare and smoothed charge densities in Figure 5.4 illustrate that such molecular details are not needed for the accurate description of long-wavelength dielectric response. The analytic approximations for the induced charge densities in Equations 5.14 and 5.15 describe the simulation data remarkably well, illustrating that far-field electrostatics follows dielectric continuum theory. Since the only property of the fluid in the expressions for $\rho_Q^q(r)$ and $\rho_Q^{q\sigma}(r)$ is the dielectric constant, we can conclude that this is all that is needed for a model to accurately describe long-wavelength dielectric response. Indeed, the dielectric constants of SPC/E and TIP5P are quite similar, $\epsilon_{\text{SPC/E}} = 72$ while $\epsilon_{\text{TIP5P}} = 81.5$, and their responses to a Gaussian test charge are nearly identical.
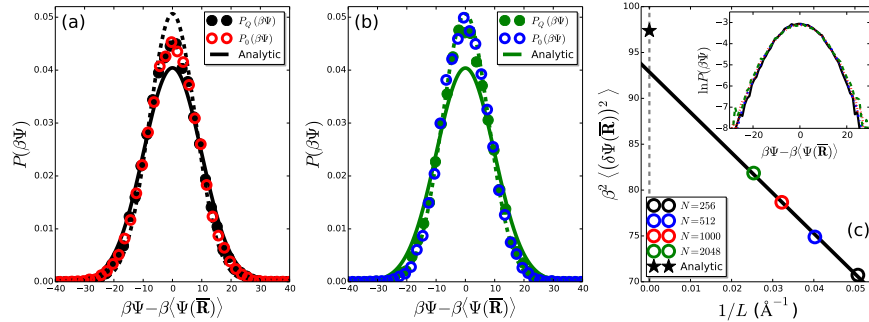
Figure 5.5: Probability distributions of the interaction energy Ψ between (a) SPC/E or (b) TIP5P water and a Gaussian test charge of magnitude $Q = +1$ and $l = 4.5$ Å in the uniform fluid, $P_0(\Psi)$, and in the presence of the test charge, $P_Q(\Psi)$. Solid lines are the corresponding analytic approximations given by Equation 5.24. Dashed lines are the finite size corrected approximations to the distributions obtained with a variance estimated by Equation 5.25. (c) The variance of the interaction energy in SPC/E water as a function of inverse box length L. The solid line is a linear fit to the data points and the starred data point is the continuum approximation to the variance given by Equation 5.23. (inset) Natural logarithm of the probability distributions corresponding to the data points in the main figure.

In addition to providing an accurate description of the static dielectric response, fluctuations in the energy are well approximated by the framework developed herein, as evidenced by the probability distributions of the interaction energy Ψ in Figure 5.5. For both SPC/E and TIP5P water models, the distribution $P_0(\Psi)$ obtained from the uniform bulk is nearly identical to the distribution $P_Q(\Psi)$ calculated in the presence of the Gaussian test charge when shifted by their respective means. This demonstrates that fluctuations in the water-test charge interaction energy do in fact follow Gaussian statistics, such that their variances are equal. This variance is well approximated by Equation 5.23, as evidenced by the solid lines in Figure 5.5 obtained through the use of Equation 5.23 in Equation 5.24. However, Equation 5.23 slightly overestimates the width of $P_{0/Q}(\Psi)$.

A large portion of this overestimation is simply due to finite size effects. Equation 5.23 assumes an infinite system size, whereas the simulation results in Figures 5.5a and 5.5b were obtained with cubic cells containing $N = 1000$ water molecules. We can account for such finite size effects in our formalism in an approximate manner by assuming a spherical cutoff at the edge of simulation cell. At this cutoff, $L/2 \gg l$, the potential of the Gaussian test charge is nearly equal to the Coulomb potential, $v_Q(r) \approx 1/r$. Therefore, we can estimate the finite size effects with a simple Born model. The contribution to the free energy outside the cutoff radius is $\Delta G(L/2) = -Q^2(1 - 1/\epsilon)/L$. The variance of the fluctuations in interaction energy in a finite system of radius $L/2$ can then be written

as

$$\left\langle (\delta\Psi(\overline{\mathbf{R}}))^2 \right\rangle_{\text{FS}} \approx \left\langle (\delta\Psi(\overline{\mathbf{R}}))^2 \right\rangle - \frac{2k_{\text{B}}TQ^2}{L}\left(1 - \frac{1}{\epsilon}\right), \tag{5.25}$$

where the subscript "FS" indicates that the average is obtained in a system of finite size, the first term on the right hand side is the variance given by Equation 5.23, and the second term removes the portion of the variance from interactions outside the cutoff radius $L/2$. Distributions calculated using Equation 5.25 are in better agreement with the simulation results than the infinite system limit, as evidenced by the dashed lines in Figure 5.5.

Finite size effects on the variance of the distribution $P(\Psi)$ can be quantitatively analyzed by performing simulations for a range of N, and the results obtained for this process are shown in Figure 5.5c. The linear dependence on L^{-1} expected from Equation 5.25 is confirmed, and extrapolation to the limit $L \to \infty$ yields a variance of $\beta^2 \left\langle (\delta\Psi(\overline{\mathbf{R}}))^2 \right\rangle \approx 93$, much closer to the continuum estimate of $\beta^2 \left\langle (\delta\Psi(\overline{\mathbf{R}}))^2 \right\rangle \approx 97$. When such finite size effects are taken into account, the above formalism describes the simulation results with great accuracy, although the continuum estimates for the energy fluctuations are still not in perfect agreement the simulation results.

We expect the remaining discrepancies in the widths of the distributions arise from the neglect of correlations of order k^4 and possibly higher. This is supported by comparison of the variances of the SPC/E and TIP5P models, which differ more than their respective dielectric constants would predict. There is no general relation for the fourth moment of the charge-charge linear response function, because it depends on the nature of the short ranged, non-electrostatic interactions of the fluid, and for the one-component plasma and two-component primitive model is inversely proportional to the compressibility [26], $\hat{\chi}_0^{(4)qq} \propto \kappa_T^{-1}$. Consequently, we expect even long-wavelength fluctuations of the dielectric response to depend on the microscopic details of the fluid under consideration to a small extent, while the static thermodynamic and structural responses on these length-scales are insensitive to features beyond the dielectric constant.

The formalism developed herein is readily amenable to dielectrics other than water. For example, we can also test the above approximations on dielectrics that do not screen charge as efficiently as water, such as carbon tetrachloride (CCl_4). CCl_4 is tetrahedral and symmetric, and therefore does not have a dipole moment in the gas phase, although it does have a dielectric constant greater than unity in the liquid phase. The induced dipole in the condensed phase can be mimicked in rigid, point charge models by adding a fixed dipole moment that reproduces the dielectric constant. This task has been performed by Fennell et $al.$ [111]. There both localized (L) and delocalized (D) dipole moment models of CCl_4 were parametrized, and these are depicted in Figures 5.6a and 5.6b, respectively. These models place a fixed dipole on CCl_4 by putting a partial positive charge on the carbon atom and a negative charge on a single chlorine atom in the localized model or negative charges on three of the four chlorine atoms in the delocalized dipole model.

For whatever reason, I am unable to reproduce the results from the original paper with the
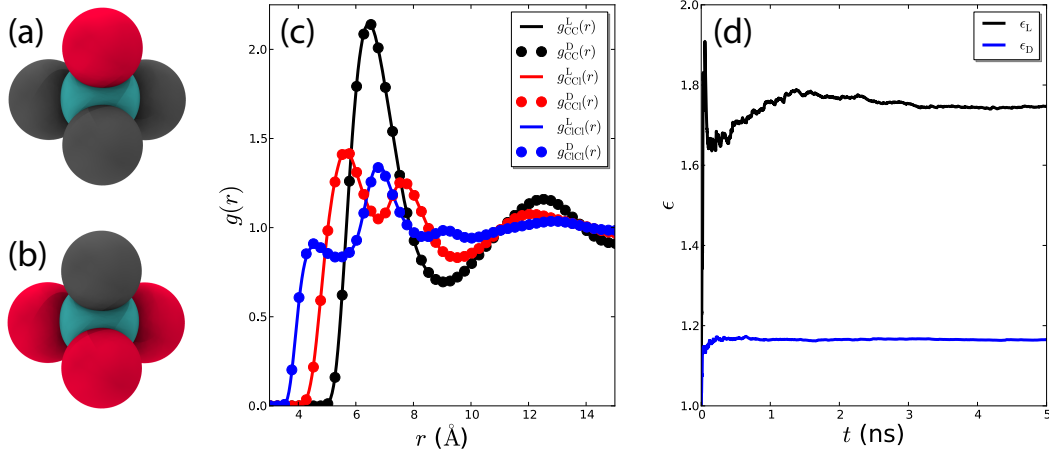
Figure 5.6: Schematic depiction of the (a) localized and (b) delocalized dipole models of CCl_4 parametrized by Fennell *et al.* [111]. The positively charged carbon site is shown in cyan, uncharged chlorine atoms are colored grey, while negatively charged chlorides are shown in red. (b) Site-site pair distribution functions in the localized and delocalized models. Carbon-chlorine and chlorine-chlorine distribution functions are averaged over all chlorine atoms. (d) Running average of the dielectric constant for both CCl_4 models under study.

parameters listed there [111]. However, the models do serve as an interesting test of our formalism and as a case study in dielectric response in their own right. The site-site pair distribution functions between various sites of CCl_4 are shown in Figure 5.6c, and indicate that the bulk structure of the two models is identical. Despite this fact, the dielectric constants of the two models differ significantly, with $\epsilon_L = 1.76$ and $\epsilon_D = 1.17$ [2]. The running averages of the dielectric constants are shown in Figure 5.6d and were obtained from the relation

$$\epsilon = 1 + \frac{4\pi\beta \left\langle \delta \mathbf{M}^2 \right\rangle}{3 \left\langle V \right\rangle}, \tag{5.26}$$

where $\delta \mathbf{M} = \mathbf{M} - \langle \mathbf{M} \rangle$ and $\mathbf{M}$ is dipole moment of the simulation cell. Hence, these models represent the interesting case of two liquids with identical bulk structure but differing dielectric responses.

The first peak in the carbon-carbon $g(r)$ is located at $r \approx 6.5$ Å, and I have found that the

---

[2]Fennell *et al.* obtain nearly equal dielectric constants for the localized and delocalized models, $\epsilon_L = 2.02$ and $\epsilon_D = 2.112$, respectively.
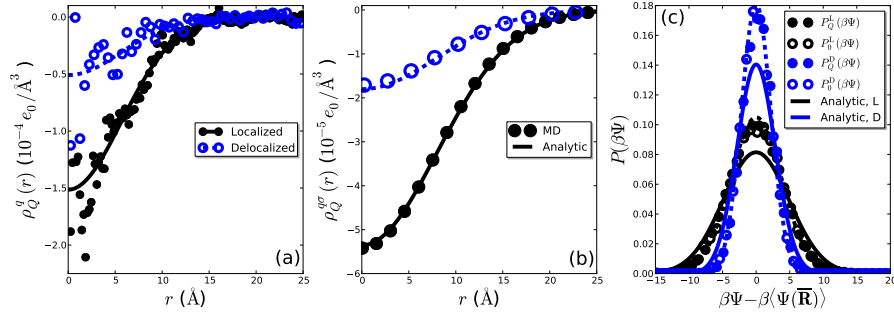
Figure 5.7: (a) Bare and (b) Gaussian smoothed charge densities for localized and delocalized dipole models of CCl_4 obtained in the presence of Gaussian test charge of magnitude $Q = +1$ and width $l = 8$ Å. Data points are simulation results while lines in (a) and (b) are the analytic approximations of Equations 5.14 and 5.15, respectively. Smoothed charge densities were calculated using a smoothing length of $\sigma = l$. (c) Probability distributions of the interaction energy Ψ between the localized (L) or delocalized (D) dipole models of CCl_4 and a Gaussian test charge of magnitude $Q = +1$ and $l = 8$ Å in the uniform fluid, $P_0(\Psi)$, and in the presence of the test charge, $P_Q(\Psi)$. Solid lines are the corresponding analytic approximations given by Equation 5.24. Dashed lines are the finite size corrected approximations to the distributions obtained with a variance estimated by Equation 5.25.

minimum LMF smoothing length needed to capture the structure of the bulk fluid is roughly $\sigma_{\min} \approx 8.0$ Å. Therefore, I have chosen to insert a Gaussian of width $l = 8$ Å into CCl_4, ensuring that the charge distribution acts over a length scale of several molecules. The induced bare and smoothed charge densities are shown in Figure 5.7. While the bare charge densities suffer from statistical noise, they still appear to be approximated rather well by the linear response approximations derived in Section I. Gaussian smoothing of $\rho_Q^q(r)$ eliminates much of the simulation noise, and smooth profiles are obtained for $\rho_Q^{q\sigma}(r)$ that are very well described by Equation 5.15, shown as points in Figure 5.7b.

As was the case for water, the probability distributions of the test charge-CCl_4 interaction energy shown in Figure 5.7c are remarkably Gaussian, evidenced by the fact that $\left\langle (\delta\Psi(\overline{\mathbf{R}}))^2 \right\rangle_0 = \left\langle (\delta\Psi(\overline{\mathbf{R}}))^2 \right\rangle_Q$. However, Equation 5.23 again overestimates the widths of the distributions for both L-CCl_4 and D-CCl_4, though much of this overestimation is due to finite size effects, and the distributions are almost exactly captured by estimating the variance with Equation 5.25. It is also interesting to note that the two models differ from their respective continuum estimates by nearly the same amount. One might expect fluctuations in the two models to differ equally from the continuum approximations because the short ranged, non-electrostatic interactions are nearly equivalent in the two models of CCl_4. These molecular-scale details control the behavior of the higher order moments of $\hat{\chi}_0^{qq}(\mathbf{k})$ that are neglected in the continuum approximations detailed above.

5.4 Conductors Require More Detail

As a more rigorous test of our ideas, we apply the above dielectric continuum formalism to a conductor, the symmetric primitive model (SPM) electrolyte. In lieu of the traditional SPM, which consists of charged hard spheres of equal diameter, the data below is for charged WCA spheres with equal LJ diameters, which is easier to treat using conventional molecular dynamics simulations. However, I have carried out Monte Carlo simulations of the traditional SPM for a few systems studied herein, and the results obtained are in agreement with those for its WCA variant.

In a conducting medium, $\epsilon = \infty$, and Equation 5.14 becomes

$$\rho_Q^q(\mathbf{r}) = -\frac{Q}{l^3 \pi^{3/2}} e^{-r^2/l^2}. \tag{5.27}$$

Within this level of approximation, the induced charge density is equal and opposite to the Gaussian charge distribution itself! Therefore, the total charge density is given by $\rho_{\text{tot}}^q(\mathbf{r}) = 0$, which is just a statement of neutrality, the zeroth moment condition [26, 107, 108, 109]. Unlike the case of a dielectric medium, to zeroth order, our approximation for the *total charge density* has no non-zero terms. We may anticipate that at least the first non-zero term in the small k expansion of the charge density is needed for an accurate description of the response of a conducting fluid to a Gaussian test charge, and this can be done by keeping up to the k^4 term in the expansion of the linear response function.

As in Section 5.2, we can write the charge density in k-space as

$$\hat{\rho}_Q^q(\mathbf{k}) \approx -\beta \hat{\chi}_0^{qq}(\mathbf{k}) \hat{v}_Q(\mathbf{k}), \tag{5.28}$$

and again expand the linear response function, but keeping terms to fourth order in k now,

$$\hat{\chi}_0^{qq}(\mathbf{k}) \sim \hat{\chi}_0^{(0)qq} + k^2 \hat{\chi}_0^{(2)qq} + k^4 \hat{\chi}_0^{(4)qq} = k^2 \hat{\chi}_0^{(2)qq} + k^4 \hat{\chi}_0^{(4)qq}. \tag{5.29}$$

The induced charge density can then be written as

$$\hat{\rho}_Q^q(\mathbf{k}) \approx -Q e^{-k^2 l^2/4} - 4\pi \beta Q k^2 \hat{\chi}_0^{(4)qq} e^{-k^2 l^2/4}, \tag{5.30}$$

which, in r-space is

$$\rho_Q^q(\mathbf{r}) = -\frac{Q}{l^3 \pi^{3/2}} e^{-r^2/l^2} + \frac{4\pi \beta Q \hat{\chi}_0^{(4)qq}}{l^5 \pi^{3/2}} \left[\left(\frac{2r}{l}\right)^2 e^{-r^2/l^2} - 6 e^{-r^2/l^2} \right]. \tag{5.31}$$

This expression includes the first nonzero term in the small k expansion of the *total* charge density, which involves the fourth moment of the bulk linear response function. However, $\hat{\chi}_0^{(4)qq}$ has no general analytic expression and depends sensitively on the details of the intermolecular potentials

(both short and long ranged), and must be determined by other means.

In analogy to the results obtained for dielectric media, we can use the expression for the charge density in Equation 5.31 to obtain the free energy of inserting a Gaussian test charge and the fluctuations in the interaction energy. In this level of approximation, the free energy ΔG_l of inserting a Gaussian test charge into a conducting medium is

$$\Delta G_l = -\frac{Q^2}{l\sqrt{2\pi}}\left(1 + \frac{4\pi\beta\hat{\chi}_0^{(4)qq}}{l^2}\right) \tag{5.32}$$

and the variance of the interaction energy is

$$\left\langle \left(\delta\Psi(\overline{\mathbf{R}})\right)^2 \right\rangle_{0/Q} = \frac{2k_{\mathrm{B}}TQ^2}{l\sqrt{2\pi}}\left(1 + \frac{4\pi\beta\hat{\chi}_0^{(4)qq}}{l^2}\right). \tag{5.33}$$

In order to apply Equations 5.31–5.33, we need to estimate $\hat{\chi}_0^{(4)qq}$. The generalized Debye-Hückel (GDH) theory of Lee and Fisher [112, 113, 114] provides an expression for the fourth-moment of the charge-charge linear response function,

$$\hat{\chi}_{0,\mathrm{GDH}}^{(4)qq} = \rho\xi_D^4\left[1 + \frac{2}{3}\ln(1+x) - \frac{2}{3}x - \frac{1}{6}x^2\right], \tag{5.34}$$

where $\xi_D = \sqrt{k_{\mathrm{B}}T/(8\pi q^2\rho)}$ is the Debye length, q is the magnitude of the charge of the ions, and $x = d/\xi_D$ is the diameter of an ion in units of the Debye length. The GDH theory satisfies both the zeroth and second moment conditions of Stillinger and Lovett [107, 108, 109, 112, 114], and yields exact results for correlations in the low density limit. However, GDH predictions are only semi-quantitative, and in general will not yield accurate estimates of $\hat{\chi}_0^{(4)qq}$ for all ρ and Γ. Nevertheless, simulation results [114] seem to indicate that at our chosen state point, which is far from the critical point, GDH theory will yield reasonable estimates for the fourth moment of the linear response function. We indeed find this to be true, as detailed below.

We probe the response of a neutral SPM composed of $N = N_+ + N_- = 1000$ ions at a density of $\rho d^3 = 0.3816$ and a coupling strength of $\Gamma = \beta q^2/d = 5$ to Gaussian test charges of varying width and magnitude, where $d \approx \sigma_{\mathrm{LJ}}$ is the approximate diameter of an ion of the SPM, with a LJ well depth of $\varepsilon_{\mathrm{LJ}} = k_{\mathrm{B}}T$. For all Q and l studied, we find that terms of order k^4 in the expansion of the linear response function (which are of order k^2 in the nonuniform charge density) are needed to accurately describe the structural response for all r, as indicated by the smoothed charge densities shown in Figure 5.8. However, as expected, at large enough r both expressions for the induced charge density converge to the same value and accurately describe the asymptotic density response.
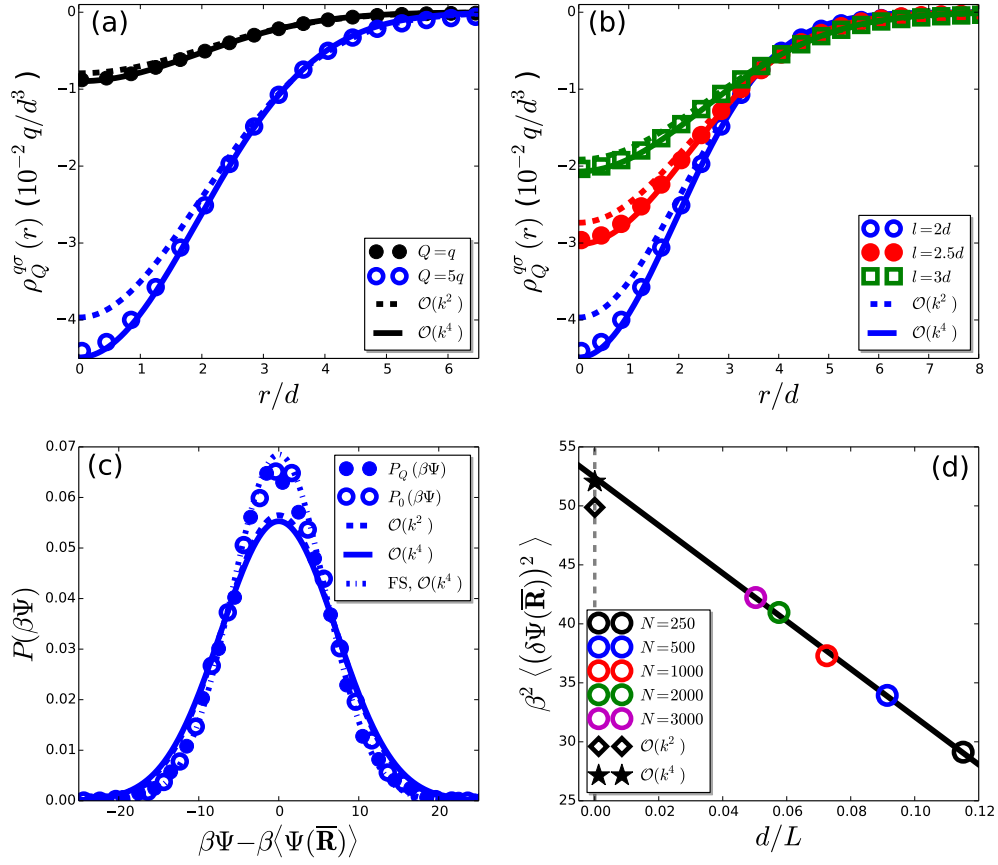
Figure 5.8: Gaussian smoothed charge densities of the SPM in response to Gaussian charge distributions of (a) varying charge with fixed width $l = 2d$ and (b) varying width with $Q = 5q$. Symbols are simulation results, the approximations to second and fourther order in the expansion of the linear response function are indicated by dashed lines and solid lines, respectively. Gaussian smoothing was performed using $\sigma = 2d$. (c) Probability distributions of the interaction energy Ψ for a Gaussian test charge of magnitude $Q = 5d$ and $l = 2d$ in the uniform fluid, $P_0(\Psi)$, and in the presence of the test charge, $P_Q(\Psi)$. Dashed and solid lines are the corresponding analytic approximations with the variance of the distribution given by Equations 5.23 and 5.33, respectively. (d) Variance of the interaction energy as a function of L^{-1} for a Gaussian test charge with $Q = 5d$ and $l = 2d$ in the RPM. The solid line is a linear fit to the data points and the starred data point is the continuum approximation to the variance given by Equation 5.33.

Fluctuations in the test charge-SPM interaction energy follow Gaussian statistics for all systems under study. The width of the distributions are underestimated by the continuum approximations, again due to finite size effects, and including contributions from $\hat{\chi}_0^{(4)qq}$ slightly *increases* the variance. Accounting for such finite size effects can be accomplished by combining the simple Born correction of Equation 5.25 with the estimate for the variance in Equation 5.33, as evidenced by the curve labeled "FS, $\mathcal{O}(k^4)$" in Figure 5.8c. Therefore, the variance of the distributions will again scale linearly with $1/L$. Indeed, simulation results obtained by varying N from 250 to 3000 ions yields this expected scaling behavior, as shown in Figure 5.8d. In fact, the $L \to \infty$ limit obtained from linear fitting of the variance as a function of $1/L$ agrees well with the estimate of Equation 5.33. In contrast, neglect of terms of order k^4 in the expansion of the charge-charge linear response function leads to an underestimation of the infinite system limit as obtained from simulation, illustrated by the point labeled $\mathcal{O}(k^2)$ in Figure 5.8d. Therefore, by accounting for the leading order contribution to the density response of the SPM arising from short ranged interactions in an approximate manner, we are able to completely describe the electrostatic response of a conducting fluid to a Gaussian test charge with quantitative accuracy.

5.5 Ewald Finite Size Effects in the Gaussian Electrostatic Potential

Before concluding this chapter, it is appropriate to briefly discuss the finite size effects that can arise from the periodicity of the Ewald method when using lattice summations to evaluate the interactions between the Gaussian test charge and the dielectric or conducting fluid in which the charge is immersed. In the continuum, infinite system case, the electrostatic potential of such a charge distribution can be obtained from the Poisson's equation

$$\nabla_{\mathbf{r}}^2 v_Q(\mathbf{r}) = -4\pi\rho^q(\mathbf{r}) = -4\pi Q\rho_G(\mathbf{r}), \tag{5.35}$$

where $\rho_G(\mathbf{r}) = (\pi^{3/2}l^3)^{-1} \exp(-|\mathbf{r}|^2/l^2)$ is a Gaussian distribution of width l. This can be readily solved, (the solution is especially easy after transforming to Fourier space), and is given by

$$v_Q(\mathbf{r}) = \frac{Q \, \mathrm{erf}(r/l)}{r}, \tag{5.36}$$

which is just the long ranged portion of the Coulomb potential as defined in LMF theory. Therefore, the potential $v_Q(r)$ has the typical long ranged divergences associated with the Coulomb potential when attempting to perform simulations. In simulations, however, we cannot study infinite systems, and are instead confined to the study of systems with a finite size. In order to give the appearance of an infinite system, periodic boundary conditions (PBCs) are typically used, in which the central simulation cell is replicated "to infinity" in all directions.

In order to accomplish this task, we consider an infinite periodic array of Gaussian charge
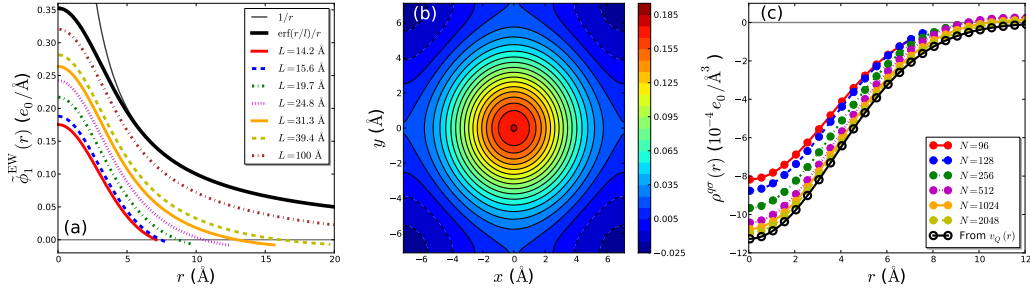
Figure 5.9: (a) Rotationally averaged Gaussian Ewald potentials $\tilde{\phi}_1^{\mathrm{EW}}(r)$ for various box lengths L compared to the full Gaussian potential $\mathrm{erf}(r/\sigma)/r$ and $1/r$. (b) Gaussian Ewald potential as a function of x- and y-coordinates in the $z = 0$ plane, $\phi_1^{\mathrm{EW}}(x, y, z = 0)$, for $L = 14.2$ Å. (c) Gaussian smoothed charge densities for simulation cells of SPC/E water corresponding to the values of L in (a). The Gaussian test charge has width $l = 3.2$ Å and Gaussian smoothing of bare charge density was performed with $\sigma = 4.5$ Å. Also shown is the Gaussian smoothed charge density obtained without Ewald summation for test charge-water interactions (From $v_Q(r)$), which is consistent with the continuum, infinite system limit.

distributions with their corresponding uniform neutralizing background charge densities (in order to avoid an infinite build up of charge). The Poisson's equation for this system is

$$\nabla_{\mathbf{r}}^2 \phi(\mathbf{r}) = -4\pi Q \left[\sum_{\mathbf{n}=-\infty}^{\infty} \rho_G(\mathbf{r} - \mathbf{n}L) - \frac{1}{L^3} \right], \tag{5.37}$$

where L is the length of a side of the cubic simulation cell, and $\mathbf{n} = (n_x, n_y, n_z)$ is a lattice vector, such that $n_\alpha = (..., -2, -1, 0, 1, 2, ...)$. As one familiar with Ewald summation may have anticipated, the solution to this equation is the long ranged portion of the Ewald potential,

$$\phi_1^{\mathrm{EW}}(\mathbf{r}) = \frac{Q}{L^3} \sum_{\mathbf{k} \neq 0} \frac{4\pi}{k^2} e^{-k^2 l^2/4} e^{i\mathbf{k}\cdot\mathbf{r}} - \frac{Q\pi l^2}{L^3}, \tag{5.38}$$

where the second term in Equation 5.38 is the potential from the neutralizing background charge density. Note that in the usual discussions of the Ewald potential, the substitution $\eta = 1/l$ is typically made, however, I have decided to use l here to make clear any connections with LMF theory and our use of Gaussian test charges throughout this chapter.

Due to the periodicity of the system, the Gaussian Ewald potential is only equal to $v_Q(r)$ in the limit $L \to \infty$. For finite L, $\phi_1^{\mathrm{EW}}(\mathbf{r}) < v_Q(r)$, and the Ewald potential and its derivative must be

continuous at the edge of the central simulation cell. Therefore, the shape of the Gaussian Ewald potential is not spherically symmetric and must differ from that of its infinite limit, $v_Q(r)$. The rotationally averaged potentials

$$\tilde{\phi}_1^{\mathrm{EW}}(r) = \frac{1}{4\pi} \int_0^{2\pi} d\varphi \int_0^{\pi} d\theta \sin\theta \phi_1^{\mathrm{EW}}(r, \varphi, \theta), \tag{5.39}$$

shown in Figure 5.9a, display significant finite size effects and only slowly approach $v_Q(r)$ as L is increased. Indeed, $\tilde{\phi}_1^{\mathrm{EW}}(r) \neq v_Q(r)$ even for $L = 100$ Å!

Similar to what was found by Levy and coworkers [95] for the case of a periodic array of point charges, the periodic Ewald potential $\phi_1^{\mathrm{EW}}(\mathbf{r})$ of an array of Gaussian charges is *not* spherically symmetric, as illustrated by $\phi_1^{\mathrm{EW}}(x, y, z = 0)$, shown in Figure 5.9b for a representative value of L. Therefore, when determining the response of a dielectric fluid to a Gaussian charge distribution using PBCs, one must take into account both the finite-size effects and the asymmetry of the potential. Thus, we should not expect the response of a dielectric to $\phi_1^{\mathrm{EW}}(\mathbf{r})$ to be the same as the response of the same material to $v_Q(r)$, even for large box sizes.

Indeed, the Gaussian smoothed charge densities obtained for SPC/E in the presence of such a periodic array of Gaussian test charges shown in Figure 5.9c exhibit finite size effects consistent with the spherically averaged potentials shown in Figure 5.9a. While the effects of the Ewald periodicity are readily observed near $r = 0$, with $\rho^{q\sigma}(0)$ decreasing toward the infinite limit with increasing L, interesting non-physical effects are found at large distances. In particular, $\rho^{q\sigma}(r)$ changes sign near the point where the corresponding potential $\tilde{\phi}_1^{\mathrm{EW}}(r)$ becomes negative. This does not occur in the absence of periodicity, and indeed our theoretical approximations for the charge density predict no such "overcharging" behavior, in which a net charge of opposite sign builds up around the Gaussian test charge. These effects are not expected in a "real," physical fluid, and is precisely why Ewald summation was not used to evaluate test charge-water interactions when obtaining the data used throughout most of this chapter.

5.6 Conclusions

In this chapter, we have examined the response of dielectric and conducting fluids to a Gaussian test charge distribution. We presented a theoretical formalism to estimate the structural and thermodynamic response of these fluids in a quantitatively accurate manner through physically sound approximations. It was shown that the structural response of a dielectric fluid to Gaussian charges depends only on the dielectric constant and is insensitive to other molecular-scale details. The analogous response in a conducting fluid depends only slightly on the short ranged details of the models. In both dielectric and conducting fluids, a quantitatively accurate description of the observed Gaussian energy fluctuations requires some molecular-scale details and the finite size of the system

must be taken into account.

These developments will prove useful to estimate ion solvation thermodynamics by simulation. Through the use of the LMF-based solvation process in Figure 5.3, one can calculate the far field electrostatic component of the free energy analytically. The free energy contributions from the remaining steps must be obtained from simulation. However, one can again use ideas from LMF theory, especially the solvation theory developed in the next chapter, to obtain the remaining portions of the free energy from computationally efficient simulations of purely short ranged systems.

The formalism presented herein can also be utilized to determine dielectric constants from the structural response of a dielectric fluid to the presence of a Gaussian test charge. For example, one can determine $\rho^{q\sigma}(r)$ from simulation with high accuracy, then fit this smoothed charge density to Equation 5.15 to obtain ϵ. In addition, the structural response could even be determined from simulations of the bulk fluid using Equation 5.16, readily allowing for the determination of the charge density induced by a range of Gaussian test charges with varying Q and l. This may find use in determining dielectric constants from computationally intense quantum mechanics-based simulations, where the continuous nature of the electron density makes it difficult to define molecular units and expressions like Equation 5.26 become intractable.

Another avenue for further investigation is to examine the state point-dependence of the approximations developed herein for both dielectric and conducting systems. In particular, we expect the above formalism to break down in the critical region; it has been found that the Stillinger-Lovett second moment condition breaks down and $\hat{\chi}_0^{(4)qq}$ diverges at the critical point [114]. However, Equation 5.31 may be used to determine $\hat{\chi}_0^{(4)qq}$ away from the critical point from fits to $\rho^q(r)$ and $\rho^{q\sigma}(r)$, in analogy to the above discussion for the dielectric constant, and may even be used to study the divergence of charge-charge correlations on the approach to Coulomb criticality.

Good theories are either Gaussian or everything.

Lawrence R. Pratt

6

Free Energy Calculations with Local Molecular Field Theory

6.1   Introduction

The complete description of any chemical or biological process requires an understanding of the underlying free energy landscape. Consequently, a fundamental problem in statistical mechanics is the development of accurate and efficient means to calculate thermodynamic properties of molecular systems. Much progress in this area has been made in the past fifty years, from the development of a solid foundation consisting of perturbation theory [115, 116], and thermodynamic integration [117], to advanced computer simulation techniques to overcome sampling bottlenecks, like the umbrella sampling methods used throughout this thesis [118]. Free energy calculations have even been extended to non-equilibrium systems, with the advent of the Jarzynski equality [119], Crooks fluctuation relation [120], and techniques for sampling in the space of trajectories [121], as opposed to traditional sampling performed in configuration space.

The development of such techniques for free energy computation in conjunction with recent rapid technological growth has revolutionized the area of computer simulations. Despite the immense progress made in free energy calculation methodology, all are plagued by the same inefficiencies when electrostatic interactions are present. These inefficiencies arise from the long range nature of the Coulomb potential, which is typically evaluated using lattice summation techniques like that due to Ewald [31]. The computational time associated with the Ewald summation in typical

implementations scales as $\mathcal{O}(N^2)$, where N is the number of charged particles in the system. Even its most efficient implementation, the particle mesh Ewald (PME) method, scales with the number of sites as $\mathcal{O}(N \log N)$, but with a large prefactor, and the method does not scale well in massively-parallel simulations [122]. Thus systems with Coulomb interactions present significantly more computational problems than a system with only short ranged interactions, like a LJ fluid, which scales linearly with N. The situation only worsens when one considers the fact that, unlike the internal energy or pressure, the free energy cannot typically be obtained directly from a single simulation, as will be discussed in detail later, but one must perform a series of long computer simulations to calculate even a single free energy or free energy landscape.

In addition to sampling issues, the use of lattice summation techniques with periodic boundary conditions in finite size systems lead to significant errors to due artifacts in the periodic potential. In particular, spurious interactions between images of solutes in nonuniform systems can occur, as observed for proteins in water [123]. In addition, the forced neutrality and continuity of the potential and force at the boundaries of the simulation cell lead to distorted electrostatic potentials that are not spherically symmetric [95], as discussed in the previous chapter.

Local molecular field theory is a promising avenue for substantially improving *all* free energy calculations by removing many of the computational and conceptual burdens associated with long ranged interactions. LMF theory prescribes a way to obtain the structure of a full system, with computationally difficult long ranged interactions, from a mimic system wherein particles interact with short ranged potentials only. It will be shown that LMF theory contrasts traditional "top-down" approaches to molecular structure and thermodynamics, like classical DFT [10], wherein thermodynamic functions obtained from uncontrolled approximations to the free energy functional itself are differentiated to obtain structural properties. Instead, LMF theory can be considered a "bottom-up" approach to thermodynamics. LMF theory first focuses on the underlying *forces* in a molecular system, and then determines accurate structural properties by compensating for the averaged effects of long ranged interactions with the presence of an effective field in the mimic system. Once the desired structure is obtained, we can integrate over structural properties in order to obtain thermodynamic properties like the free energy, akin to what is done in perturbation theories of uniform fluids [6]. Hence, LMF theory starts at the "bottom" with intermolecular forces, and successively integrates "up" to obtain thermodynamics.

In this chapter, we develop the formalism for performing LMF-based free energy calculations and demonstrate its accuracy on numerous systems of interest. We focus on three major classes of free energy calculations [116], (i) solvation free energies, (ii) alchemical transformations, and (iii) potentials of mean force. The basis for LMF free energy calculations is developed in the next section within the context of solvation free energies, wherein a solute is gradually transformed from a non-interacting particle into the full solute of interest. This LMF approach can then be readily applied to the process of changing one solute into another, through modification of the solute-solvent interaction potentials. The study of such alchemical transformations is performed in Section 6.3. We then extend the LMF

formalism to calculate free energies as a function of an order parameter describing a process of interest. The calculation of such potentials of mean force involves combining LMF theory with umbrella sampling, and this is accomplished in Section 6.4 before concluding the chapter in Section 6.5.

6.2   LMF Theory of Solvation

In this section, we derive the basis of the LMF theory-based framework for free energy calculations. For simplicity and clarity, we consider the solvation of a rigid solute fixed at the origin in a single component fluid as a basis for the treatment of more general solvation phenomena. Figure 6.1 schematically depicts the solvation of such a solute in a LJ fluid, but similar considerations immediately apply to more complex solvents, including mixtures and fluids with long ranged Coulomb interactions.

We consider the process of gradually "turning on" a solute-solvent interaction potential $\phi(\mathbf{r})$, such that the solvation free energy Ω_{solv} is the difference in the Grand free energy of the solvent-solute system and the pure solvent in zero solute field: $\Omega_{\mathrm{solv}}[\phi] \equiv \Omega[\phi] - \Omega[\phi = 0]$, such that Ω_{solv} is a functional of the solute field ϕ. The lower left panel of Figure 6.1 shows the core positions of the mobile bulk solvent (M) in a typical configuration. The solvent molecules interact with a pair potential $u(r) = u_0(r) + u_1(r)$, where $u_1(r)$ is the long ranged, slowly varying portion of the solvent-solvent potential. This long ranged portion of the potential can arise from electrostatic interactions or the attractive tail of the LJ potential, for example. The lower right panel of Figure 6.1 schematically depicts an equilibrium configuration of the full solute-solvent system, where the solute (S) has been inserted into the fluid. The solute-solvent potential $\phi(\mathbf{r})$ is harshly repulsive at short distances where cores will overlap, and may also contain other short ranged forces describing hydrogen bonding and other local interactions. There will also exist long ranged solute-solvent interactions in general, but we can assume that far from the solute an unperturbed, neutral bulk solvent will exist.

In practice, the solvation free energy cannot generally be computed by simulating only the two states depicted in the lower leg of Figure 6.1. Instead, one must consider the gradual transformation of a non-interacting point solute into the full solute through a series of generally non-physical intermediate states. Such stratification techniques can be performed with high accuracy, but the transformation process typically must be carried out in small steps, especially when the harshly repulsive core interactions are altered between neighboring states. In addition, this multistep process requires an accurate treatment of long ranged interactions at every step. This is particularly cumbersome when Coulomb interactions are present, since standard lattice summation techniques, like those due to Ewald [31] and Lekner [124], add significant overhead to the simulation time at each step. We indicate this general problem by using a red arrow to connect the two lower panels of Figure 6.1.

The LMF theory of solvation presented herein introduces a thermodynamic cycle involving a short

117

ranged mimic system that allows one to eliminate much of the overhead arising from conventional treatments of long ranged forces. Moreover, it provides a natural and physically suggestive way of partitioning the free energy into short ranged or *near field* and long ranged or *far field* components that is conceptually related to some elements of the formally exact partitioning scheme used with great success in the quasichemical theory of solvation [82, 125].

The LMF thermodynamic cycle uses the two upper panels in Figure 6.1, which describes solvation in a mimic system with short ranged intermolecular interactions. The upper left panel illustrates a configuration of the strong coupling or mimic solvent (M_0), such that the red color indicates truncated solvent-solvent interactions ($u_0(r)$ for a LJ fluid). The slowly varying, long ranged components of the intermolecular forces tend to cancel in a uniform fluid, and therefore the particle arrangements are similar in the bulk M and M_0 panels.

Solvation in the mimic system involves insertion of a mimic solute (S_R), described by the *renormalized* potential ϕ_R given by LMF theory, and the determination of the free energy associated with this process is discussed later in Section 6.2.1. This potential contains all the short ranged solute-solvent interactions $\phi_0(\mathbf{r})$ that are in the full potential $\phi(\mathbf{r})$. In addition, the averaged effects of the slowly-varying long ranged interactions on the solvent structure are taken into account using LMF theory, as suggested by the patterning of the solute color in the upper right panel of Figure 6.1.

The solvation free energy of the mimic system $\Omega_{R,solv}[\phi_R]$ can be determined using conventional methods, and will be discussed in more detail below. Since $\phi_R(\mathbf{r})$ contains all the short ranged portions of $\phi(\mathbf{r})$, this process is inherently difficult, and will typically contain just as many intermediate steps as the analogous process in the full system. However, each step can be carried out more efficiently because we have eliminated the overhead arising from the evaluation of long ranged forces. Since the simulations involve non-physical intermediate states, there is no need to confine our calculations to "real" physical systems, and the desired transformations can be carried out more efficiently in the simpler mimic system with no loss of accuracy. This partial simplification is depicted by the red and green stripes on the arrow connecting the upper panels in Figure 6.1, and contrasts with the red arrow connecting the lower panels.

The difference in the solvation free energy between the full and mimic systems is given by the sum of the free energy changes between the lower and upper panels on the left and right sides of Figure 6.1, indicated by the vertical green arrows. We derive a simple, analytic expression for this free energy difference $\Omega_{LMF}[\phi_R]$ herein, and the green arrow color indicates the simplicity of this step. We start by linearly coupling the slowly-varying portion of the solvent-solvent interaction potential with a parameter λ,

$$u^{(\lambda)}(r) = u_0(r) + \lambda u_1(r).$$

The renormalized solute-solvent field is also coupled to λ, but no assumptions are made regarding the exact λ-dependence of $\phi_R^{(\lambda)}(\mathbf{r})$ yet. However, when $\lambda = 0$, $\phi_R^{(\lambda)}(\mathbf{r}) = \phi_R(\mathbf{r})$, corresponding to the mimic system with bulk density ρ_B and chemical potential μ_R. The bare field $\phi(r)$ is recovered when
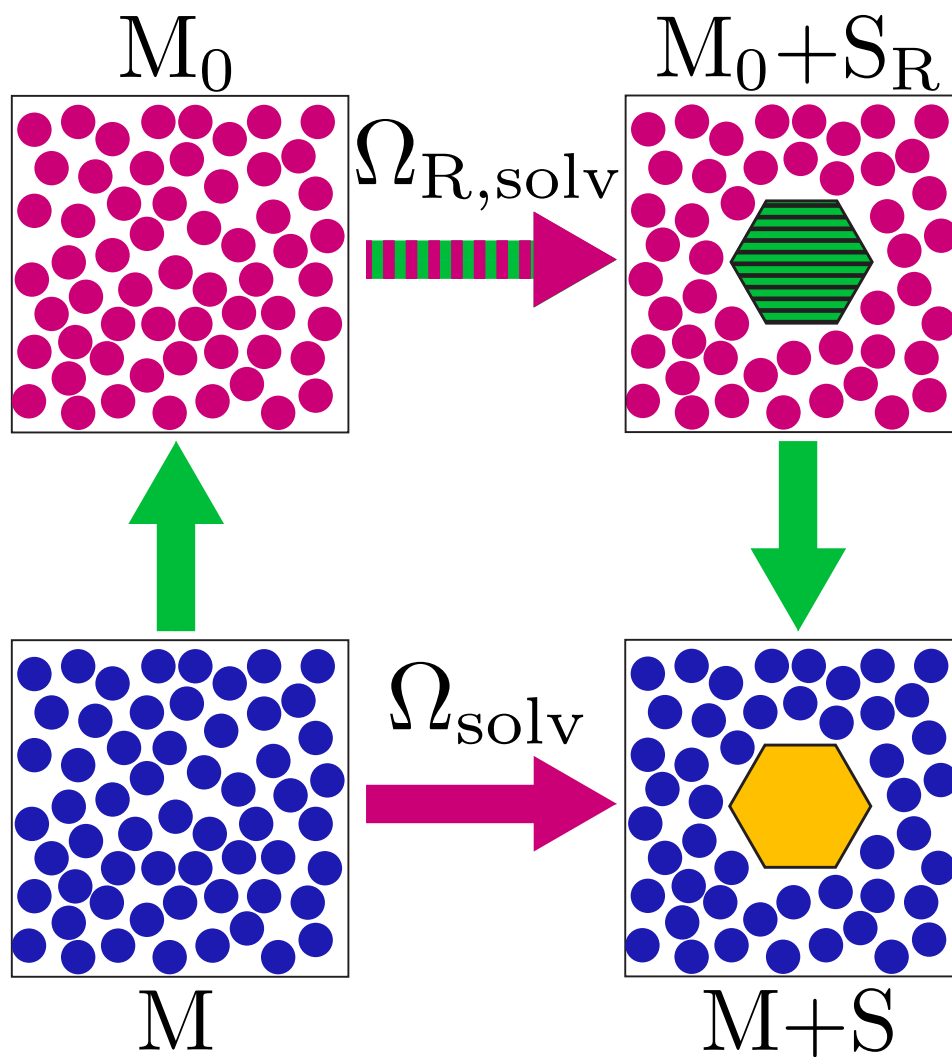
Figure 6.1: Thermodynamic cycle for LMF theory of solvation. The bottom leg of the cycle corresponds to inserting a solute (S) into a mobile solvent (M), both of which are described by short and long ranged interactions. This process is characterized by the solvation free energy Ω_{solv}. The top leg of the cycle depicts the insertion of a LMF-based *renormalized* solute (S_R) into a short ranged mobile solvent (M_0), such that the systems in both the upper left and upper right panels are described only by short ranged interactions, and the solvation free energy in this mimic system is $\Omega_{\mathrm{R,solv}}$. The sum of the free energies of the paths depicted by green arrows is Ω_{LMF}, as described in the text.

$\lambda = 1$, such that this state corresponds to the full system with bulk density ρ_B and chemical potential μ. We seek to determine the free energy difference between these two systems.

First note that the grand partition function of state λ can be written as

$$\Xi_\lambda = \operatorname*{Tr}_{\overline{\mathbf{R}}} \left\{ e^{-\beta\mathcal{H}_\lambda(\overline{\mathbf{R}})} \right\}, \tag{6.1}$$

where $\operatorname{Tr}\{\cdot\} \equiv \sum_N \left[N! \Lambda^{3N} \right]^{-1} \int d\overline{\mathbf{R}} \{\cdot\}$ indicates the classical trace, such that Λ is the usual de Broglie wavelength, and $\overline{\mathbf{R}}$ is a point in phase space [126]. We have also defined the Hamiltonian

$$\mathcal{H}_\lambda(\overline{\mathbf{R}}) = \Phi_\lambda(\overline{\mathbf{R}}) + U_0(\overline{\mathbf{R}}) + \lambda U_1(\overline{\mathbf{R}}), \tag{6.2}$$

where $\Phi_\lambda(\overline{\mathbf{R}}) = \int d\mathbf{r} \varphi_\lambda(\mathbf{r}) \rho(\mathbf{r}; \overline{\mathbf{R}})$, such that $\varphi_\lambda(\mathbf{r}) \equiv \phi_R^{(\lambda)}(\mathbf{r}) - \mu_\lambda$ is the *intrinsic chemical potential*. The quantities $U_0(\overline{\mathbf{R}})$ and $U_1(\overline{\mathbf{R}})$ are the total energies from the short ranged and long ranged solvent-solvent potentials, respectively, at the phase space point $\overline{\mathbf{R}}$.

The grand free energy of state λ is defined by $\beta\Omega_\lambda \equiv -\ln\Xi_\lambda$, and we proceed by differentiating this free energy with respect to λ,

$$\begin{aligned}
\frac{\partial \beta\Omega_\lambda}{\partial \lambda} &= \frac{\operatorname{Tr}\left\{ \left[\beta \frac{d\Phi_\lambda(\overline{\mathbf{R}})}{d\lambda} + \beta U_1(\overline{\mathbf{R}}) \right] e^{-\beta\mathcal{H}_\lambda(\overline{\mathbf{R}})} \right\}}{\operatorname{Tr}\left\{ e^{-\beta\mathcal{H}_\lambda(\overline{\mathbf{R}})} \right\}} \\
&= \left\langle \beta \frac{d\Phi_\lambda(\overline{\mathbf{R}})}{d\lambda} + \beta U_1(\overline{\mathbf{R}}) \right\rangle_\lambda,
\end{aligned} \tag{6.3}$$

where $\langle \cdots \rangle_\lambda$ indicates an ensemble average in the system with coupling parameter λ. This is a classic result, and appears as an intermediate step when obtaining free energy differences by thermodynamic integration [26]. When $U_1(\overline{\mathbf{R}})$ is given as a sum of pair interactions, this can be equivalently written in a form more conducive to LMF theory, such that the singlet and pair density distribution functions appear:

$$\frac{\partial \beta\Omega^{(\lambda)}}{\partial \lambda} = \beta \int d\mathbf{r} \frac{d\varphi_\lambda(\mathbf{r})}{d\lambda} \rho_\lambda(\mathbf{r}) + \frac{\beta}{2} \int d\mathbf{r} \int d\mathbf{r}' \rho_\lambda^{(2)}(\mathbf{r}, \mathbf{r}') u_1(|\mathbf{r} - \mathbf{r}'|), \tag{6.4}$$

where $\rho_\lambda(\mathbf{r})$ and $\rho_\lambda^{(2)}(\mathbf{r}, \mathbf{r}')$ are the singlet and pair density distribution functions in the system with coupling parameter λ.

To obtain the free energy difference between the full and mimic systems, we integrate over the coupling parameter λ. As noted by Weeks [127], because the singlet density at the endpoints are equivalent by definition, $\rho_{\lambda=1}(\mathbf{r}) = \rho_{\lambda=0}(\mathbf{r})$, we can choose a particular integration path in λ-space, or equivalently the lambda dependence of $\phi_R^{(\lambda)}(\mathbf{r})$, such that the singlet density remains unchanged

for all λ, $\rho_\lambda(\mathbf{r}) = \rho(\mathbf{r})$. Performing the integration for this path in Equation 6.4 yields

$$
\begin{aligned}
\beta\Omega[\phi] - \beta\Omega_{\mathrm{R}}[\phi_{\mathrm{R}}] &= \beta \int d\mathbf{r}\rho(\mathbf{r})\left[\phi(\mathbf{r}) - \mu - \phi_{\mathrm{R}}(\mathbf{r}) + \mu_{\mathrm{R}}\right] \\
&+ \frac{\beta}{2}\int_0^1 d\lambda \int d\mathbf{r} \int d\mathbf{r}' \rho_\lambda^{(2)}(\mathbf{r}, \mathbf{r}')u_1(|\mathbf{r} - \mathbf{r}'|),
\end{aligned}
\tag{6.5}
$$

where we have used the fact that $\Omega_{\lambda=1} = \Omega[\phi]$ is the free energy of the full system, and $\Omega_{\lambda=0} = \Omega_{\mathrm{R}}[\phi_{\mathrm{R}}]$ is the free energy of the mimic system.

At this point, we note that the solvation free energy is defined as the free energy difference between the system with and without a solute, $\Omega_{\mathrm{solv}}[\phi] \equiv \Omega[\phi] - \Omega[\phi = 0]$. This allows for the use of Equation 6.5 to write the difference in solvation free energies between the full and mimic systems,

$$
\begin{aligned}
\beta\Omega_{\mathrm{solv}}[\phi] - \beta\Omega_{\mathrm{R,solv}}[\phi_{\mathrm{R}}] &= \beta \int d\mathbf{r}[\mu_{\mathrm{R}} - \mu][\rho(\mathbf{r}) - \rho_{\mathrm{B}}] - \beta \int d\mathbf{r}\rho(\mathbf{r})[\phi_{\mathrm{R}}(\mathbf{r}) - \phi(\mathbf{r})] \\
&+ \frac{\beta}{2}\int_0^1 d\lambda \int d\mathbf{r} \int d\mathbf{r}'[\rho_\lambda^{(2)}(\mathbf{r}, \mathbf{r}') - \rho_{\mathrm{B},\lambda}^{(2)}(|\mathbf{r} - \mathbf{r}'|)]u_1(|\mathbf{r} - \mathbf{r}'|),
\end{aligned}
\tag{6.6}
$$

where $\rho_{\mathrm{B},\lambda}^{(2)}(r)$ is the pair density distribution in the bulk solvent. Equation 6.6 is an exact formula for the solvation free energy difference corresponding to the green vertical arrows in Figure 6.1. However, the last term involves the partially coupled nonuniform pair distribution function $\rho_\lambda^{(2)}(\mathbf{r}, \mathbf{r}')$, which in general varies with λ even though the singlet density remains constant, making this term seem prohibitively complicated for practical use. But we show here that when LMF theory provides an accurate description of the structure of the system, we obtain a very simple and accurate approximation for the right hand side of Equation 6.6.

In order to obtain this expression, we note that the first term in Equation 6.6 generates a Legendre transform to the intrinsic free energy

$$
W[\rho] \equiv \Omega[\phi] - \int d\mathbf{r}\rho(\mathbf{r})[\phi(\mathbf{r}) - \mu],
\tag{6.7}
$$

which is explicitly a functional of the density and regularly appears in classical density functional theories of fluids [10]. Equation 6.6 can then be exactly rewritten in this ensemble as

$$
\beta(W_{\mathrm{solv}}[\rho] - W_{\mathrm{R,solv}}[\rho]) = \frac{\beta}{2}\int_0^1 d\lambda \int d\mathbf{r} \int d\mathbf{r}'[\rho_\lambda^{(2)}(\mathbf{r}, \mathbf{r}') - \rho_{\mathrm{B},\lambda}^{(2)}(|\mathbf{r} - \mathbf{r}'|)]u_1(|\mathbf{r} - \mathbf{r}'|).
\tag{6.8}
$$

The free energies in Equation 6.8 are all functionals of the common singlet density $\rho(\mathbf{r}) = \rho_\lambda(\mathbf{r}) = \rho_{\mathrm{R}}(\mathbf{r})$ because of the integration path we have chosen. By definition of the Legendre

transform, the functional derivative of the intrinsic free energy with respect to the singlet density is

$$\frac{\delta W[\rho]}{\delta \rho(\mathbf{r})} = -\varphi(\mathbf{r}) = \mu - \phi(\mathbf{r}),$$ (6.9)

with an analogous relation holding for the mimic system. Thus, one can functionally differentiate Equation 6.8 to obtain a formally *exact* relation between $\phi_R(\mathbf{r})$ and $\phi(\mathbf{r})$:

$$\beta\phi_R(\mathbf{r}) = \beta\phi(\mathbf{r}) + \frac{\delta}{\delta\rho(\mathbf{r})}\left\{\frac{\beta}{2}\int_0^1 d\lambda \int d\mathbf{r} \int d\mathbf{r}'[\rho_\lambda^{(2)}(\mathbf{r},\mathbf{r}') - \rho_{B,\lambda}^{(2)}(|\mathbf{r}-\mathbf{r}'|)]u_1(|\mathbf{r}-\mathbf{r}'|)\right.$$

$$\left. + \beta\int d\mathbf{r}[\rho(\mathbf{r})-\rho_B][\mu_R-\mu]\right\}.$$ (6.10)

We have chosen constants so that the term in the braces vanishes in the uniform bulk system with singlet density $\rho(\mathbf{r}) = \rho_B$.

The LMF Equation 1.7, derived *independently* by an approximate integration of the first member of the Yvon-Born-Green hierarchy of equations relating intermolecular forces to induced structure [1], gives a separate and very accurate relation between $\phi_R(\mathbf{r})$ and $\phi(\mathbf{r})$. It can be exactly rewritten in a form analogous to the exact Equation 6.10 as

$$\beta\phi_R(\mathbf{r}) = \beta\phi(\mathbf{r}) + \frac{\delta}{\delta\rho(\mathbf{r})}\left\{\frac{\beta}{2}\int d\mathbf{r}\int d\mathbf{r}'[\rho(\mathbf{r})-\rho_B][\rho(\mathbf{r}')-\rho_B]u_1(|\mathbf{r}-\mathbf{r}'|)\right\},$$ (6.11)

where constants have been chosen such that the term in the curly braces again vanishes in the bulk.

If the LMF Equation 6.11 is accurate, we can now subtract Equation 6.11 from Equation 6.10 and formally perform the functional integrals over $\rho(\mathbf{r})$ to obtain

$$\frac{\beta}{2}\int_0^1 d\lambda \int d\mathbf{r} \int d\mathbf{r}'[\rho_\lambda^{(2)}(\mathbf{r},\mathbf{r}') - \rho_{B,\lambda}^{(2)}(|\mathbf{r}-\mathbf{r}'|)]u_1(|\mathbf{r}-\mathbf{r}'|) + \beta\int d\mathbf{r}[\rho(\mathbf{r})-\rho_B][\mu_R-\mu]$$

$$= \frac{\beta}{2}\int d\mathbf{r}\int d\mathbf{r}'[\rho(\mathbf{r})-\rho_B][\rho(\mathbf{r}')-\rho_B]u_1(|\mathbf{r}-\mathbf{r}'|).$$ (6.12)

Thus, the complicated formal expression inside the curly braces in Equation 6.10 involving the nonuniform pair density and exact values of μ and μ_R is equivalent to the simple mean-field like expression given by Equation 6.11 where only nonuniform singlet densities appear! Moreover, we

122

can utilize the LMF equation to exactly reexpress Equation 6.12 as

$$\frac{\beta}{2} \int_0^1 d\lambda \int d\mathbf{r} \int d\mathbf{r}'[\rho_\lambda^{(2)}(\mathbf{r},\mathbf{r}') - \rho_{\mathrm{B},\lambda}^{(2)}(|\mathbf{r}-\mathbf{r}'|)]u_1(|\mathbf{r}-\mathbf{r}'|)$$
$$= \frac{\beta}{2} \int d\mathbf{r}[\rho(\mathbf{r}) - \rho_\mathrm{B}][\phi_\mathrm{R}(\mathbf{r}) - \phi(\mathbf{r})] - \beta \int d\mathbf{r}[\rho(\mathbf{r}) - \rho_\mathrm{B}][\mu_\mathrm{R} - \mu], \tag{6.13}$$

an even simpler expression involving integration of the self-consistent LMF potential $\phi_\mathrm{R}(\mathbf{r})$. Equation 6.13 can then be substituted for the complicated RHS of Equaton 6.8.

Making the Legendre transform back to the grand ensemble, the solvation free energy in the full system can be written as

$$\beta\Omega_{\mathrm{solv}}[\phi] = \beta\Omega_{\mathrm{R,solv}}[\phi_\mathrm{R}] - \frac{\beta}{2} \int d\mathbf{r}[\rho(\mathbf{r}) + \rho_\mathrm{B}][\phi_\mathrm{R}(\mathbf{r}) - \phi(\mathbf{r})], \tag{6.14}$$

such that

$$\beta\Omega_{\mathrm{LMF}}[\phi_\mathrm{R}] = -\frac{\beta}{2} \int d\mathbf{r}[\rho(\mathbf{r}) + \rho_\mathrm{B}][\phi_\mathrm{R}(\mathbf{r}) - \phi(\mathbf{r})] \tag{6.15}$$

is the free energy contribution due to the processes indicated by the green vertical arrows of the thermodynamic cycle in Figure 6.1. Equation 6.15 is a simple expression for the free energy difference between the full and mimic systems that can be readily evaluated analytically, and is the principle result of this section.

Finally, we note that Equation 6.14 can be equivalently written as

$$\beta\Omega_{\mathrm{solv}}[\phi] = \beta\Omega_{\mathrm{R,solv}}[\phi_\mathrm{R}] - \frac{\beta}{2} \int d\mathbf{r} \int d\mathbf{r}' \left[\rho(\mathbf{r})\rho(\mathbf{r}') - \rho_\mathrm{B}^2\right] u_1(|\mathbf{r}-\mathbf{r}'|), \tag{6.16}$$

which could have been obtained by using uncontrolled mean field (MF) approximations everywhere in Equation 6.6, as is typically done in classical density functional theory (DFT) descriptions of fluids; this is demonstrated in Appendix H. However, in deriving our central result Equation 6.15 using the LMF equation, which itself is obtained from rigorous statistical mechanics relating structure to intermolecular forces, we also indicate the conditions under which the MF approximations commonly used in DFT are accurate. In particular, Equation 6.16 holds only when the LMF equation is accurate, or equivalently, when the long-ranged $u_1(r)$ is chosen to vary sufficiently slowly over characteristic nearest neighbor distances and $u_0(r)$ captures the local interactions on these molecular length-scales.
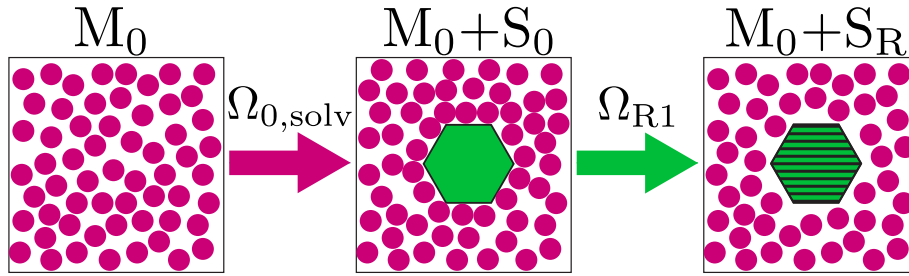
Figure 6.2: Schematic illustration of the decomposition of the mimic system solvation free energy, $\Omega_{R,solv}$, into the solvation free energy of the SCA system, $\Omega_{0,solv}$, and the free energy of turning on the slowly varying portion of the LMF, Ω_{R1}.

6.2.1 Calculating the Free Energy of the Mimic System

The solvation free energy (SFE) can be determined from simulation as

$$\Omega_{solv}[\phi] = \Omega_{R,solv}[\phi_R] + \Omega_{LMF}[\phi_R], \tag{6.17}$$

where the formalism is readily extended to ensembles other than the Grand ensemble [1] We can thus very simply correct the SFE of the mimic system using LMF theory, but we still need to determine the free energy of the mimic system, $\Omega_{R,solv}$. The process for doing this is sketched in Figure 6.2.

The SFE in the mimic system, $\Omega_{R,solv}[\phi_R]$, can be further divided into the solvation free energy of the SCA system in the known strong coupling field $\phi_0(\mathbf{r})$, $\Omega_{0,solv}[\phi_0]$, and the free energy of turning on the slowly-varying portion of the LMF potential, $\Omega_{R1}[\phi_{R1}]$, such that

$$\Omega_{R,solv}[\phi_R] = \Omega_{0,solv}[\phi_0] + \Omega_{R1}[\phi_{R1}]. \tag{6.18}$$

The free energy of the SCA can be determined through conventional means by "growing" a point solute into the full SCA solute described by the solute-solvent field $\phi_0(\mathbf{r})$. In general this will require multiple intermediate states and changes in the harshly repulsive core interactions between states, as indicated by the red arrow between the first two panels of Figure 6.2.

The quantity Ω_{R1} is the free energy of turning on the slowly varying portion of the LMF, $\phi_{R1}(\mathbf{r}) = \phi_R(\mathbf{r}) - \phi_0(\mathbf{r})$. This process is schematically illustrated by the change from the center to

---

[1] In the calculations below we will concern ourselves with the isothermal-isobaric ensemble, which is characterized by the Gibbs free energy G, and all solvation free energies calculated from simulations will then be referred to by ΔG, as in Chapter 3.

right panels in Figure 6.2. The free energy of turning on this field can be exactly written as

$$\beta\Omega_{R1} = -\ln\left\langle e^{-\beta\Phi_{R1}}\right\rangle_0 = -\ln\int d\Phi_{R1}P_0(\Phi_{R1})e^{-\beta\Phi_{R1}}. \tag{6.19}$$

In Equation 6.19, $\langle\cdots\rangle_0$ indicates an ensemble average in the strong-coupling system, where the solute field is given by the short ranged field $\phi_0(\mathbf{r})$, $\Phi_{R1} = \sum_i \phi_{R1}(\mathbf{r}_i)$, and $P_0(\Phi_{R1})$ is the probably distribution of Φ_{R1} calculated from configurations in the strong-coupling system.

This contribution to the free energy can be written equivalently in terms of averages in the mimic system,

$$\beta\Omega_{R1} = \ln\left\langle e^{\beta\Phi_{R1}}\right\rangle_R = \ln\int d\Phi_{R1}P_R(\Phi_{R1})e^{\beta\Phi_{R1}}, \tag{6.20}$$

where $\langle\cdots\rangle_R$ indicates an ensemble average in the presence of the field $\phi_R(\mathbf{r})$ (the mimic system) and $P_R(\Phi_{R1})$ is the probability of Φ_{R1} in the mimic system. Due to the slowly-varying nature of $\phi_{R1}(\mathbf{r})$, we expect the distributions $P_0(\Phi_{R1})$ and $P_R(\Phi_{R1})$ to be Gaussian to a good approximation, allowing the use of computationally efficient approximations, and this is indicated by the green arrow in Figure 6.2. If this is the case, Ω_{R1} can be estimated from cumulant expansions of Equations 6.19 and 6.20, truncated at second order [58, 116]:

$$\beta\Omega_{R1} = \beta\langle\Phi_{R1}\rangle_0 - \frac{\beta^2}{2}\left\langle(\delta\Phi_{R1})^2\right\rangle_0 = \beta\langle\Phi_{R1}\rangle_R + \frac{\beta^2}{2}\left\langle(\delta\Phi_{R1})^2\right\rangle_R, \tag{6.21}$$

where $\delta\Phi_{R1} = \Phi_{R1} - \langle\Phi_{R1}\rangle$. Averaging the two equivalent forms of the free energy in Equation 6.21 yields,

$$\beta\Omega_{R1} = \frac{\beta}{2}\left[\langle\Phi_{R1}\rangle_0 + \langle\Phi_{R1}\rangle_R\right] + \frac{\beta^2}{4}\left[\left\langle(\delta\Phi_{R1})^2\right\rangle_R - \left\langle(\delta\Phi_{R1})^2\right\rangle_0\right]. \tag{6.22}$$

However, the probabilities of the energy Φ_{R1} in the strong-coupling and mimic systems are related by the following exact relation due to Bennett [57],

$$P_R(\Phi_{R1}) = e^{-\beta(\Phi_{R1}-\Omega_{R1})}P_0(\Phi_{R1}). \tag{6.23}$$

Therefore, if one distribution is approximately Gaussian, the other will be Gaussian with the same variance, such that the variances in the second term of Equation 6.22 cancel. Thus, our final Gaussian estimate for the free energy of turning on the field $\phi_{R1}(\mathbf{r})$ is given by

$$\beta\Omega_{R1} = \frac{\beta}{2}\left[\langle\Phi_{R1}\rangle_0 + \langle\Phi_{R1}\rangle_R\right]. \tag{6.24}$$
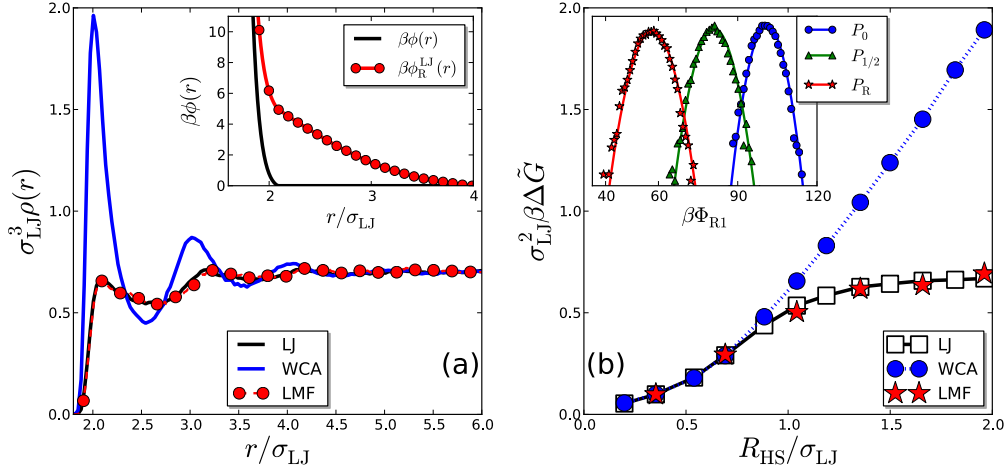
Figure 6.3: (a) Nonuniform density around a hard sphere solute of radius $R_{HS} \approx 2\sigma_{LJ}$ in a LJ fluid and in its corresponding WCA reference system and LMF mimic system. The inset shows the bare and renormalized solute fields, $\phi(r)$ and $\phi_R^{LJ}(r)$, respectively. (b) Solvation free energies as a function of solute radius in LJ and WCA fluids. Stars indicate the results obtained using the LMF theory of solvation. The inset in (b) depicts the probability distributions $P(\beta\Phi_{R1}/2)$ in the mimic (P_R) and SCA (P_0) systems on a logarithmic scale. Given the very different densities shown in (a), the distributions of the mimic and SCA systems do not overlap significantly, and therefore an intermediate state sampled with a solute-solvent field $\phi_{R1}(\mathbf{r})/2$ was also simulated in order to obtain the mimic system free energy using stratification. The probability distribution obtained from sampling this ensemble is indicated by $P_{1/2}$. Gaussian distributions with the same mean and variance as the corresponding simulation data are shown as the solid lines.

We will show below that the distributions of the slowly-varying portion of the renormalized field indeed turn out to be remarkably Gaussian for all systems under study, and therefore Equation 6.24 provides an accurate estimate of Ω_{R1}. Now that we have laid the theoretical foundation for determining solvation free energies with LMF theory, we demonstrate its accuracy below with several non-trivial examples in the subsequent sections.

6.2.2 Hard Sphere Solvation

The crux of the LMF theory of solvation is that good thermodynamic properties follow from an accurate representation of the structure in a molecular system. Therefore, we first show that LMF theory can quantitatively capture the drying observed at the surface of a hard sphere of radius

$R_{\mathrm{HS}} \approx 2\sigma_{\mathrm{LJ}}$ in a LJ fluid in Figure 6.3a. This is a challenging problem for LMF theory since there is a large change in the density due to the unbalanced LJ forces; indeed this presents more difficulties than almost all applications of LMF theory to Coulomb interactions, as will be discussed later. While a LJ fluid dries at the interface of a large purely repulsive solute due to unbalanced forces arising from the bulk region, removal of such forces in the corresponding WCA reference system leads to wetting of the solute surface and there is a very large change in density between the blue and red curves in Figure 6.3a. Nevertheless, drying can be obtained with a WCA solvent by accounting for the averaged effects of such unbalanced LJ forces at the fluid-solute interface with the LJ LMF

$$\phi_{\mathrm{R}}^{\mathrm{LJ}}(\mathbf{r}) = \phi(\mathbf{r}) + \int d\mathbf{r}' \left[\rho_{\mathrm{R}}(\mathbf{r}') - \rho_{\mathrm{B}}\right] u_1(|\mathbf{r} - \mathbf{r}'|), \tag{6.25}$$

which is compared to the bare solute-solvent potential $\phi(\mathbf{r})$ in the inset of Figure 6.3a. The renormalized potential $\phi_{\mathrm{R}}^{\mathrm{LJ}}(r)$ provides an effective "push" on solvent particles near the interface, such that the density in the mimic system is nearly identical to that in the full LJ system, as shown by the curve labeled "LMF" in Figure 6.3a. Therefore, LMF theory can readily account for the significant structural change induced by interfacial unbalancing potentials with quantitative accuracy.

From the accurate structure obtained from LMF theory, we can proceed to study the solvation thermodynamics of hard spherical solutes of various sizes. As demonstrated in Chapter 3, solvation free energies of hard spherical solutes display a crossover from scaling with solute volume to scaling with solute surface area at $R_{\mathrm{HS}} \approx \sigma_{\mathrm{LJ}}$, consistent with the appearance of interfacial drying. It was also shown that this crossover does not occur if the unbalanced forces arising from the LJ attractions of the fluid are not taken into account because the solvent wets the solute surface for all solute sizes, and this is again shown in Figure 6.3. After utilizing LMF theory to determine the structural properties of the mimic system, the LMF theory of solvation is used to integrate over this structure and obtain estimates for the solvation free energies.

The hard sphere solvation free energies per unit solute surface area determined through this LMF-based framework are compared with those obtained in the full LJ and WCA systems in Figure 6.3b. The LMF free energies recover the length scale transition and reproduce the solvation free energies with quantitative accuracy. We should also emphasize that the Gaussian approximation Equation 6.24 holds remarkably well when estimating $\Delta G_{\mathrm{R}1}$, even in cases where significant structural transitions occur upon the inclusion of $\phi_{\mathrm{R}1}(\mathbf{r})$, as shown in the inset of Figure 6.3b. However, when there is low phase space overlap between the SCA and mimic systems, and therefore distributions of the energy do not display significant overlap (Figure 6.3b), an intermediate state needs to be studied in order to employ Gaussian approximations to the free energy [58]. For example, to determine the free energy of the state shown in Figure 6.3a, $R_{\mathrm{HS}}/\sigma_{\mathrm{LJ}} = 2$, we have also simulated a system with a nonphysical, partially coupled LMF, $\phi_{\mathrm{R}}^{(1/2)}(\mathbf{r}) = \phi_{\mathrm{R}}(\mathbf{r})/2$. The free energy $\Delta G_{\mathrm{R}1}$ was then determined from these three states as the sum of the Gaussian approximated free

energy changes between neighboring states.

A similar length scale transition occurs when apolar particles are solvated by water, although the details of the transition in aqueous media with hydrogen bonds differ in many important aspects, as discussed in Chapter 3. There it was demonstrated that this length scale transition also occurs when long ranged electrostatics are neglected in GT water, although the lower surface tension of GT water leads to solvation free energies that are somewhat less unfavorable than those in the full SPC/E model, Figure 6.4a.

We can again use the LMF-based framework for solvation free energies developed above to obtain accurate estimates of ΔG while neglecting long ranged electrostatic interactions. The situation is even more favorable here than for the LJ system, because the Coulomb interaction is more slowly-varying at long distances and we can choose the smoothing length σ in an optimal manner. Therefore, in contrast to the above example of solvation in a LJ fluid, the phase space of the GT SCA system is sufficiently close to that of the full system, and accurate estimates for $\mathcal{V}_{R1}(r)$ and $\rho_R^q(r)$ can be obtained by iterating over GT water configurations using only LRT [2]. Therefore, simulations of the mimic system do not need to be performed. Within the accuracy of LRT, the free energy difference between the SCA and mimic systems can be approximated as

$$\Delta G_{R1} \approx \frac{1}{2} \left[\langle \Phi_{R1} \rangle_0 + \langle \Phi_{R1} \rangle_R \right] = \frac{1}{2} \int d\mathbf{r} \left[\rho_0^q(\mathbf{r}) + \rho_R^q(\mathbf{r}) \right] \mathcal{V}_{R1}(\mathbf{r}), \tag{6.26}$$

where the subscript 0 indicates quantities evaluated in the SCA system and the averages in the mimic system are obtained from GT configurations using LRT. Combining the LRT estimates for $\rho_R^q(r)$ and ΔG_{R1} with the LMF theory for solvation, we obtain accurate full system free energies from simulations of a system without long ranged electrostatics, as shown by the curve labeled "LRT-LMF" in Figure 6.4a.

While the LMF free energy "corrections" appear small on the scale of Figure 6.4a, they become significant for large solute sizes. Differences between the full free energies and those obtained in GT water and from the LRT-LMF estimates are shown in Figure 6.4b. The difference $\Delta \Delta G = \Delta G^{\mathrm{SPC/E}} - \Delta G$ is roughly zero in both the GT and LMF systems for small solute sizes, as one might expect because the structure and thermodynamics is determined exclusively by local interactions in this regime. In the large solute regime, however, long ranged interactions become increasingly important, and solvation free energies in GT water differ from those in SPC/E water by as much as $9\,k_BT$ for a solute with a radius of 11.5 Å, and this difference will continue to grow with increasing solute size. The LMF estimates for these free energies readily correct these errors and

---

[2]When LRT can be used with high accuracy, this also indicates that the probability distributions of the relevant field (here the LMF) will follow a Gaussian distribution and the distributions for the two states in question will overlap significantly. Therefore, $\Delta G_{R1}[\mathcal{V}_{R1}]$ can be obtained with high accuracy from the Gaussian approximation Equation 6.24, even more so than was the case for $\Delta G_{R1}[\phi_{R1}^{LJ}]$, due to the very slowly-varying nature of $v_1(r) = \mathrm{erf}(r/\sigma)/r$.

Figure 6.4: (a) Solvation free energies of hard spheres in SPC/E and GT water as a function of solute radius. Stars indicate solvation free energies determined from configurations in the strong-coupling, GT water system obtained through a combination of linear response theory (LRT) and LMF theory (LRT-LMF). (b) Difference between the GT or LRT-LMF solvation free energies and those obtained in SPC/E water, $\Delta\Delta G = \Delta G^{\mathrm{SPC/E}} - \Delta G$.

$\Delta\Delta G^{\mathrm{LRT-LMF}}$ fluctuates about zero for all solute sizes, indicating good agreement with the full system results.

Another stringent test of the LMF theory of solvation is to examine hard sphere solvation in GTRC water, in which the LJ attractions are further removed from GT water. Computing solvation free energies of GT water from a GTRC mimic system is completely analogous to computing solvation free energies in the LJ fluid from a WCA mimic system. Removal of the LJ attractions in GTRC water suppresses any drying at the solute-water interface, and therefore eliminates the length scale transition in solvation free energies, Figure 6.5a. As was done for the WCA fluid, LMF theory can be used to account for the averaged effects of LJ attractions through the field $\phi_{\mathrm{R}}^{\mathrm{LJ}}(r)$. Upon doing so, drying is recovered, and quantitatively accurate results for the solvation free energies are obtained from the LMF-based framework, indicated by "LMF" in Figure 6.5a.

Inherent in the LMF theory of solvation is a natural separation of short and long ranged interactions. The near field contribution to the solvation free energy is equivalent to that of the appropriate SCA reference system, ΔG_0. The remainder of the solvation free energy is due to far field components, $\Delta G_{\mathrm{LR}} = \Delta G_{\mathrm{R1}} + \Delta G_{\mathrm{LMF}}$. For the case of hard sphere solvation in water, we can choose the appropriate SCA system to be GTRC water, so that there are two far field components of
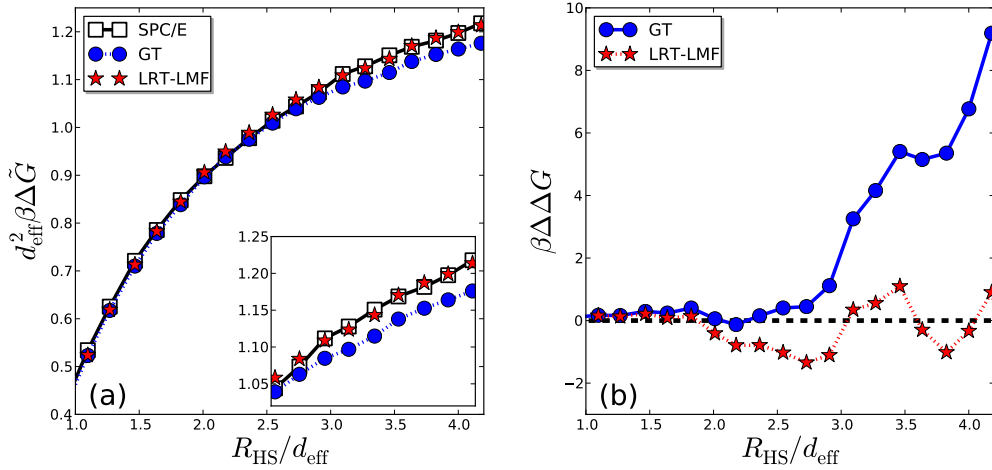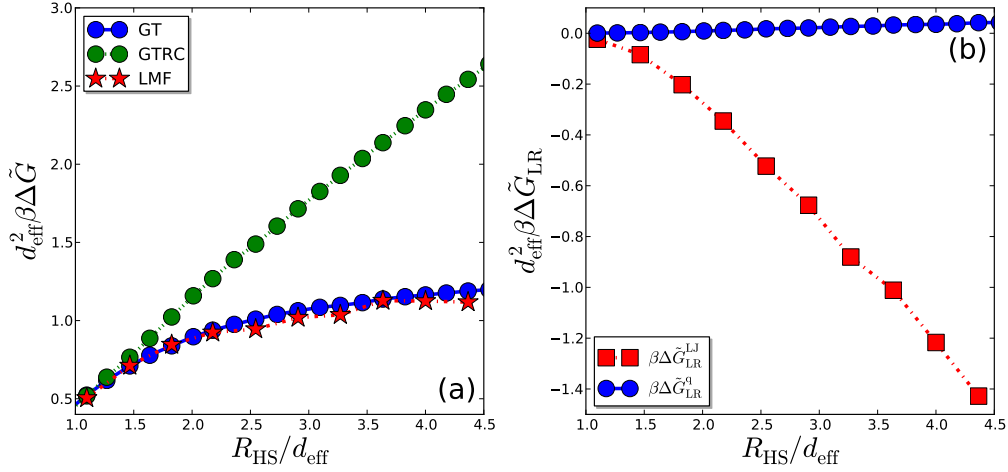
Figure 6.5: (a) Solvation free energies of hard spheres in GT and GTRC water as a function of solute radius. Stars indicate solvation free energies determined from LMF theory for the LJ attractions. (b) Contributions to the solvation free energies from long ranged LJ attractions (ΔG_{R1}^{LJ}) and long ranged electrostatics (ΔG_{R1}^q) as a function of solute size. The former is determined from the data in (a), while the latter contributions were determined from data in Figure 6.4a.

the free energy, one due to LJ attractions, $\Delta G_{LR}^{LJ}[\phi_{R1}^{LJ}]$, and one due to long ranged electrostatic interactions, $\Delta G_{LR}^q[\mathcal{V}_{R1}]$, both of which are functionals of their respective LMF potentials.

The long ranged LJ and electrostatic components of the hard sphere solvation free energies per unit solute surface area as a function of solute radius are shown in Figure 6.5b. The electrostatic component ΔG_{LR}^q only slightly increases from zero as a function of solute size over the range of sizes examined, in agreement with the fact that long ranged electrostatics play only a small role in the solvation of a hydrophobic solute. On the other hand, solvent LJ attractions comprise a significant portion of the solvation free energy, and become increasingly negative as the solute size is increased. In the large solute regime, the introduction of the field $\phi_R^{LJ}(r)$ moves the system from a state of interfacial wetting to drying. The appearance of a dry interface increases the ease with which a hard sphere is solvated by water, or equivalently, the probability of finding a cavity the size and shape of the hard solute, completely consistent with the large negative values of ΔG_{LR}^{LJ} shown in Figure 6.5b.

6.2.3   Ion Hydration

We conclude this section with the calculation of the solvation free energy of a single ion in water. Traditional approaches to ion solvation, like the highly successful formalism developed by Hummer

130

and coworkers [80], involve the simulation of a single ion in a dielectric solvent. The electrostatics are treated by Ewald summation in these systems, and therefore require the presence of a neutralizing background charge density. In addition, significant finite size effects due to the periodicity of the Ewald sum are present [95], as discussed in the preceding chapter, although successful finite-size corrections to the solvation free energy have been developed [80, 95].

LMF theory provides a useful alternative to periodic lattice summation techniques when studying ion solvation. Aside from the efficient simulation of purely short ranged systems afforded by LMF theory, the conceptual difficulties associated with a non-uniform electrostatic potential that depends on the size of the simulation cell can be eliminated. Instead, the LMF potential will display the asymptotic behavior predicted by classical electrostatics, $Q/\epsilon r$ for large r, producing a physically reasonable depiction of ion hydration and enabling the use of simple finite size corrections in the form of a Born model. We extend LMF theory to ion hydration herein.

As discussed in Appendix A, great care is to be taken when solving the LMF equation for electrostatics. In particular, if the proper asymptotic behavior of the LMF equation is not maintained, the self-consistent iteration process can diverge. However, this problem is easily overcome by forcing neutrality at each step of the iteration process for neutral systems. Analogously, we must ensure that $\mathcal{V}_R(\mathbf{r})$ follows the expected behavior at small k for a non-neutral system when describing a single ion solvated by bulk water. Such a stable iteration scheme is presented in Appendix I, and this method of self-consistently solving the LMF equation is employed when calculating the ion solvation free energies.

We consider the calculation of the solvation free energy of a charged methane "particle" in SPC water, as studied by Hummer *et al.* [80]. In this case, methane is modeled in the united atom (UA) scheme, such that methane (Me) is represented as a single LJ particle with Me-water interaction parameters of $\varepsilon_{\mathrm{LJ}}^{\mathrm{Me-O}} = 0.893228$ kJ/mol and $\sigma_{\mathrm{LJ}}^{\mathrm{Me-O}} = 3.44778$ Å. We consider a cationic state of this particle, with charge $Q_{\mathrm{Me+}} = +1$. Charging of an anionic state of the particle is a more difficult process due to artifacts of classical ion-water interaction potentials. In these potentials, the repulsive ion core only interacts with the LJ potential of the oxygen site. Therefore, the positively charged hydrogen site can penetrate well into the ionic core due to a lack of any repulsive core interactions. This leads to profound nonlinearities in the charging process for ions, and further work is needed to address the physical significance, if any, of this behavior.

We separate the solvation free energy $\Delta G^{\mathrm{Me^+}}$ of the positively charged methane ion following LMF theory:

$$\Delta G^{\mathrm{Me^+}} = \Delta G_0 + \Delta G_{\mathrm{R1}} + \Delta G_{\mathrm{LMF}}. \tag{6.27}$$

The last two terms ΔG_{R1} and ΔG_{LMF} are the free energy of turning on the renormalized electrostatic potential and the analytic LMF "correction" to the free energy of mimic system given by the form of

Table 6.1: Contributions to the Ion Solvation Free Energy (kJ/mol)

Charge	ΔG_{Q_0}	ΔG_{R1}	ΔG_{LMF}	ΔG	Hummer *et al.* [80]
1	-73	-63	-58	-244	-240

Equation 6.15 appropriate for electrostatic interactions,

$$\Delta G_{\mathrm{LMF}} = -\frac{1}{2} \int d\mathbf{r} \rho_R^q(\mathbf{r}) \left[\mathcal{V}_R(\mathbf{r}) - \mathcal{V}(\mathbf{r}) \right]. \tag{6.28}$$

The free energy ΔG_{R1} of turning on the field $\mathcal{V}_{R1}(\mathbf{r})$ was obtained using a Gaussian approximation as discussed above.

The first term in Equation 6.27 is the solvation free energy of the ion in the SCA system. This can be divided into a free energy of inserting an uncharged cavity into the GT variant of SPC water, ΔG_{cav}, and a free energy of turning on the near-field portion of the ion charge, ΔG_{Q_0}, such that $\Delta G_0 = \Delta G_{\mathrm{cav}} + \Delta G_{Q_0}$. The free energy of inserting the ion core can be readily determined by Widom particle insertion [116], and here we used the value determined by Hummer and coworkers [80], $\Delta G_{\mathrm{cav}} = 10.2$ kJ/mol. The free energy of the near-field charging process was determined by performing simulations of charged states $Q = 0, 0.25, 0.5, 0.75$, and 1.0 and calculating the free energy as a function of Q using the Bennett acceptance ratio [57].

The solvation free energies of a methane-like cation in SPC water determined from LMF theory-based free energy calculations are compared with the results of Hummer *et al.* [80] in Table 6.1. The total solvation free energy ΔG listed there is corrected for finite system size by the addition of $\Delta G_{\mathrm{FS}} = Q^2 \xi (1 - 1/\epsilon)/(2L)$, where $\xi = -2.38$ for a cubic simulation cell [80]. LMF theory captures the thermodynamics of ionic hydration with reasonable accuracy, and the results obtained from the above formalism compare well with the solvation free energies obtained in previous work [80]. It is important to emphasize that the accurate LMF ion hydration free energies obtained from relatively simple simulations of purely short ranged systems and the many difficulties associated with traditional approaches to ion solvation using Ewald summation are avoided. The only essential correction to the free energy is simply to account for the finite size of the simulation cell.

6.3 Alchemical Free Energy Calculations

In so-called "computational alchemy," we are interested in the free energy change upon transforming one molecule into another, *i.e.* methane into methanol. This type of free energy difference is important in numerous areas, such as protein-ligand binding. In aspects of computer-aided drug design, one is interested in designing a new drug molecule that will bind to a specific protein and

possibly promote or inhibit some aspect of its function. To achieve this task, we could take on the computationally intense task of calculating the protein-ligand binding free energy of each molecule of interest, a process akin to calculating solvation free energies. However, it is not the binding free energies that are of interest but the differences in binding free energies between molecules, such that we can rank the candidate molecules in order of binding strength. Computing such differences can be accomplished by calculating the free energy change upon transforming one bound molecule into another, while it is still bound to the protein. Although this may not be simple in practice, it is more efficient than computing the absolute binding free energy of each molecule. I will describe how to compute such alchemical free energy changes using LMF theory below.

6.3.1   Thermodynamic Cycle for Computational Alchemy

We now consider an arbitrary solute in solution, interacting with a solvent. This solvent could be water, a mixture of a number of solvents, a protein, and so forth. Here solvent just refers to the environment surrounding the solute of interest. The solvent-solvent interactions can be both electrostatic and non-electrostatic in nature, and the solvent molecules also interact with the solute via the potential $\psi(\mathbf{r}; \lambda)$. This solute-solvent potential, fixed at the origin, is coupled to a parameter λ which controls the alchemical transformation. Note that this can be readily generalized to the case of a set of potentials $\{\psi_i(\mathbf{r}; \{\lambda_j\})\}$ coupled to numerous parameters $\{\lambda_j\}$ that control various aspects of the potential. This is what would be needed when fixing a molecule, for example, and transforming this molecule into another.

   When the coupling parameter λ is zero, the solute-solvent interaction is that of the initial solute of interest, schematically illustrated in the lower left panel of Figure 6.6. We are interested in the free energy change $\Omega^{(0\to1)}$ upon transforming this solute ($\lambda = 0$) to another ($\lambda = 1$), as indicated by the lower path in Figure 6.6. In general, this path may require many non-physical intermediate states, each requiring the accurate evaluation of long ranged interactions at every state, and these difficulties are schematically indicated by the red arrow connecting the lower panels in Figure 6.6. However, we wish to calculate this free energy difference using short ranged systems only, and to do so we will use LMF theory by defining an alternative path to calculate $\Omega^{(0\to1)}$.

   This alternative path corresponds to the upper panels in Figure 6.6. In this LMF alchemical transformation, we begin with a mimic system that has the same structure as that of the fully interacting initial state. This LMF system is described by short ranged solvent-solvent interactions $v_0(r)$ and renormalized solute-solvent interactions $\psi_R(\mathbf{r}; \lambda = 0)$. We can then consider performing the alchemical transformation in the mimic system, where the renormalized solute potential $\psi_R(\mathbf{r}; \lambda = 0)$ is slowly transformed into a different renormalized solute with potential $\psi_R(\mathbf{r}; \lambda = 1)$. This process is illustrated by the upper leg of the thermodynamic cycle in Figure 6.6 and is associated with the free energy $\Omega_R^{(0\to1)}$. As was the case for solvation free energies, this process will in general

133
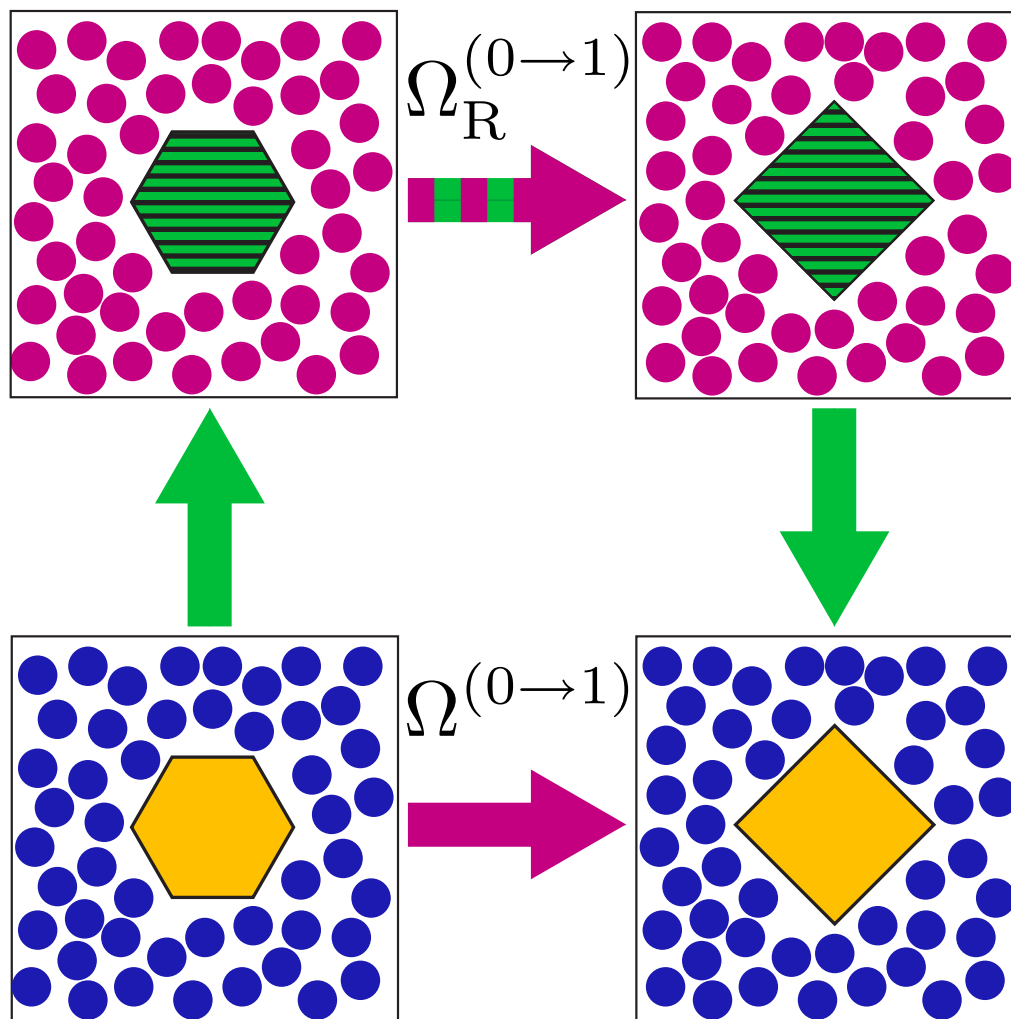
Figure 6.6: Thermodynamic cycle for calculating alchemical free energy changes via LMF theory. The bottom leg of the cycle corresponds to changing the solute from state $\lambda = 0$ to state $\lambda = 1$, and in general can involve a change in the shape of the solute and the nature of the solute-solvent interactions. This transformation occurs in the full system, where both the solute-solvent and solvent-solvent interactions can be long ranged, and is therefore described by the free energy $\Omega^{(0 \to 1)}$. The top leg of the cycle depicts the analogous transformation being performed in the mimic system, with a short ranged reference solvent and a renormalized solute at both state $\lambda = 1$ and state $\lambda = 0$. Performing the alchemical transformation in the mimic system is characterized by the free energy $\Omega_R^{(0 \to 1)}$. The sum of the free energies of the paths depicted by green arrows is a difference of analytic LMF corrections derived for solvation free energies, as described in the text.

134

require as many steps as performing the transformation in the full system. However, this process is computationally more efficient, since we have eliminated much of the overhead arising from the evaluation of long ranged interactions at each step of the transformation process. Hence, we have connected the upper panels with a red and green striped arrow.

The free energy contributions associated with the green vertical arrows in Figure 6.6 can be evaluated analytically using Equation 6.15. Therefore, we find that the free energy of the alchemical transformation is given by

$$
\begin{aligned}
\beta\Omega^{(0\to1)} &= \beta\Omega_{\mathrm{R}}^{(0\to1)} + \beta\Omega_{\mathrm{LMF}}^{(\lambda=1)} - \beta\Omega_{\mathrm{LMF}}^{(\lambda=0)} \\
&= \beta\Omega_{\mathrm{R}}^{(0\to1)} - \frac{\beta}{2}\int d\mathbf{r}\left[\psi_{\mathrm{R}}(\mathbf{r};\lambda=1) - \psi(\mathbf{r};\lambda=1)\right]\left[\rho_{\mathrm{R}}(\mathbf{r};\lambda=1) + \rho_{\mathrm{B}}\right] \\
&\quad + \frac{\beta}{2}\int d\mathbf{r}\left[\psi_{\mathrm{R}}(\mathbf{r};\lambda=0) - \psi(\mathbf{r};\lambda=0)\right]\left[\rho_{\mathrm{R}}(\mathbf{r};\lambda=0) + \rho_{\mathrm{B}}\right].
\end{aligned}
\tag{6.29}
$$

The free energy of the transformation in the mimic system $\Omega_{\mathrm{R}}^{(0\to1)}$ can be obtained using the techniques described in Section II. A. We can therefore calculate general free energy changes in a fully interacting, long ranged system from simulations involving short ranged systems alone. Note that this will require at least two additional simulations (the LMF systems) when LRT approximations to the density and LMF potentials are not valid. However, all simulations will be much more efficient as the interactions are short ranged at all steps

6.3.2 The Addition of Solute-Solvent Attractions

A simple example of an alchemical transformation is simply adding attractive interactions to a purely repulsive spherical solute. In this subsection I explore this process for solutes of various sizes in water. The solutes are the large apolar spherical solutes of Chapter 3, and we can write the solute-water interaction potential with the attractive interactions coupled linearly to the parameter λ,

$$
U_{\mathrm{sw}}^{(\lambda)} = U_{0,\mathrm{sw}} + \lambda U_{1,\mathrm{sw}},
\tag{6.30}
$$

where $U_{0,\mathrm{sw}}$ and $U_{1,\mathrm{sw}}$ are the repulsive and attractive portions of the solute-water interaction energy, respectively, such that $U_{\mathrm{sw}}^{(\lambda)} = \sum_{i=1}^{N} u_{\mathrm{sw}}(r_i;\lambda)$. This type of solute-solvent potential is included in the nonelectrostatic portion of the external field, $\phi(\mathbf{r};\lambda) = u_{\mathrm{sw}}(\mathbf{r};\lambda)$, because no solute-solvent electrostatic interactions are present. The renormalized potential acting on site α can then be written as

$$
\psi_{\mathrm{R},\alpha}(\mathbf{r};\lambda) = \phi_{\alpha}(\mathbf{r};\lambda) + q_{\alpha}\mathcal{V}_{\mathrm{R}}(\mathbf{r};\lambda),
\tag{6.31}
$$

where the LMF treatment has only been applied to electrostatic interactions and ϕ_{α} is the nonelectrostatic solute-solvent potential acting on solute site α. If we separate only the electrostatic

135
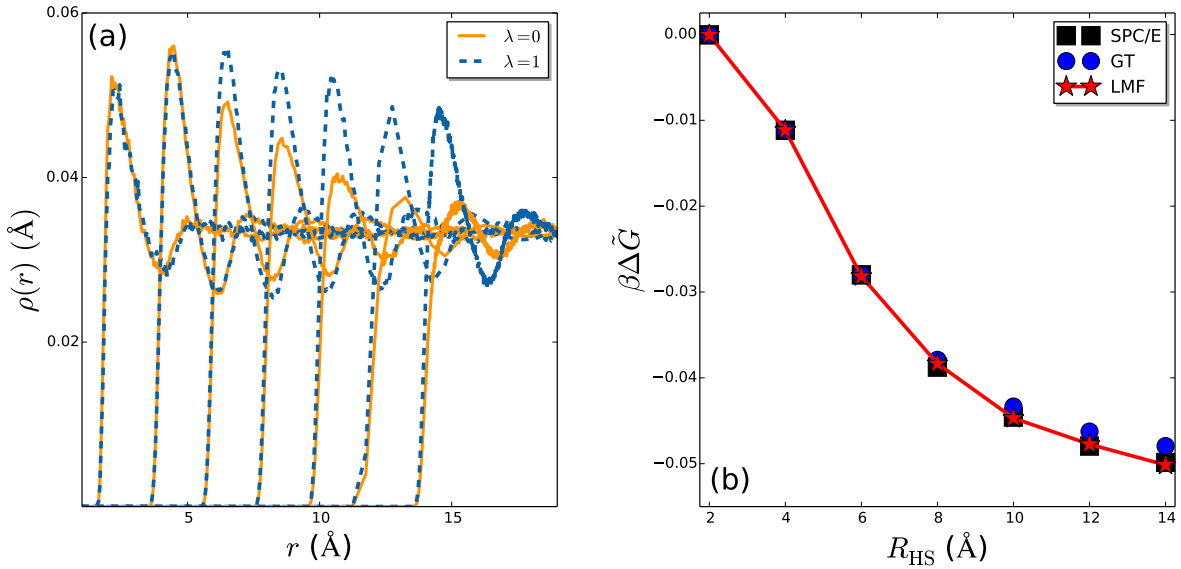
Figure 6.7: (a) Nonuniform density around solutes with HS radii from $R_{\mathrm{HS}} = 2$ Å to $R_{\mathrm{HS}} = 14$ Å with ($\lambda = 1$) and without ($\lambda = 0$) solute-solvent LJ attractions. (b) Free energy change per unit solute surface area upon turning on the attractive portion of the solute-water potential $U_{1,\mathrm{sw}}$ calculated in the full, SPC/E water system, the short ranged GT water system, and from LMF theory.

portion of the renormalized potential into short and long ranged components for use with LMF theory, this field can be written as $\psi_{\mathrm{R},\alpha}(\mathbf{r}; \lambda) = \psi_{0,\alpha}(\mathbf{r}; \lambda) + \psi_{\mathrm{R}1,\alpha}(\mathbf{r}; \lambda)$, where the short ranged portion is

$$\psi_{0,\alpha}(\mathbf{r}; \lambda) = \phi_\alpha(\mathbf{r}; \lambda) + q_\alpha \mathcal{V}_0(\mathbf{r}; \lambda) \tag{6.32}$$

and the long ranged component is simply given by

$$\psi_{\mathrm{R}1,\alpha}(\mathbf{r}; \lambda) = q_\alpha \mathcal{V}_{\mathrm{R}1}(\mathbf{r}; \lambda). \tag{6.33}$$

For the solute-solvent potentials considered herein, given by Equation 6.30, the local electrostatic component of the renormalized solute field is zero, $\mathcal{V}_0(\mathbf{r}) = 0$, but note that $\mathcal{V}_{\mathrm{R}1}(\mathbf{r}) \neq 0$, as this contains the averaged effects of the long ranged solvent-solvent electrostatic interactions.

Density distributions of water around solutes of varying size are shown in Figure 6.7a in the presence ($\lambda = 1$) and absence ($\lambda = 0$) of attractive interactions. For small solutes, the solvation structure is determined entirely by the need for water to maintain its hydrogen bond network around the solute. Therefore, for R_{HS} less than roughly 5 Å, attractive interactions have a negligible affect on
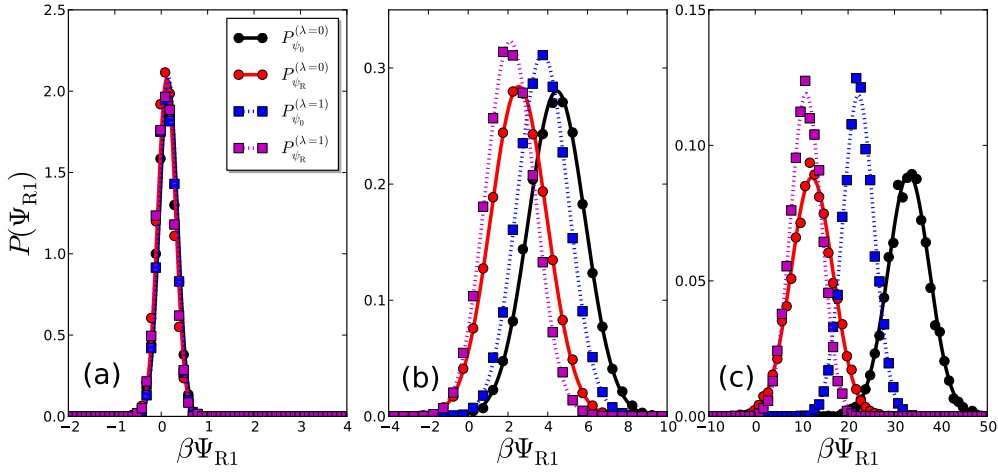
Figure 6.8: Probability distributions of the potential energy due to the slowly-varying portion of the electrostatic LMF $\mathcal{V}_{R1}$ for solutes with effective hard sphere radii of (a) $R_{HS} = 4$ Å, (b) $R_{HS} = 10$ Å, and (c) $R_{HS} = 14$ Å. Symbols are data obtained from simulation and lines are Gaussian distributions with the same mean and variance of the corresponding computed distributions.

the solvation structure.

The hydrogen bond network of water cannot be maintained around large solutes, and a soft, liquid-vapor like interface is nucleated in the vicinity of the solute surface, resulting in the phenomena of drying in the interfacial region, which becomes more pronounced as the solute size is increased. This soft interface is highly responsive to perturbations, and attractive interactions significantly alter the solvation structure, effectively "pulling" water molecules toward the solute surface, increasing the magnitude of the first peak in $\rho(r)$ with respect to that observed in the absence of solute-solvent attractions.

We again determined the free energy of turning on the slowly varying portion of the LMF potential, $\Delta G_{R1,\lambda}$, using the Gaussian approximation of Equation 6.24. To verify the accuracy of this approximation, I have calculated the probability distributions $P_0^{(\lambda)}(\Psi_{R1})$ and $P_R^{(\lambda)}(\Psi_{R1})$, where $\Psi_{R1} = \sum_{i=1}^{N} \psi_{R1}(\mathbf{r}_i)$. These distributions are shown in Figure 6.8 for several solute sizes and for both values of λ in the corresponding SCA and mimic systems. The symbols in Figure 6.8 are data calculated from simulation, while solid lines are Gaussian distributions with the same mean and variance as the calculated distribution. All distributions for all solute sizes studied are found to follow Gaussian statistics, verifying the use of Equation 6.24 to estimate the free energy $\Delta G_{R1,\lambda}$.

The free energy change along the transformation $\lambda = 0 \rightarrow \lambda = 1$ can be obtained by

thermodynamic integration,

$$\Delta G_{0\to 1} = \int_0^1 d\lambda \left\langle \frac{\partial \mathcal{H}^{(\lambda)}}{\partial \lambda} \right\rangle_\lambda = \int_0^1 d\lambda \left\langle U_{1,\text{sw}} \right\rangle_\lambda, \tag{6.34}$$

where $\mathcal{H}^{(\lambda)}$ is the λ-dependent Hamiltonian of the system and $\langle \cdots \rangle_\lambda$ indicates an ensemble average over configurations of the system interacting with coupling parameter λ. The free energy differences calculated using the full SPC/E model are compared with those calculated using the short ranged GT water model and with those computed from LMF theory in Figure 6.7b for a range of solute radii. The LMF route to calculating free energy differences is found to reproduce the results of the full system almost exactly for all solute sizes examined. Therefore, the results presented for this simple test case effectively illustrate that the LMF theoretic framework can be applied to alchemical transformations with quantitative accuracy.

6.4 Density Fluctuations and Hard Sphere Solvation

The preceding sections describe LMF-based methods for computing free energy changes of a solute in solution as it is changed from one state to another (a point solute to the full solute in the case of solvation free energies). In general, thermodynamics is not limited to the description of solvation processes, and a free energy can be computed along some relevant order parameter or *reaction coordinate* describing any process of interest. For example, the association of two model methane molecules in water was studied by computing the free energy as a function of methane-methane distance in Chapter 3. However, to compute such free energy profiles, one often needs to employ advanced non-Boltzmann sampling techniques [31].

One type of non-Boltzmann sampling employed throughout this thesis is umbrella sampling [118], in which many simulations of a system are performed, each with a unique "umbrella" potential that biases the system toward a particular value of the reaction coordinate. The results of this set of simulations can then be stitched together through a number of means, one of which is the multi-state Bennett acceptance ratio [68] (MBAR) used many times throughout this work. Therefore, in order to use the LMF framework to calculate general free energy landscapes as a function of an order parameter of interest, we need to combine LMF theory with such non-Boltzmann sampling techniques.

We have developed such a formalism, and the technical details are described in Appendix J. We combine LMF theory, umbrella sampling, and MBAR to calculate ensemble averages in a full system from sampling performed in a mimic or SCA system. Umbrella sampling is performed with an appropriate biasing potential for each window *and* an accompanying window-specific LMF potential. This ensures an accurate representation of the full system structure in *each window.* Free energy differences between these windows, and the associated free energy landscape, can then be determined

for the mimic system using MBAR. Finally, the analytic LMF contribution to the free energy given by Equation 6.15 can be used to *reweight* mimic system ensemble averages in order to obtain the corresponding averages in the full system. An analogous procedure can be performed for the SCA system when LRT is accurate, however the reweighting must also account for the free energy differences between the SCA and mimic systems.

As a demonstration of these theoretical developments, we study density fluctuations in bulk water. Specifically, we seek to calculate the probability of observing N water molecules within a spherical volume v. This probability $P_v(N)$ is intimately related to the free energy of solvation ΔG_{HS} of a hard sphere of the same volume through the potential distribution theorem,

$$e^{-\beta \Delta G_{\mathrm{HS}}} = \left\langle e^{-\beta U_{\mathrm{HS}}} \right\rangle_{\mathrm{M}} = \left\langle \delta_{N_v,0} \right\rangle_{\mathrm{M}} = P_v(0), \tag{6.35}$$

where the ensemble averages are performed over the bulk mobile fluid ensemble (M) in the absence of a hard sphere, $U_{\mathrm{HS}} = \sum_{i=1}^{M} u_{\mathrm{HS}}(r_i) = \delta_{N,0}$ is the total solute-solvent interaction energy, and $\delta_{N,N'}$ is the Kronecker delta function. Therefore, $\beta \Delta G_{\mathrm{HS}} = -\ln P_v(0)$, where $P_v(0)$ is the probability of observing a cavity the same size and shape of the solute volume v. It was shown earlier in this chapter that one can use LMF theory to determine ΔG_{HS}, and therefore $-\ln P_v(0)$, from a purely short ranged system with quantitative accuracy for both small and large solute volumes. In this section, we demonstrate that the full distribution $P_v(N)$ can also be obtained from short ranged systems with high accuracy by combining LMF theory and non-Boltzmann sampling techniques.

For relatively small probe volumes, the distributions $P_v(N)$ can be calculated using the Widom particle insertion method [31]. However, large volume density fluctuations are rare events not accurately sampled by conventional simulations, and some type of biased, non-Boltzmann sampling technique is needed to calculate $P_v(N)$ accurately. In this case, we use umbrella sampling techniques to bias the simulation. At first glance, one would like a biasing potential in terms of the variable of interest, N. However, N is a discrete variable, and this presents issues with MD simulations, because the potentials and forces will not be continuous (although this is not a problem in Monte Carlo simulations). Instead, the INDUS method allows N to be coarse-grained by smoothing N with a truncated and shifted Gaussian distribution, resulting in the continuous coarse-grained variable $\tilde{N}$ [74]. We can then bias the simulation toward desired values of $\tilde{N}$, which, with correctly tuned parameters, will closely follow N. After performing a set of n_w simulations that adequately sample N and $\tilde{N}$, with sufficient overlap of the $P_v(N, \tilde{N})$ distributions between neighboring windows, we can reconstruct the desired $P_v(N)$ using MBAR [68]. In all cases, a simple harmonic potential was used to bias the system toward the desired value of $\tilde{N}$,

$$V_k(\tilde{N}) = \frac{\kappa}{2} \left(\tilde{N} - \eta_k \right)^2, \tag{6.36}$$
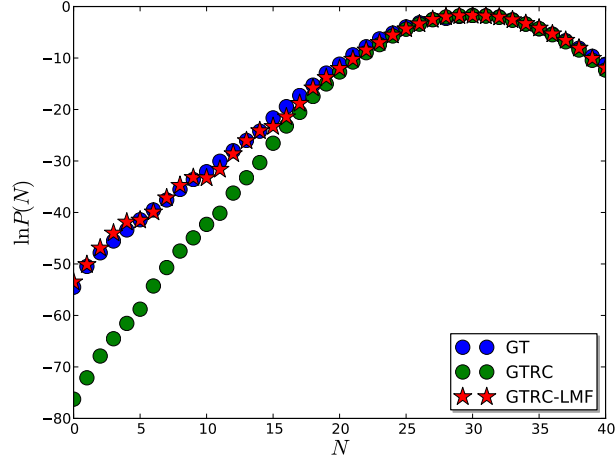
Figure 6.9: Probability distribution $P_v(N)$ of finding N water molecules in a spherical observation volume v with a radius of 6 Å determined in GT and GTRC water. Also included are the results obtained from a combination of LRT and LMF theory, and described in Section J.3.

where η_k is the desired value of $\tilde{N}$ in window k, and the force constant κ was chosen independently for each window to yield sufficient overlap between neighboring windows.

In order to maintain a constant bulk density far from the probe volume across all biased ensembles, we perform simulations in the isothermal-isobaric (NPT) ensemble, and therefore must account for the biasing potential in the calculation of the virial pressure. The contribution to the pressure from the biasing potential is simply,

$$P^{\text{INDUS}} \equiv -\frac{\partial V_k}{\partial V} = \frac{1}{3V} \sum_{i=1}^{M} \mathbf{r}_i \cdot \mathbf{f}_i^{\text{INDUS}}, \tag{6.37}$$

where M is the number of particles interacting with the biasing potential, $\mathbf{r}_i$ is the position of particle i, and $\mathbf{f}_i^{\text{INDUS}}$ is the force on particle i due to the biasing potential [74].

For small volumes, below the crossover size, long ranged interactions have a negligible influence on the solvation behavior. Therefore, density fluctuations in the bulk fluid are determined by local, hydrogen bonding interactions on such small length scale, and these fluctuations are not altered upon the inclusion of an LMF in the short ranged reference system. In contrast, in the large scale regime, $P_v(N)$ displays non-Gaussian tails at low N in GT water, as shown in Figure 6.9. The appearance of such fat tails in $P_v(N)$ are a manifestation of the nucleation of a nanoscale liquid-vapor interface at the surface of a large cavity, and are consistent with the appearance of interfacial drying. Indeed,

140

removal of the unbalanced attractive LJ forces in GTRC water eliminates drying, and therefore the $P_v(N)$ of GTRC lacks such fat tails at low N, as can be expected from the results presented in Chapter 3. In addition, the GTRC $P_v(N)$ is nearly Gaussian for all N, similar to what is observed in a hard sphere fluid [128].

Using LRT, we determine the densities and LMF fields in each biased ensemble necessary for performing the reweighting described in Section J.3. Upon doing so, averages obtained from configurations obtained in the GTRC system are appropriately reweighted, yielding a $P_v(N)$ distribution consistent with GT water, as shown by the red stars in Figure 6.9. By including the averaged effects of the unbalanced LJ forces *in each biased ensemble*, we can capture the non-trivial fat tails observed at low N with high accuracy, as shown in Figure 6.9.

6.5   Conclusions

In this chapter we have developed a LMF theory-based framework for performing the major types of free energy calculations. The accuracy of this theoretical framework was demonstrated through the study of hard sphere solvation in water and LJ fluids, and ion hydration. Such systems represent the most challenging test cases for LMF theory, where unbalanced interfacial forces arising from long ranged interactions are quite important for structure and thermodynamics, leading to interfacial drying and the length scale transition of solvophobic solvation. LMF theory provides an exceptionally accurate description of these systems, and we expect that the framework developed herein will be readily applicable to more complex systems.

The most natural extension of our theoretical framework is to the solvation of molecularly detailed solutes consisting of multiple atomic sites. In general, a fixed solute of this type will generate a nonuniform LMF $\mathcal{V}_R(\mathbf{r})$ with no symmetries. One may exploit the ability of the LMF equation to be rewritten in the form of a Poisson's equation involving the Gaussian smoothed total charge density of the system [1], $\nabla^2 \mathcal{V}_{R1}(\mathbf{r}) = -\rho_{tot}^{q\sigma}(\mathbf{r})/\epsilon$, to solve for $\mathcal{V}_{R1}(\mathbf{r})$ with a numerical Poisson Solver [129], but evaluation of a three-dimensional potential may still be computationally difficult. Another promising avenue to use LMF theory for molecular solutes is to extend the superposition-like approximation made by Denesyuk and Weeks (DW) [44]. Within this approximation, the nonuniform LMF potential is approximated by the sum of the spherically symmetric potentials centered on the atomic sites of the solute molecule,

$$\mathcal{V}_R(\mathbf{r}) \approx \sum_{\alpha=1}^{N_\alpha} \mathcal{V}_{R,\alpha}(|\mathbf{r} - \mathbf{r}_\alpha|), \tag{6.38}$$

where there are N_α charged sites in the solute, each of which are indexed by α. DW have successfully applied such approximations to the description of bulk electrolytes and the collapse of model polypeptides in electrolyte solutions [44, 130]. Although DW represented the solvent as a uniform continuum with dielectric constant ϵ and used further Debye-Hückel-based approximations to solve

the LMF equation, we expect that expressions like Equation 6.38 will still be accurate in systems where the solvent is modeled explicitly and the LMF equation is solved in more detail.

The LMF framework for free energy calculations should be of significant importance to the study of biomolecular and materials research. The study of the large-scale systems involved in these areas often make a characterization of the free energy landscapes necessary to understand the relevant processes of interest prohibitively expensive. LMF theory reduces such computational burdens, allowing for the in depth study of large-scale systems involving macromolecules like proteins or molecular assemblies like membranes and micelles. Indeed, the extension of LMF theory to these important areas is currently underway.

Contrary to the outstanding work of art,
outstanding theory is susceptible to improvements.

Karl Popper

7

Conclusions and Future Work

Throughout this dissertation, we have utilized LMF theory and its underlying concepts to examine the thermodynamic consequences of nanoscale structural details. We first focused on several anomalous thermodynamic properties of bulk water, and examined the structural origins of such anomalies using LMF-based truncations of the SPC/E water model. Long ranged electrostatic interactions play a minimal role in the studied anomalies, as may be expected from the accuracy of the force cancellation picture for such slowly-varying interactions. This is reflective of a hierarchical ordering of importance of the (i) hydrogen bond network, (ii) longer ranged LJ attractions, and (iii) long ranged multipolar interactions. The anomalous structural and thermodynamic properties of water arise from a competition of the local repulsive and attractive forces leading to the hydrogen bond network and the cohesive energy provided by long ranged attractive interactions.

In addition, LMF-based truncated models were employed to illustrate the role of unbalancing potentials in hydrophobic effects, and to facilitate a comparsion between solvophobic solvation in water and simple liquids. In particular, the use of such truncated models in conjunction with LMF theory allowed us to clearly illustrate the role of the hydrogen bond network in determining the solute size at which a crossover from small to large length-scale solvation occurs in water. Such strong local interactions lead to significantly different physics underlying the crossover in water than in a simple LJ fluid.

Local molecular field theory ideas were then employed to study ion hydration, and subtleties surrounding the calculation of electrostatic potentials arising in dielectric continuum theories were explored. It was also illustrated that any non-Gaussian behavior in the response of water to the

presence of a charged hard sphere arises from short ranged, near-field electrostatics. The far-field components of the electrostatic response, on the other hand, are relatively insensitive to the molecular details of the solvent, and the solvent can be treated as a continuum on such long-wavelengths. This was further exemplified by probing the dielectric response of molecular systems to Gaussian test charges. Such Gaussian distributions of charge are the appropriate generalization of the concept of a classical test charge to probe the dielectric response of molecularly detailed systems as studied by simulation.

A highly accurate LMF-theoretic framework was then developed for free energy calculations, in which long ranged components of the free energy are computed analytically while the remaining steps are performed using computationally efficient simulations of purely short ranged models. This approach was then applied to several challenging problems, in which unbalancing forces play a significant role in determining the structure and thermodynamics of the system. The calculation of thermodynamic properties from LMF theory is directly applicable to most methods of free energy calculation, and should therefore find widespread use. Further development of this framework for more complex systems is an active area of research.

Of particular interest for future research is to extend the use of truncated models to the study the behavior of "cold" water. It has been proposed that water has a liquid-liquid critical (LLCP) point located at low temperature and high pressure [131]. The LLCP hypothesis has been used to provide a theoretical explanation for the many anomalous properties of water based on the existence of two distinct liquid states. However, this LLCP has eluded experimental detection because it is located in the so-called "No-Man's Land" of the water phase diagram, so named because it is below the homogenous nucleation temperature of ice and therefore one cannot equilibrate a metastable liquid phase. The existence of such a critical point, and the liquid-liquid phase transition (LLPT) line it implies, has been a subject of great debate, with mounting evidence both for [132, 133, 134] and against [135, 136, 137]. In particular, Limmer and Chandler have argued persuasively that there are not two distinct liquid phases at low temperatures in most realistic water models. Instead, they propose that the previously observed high density liquid (HDL) and low density liquid (LDL) phases were a misinterpretation of nonequilibrium phenomena associated with coarsening dynamics of the metastable liquid state during crystallization [136].

Examination of the low temperature behavior of the GTRC model in particular could shed some light on these issues. This minimal representation of the hydrogen bond network of water yields a low density liquid (not the LDL described above) that lacks the cohesive energy necessary to introduce a fifth nearest neighbor into the hydration shell of a water molecule. As such, we expect that this model cannot have a HDL phase. Therefore, if it displays the characteristic increase in response functions as the temperature is lowered, this cannot be rationalized by the existence of two phases. In addition, the density of GTRC is less than that of ice at ambient conditions, and studying the melting transition of this model should also prove quite instructive.

Another area of future research that is currently underway is to utilize truncated models in

conjunction with LMF theory to study ion specific effects at the liquid-vapor interface. Contrary to classical dielectric continuum theory predictions, which state that ions should be repelled from a liquid-vapor interface, both experiments and simulations have observed that ions can adsorb to such interfaces. One particularly simple and heavily studied ion is Iodide, I^-, an anion of relatively low charge density. Recent results have shown, quite surprisingly, that the energetics of ion adsorption are dominated by local ion-water interactions, such that I^- perturbs only water molecules in the first hydration shell [138, 139]. However, the presence of I^- at the water-vapor interface leads to an entropic penalty through the suppression of interfacial density fluctuations [138, 139]. Such *capillary waves* are typically viewed as a long-wavelength phenomenon, and an accurate description of these interface fluctuations can be provided by field theories neglecting molecular-scale details. This energy-entropy balance may seem contradictory, because the energetic contribution to the free energy is dominated by local interactions while the entropic component arises from non-local effects. As such, attempts have been made to disentangle the effects of interfacial fluctuations on the free energy of ion adsorption [140].

Unlike previous studies, the use of LMF-based truncated models allows for the direct decomposition of effects arising from local and non-local interactions. A strong coupling system consisting of GT water and a short ranged I^-, for example, will contain only short ranged electrostatic interactions. The surface tension of GT water is slightly less than that of SPC/E, and will therefore have a slightly larger amplitude of capillary wave fluctuations. This system provides a useful test of the hypothesis that ion adsorption is dominated by local electrostatics. This is indeed the case, and free energies as a function of distance perpendicular to the average position of the liquid-vapor interface show a minimum at nearly the same location in both SPC/E water and its GT variant, as shown in Figure 7.1 [1].

The suppression of capillary waves can also be studied using LMF theory and truncated models. We can utilize the useful "feature" that mean field theory cannot capture long-wavelength capillary waves [8] to simulate a liquid vapor interface without these fluctuations. In particular, we can use the GTRC model with LMF theory for LJ attractions to capture the average structure of the liquid-vapor interface. However, this interface lacks long-wavelength density fluctuations, and simulation results indicate that interfacial height fluctuations are reduced by roughly 70 % in the LJ-LMF system, such that only local distortions of the interface can occur. Surprisingly, a distinct minimum in the potential of mean force is present even in this system, as shown in Figure 7.1. Although decomposition of the free energy into its energetic and entropic components is necessary to determine the relative balance of these contributions, these results at least indicate that ion adsorption suppresses local fluctuations of the interface, and not the traditional long-wavelength capillary waves.

A major theoretical development that remains for LMF theory is its extension to dynamics of

---

[1] More details regarding the liquid-vapor interfaces of truncated models are given in Appendix K
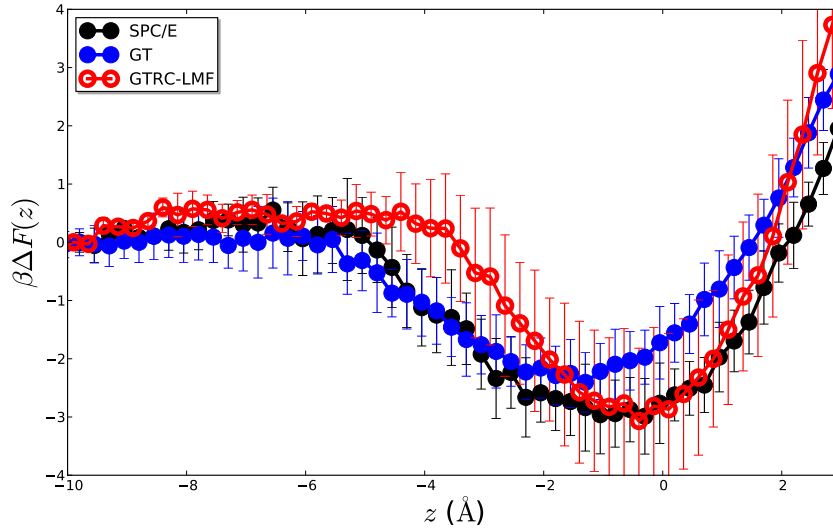
Figure 7.1: Change in free energy $\Delta F(z)$ for moving a fractionally charged iodide as a function of distance z from the mean liquid-vapor interface located at $z = 0$ with full electrostatics (SPC/E), in the GT reference system, and in GTRC water in the presence of $\phi_{\mathrm{R}}^{\mathrm{LJ}}(z)$ as described in the text. The I$^-$ ion is modeled as a LJ particle with fractional charge $Q_I = -0.8\,e_0$. The oxygen-I$^-$ LJ interaction parameters are $\varepsilon_{\mathrm{LJ}} = 0.5215$ kJ/mol and $\sigma_{\mathrm{LJ}} = 4.14525$ Å [138].

molecular systems, both in and out of equilibrium. We can illustrate the successes and failures of LMF theory in the description of dynamical properties of molecular systems through the examination of a one-component LJ fluid, its WCA reference system, and the corresponding LMF system at a state point of $\rho\sigma_{\mathrm{LJ}}^3 = 0.85$ and $T^* = 0.65$ [141]. The structure of the LJ fluid, quantified by the pair distribution function $g(r)$, is accurately captured by the LMF system, while small deviations are found for the WCA reference consistent with previous findings [6]. We quantify the dynamic properties of the systems through the velocity autocorrelation function $C_v(t)$,

$$C_v(t) = \frac{\langle \mathbf{v}(t) \cdot \mathbf{v}(0) \rangle}{\langle \mathbf{v}^2(0) \rangle}, \tag{7.1}$$

where $\mathbf{v}(t)$ is the three-dimensional velocity vector of a particle at time t, and the mean-squared displacement, $\mathrm{MSD}(t)$.

We can begin to see where LMF theory needs improvement by dividing space-time into three distinct regimes. Following Hansen and McDonald [26], we set the relevant length- and time-scales to be the mean free path l_C and the mean collision time τ_C. The fastest time-scale, associated with the
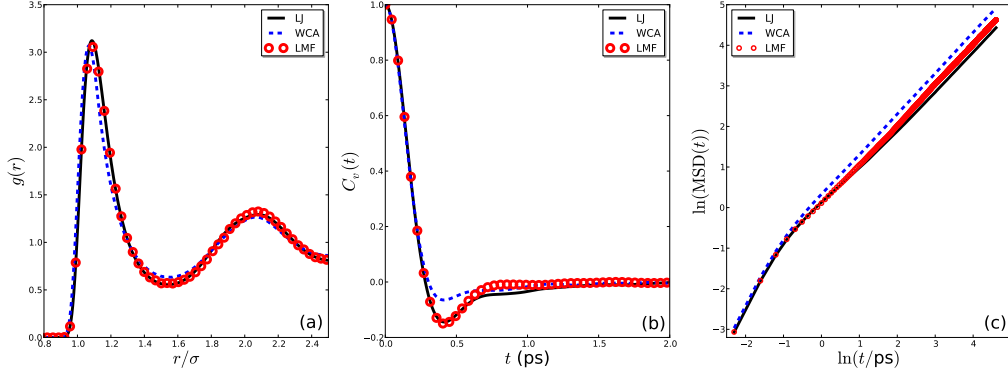
Figure 7.2: (a) Pair distribution functions obtained for a LJ fluid, its WCA reference, and the corresponding LMF system at the state point $\rho\sigma_{\mathrm{LJ}}^3 = 0.85$ and $T^* = 0.65$. (b) Velocity autocorrelation functions and (c) mean squared displacments for the three systems. Note the log-log scale in (c). Times are obtained using the appropriate units for argon.

shortest lengths, is the *free-particle regime*, wherein $kl_C >> 1$ and $\omega\tau_C >> 1$ (ω indicates frequency, the Fourier-space analog of time). In this regime, particles move almost independently of one another, and LMF theory, or even the strong coupling approximation, will trivially capture the dynamics occurring on such short timescales, as evidenced by Figure 7.2.

An intermediate regime also exists, characterized by $kl_C \approx 1$ and $\omega\tau_C \approx 1$, termed the *kinetic regime* [26]. In this regime, the molecular structure of the fluid is of substantial importance. For argon, τ_C is on the order of 0.1 ps [26], and we expect that $kl_C \approx k\rho^{-1/3} \leq 2^{1/6}\sigma_{\mathrm{LJ}}k$ to a good approximation at densities near the triple point. Therefore the structure and dynamics on this space-timescale will also be captured by LMF theory, but may not be captured in the corresponding SCA system which lacks the correct equilibrium structure. Indeed, this is the case, as $C_v(t)$ and $\mathrm{MSD}(t)$ in Figure 7.2 are both accurately described by the LMF system for $t < 0.5$ ps, while the WCA reference system fails to reproduce the depth of the minimum in $C_v(t)$ near 0.4 ps and the MSD of this system increases more rapidly than the full LJ system.

The third and final regime under consideration is the *hydrodynamic regime* associated with long-wavelength, long-time fluctuations [26], $kl_C << 1$ and $\omega\tau_C << 1$. Due to the mean field nature of the LMF approach, long-wavelength fluctuations are neglected. While this is not problematic when the structure and thermodynamics of systems in equilibrium are concerned, such fluctuations are important when the hydrodynamic properties of a system are under consideration. Therefore, we might expect that LMF theory cannot capture the long-time behavior of the dynamics in its current formulation. Indeed, the data presented in Figure 7.2 indicate that LMF theory does not

reproduce the collective effects leading to the long-time dynamics of the full LJ fluid. However, because hydrodynamics does not depend sensitively on the microscopic details of a fluid, general, time-dependent corrections to LMF theory from fluctuating hydrodynamic fields should be possible.

A

LMF Theory in Practice

This Appendix describes how LMF theory is implemented in practice for a system examined in this thesis. Although it is more than a "toy" model, I will demonstrate the use of LMF theory on the case of a large repulsive spherical solute of the type examined in Chapter 3 with an effective hard sphere radius of $R_{\mathrm{HS}} \approx 20$ Å in 6022 SPC/E water molecules. Although this system is quite large, similar results hold for smaller solutes that are still in the solute size regime in which the H-bond network cannot be maintained around the solute, roughly $R_{\mathrm{HS}} \geq 6$ Å. However, the differences between truncated and full water models become more pronounced as the solute size is increased.

The potential energy of a uniform, bulk system of N molecules of SPC/E water is given by

$$U = \frac{1}{2} \sum_{i=1}^{N} \sum_{j=1}^{N}{}' u\left(r_{ij}\right) + \frac{1}{2} \sum_{i=1}^{3N} \sum_{j=1}^{3N}{}' \frac{q_i q_j}{\epsilon} v\left(r_{ij}\right), \tag{A.1}$$

where the prime over the second sum indicates that terms when sites i and j are on the same molecule are omitted and $r_{ij} = |\mathbf{r}_j - \mathbf{r}_i|$ is the distance between sites i and j. The first term corresponds to the LJ interactions in the system, with one LJ site per molecule. The LJ potential is given by

$$u(r) = 4\varepsilon_{\mathrm{LJ}} \left[\left(\frac{\sigma_{\mathrm{LJ}}}{r}\right)^{12} - \left(\frac{\sigma_{\mathrm{LJ}}}{r}\right)^{6} \right], \tag{A.2}$$

and the energy and length-scale parameters for water are $\varepsilon_{\mathrm{LJ}} = 0.65$ kJ/mol and $\sigma_{\mathrm{LJ}} = 3.166$ Å,

respectively. The second term corresponds to the evaluation of electrostatic interactions, and, as there are three charges per SPC/E water molecule, the summations are over the $3N$ charged sites in the system. The electrostatic interaction is the Coulomb potential,

$$\frac{q_i q_j}{\epsilon} v(r) = \frac{q_i q_j}{\epsilon r}, \tag{A.3}$$

where q_i is the partial charge of site i and ϵ is the dielectric constant of the media (taken to be 1 in the case of vacuum).

Here, I will only focus on separating $v(r) = 1/r$, and not the LJ potential (solving the LMF equation is similar, and actually easier with the LJ potential). In this case, the $1/r$ portion of the Coulomb potential is separated into a rapidly-varying short ranged portion and a slowly-varying long ranged portion as

$$v(r) = v_0(r) + v_1(r) = \frac{\text{erfc}(r/\sigma)}{r} + \frac{\text{erf}(r/\sigma)}{r}, \tag{A.4}$$

where the separation length scale σ has been chosen (rather conservatively) to be equal to 4.5 Å (I say conservatively because even a value of $\sigma = 3.0$ Å will capture the bulk structure of SPC/E water at a fixed volume). Using only $v_0(r)$ in place of $1/r$ in the Coulomb potential leads to the Gaussian-Truncated (GT) model of water, which will be used to illustrate the process of solving the LMF equation. Note that the potential energy of a uniform, bulk system of N molecules of GT water is then given by

$$U_{\text{GT}} = \frac{1}{2} \sum_{i=1}^{N} \sum_{j=1}^{N} {}' u(r_{ij}) + \frac{1}{2} \sum_{i=1}^{3N} \sum_{j=1}^{3N} {}' \frac{q_i q_j}{\epsilon} v_0(r_{ij}), \tag{A.5}$$

in analogy with that of the SPC/E model described above.

A.1 Obtaining a Self-Consistent Solution of the LMF Equation

The first step of solving the LMF equation is to perform a simulation of the short ranged system to provide an initial charge density to input into the LMF equation. Note that if one can provide a good "guess" to the charge density as input to the LMF equation, this can be input to the LMF equation first and simulate with an initial field (see Reference [110] for further details and an example).

We will examine four properties of the system in order to compare the full SPC/E, GT, and LMF systems: (i) the microscopic charge density in a configuration $\bar{\mathbf{R}}$,

$$\rho^q(\mathbf{r}; \bar{\mathbf{R}}) \equiv \sum_i q_i \delta(\mathbf{r} - \mathbf{r}_i(\bar{\mathbf{R}})),$$
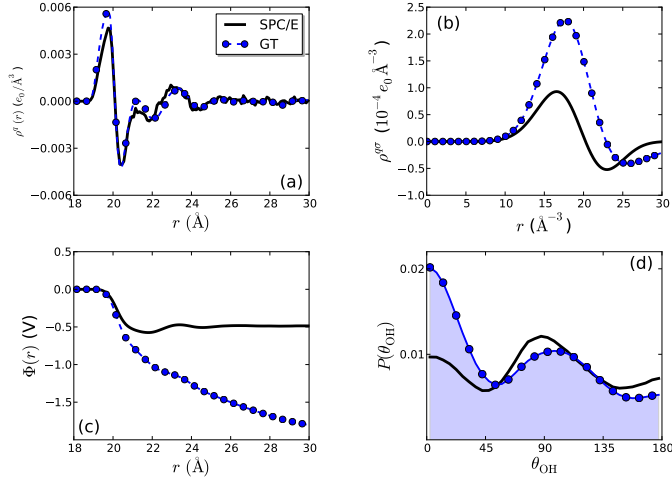
Figure A.1: (a) Charge densities, (b) Gaussian-smoothed charge densities, (c) electrostatic potentials, and (d) probability distributions of θ_{OH} for SPC/E and GT water models around a purely repulsive spherical solute of radius $R_{\text{HS}} \approx 20$ Å.

the ensemble average of which is $\rho^q(\mathbf{r}) = \langle \rho^q(\mathbf{r}; \bar{\mathbf{R}}) \rangle$, (ii) the Gaussian-smoothed charge density,

$$\rho^{q\sigma}(\mathbf{r}) = \frac{1}{\pi^{3/2}\sigma^3} \int d\mathbf{r}' \rho^q(\mathbf{r}') \exp\left[-\left(\frac{|\mathbf{r} - \mathbf{r}'|^2}{\sigma^2}\right)\right],$$

which, in a spherically symmetric system is given by

$$\rho^{q\sigma}(r) = \frac{1}{r\sigma\sqrt{\pi}} \int_0^\infty dr' r' \rho^q(r') \left[\exp\left(-\frac{|\mathbf{r} - \mathbf{r}'|^2}{\sigma^2}\right) - \exp\left(-\frac{|\mathbf{r} + \mathbf{r}'|^2}{\sigma^2}\right)\right],$$

(iii) the electrostatic (or polarization) potential

$$\Phi(r) = \frac{1}{4\pi\epsilon_0} \int d\mathbf{r}' \frac{\rho^q(r')}{|\mathbf{r} - \mathbf{r}'|} = -\frac{1}{\epsilon_0} \int_0^r \frac{dr'}{r'^2} \int_0^{r'} dr'' r''^2 \rho^q(r''),$$

and (iv) the probability distribution of the angle formed by the O-H bond vector of a water molecule and the vector connecting the water oxygen site and the solute, $P(\theta_{\text{OH}})$, which was calculated for water molecules within 1 Å of the solute surface.

The above-mentioned quantities are shown for the SPC/E and GT water models in Figure A.1. Although only slight differences are observed between the charge densities of the two systems, like the larger first peak in that for the GT model, large differences are found for the remaining quantities. This illustrates that while the truncated and full systems have only small differences in their charge densities (and oxygen densities, not shown), there are large effects on other electrostatic and orientational properties of water. The origin of these effects are discussed in Chapter 3.

A.2 Solving the LMF equation at each iteration

A.2.1 One-dimensional LMF equation in a spherically symmetric system

The next step is to evaluate the LMF equation in a single iteration. In spherically symmetric charged systems, the LMF equation we wish to solve is given by

$$\mathcal{V}_\text{R}(r) = \mathcal{V}_0(r) + \frac{1}{\epsilon} \int d\mathbf{r}' \rho^q \left(\mathbf{r}'; [\mathcal{V}_\text{R}]\right) v_1 \left(|\mathbf{r} - \mathbf{r}'|\right) + C, \tag{A.6}$$

where we have separated the electrostatic LMF into short ranged and long ranged portions, $\mathcal{V}_\text{R}(r) = \mathcal{V}_0(r) + \mathcal{V}_{\text{R}1}(r)$. In order to convert this to a numerically integrable one-dimensional equation, we seek a Green's function, $G(r; r')$, that satisfies the relation

$$\mathcal{V}_\text{R}(r) = \mathcal{V}_0(r) + \frac{1}{\epsilon} \int d\mathbf{r}' \rho^q \left(\mathbf{r}'; [\mathcal{V}_\text{R}]\right) G(r; r') + C. \tag{A.7}$$

Physically, $G(r; r')$ can be considered the potential at position r due to a unit charge smoothed into spherical shell at position r', which is then Gaussian-smoothed. We can then rewrite Equation A.7 in the following manner,

$$\mathcal{V}_\text{R}(r) = \mathcal{V}_0(r) + \frac{1}{\epsilon} \int d\mathbf{r}' \rho^q \left(\mathbf{r}'; [\mathcal{V}_\text{R}]\right) \int d\mathbf{r}'' \frac{\delta \left(r' - r''\right)}{4\pi r'^2} v_1 \left(\mathbf{r} - \mathbf{r}''\right) + C, \tag{A.8}$$

making it evident that the function $G(r; r')$ is given by

$$\begin{aligned} G(r; r') &= \int_0^{2\pi} d\phi \int_{-1}^{1} d\left(cos\theta\right) \int_0^\infty dr'' r''^2 \frac{\delta \left(r' - r''\right)}{4\pi r'^2} \frac{\text{erf}\left(\frac{|\mathbf{r} - \mathbf{r}''|}{\sigma}\right)}{|\mathbf{r} - \mathbf{r}''|} \\ &= \frac{1}{2} \int_{-1}^{1} d\left(cos\theta\right) \frac{\text{erf}\left(\frac{|\mathbf{r} - \mathbf{r}'|}{\sigma}\right)}{|\mathbf{r} - \mathbf{r}'|}. \end{aligned} \tag{A.9}$$

In order to evaluate this integral, we make a transformation to bipolar coordinates,

$$G(r; r') = \frac{1}{2rr'} \int_{|r-r'|}^{|r+r'|} dy \, \text{erf}\,(y/\sigma) \tag{A.10}$$

Now, upon making the substitutions $y/\sigma = s$ and $dy = \sigma ds$, the integral can be easily evaluated as

$$
\begin{aligned}
G(r; r') &= \frac{\sigma}{2rr'} \int_{|r-r'|/\sigma}^{|r+r'|/\sigma} ds \, \text{erf}(s) \\
&= \frac{\sigma}{2rr'} \left(s \, \text{erf}(s) + \frac{1}{\sqrt{\pi}} e^{-s^2} \right) \Big|_{|r-r'|/\sigma}^{|r+r'|/\sigma} \\
&= \frac{1}{2rr'} \left[|r+r'| \, \text{erf}\left(\frac{|r+r'|}{\sigma} \right) + \frac{\sigma}{\sqrt{\pi}} e^{-\left(\frac{|r+r'|}{\sigma} \right)^2} \right. \\
&\quad - \left. |r-r'| \, \text{erf}\left(\frac{|r-r'|}{\sigma} \right) - \frac{\sigma}{\sqrt{\pi}} e^{-\left(\frac{|r-r'|}{\sigma} \right)^2} \right]. \tag{A.11}
\end{aligned}
$$

Through the use of the Green's function $G(r; r')$ given in Equation A.11, $\mathcal{V}_R$ can be readily obtained through numerical integration of Equation A.7.

A.2.2 k-space stable form of the LMF equation

When dealing with charged systems, one typically must take care that the proper asymptotic sum rules are satisfied, and LMF theory is no different. Consider the Fourier transform of the long ranged slowly-varying portion of the LMF equation for electrostatics,

$$\hat{\mathcal{V}}_{R1}(\mathbf{k}) = \frac{1}{\epsilon} \hat{\rho}^q(\mathbf{k}) e^{\left(-\frac{k^2 \sigma^2}{4} \right)} \frac{4\pi}{k^2} = \frac{1}{\epsilon} \hat{\rho}^{q\sigma}(\mathbf{k}) \frac{4\pi}{k^2}, \tag{A.12}$$

where we have defined the three-dimensional Fourier transform and inverse Fourier transform of a function f as

$$\hat{f}(\mathbf{k}) = \int d\mathbf{r} e^{-i\mathbf{k}\cdot\mathbf{r}} f(r)$$

and

$$f(\mathbf{r}) = \frac{1}{(2\pi)^3} \int d\mathbf{k} e^{i\mathbf{k}\cdot\mathbf{r}} \hat{f}(\mathbf{k}),$$

respectively. From the Stillinger-Lovett sum rules [26, 107, 108, 109], we expect that the charge density will satisfy

$$\hat{\rho}^q(k) \sim 0 + \alpha k^2 + \mathcal{O}(k^4), \tag{A.13}$$

at small k for the "correct" $\mathcal{V}_{R1}$. However, for incorrect $\mathcal{V}_{R1}$, *i.e.* before self-consistency of the LMF equation is obtained as in the case of GT water, the charge density may asymptotically behave as

$$\hat{\rho}^q(k) \sim C + \alpha k^2 + \mathcal{O}(k^4) \tag{A.14}$$

for small k, where C is a constant. If $C \neq 0$, then the iteration of the LMF equation will diverge in k-space, and therefore we need some type of stable iteration scheme.

A scheme for iterating the LMF equation has been developed [1], and the k-space stable solution of the LMF equation is

$$\mathcal{V}_{R1}(\mathbf{r}) = \frac{1}{\epsilon} \int d\mathbf{r}' \left[\rho^{q\sigma}(\mathbf{r}') - \rho^{q\sigma l}(\mathbf{r}') \right] \frac{1}{|\mathbf{r} - \mathbf{r}'|} + \frac{1}{l^3 \pi^{3/2}} \int d\mathbf{r}' \mathcal{V}_{R1}(\mathbf{r}') e^{-\frac{|\mathbf{r}-\mathbf{r}'|^2}{l^2}}, \tag{A.15}$$

where we have defined the smoothed charge density

$$\rho^{q\sigma l}(\mathbf{r}) = \int d\mathbf{r}' \rho^q(\mathbf{r}') \rho_G(|\mathbf{r} - \mathbf{r}'| ; \sqrt{\sigma^2 + l^2}), \tag{A.16}$$

such that

$$\rho_G(\mathbf{r}; \alpha) = \frac{1}{\pi^{3/2} \alpha^3} e^{-\frac{|\mathbf{r}|^2}{\alpha^2}}.$$

The length l is typically chosen on the order of σ.

For a spherically symmetric system, the one-dimensional k-space stable LMF equation is

$$
\begin{aligned}
\mathcal{V}_{R1}(r) &= \frac{1}{\epsilon} \int d'\mathbf{r} \rho_R^q(r') G(r; r'; \sigma) \\
&\quad - \frac{1}{\epsilon} \int d'\mathbf{r} \rho_R^q(r') G(r; r'; \sqrt{\sigma^2 + l^2}) \\
&\quad + I(r) + C,
\end{aligned} \tag{A.17}
$$

---

[1] The original k-space stable form of the LMF equation developed by Kirill Katsov took on a different form [142, 143]. This current form is due to John Weeks.
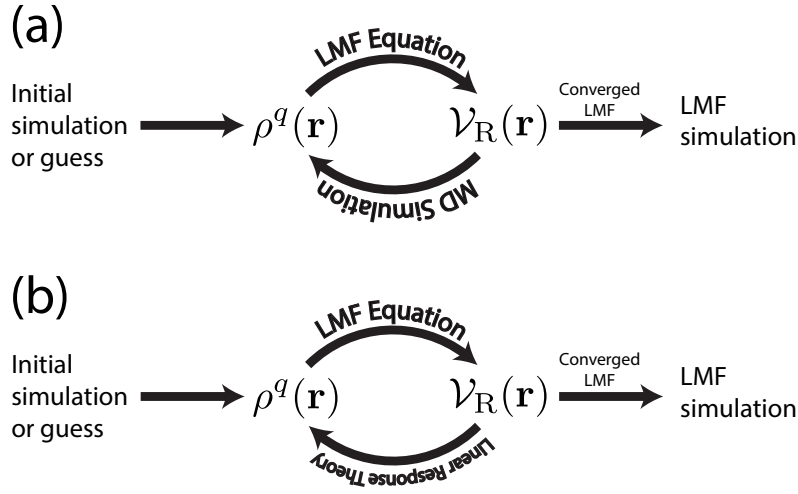
Figure A.2: Diagrams depicting (a) traditional iteration using simulation to solve for the density at each step and (b) linear response theory based method to obtain the density at each iteration.

where the Green's function is given by

$$
\begin{aligned}
G(r; r'; \gamma) \;=\; & \frac{1}{2rr'}\left[|r + r'|\,\mathrm{erf}\left(\frac{|r + r'|}{\gamma}\right) + \frac{\gamma}{\sqrt{\pi}}e^{-\left(\frac{|r+r'|}{\gamma}\right)^2} \right. \\
& \left. - \;|r - r'|\,\mathrm{erf}\left(\frac{|r - r'|}{\gamma}\right) - \frac{\gamma}{\sqrt{\pi}}e^{-\left(\frac{|r-r'|}{\gamma}\right)^2} \right],
\end{aligned}
\tag{A.18}
$$

and $I(r)$ is the integral

$$
I(r) = \frac{1}{\pi l r}\int_0^\infty dr'\,r'\,\mathcal{V}_{\mathrm{R1}}(r')\left[e^{-\left(\frac{|r-r'|}{l}\right)^2} - e^{-\left(\frac{|r+r'|}{l}\right)^2} \right].
$$

A.3 Iterating the LMF equation with linear response theory

Finally, an iterative solution of the LMF equation needs to be obtained. Traditionally, this has been done by obtaining a new density at each step through simulation (Figure A.2a). Recent work has led to the development of a linear response theory based framework to iterate the equation (Figure A.2b), and this is described below.
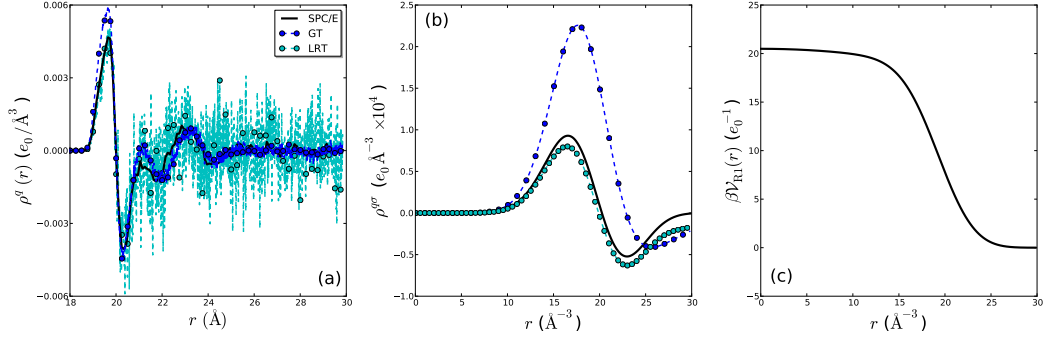
$$(A.19)$$

Figure A.3: (a) Charge densities and (b) Gaussian-smoothed charge densities for SPC/E and GT water models, as well as that obtained from iterating the LMF equation via linear response theory (LRT), Equation A.22. (c) The electrostatic LMF obtained from linear response theory iteration of the LMF equation.

A.3.1 Linear response theory for the density

In this section, I will describe how to solve the self-consistent LMF equation using linear response theory (LRT). Our goal will be to obtain a charge density response to a new field *without* performing another simulation with that field. First, we define the total potential energy due to $\mathcal{V}_{R1}(\mathbf{r})$ in a configuration $\bar{\mathbf{R}}$ as

$$\Phi_{R1}\left(\bar{\mathbf{R}}\right) \equiv \sum_{i=1}^{N} q_i \mathcal{V}_{R1}\left(\mathbf{r}_i\right) = \int d\mathbf{r} \rho^q\left(\mathbf{r}; \bar{\mathbf{R}}\right) \mathcal{V}_{R1}(\mathbf{r}), \tag{A.20}$$

for a system of N charges. Using density response theory, the new charge density is given by

$$\left\langle \rho^q\left(\mathbf{r}; \bar{\mathbf{R}}\right) \right\rangle_{\mathcal{V}_{R1}} = \frac{\left\langle \rho^q\left(\mathbf{r}; \bar{\mathbf{R}}\right) \exp\left(-\beta \Phi_{R1}\left(\bar{\mathbf{R}}\right)\right)\right\rangle_{\mathcal{V}_0}}{\left\langle \exp\left(-\beta \Phi_{R1}\left(\bar{\mathbf{R}}\right)\right)\right\rangle_{\mathcal{V}_0}}, \tag{A.21}$$

where $\left\langle \cdots \right\rangle_{\mathcal{V}_0}$ indicates an ensemble average over the configurations of the strong-coupling system or the system in the presence of an intermediate field. Such an average over exponentials is usually difficult to accurately evaluate numerically, and therefore using LRT allows one to determine the new density without performing such averages. The LRT result for the new charge density is given by

$$\left\langle \rho^q\left(\mathbf{r}; \bar{\mathbf{R}}\right) \right\rangle_{\mathcal{V}_{R1}} \simeq \left\langle \rho^q\left(\mathbf{r}; \bar{\mathbf{R}}\right) \right\rangle_{\mathcal{V}_0} - \beta \left\langle \delta\rho^q\left(\mathbf{r}; \bar{\mathbf{R}}\right) \delta\Phi_{R1}\left(\bar{\mathbf{R}}\right) \right\rangle_{\mathcal{V}_0}, \tag{A.22}$$

156

Figure A.4: (a) Charge densities, (b) Gaussian-smoothed charge densities, (c) electrostatic potentials, and (d) probability distributions of θ_{OH} for SPC/E and GT water models, as well as GT water in the presence of the electrostatic LMF around a purely repulsive spherical solute of radius $R_{\mathrm{HS}} \approx 20$ Å.

where
$$\delta\rho^q\left(\mathbf{r};\bar{\mathbf{R}}\right) \equiv \rho^q\left(\mathbf{r};\bar{\mathbf{R}}\right) - \left\langle\rho^q\left(\mathbf{r};\bar{\mathbf{R}}\right)\right\rangle_{\mathcal{V}_0}$$
and
$$\delta\Phi_{\mathrm{R1}}\left(\bar{\mathbf{R}}\right) \equiv \Phi_{\mathrm{R1}}\left(\bar{\mathbf{R}}\right) - \left\langle\Phi_{\mathrm{R1}}\left(\bar{\mathbf{R}}\right)\right\rangle_{\mathcal{V}_0}.$$

Now, instead of iterating the LMF equation to self-consistency using simulations, we can iterate using Equation A.22 in conjunction with the LMF Equation until convergence of a new LMF is obtained. This technique, schematically depicted in Figure A.2b, is far more efficient than iterating the LMF equation using simulations, and was used to perform the LMF simulations discussed in this work.

The charge density obtained from iteration of the LMF equation via linear response theory (LRT) is compared to that of the SPC/E and GT water models in Figure A.3a. Although $\rho^q(r)$ obtained from LRT is much noisier than those of the SPC/E and GT models, near quantitative agreement with the SPC/E model is observed, especially in the height of the first peak. Upon Gaussian-smoothing, $\rho^{q\sigma}(r)$ from LRT is found to be in much better agreement with SPC/E than that of the GT model in the absence of the renormalized field. Finally, the LMF $\mathcal{V}_{\mathrm{R}}(r)$ obtained from iteration via LRT (scheme shown in Figure A.2b) is shown in Figure A.3c. This field is used to obtain the results shown for the LMF system in the next section.

A.3.2 Comparison with the full system

Finally, we perform a simulation of the truncated system, GT water, in the presence of the converged LMF in order to obtain equilibrium properties of the system. Th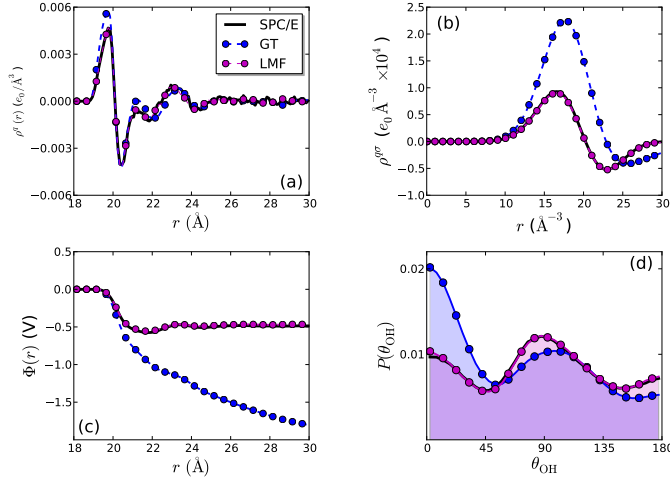e charge densities, Gaussian-smoothed charge densities, electrostatic potentials, and probability distributions of θ_{OH} are shown in Figure A.4 for SPC/E and GT water, as well as GT water in the presence of the electrostatic LMF depicted in Figure A.3c. We find that the inclusion of the renormalized potential $\mathcal{V}_R(r)$ leads to properties in quantitative agreement with the full SPC/E system. The quantities obtained from the LMF system were averaged over 20,000 configurations equally spaced over a 1 ns simulation.

$\mathcal{B}$

Derivation of the Bethe Potential

Consider a neutral system with zero dipole and traceless quadrupole moments, but nonzero second moment tensor, or equivalently, nonzero primitive quadrupole tensor. We seek to evaluate the average potential over the cell, defined as

$$\langle \overline{\phi}_V \rangle = \left\langle \frac{1}{V} \int_{\text{cell}} \phi(\mathbf{r}; \overline{\mathbf{R}}) \right\rangle = \left\langle \lim_{k \to 0} \hat{\phi}(\mathbf{k}; \overline{\mathbf{R}}) \right\rangle, \tag{B.1}$$

where $\hat{\phi}(\mathbf{k}; \overline{\mathbf{R}})$ indicates the Fourier transform of $\phi(\mathbf{r}; \overline{\mathbf{R}})$. Using Poisson's equation, the average potential over the volume of the cell can be written as

$$\langle \overline{\phi}_V \rangle = \left\langle \lim_{k \to 0} \frac{4\pi}{k^2} \hat{\rho}^q(\mathbf{k}; \overline{\mathbf{R}}) \right\rangle. \tag{B.2}$$

159

Since we are interested in the behavior of the potential in the limit that the wavevector k approaches zero, we can expand the Fourier transform of the charge density for small k:

$$
\begin{aligned}
\langle \hat{\rho}^q(\mathbf{k}; \overline{\mathbf{R}}) \rangle &= \left\langle \frac{1}{V} \int d\mathbf{r} e^{-i\mathbf{k}\cdot\mathbf{r}} \rho^q(\mathbf{r}; \overline{\mathbf{R}}) \right\rangle \\
&\sim \left\langle \frac{1}{V} \int d\mathbf{r} \rho^q(\mathbf{r}; \overline{\mathbf{R}}) \left[1 - i\mathbf{k}\cdot\mathbf{r} - \frac{1}{2}(\mathbf{k}\cdot\mathbf{r})^2 \right] \right\rangle \\
&= \frac{1}{V} \left[\mathcal{M}(0) - \mathbf{k}\cdot\mathcal{M}(1) - \mathbf{k}\otimes\mathbf{k} : \mathcal{M}(2) \right],
\end{aligned}
\tag{B.3}
$$

where $\otimes$ is a symmetric outer product, $\mathbf{A} : \mathbf{B}$ indicates the Frobenius inner product of the tensors $\mathbf{A}$ and $\mathbf{B}$, and $\mathcal{M}(n)$ is the ensemble averaged nth multipole moment of the charge distribution, which is a rank n tensor, as detailed in Appendix E.1.

The conditions of neutrality and zero dipole moment lead to $\mathcal{M}(0) = 0$ and $\mathcal{M}(1) = 0$, so that the charge density at small k can be written as

$$
\langle \hat{\rho}^q(\mathbf{k}; \overline{\mathbf{R}}) \rangle \approx -\frac{1}{V}\mathbf{k}\otimes\mathbf{k} : \mathcal{M}(2).
\tag{B.4}
$$

If the second moment tensor is nonzero, but the traceless quadrupole moment is zero, this means that $\mathcal{M}(2)$ is diagonal,

$$
\mathcal{M}(2) = \begin{pmatrix} \mathcal{M}_{xx} & 0 & 0 \\ 0 & \mathcal{M}_{yy} & 0 \\ 0 & 0 & \mathcal{M}_{zz} \end{pmatrix}.
\tag{B.5}
$$

Now, noting that the diagonal components of $\mathbf{k}\otimes\mathbf{k}$ are given by $(\mathbf{k}\otimes\mathbf{k})_{ii} = k^2/3$, we can perform the tensor product in Equation B.4 and arrive at

$$
\langle \hat{\rho}^q(\mathbf{k}; \overline{\mathbf{R}}) \rangle \approx -\frac{1}{3}\frac{k^2}{2V} \int d\mathbf{r} r^2 \langle \rho^q(\mathbf{r}; \overline{\mathbf{R}}) \rangle = -\frac{1}{3}k^2 T,
\tag{B.6}
$$

where T is the trace of the second moment tensor $\mathcal{M}(2)$. Using this expression, Equation B.2 becomes

$$
\langle \overline{\phi}_V \rangle = -\frac{4\pi}{3}T = \phi_{\text{Bethe}}.
\tag{B.7}
$$

Ion Solvation from Potential Distribution Theory

We can arrive at an expression for $\Delta\mu_Q$ using the potential distribution theory (PDT) framework. PDT yields the free energy of charging as an exponential average:

$$
\begin{aligned}
e^{-\beta\Delta\mu_Q} &= \left\langle e^{-\beta\Psi(\overline{\mathbf{R}})} \right\rangle_0 = \left\langle \exp\left[-\beta Q\phi(0;\overline{\mathbf{R}}) + \frac{\beta Q}{V}\int d\mathbf{r}\,\phi(\mathbf{r};\overline{\mathbf{R}}) \right] \right\rangle_0 \\
&= \left\langle e^{-\beta Q\phi_{\mathrm{Bethe}}} e^{-\beta Q\Delta\phi(0;\overline{\mathbf{R}})} e^{\beta Q\phi_{\mathrm{Bethe}}} \right\rangle_0 = \left\langle e^{-\beta Q\Delta\phi(0;\overline{\mathbf{R}})} \right\rangle_0,
\end{aligned}
\tag{C.1}
$$

or equivalently,

$$
\Delta\mu_Q = -k_{\mathrm{B}}T\ln\left\langle e^{-\beta Q\Delta\phi(0;\overline{\mathbf{R}})} \right\rangle_0,
\tag{C.2}
$$

where $\langle \cdots \rangle_0$ indicates an ensemble average performed over the system with no charge present.

Equivalently, one could use the inverse form of PDT, $e^{-\beta\Delta\mu_Q} = \left\langle e^{\beta\Psi(\mathbf{R})} \right\rangle_Q^{-1}$, where the ensemble average is performed over configurations sampled with a charge of magnitude Q present in the system (and its neutralizing background). This yields

$$
\Delta\mu_Q = k_{\mathrm{B}}T\ln\left\langle e^{\beta Q\Delta\phi(0;\overline{\mathbf{R}})} \right\rangle_Q.
\tag{C.3}
$$

Like the coupling parameter formula 4.18, these PDT expressions for the free energy are formally exact. However, in practice such exponential averages are difficult to evaluate. Linearization of the exponential terms and averaging the two forms for $\Delta\mu_Q$ permits the evaluation of approximate expressions for the free energy of the form

$$\Delta\mu_Q \approx \frac{1}{2}\left[\left\langle Q\Delta\phi(0;\overline{\mathbf{R}})\right\rangle_0 + \left\langle Q\Delta\phi(0;\overline{\mathbf{R}})\right\rangle_Q\right],\tag{C.4}$$

which is only appropriate when the distribution of $\Delta\phi(0;\overline{\mathbf{R}})$ is a Gaussian, and this may not be true in general.

It is important to note that the quantity appearing in both expressions for the free energy from PDT involve only the portion of the solvent electrostatic potential that is induced by the solute. In fact, this is the exact quantity that appears in the averages that are integrated over in the coupling parameter integration expression for the free energy Equation 4.18, and the PDT-based Gaussian approximation to the free energy is just the average of the end points in the λ-integration. However, such Gaussian approximations are not valid in general, and exponential averages like Equations C.2 and C.3, while easy to derive and formally exact, are much more difficult to evaluate than Equation 4.18. More specifically, charging a neutral cavity to a charge Q typically induces a large structural change that strongly orients interfacial water molecules. Such large structural changes are typically nonlinear, and we can expect Gaussian approximations like Equation C.4 to be less accurate than similar equations describing the turning on of LJ attractions, for example. Therefore, the λ-integration form of the free energy in Equation 4.18 may be more practical when evaluating such free energies from simulation.

$\mathcal{D}$
Derivation of Equation 4.6

The Bethe potential is defined as

$$\phi_{\text{Bethe}} = -\frac{4\pi}{3}T = -\frac{4\pi}{3}\frac{1}{2}\left\langle \frac{1}{V}\int d\mathbf{r}\rho^q(\mathbf{r};\overline{\mathbf{R}})r^2 \right\rangle. \tag{D.1}$$

We can now use the definition of the classical charge density, $\rho^q(\mathbf{r};\overline{\mathbf{R}}) = \sum_{i=1}^{M} q_i\delta(\mathbf{r}-\mathbf{r}_i(\overline{\mathbf{R}}))$, where there are M charges in the system with spatial coordinates $\mathbf{r}_i(\overline{\mathbf{R}})$. The Bethe potential can then be written as

$$\phi_{\text{Bethe}} = -\frac{4\pi}{3}\frac{1}{2}\left\langle \frac{1}{V}\int d\mathbf{r}\sum_{i=1}^{M} q_i\delta(\mathbf{r}-\mathbf{r}_i(\overline{\mathbf{R}}))r^2 \right\rangle = -\frac{4\pi}{3}\frac{1}{2}\left\langle \frac{1}{V}\sum_{i=1}^{M} q_ir_i^2(\overline{\mathbf{R}}) \right\rangle. \tag{D.2}$$

We can now split the sum over M charges into a sum over N molecules, indexed by $n = 1, ..., N$, and Γ charged sites per molecule, indexed by $\gamma = 1, ..., \Gamma$. Each charge q_γ will have a position $\mathbf{r}_\gamma$, which is equivalent to the $\mathbf{r}_i$ used above. The Bethe potential can then be written as

$$\phi_{\text{Bethe}} = -\frac{4\pi}{3}\frac{1}{2}\left\langle \frac{1}{V}\sum_{n=1}^{N}\sum_{\gamma=1}^{\Gamma} q_\gamma r_\gamma^2(\overline{\mathbf{R}}) \right\rangle. \tag{D.3}$$

At this point, we make the coordinate transformation $\mathbf{r}_\gamma^2 = |\mathbf{r}_{\gamma n} - \mathbf{r}_n|^2$, where $\mathbf{r}_n$ is the location of the
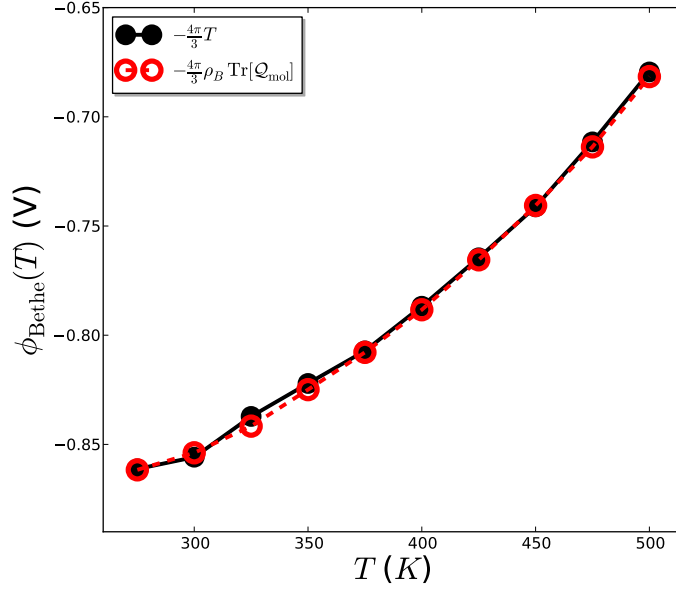
Figure D.1: Bethe potential $\phi_{\mathrm{Bethe}}(T)$ as a function of temperature for the SPC/E model along the $P = 1$ atm isobar computed using Equation 4.3 and Equation 4.6. Error bars are smaller than the symbol size.

center of molecule n and $\mathbf{r}_{\gamma n}$ is the location of site γ relative to the center of molecule n. Making this transformation, we obtain

$$
\begin{aligned}
\phi_{\mathrm{Bethe}} &= -\frac{4\pi}{3}\frac{1}{2}\left\langle \frac{1}{V}\sum_{n=1}^{N}\sum_{\gamma=1}^{\Gamma} q_\gamma \left|\mathbf{r}_{\gamma n} - \mathbf{r}_n\right|^2 \right\rangle \\
&= -\frac{4\pi}{3}\frac{1}{2}\left\{ \left\langle \frac{1}{V}\sum_{n=1}^{N}\sum_{\gamma=1}^{\Gamma} q_\gamma r_{\gamma n}^2 \right\rangle + \left\langle \frac{1}{V}\sum_{n=1}^{N} r_n^2 \left(\sum_{\gamma=1}^{\Gamma} q_\gamma\right) \right\rangle \right. \\
&\quad \left. - 2\left\langle \frac{1}{V}\sum_{n=1}^{N} r_n \sum_{\gamma=1}^{\Gamma} q_\gamma r_{\gamma n}\cos\theta \right\rangle \right\},
\end{aligned}
\tag{D.4}
$$

where θ is the angle form by the vectors $\mathbf{r}_{\gamma n}$ and $\mathbf{r}_n$ and we have omitted the dependence of the distances on $\overline{\mathbf{R}}$ for convenience.

164

The second term in Equation D.4 vanishes due to neutrality, $\sum_{\gamma=1}^{\Gamma} q_\gamma = 0$. The third term also vanishes because the average dipole moment of the cell is zero. Therefore, the Bethe potential can be written as

$$\phi_{\text{Bethe}} = -\frac{4\pi}{3} \frac{1}{2} \left\langle \frac{1}{V} \sum_{n=1}^{N} \sum_{\gamma=1}^{\Gamma} q_\gamma r_{\gamma n}^2 \right\rangle. \tag{D.5}$$

At this point, we note that

$$\sum_{\gamma=1}^{\Gamma} q_\gamma r_{\gamma n}^2 (\overline{\mathbf{R}}) = \sum_{\gamma=1}^{\Gamma} q_\gamma r_{\gamma 1}^2 (\overline{\mathbf{R}}) \; \forall \, n, \overline{\mathbf{R}}, \tag{D.6}$$

i.e. the molecular quadrupole moments are the same for all molecules independent of configuration in the case of rigid molecular models like SPC/E and TIP5P water. Therefore, our final result for the Bethe potential is

$$
\begin{aligned}
\phi_{\text{Bethe}} &= -\frac{4\pi}{3} \frac{1}{2} \left\langle \frac{1}{V} \sum_{n=1}^{N} \sum_{\gamma=1}^{\Gamma} q_\gamma r_{\gamma 1}^2 \right\rangle = -\frac{4\pi}{3} \frac{1}{2} \left\langle \frac{N}{V} \right\rangle \sum_{\gamma=1}^{\Gamma} q_\gamma r_{\gamma 1}^2 \\
&= -\frac{4\pi}{3} \rho_{\text{B}} \frac{1}{2} \sum_{\gamma=1}^{\Gamma} q_\gamma r_{\gamma 1}^2 = -\frac{4\pi}{3} \rho_{\text{B}} \, \text{Tr} \left\{ \mathcal{Q}_{\text{mol}} \right\},
\end{aligned} \tag{D.7}
$$

which is Equation 4.6. In the case of rigid intramolecular charge distributions, Equation 4.6 is completely equivalent to Equation 4.3, as shown in Figure D.1, although the latter is always valid.

$\mathcal{E}$

LMF-Based Multipole Expansions

E.1   Multipole Moment Expansion of Gaussian-Smoothed Charge Densities

Here I present the multipole expansion for the Gaussian-smoothed charge density, $\rho^{q\sigma}(\mathbf{r})$, and how it relates to that of the bare charge density $\rho^{q}(\mathbf{r})$. We consider first the energy of interaction between two d-dimensional Gaussian-smoothed charge densities, with centers $\mathbf{r}_i$ and $\mathbf{r}_j$, where the position vector is defined by

$$\mathbf{r} = (x_1, x_2, ..., x_d), \tag{E.1}$$

and $d \in \mathbb{N}$. The interaction energy of the two charge distributions under consideration, $\rho_i^{q\sigma}(\mathbf{r}_i)$ and $\rho_j^{q\sigma}(\mathbf{r}_j)$, respectively, is assumed to be of the form

$$w(\mathbf{r}_{ij}) = \int d\mathbf{r} \int d\mathbf{r}' \rho_i^{q\sigma}(\mathbf{r} - \mathbf{r}_i) \rho_j^{q\sigma}(\mathbf{r}' - \mathbf{r}_j) \frac{1}{\epsilon |\mathbf{r} - \mathbf{r}'|}. \tag{E.2}$$

This interaction energy can be rewritten as a $\mathbf{k}$-space integral,

$$w(\mathbf{r}_{ij}) = \frac{1}{(2\pi)^d} \int d\mathbf{k} \hat{\rho}_i^{q\sigma}(-\mathbf{k}) \hat{\rho}_j^{q\sigma}(\mathbf{k}) e^{-i\mathbf{k}\cdot\mathbf{r}_{ij}} \frac{4\pi}{\epsilon k^2}, \tag{E.3}$$

where we have defined the d-dimensional Fourier transform and inverse Fourier transform of a function f as

$$\hat{f}(\mathbf{k}) = \int d\mathbf{r} e^{-i\mathbf{k}\cdot\mathbf{r}} f(r)$$

and

$$f(\mathbf{r}) = \frac{1}{(2\pi)^d} \int d\mathbf{k} e^{i\mathbf{k}\cdot\mathbf{r}} \hat{f}(\mathbf{k}),$$

respectively.

Now we want to examine the asymptotic behavior as $k \to 0$, so we Tayor expand the smoothed charge densities about $k = 0$ as

$$\hat{\rho}_i^{q\sigma}(\mathbf{k}) = \sum_{n_i} \frac{1}{n_i!} \mathbf{k}^{n_i} \cdot \nabla_{\mathbf{k}}^{n_i} \hat{\rho}_i^{q\sigma}(0), \tag{E.4}$$

where $\nabla_{\mathbf{k}}$ is the d-dimensional gradient with respect to k. We can then insert E.4 into E.3 to obtain

$$w(\mathbf{r}_{ij}) = \sum_{n_i,n_j} \frac{1}{n_i!n_j!} \left[\nabla_{\mathbf{k}}^{n_i} \hat{\rho}_i^{q\sigma}(0) \cdot (-i\nabla_{\mathbf{r}})^{n_i}\right] \cdot \left[\nabla_{\mathbf{k}}^{n_j} \hat{\rho}_j^{q\sigma}(0) \cdot (i\nabla_{\mathbf{r}})^{n_j}\right] \frac{1}{\epsilon r} \tag{E.5}$$

Now, we can define

$$\frac{i^{n_i}}{n_i!} \nabla_{\mathbf{k}}^{n_i} \hat{\rho}_i^{q\sigma}(0) \equiv \mathcal{M}_i^{\sigma}(n_i), \tag{E.6}$$

such that

$$\mathcal{M}_i^{\sigma}(n_i) = \frac{1}{n_i!} \int d\mathbf{r} \rho_i^{q\sigma}(\mathbf{r}) \mathbf{r}^{n_i}, \tag{E.7}$$

and $\mathcal{M}^{\sigma}(n)$ is the nth multipole moment of the smoothed charge distribution. Finally, we can rewrite E.5 as

$$w(\mathbf{r}_{ij}) = \sum_{n_i,n_j} \left[\mathcal{M}_i^{\sigma}(n_i) \cdot (-\nabla_{\mathbf{r}})^{n_i}\right] \cdot \left[\mathcal{M}_j^{\sigma}(n_j) \cdot \nabla_{\mathbf{r}}^{n_j}\right] \frac{1}{\epsilon r} \tag{E.8}$$

so that the energy is now expressed in terms of the multipole moments of the smoothed charge distributions.

One may then inquire into how these multipole moments relate to those of the bare charge densities, $\rho^q(\mathbf{r})$. In order to evaluate these expressions, we first consider the Fourier transform of the smoothed charge density, which, using the convolution theorem, can be written as

$$\hat{\rho}^{q\sigma}(\mathbf{k}) = \hat{\rho}^q(\mathbf{k})\hat{\rho}_G(\mathbf{k}), \tag{E.9}$$

where

$$\hat{\rho}_G(\mathbf{k}) = e^{-\frac{k^2\sigma^2}{4}}. \tag{E.10}$$

In general, the nth order multipole moment $\mathcal{M}^\sigma(n)$ is given by

$$\mathcal{M}^\sigma(n) = \frac{i^n}{n!} \sum_{m=0}^{n} \binom{n}{m} \hat{\rho}^{q(n-m)}(0) \otimes \hat{\rho}_G^{(m)}(0), \tag{E.11}$$

where $\hat{f}^{(n)}(0) = \left[\nabla_{\mathbf{k}}^n \hat{f}(\mathbf{k})\right]\Big|_{k=0}$ is a tensor of rank n, $\otimes$ indicates a symmetric outer product, and

$$\binom{n}{m} = \frac{n!}{m!(n-m)!}$$

is the binomial coefficient.

The gradients of the $\mathbf{k}$-space Gaussian function are given by

$$\hat{\rho}_G^{(n)}(\mathbf{k}) = (-1)^n e^{-k^2\sigma^2/4} \mathbf{H}_n\left(\frac{\mathbf{k}\sigma}{2}\right), \tag{E.12}$$

such that $\mathbf{H}_n(a\mathbf{x})$ is a rank n tensor-analog of the Hermite functions with elements

$$H_{ij\cdots v}(a\mathbf{x}; n) = (-1)^n e^{a^2\mathbf{x}^2} \frac{\partial^n}{\partial x_i \partial x_j \cdots \partial x_v}\left(e^{-a^2\mathbf{x}^2}\right), \tag{E.13}$$

where a is a constant and $\mathbf{x} = (x_1, x_2, ..., x_d)$ is a general d-dimensional vector.

All odd derivatives of $\hat{\rho}_G(\mathbf{k})$ will vanish at $k = 0$ due to symmetry, therefore, we can rewrite E.11 as

$$\mathcal{M}^\sigma(n) = \frac{i^n}{n!} \sum_{\substack{m=0 \\ m \in \mathbb{E}}}^{n} (-1)^m \binom{n}{m} \hat{\rho}^{q(n-m)}(0) \otimes \mathbf{A}_m\left(\frac{\sigma}{2}\right), \tag{E.14}$$

where $\mathbf{A}_m(a) \equiv \left[\mathbf{H}_m(a\mathbf{k})\right]\big|_{k=0}$ and $\mathbb{E} = \{x \mid x \text{ is an even whole number}\}$. Equation E.14 can be written in the equivalent form

$$\mathcal{M}^\sigma(n) = \mathcal{M}(n) + \sum_{\substack{m=2 \\ m \in \mathbb{E}}}^{n} \frac{(-1)^m i^m}{m!} \mathcal{M}(n-m) \otimes \mathbf{A}_m\left(\frac{\sigma}{2}\right), \tag{E.15}$$

making the relation between $\mathcal{M}^\sigma(n)$ and $\mathcal{M}(n)$ apparent.

In order for the condition $\mathcal{M}^\sigma(n) = \mathcal{M}(n)$ to hold, where $\mathcal{M}(n)$ is the nth multipole moment of

168

the bare charge distribution ρ^q, all multipoles of order less than $n - 1$ and of even (odd) order, for n even (odd), of the bare charge density must be identically zero,

$$\mathcal{M}^\sigma(n) = \mathcal{M}(n) \iff \mathcal{M}(s) = 0 \ \forall \ s = n - l, \tag{E.16}$$

where

$$l = \begin{cases} 2, 4, 6, ..., n; & \text{for } n \text{ even} \\ 2, 4, 6, ..., n - 1; & \text{for } n \text{ odd.} \end{cases} \tag{E.17}$$

Now, we present the first few multipole moments of the Gaussian-smoothed charge density in order to explicitly illustrate their relation to that of the bare charge density. The monopole moment of $\rho^{q\sigma}$ is trivially given by $\mathcal{M}^\sigma(0) = \mathcal{M}(0)$, and note that for neutral charge distributions the monopole moment is zero. The dipole moment, $n = 1$, is also trivially given by

$$\mathcal{M}^\sigma(1) = \mathcal{M}(1),$$

illustrating that the dipole moment of ρ^q is conserved upon Gaussian-smoothing. In addition, the quadrupole moment is given by

$$\begin{aligned} \mathcal{M}^\sigma(2) &= \mathcal{M}(2) - \frac{1}{2}\mathcal{M}(0) \otimes \mathbf{A}_2\left(\frac{\sigma}{2}\right) \\ &= \mathcal{M}(2) + \frac{\sigma^2}{4}\mathcal{M}(0)\mathbf{I}_3, \end{aligned} \tag{E.18}$$

where $\mathbf{I}_n$ is the $n \times n$ identity matrix. For neutral charge distributions, like non-ionic molecular charge distributions, both the dipole *and* quadrupole moments are conserved upon Gaussian-smoothing.

E.2 Multipole Moment Expansion of SR Charge Densities

The multipole expansion of the SR charge density $\rho^{qc}(\mathbf{r})$ proceeds in a manner analogous to the previous section. In order to keep this section brief, only the main points of the derivation are quoted herein.

The n*th* order multipole of $\rho^{qc}(\mathbf{r})$ is given by

$$\mathcal{M}^c(n) = \frac{i^n}{n!}\sum_{m=0}^{n}\binom{n}{m}\hat{\rho}^{q(n-m)}(0) \otimes \hat{\rho}_c^{(m)}(0), \tag{E.19}$$

where $\hat{\rho}_c(\mathbf{k}) = 1 - \hat{\rho}_G(\mathbf{k})$. Now, note that $\hat{\rho}_c(0) = 0$, and the gradients of $\hat{\rho}_c$ are given by $\nabla_\mathbf{k}^n \hat{\rho}_c(\mathbf{k}) = -\nabla_\mathbf{k}^n \hat{\rho}_G(\mathbf{k})$ for $n > 0$.

The multipoles of the SR charge density can finally be written as

$$\mathcal{M}^c(n) = \sum_{\substack{m=2 \\ m\in\mathbb{E}}}^{n} \frac{(-1)^{m+1}i^m}{m!}\mathcal{M}(n-m)\otimes\mathbf{A}_m\left(\frac{\sigma}{2}\right), \tag{E.20}$$

where the reader should note that the sum runs from $m = 2$ to n, illustrating that the SR charge density distribution contains *no monopole and dipole moments*. The first three moments are given by $\mathcal{M}^c(0) = 0$, $\mathcal{M}^c(1) = 0$, and

$$\mathcal{M}^c(2) = -\frac{\sigma^2}{4}\mathcal{M}(0)\mathbf{I}_3, \tag{E.21}$$

illustrating that the moments $\mathcal{M}^c(n)$ contain the portions of the multipoles that modify the bare multipoles upon Gaussian smoothing, as detailed in the previous section.

E.3 Gaussian Smoothing of a Molecule of SPC/E Water

In order to illustrate the conditions derived above, we consider Gaussian smoothing a single SPC/E water molecule, something that can be done analytically. The SPC/E model of water consists of three charged sites, all in the same plane, such that the coordinates of the oxygen, hydrogen 1, and hydrogen 2 are given by $\vec{r} = (0,0,0)$, $\vec{r}_{H_1} = (r_{OH}\sin\phi, 0, r_{OH}\cos\phi)$, and $\vec{r}_{H_2} = (-r_{OH}\sin\phi, 0, r_{OH}\cos\phi)$, respectively, where $\phi = \theta/2$ is half of the H-O-H angle $\theta = 109.47°$. The hydrogen sites each have charge q, while the oxygen has charge $-2q$, such that the molecule is neutral.

The charge density is given by

$$\rho^q(\mathbf{r}) = q\delta(\vec{r} - \vec{r}_{H_1}) + q\delta(\vec{r} - \vec{r}_{H_2}) - 2q\delta(\vec{r}), \tag{E.22}$$

which has the corresponding Gaussian smoothed charge density

$$\begin{aligned}\rho^{q\sigma}(\mathbf{r}) &= \frac{1}{\sigma^3\pi^{3/2}}\left\{ q\exp\left[-\left(\frac{|\vec{r} - \vec{r}_{H_1}|}{\sigma}\right)^2\right]\right.\\ &\quad + \left. q\exp\left[-\left(\frac{|\vec{r} - \vec{r}_{H_2}|}{\sigma}\right)^2\right] - 2q\exp\left[-\left(\frac{|\vec{r}|}{\sigma}\right)^2\right]\right\}.\end{aligned} \tag{E.23}$$

Knowing the charge densities, we can evaluate the bare and smoothed multipoles. The zeroth moment, or total charge, is trivially given by

$$\mathcal{M}(0) = \int d\mathbf{r}\rho^q(\mathbf{r}) = 0 = \mathcal{M}^\sigma(0). \tag{E.24}$$

170

The dipole moment, $\mathcal{M}(1) = (\mathcal{M}_x, \mathcal{M}_y, \mathcal{M}_z)$, has components

$$
\begin{aligned}
\mathcal{M}_x &= \int dx x \int dy \int dz \rho^q(x, y, z) = q(x_{H_1} + x_{H_2}) = 0 \\
\mathcal{M}_y &= \int dx \int dy y \int dz \rho^q(x, y, z) = 0 \\
\mathcal{M}_z &= \int dx \int dy \int dz z \rho^q(x, y, z) = q(z_{H_1} + z_{H_2}) = 2q z_H,
\end{aligned}
$$

where $z_H \equiv z_{H_1} = z_{H_2}$ and $x_{H_1} = -x_{H_2} \equiv x_H$. Performing the same integrations for $\rho^{q\sigma}$ yields $\mathcal{M}_x^\sigma = \mathcal{M}_x$, $\mathcal{M}_y^\sigma = \mathcal{M}_y$, and $\mathcal{M}_z^\sigma = \mathcal{M}_z$. Similarly, the bare and smoothed quadrupole moment tensors are found to be equivalent. The first moment that is modified by smoothing is the octupole, and therefore we focus on that now.

Two nonzero components of the bare octupole tensor $\mathcal{M}(3)$ are given by

$$
\begin{aligned}
\mathcal{M}_{xxz} &= \frac{1}{6} \int dx x^2 \int dy \int dz z \rho^q(x, y, z) = \frac{q}{3} x_H^2 z_H \\
\mathcal{M}_{zzz} &= \frac{1}{6} \int dx \int dy \int dz z^3 \rho^q(x, y, z) = \frac{q}{3} z_H^3.
\end{aligned} \tag{E.25}
$$

The same moments of the smoothed octupole tensor $\mathcal{M}^\sigma(3)$ are given by

$$
\begin{aligned}
\mathcal{M}_{xxz}^\sigma &= \frac{1}{6} \int dx x^2 \int dy \int dz z \rho^{q\sigma}(x, y, z) = \frac{q}{3} x_H^2 z_H + \frac{q \sigma^2 z_H}{6} \\
&= \mathcal{M}_{xxz} + \frac{\sigma^2}{4} \frac{\mathcal{M}_z}{3},
\end{aligned} \tag{E.26}
$$

and

$$
\begin{aligned}
\mathcal{M}_{zzz}^\sigma &= \frac{1}{6} \int dx \int dy \int dz z^3 \rho^{q\sigma}(x, y, z) = \frac{q z_H^3}{3} + \frac{\sigma^2 q z_H}{2} \\
&= \mathcal{M}_{zzz} + \frac{\sigma^2}{4} \mathcal{M}_z.
\end{aligned} \tag{E.27}
$$

This illustrates that the octupole moment is indeed modified nontrivially in terms of the dipole moment upon Gaussian smoothing of the charge density, but is this modification consistent with the general form of $\mathcal{M}^\sigma(n)$ presented above?

From Equation E.15, we can write

$$
\mathcal{M}^\sigma(3) = \mathcal{M}(3) - \frac{1}{2} \mathcal{M}(1) \otimes \mathbf{A}_2 \left(\frac{\sigma}{2} \right), \tag{E.28}
$$

where $\mathbf{A}_2(a) = -2a^2\mathbf{I}_3$. Now we define $\mathbf{T} \equiv \mathcal{M}(1) \otimes \mathbf{A}_2\left(\frac{\sigma}{2}\right)$ as the rank 3 tensor formed by the symmetric outer product of $\mathcal{M}(1)$ and $\mathbf{A}_2\left(\frac{\sigma}{2}\right)$. The xxz and zzz components of this tensor are given by

$$
\begin{aligned}
T_{xxz} &= \frac{1}{3}\mathcal{M}_z A_{xx} = -\frac{\sigma^2}{2}\frac{\mathcal{M}_z}{3} \\
T_{zzz} &= \mathcal{M}_z A_{zz} = -\frac{\sigma^2}{2}\mathcal{M}_z.
\end{aligned}
\tag{E.29}
$$

Inserting these expressions for the components of $\mathbf{T}$ into the relation for $\mathcal{M}^\sigma(3)$ yields the smoothed octupole components

$$
\mathcal{M}^\sigma_{xxz} = \mathcal{M}_{xxz} + \frac{\sigma^2}{4}\frac{\mathcal{M}_z}{3}
\tag{E.30}
$$

$$
\mathcal{M}^\sigma_{zzz} = \mathcal{M}_{zzz} + \frac{\sigma^2}{4}\mathcal{M}_z,
\tag{E.31}
$$

consistent with the results presented above.

E.4   Point Charge Distribution

In this section, we further illustrate the above conclusions by considering a single point charge of magnitude Q, such that the bare charge density of interest is given by

$$
\rho^q(\mathbf{r}) = Q\delta(\mathbf{r}).
\tag{E.32}
$$

The point charge density is split into SR and LR portions, then the multipole expansion is performed. The SR and LR portions of a point charge are given by

$$
\rho^{qc}(\mathbf{r}) = Q\delta(\mathbf{r}) - Q\rho_G(\mathbf{r})
\tag{E.33}
$$

and

$$
\rho^{q\sigma}(\mathbf{r}) = Q\rho_G(\mathbf{r}),
\tag{E.34}
$$

respectively, where

$$
\rho_G(\mathbf{r}) = \frac{1}{\sigma^3\pi^{3/2}}e^{-\frac{r^2}{\sigma^2}}
\tag{E.35}
$$

is a normalized Gaussian distribution ($\int d\mathbf{r}\rho_G(\mathbf{r}) = 1$).

   In general, we can use the results of Appendix E.2 to determine the multipole moments of $\rho^{qc}(\mathbf{r})$, but the charge density is simple enough to readily evaluate the first three moments. The monopole

moment of $\rho^{qc}(\mathbf{r})$ is given by

$$\mathcal{M}^c_{\mathrm{PC}}(0) = \int d\mathbf{r}\rho^{qc}(\mathbf{r}) = Q \int d\mathbf{r}\delta(\mathbf{r}) - Q \int d\mathbf{r}\rho_G(\mathbf{r}) = Q - Q = 0, \qquad (E.36)$$

illustrating that the SR charge density is *neutral*. The dipole moment is also zero:

$$\mathcal{M}^c_{\mathrm{PC}}(1) = Q \int d\mathbf{rr}\delta(\mathbf{r}) - Q \int d\mathbf{rr}\rho_G(\mathbf{r}) = \mathbf{0} - \mathbf{0} = \mathbf{0}. \qquad (E.37)$$

As can be expected from Appendix E.2, the first nonzero moment will be the quadrupole moment. The diagonal components of the quadrupole tensor are given by

$$\mathcal{M}^c_{ii} = \frac{Q}{2} \int d\mathbf{r}x_i^2\delta(\mathbf{r}) - \frac{Q}{2} \int d\mathbf{r}x_i^2\rho_G(\mathbf{r}) = 0 - \frac{\sigma^2}{4}Q, \qquad (E.38)$$

and the off-diagonal elements are zero, such that the components of the quadrupole tensor are given by $\mathcal{M}^c_{ij} = -\delta_{ij}Q\sigma^2/4$, where δ_{ij} is the Kronecker delta function. Therefore, the quadrupole moment of the SR charge density is

$$\mathcal{M}^c_{\mathrm{PC}}(2) = -\frac{\sigma^2}{4}Q\mathbf{I}_3. \qquad (E.39)$$

All odd multipoles of the SR point charge density $\rho^{qc}(\mathbf{r})$ will vanish due to symmetry, and the even moments are in general given by the $m = n$ term of Equation E.20, a direct consequence of the only nonzero moment of $\rho^q(\mathbf{r})$ being the monopole.

The multipoles of the LR point charge density $\rho^{q\sigma}(\mathbf{r})$ can readily be obtained following Appendix E.1, but we can readily evaluate the first three moments for illustrative purposes. The monopole moment is given by

$$\mathcal{M}^\sigma_{\mathrm{PC}}(0) = \int d\mathbf{r}\rho^{q\sigma}(\mathbf{r}) = Q \int d\mathbf{r}\rho_G(\mathbf{r}) = Q, \qquad (E.40)$$

consistent with the idea that long-ranged electrostatics like neutrality, or in this case charge, are contained in the LR charge density. The dipole moment is again zero:

$$\mathcal{M}^\sigma_{\mathrm{PC}}(1) = \int d\mathbf{rr}\rho^{q\sigma}(\mathbf{r}) = \mathbf{0}. \qquad (E.41)$$

The discussion in Section III, as well as that in Appendix E.1, indicates that the smoothed quadrupole moment should be modified non-trivially in terms of the bare monopole. This quadrupole tensor is given simply by the negative of the SR quadrupole tensor,

$\mathcal{M}^{\sigma}_{\text{PC}}(2) = -\mathcal{M}^{c}_{\text{PC}}(2)$, which is a result specific to the special case of a bare charge distribution that has a non-zero bare monopole moment, but a zero bare quadrupole moment, as is the case for a point charge.

In general, for the very special case of taking a point charge as the bare charge distribution, all LR multipoles of order $n \geq 2$ are equal to the negative of the corresponding SR multipoles:

$$\mathcal{M}^{\sigma}_{\text{PC}}(n) = -\mathcal{M}^{c}_{\text{PC}}(n) \ \ \forall \ n \geq 2. \tag{E.42}$$

Note that this indicates that a Gaussian charge distribution not only has a nonzero monopole moment, but all even multipole moments of a Gaussian charge distribution are nonzero.

$\mathcal{F}$
Coupling Parameter Integration

We can also obtain the free energy of turning on the Gaussian charge distribution using coupling parameter integration. We first introduce a parameter λ which linearly couples to the field of the Gaussian charge,

$$v_Q^{(\lambda)}(r) = \lambda Q v_1(r) = \lambda v_Q(r), \tag{F.1}$$

so that a potential energy term,

$$\Psi_\lambda(\overline{\mathbf{R}}) = \sum_{i=1}^{N} q_i v_Q^{(\lambda)}(r_i(\overline{\mathbf{R}})) = \int d\mathbf{r} v_Q^{(\lambda)}(r)\rho^q(\mathbf{r}; \overline{\mathbf{R}}) \tag{F.2}$$

appears in the Hamiltonian.

Taking the derivative of the free energy

$$G_l(\lambda) \propto -k_{\mathrm{B}}T \ln \int d\overline{\mathbf{R}} e^{-\beta\mathcal{H}_0(\overline{\mathbf{R}})} e^{-\beta\Psi_\lambda(\overline{\mathbf{R}})}, \tag{F.3}$$

with respect to λ, where $\mathcal{H}_0$ is the portion of the Hamiltonian describing solvent-solvent interactions, we find the well known result

$$\frac{\partial G_l}{\partial \lambda} = \left\langle \frac{\partial \Psi_\lambda(\overline{\mathbf{R}})}{\partial \lambda} \right\rangle_\lambda \tag{F.4}$$

We can now integrate over the coupling parameter to arrive at

$$\Delta G_l = \int_0^1 d\lambda \int d\mathbf{r} \frac{dv_Q^{(\lambda)}(r)}{d\lambda} \rho_\lambda^q(\mathbf{r}) = \int_0^1 d\lambda \int d\mathbf{r} v_Q(r) \rho_\lambda^q(\mathbf{r}),$$ (F.5)

where $\rho_\lambda^q(\mathbf{r}) = \left\langle \rho^q(\mathbf{r}; \overline{\mathbf{R}}) \right\rangle_\lambda$.

At this point, we can utilize Equation 5.14 to write the charge density in state λ as

$$\rho_\lambda^q(\mathbf{r}) = -\lambda Q \left(1 - \frac{1}{\epsilon}\right) \frac{1}{l^3 \pi^{3/2}} e^{-r^2/l^2}.$$ (F.6)

We can now use Equation F.6 in Equation F.5, in conjunction with Parseval's theorem, to arrive at our final result

$$
\begin{aligned}
\Delta G_l &= -Q \left(1 - \frac{1}{\epsilon}\right) \int_0^1 d\lambda \lambda \int d\mathbf{r} v_Q(\mathbf{r}) \frac{e^{-r^2/l^2}}{l^3 \pi^{3/2}} \\
&= -\frac{Q^2}{2} \left(1 - \frac{1}{\epsilon}\right) \frac{1}{(2\pi)^3} \int d\mathbf{k} e^{-k^2 l^2/2} \frac{4\pi}{k^2} \\
&= -\frac{Q^2}{l\sqrt{2\pi}} \left(1 - \frac{1}{\epsilon}\right).
\end{aligned}
$$ (F.7)

$\mathcal{G}$

Further Consequences of Equation 5.7

Within the Gaussian approximation, a cumulant expansion of Equation 5.2 yields

$$
\begin{aligned}
\Delta G_l &= \left\langle \Psi(\overline{\mathbf{R}}) \right\rangle_0 - \frac{\beta}{2} \left\langle \left(\delta \Psi_0(\overline{\mathbf{R}}) \right)^2 \right\rangle_0 \\
&= \left\langle \Psi(\overline{\mathbf{R}}) \right\rangle_Q + \frac{\beta}{2} \left\langle \left(\delta \Psi_Q(\overline{\mathbf{R}}) \right)^2 \right\rangle_Q,
\end{aligned} \tag{G.1}
$$

where $\delta \Psi_{0/Q}(\overline{\mathbf{R}}) \equiv \Psi(\overline{\mathbf{R}}) - \left\langle \Psi(\overline{\mathbf{R}}) \right\rangle_{0/Q}$. When this approximation is valid,

$$
\left\langle \left(\delta \Psi_0(\overline{\mathbf{R}}) \right)^2 \right\rangle_0 = \left\langle \left(\delta \Psi_Q(\overline{\mathbf{R}}) \right)^2 \right\rangle_Q \equiv \left\langle \left(\delta \Psi(\overline{\mathbf{R}}) \right)^2 \right\rangle, \tag{G.2}
$$

where we will leave off the subscript due to the equality. Now, if we use the above result $\left\langle \Psi(\overline{\mathbf{R}}) \right\rangle_0 = 0$, we arrive at the following relation between the first and second cumulants,

$$
\left\langle \Psi(\overline{\mathbf{R}}) \right\rangle_Q = -\beta \left\langle \left(\delta \Psi(\overline{\mathbf{R}}) \right)^2 \right\rangle. \tag{G.3}
$$

This result can also be obtained utilizing Equation 5.8. We can write the energy in the presence of

the field as

$$\begin{aligned}
\langle \Psi(\overline{\mathbf{R}}) \rangle_Q &= \int d\mathbf{r} \rho_Q^q(\mathbf{r}) v_Q(r) \\
&= -\beta \int d\mathbf{r} \int d\mathbf{r}' \chi_0^{qq}(|\mathbf{r} - \mathbf{r}'|) v_Q(r) v_Q(r') \\
&= -\beta \int d\mathbf{r} \int d\mathbf{r}' \left\langle \delta\rho_0^q(\mathbf{r};\overline{\mathbf{R}}) \delta\rho_0^q(\mathbf{r}';\overline{\mathbf{R}}) \right\rangle_0 v_Q(r) v_Q(r').
\end{aligned} \tag{G.4}$$

Upon noting that $\delta\rho_0^q(\mathbf{r};\overline{\mathbf{R}}) = \rho^q(\mathbf{r};\overline{\mathbf{R}}) - \left\langle \rho^q(\mathbf{r};\overline{\mathbf{R}}) \right\rangle_0 = \rho^q(\mathbf{r};\overline{\mathbf{R}})$, we can write

$$\begin{aligned}
\langle \Psi(\overline{\mathbf{R}}) \rangle_Q &= -\beta \int d\mathbf{r} \int d\mathbf{r}' \left\langle \rho^q(\mathbf{r};\overline{\mathbf{R}}) \rho^q(\mathbf{r}';\overline{\mathbf{R}}) \right\rangle_0 v_Q(r) v_Q(r') \\
&= -\beta \left\langle \Psi^2(\overline{\mathbf{R}}) \right\rangle_0,
\end{aligned} \tag{G.5}$$

which is a specific form of Equation G.3, upon noting that $\left\langle \left(\delta\Psi(\overline{\mathbf{R}})\right)^2 \right\rangle_0 = \left\langle \Psi^2(\overline{\mathbf{R}}) \right\rangle_0$.

178

$\mathcal{H}$

Derivation of Equation 6.16 from Mean-Field Approximations to Equation 6.6

We can begin with Equation 6.14 and make the following mean-field (MF) approximations: the nonuniform pair density is approximated by

$$\rho_R^{(2)}(\mathbf{r}, \mathbf{r}') \approx \rho^{(2)}(\mathbf{r}, \mathbf{r}') \approx \rho(\mathbf{r})\rho(\mathbf{r}'), \tag{H.1}$$

the uniform pair density is given by

$$\rho_{B,R}^{(2)}(|\mathbf{r} - \mathbf{r}'|) \approx \rho_B^{(2)}(|\mathbf{r} - \mathbf{r}'|) \approx \rho_{\mathrm{B}}^2, \tag{H.2}$$

and the difference between the chemical potentials of the full and mimic systems is approximated by

$$\beta \left[\mu - \mu_{\mathrm{R}} \right] \approx -2\beta \rho_{\mathrm{B}} a, \tag{H.3}$$

where $a = -\int d\mathbf{r}' u_1(|\mathbf{r} - \mathbf{r}'|)$ is the van der Waals constant. Upon making these MF approximations, the λ integration may be performed over the path discussed in the text, and Equation 6.6 becomes

$$\beta\Omega_{\text{solv}}[\phi] - \beta\Omega_{\text{R,solv}}[\phi_{\text{R}}] = \frac{\beta}{2}\int d\mathbf{r}\int d\mathbf{r}' \left[\rho(\mathbf{r})\rho(\mathbf{r}') - \rho_{\text{B}}^2\right] u_1(|\mathbf{r} - \mathbf{r}'|)$$
$$- \beta\int d\mathbf{r}\rho(\mathbf{r})\left[\phi_{\text{R}}(\mathbf{r}) - \phi(\mathbf{r})\right]$$
$$+ 2\beta\rho_{\text{B}}a\int d\mathbf{r}\left[\rho(\mathbf{r}) - \rho_{\text{B}}\right]. \tag{H.4}$$

Now, note that $\phi_{\text{R}}(\mathbf{r}) - \phi(\mathbf{r}) = \int d\mathbf{r}' \left[\rho(\mathbf{r}') - \rho_{\text{B}}\right] u_1(|\mathbf{r} - \mathbf{r}'|)$. Equation H.4 can then be rewritten as

$$\beta\Omega_{\text{solv}}[\phi] - \beta\Omega_{\text{R,solv}}[\phi_{\text{R}}] = \frac{\beta}{2}\int d\mathbf{r}\int d\mathbf{r}' \left[\rho(\mathbf{r})\rho(\mathbf{r}') - \rho_{\text{B}}^2\right] u_1(|\mathbf{r} - \mathbf{r}'|)$$
$$- \beta\int d\mathbf{r}\rho(\mathbf{r})\left[\rho(\mathbf{r}') - \rho_{\text{B}}\right] u_1(|\mathbf{r} - \mathbf{r}'|) + 2\beta\rho_{\text{B}}a\int d\mathbf{r}\left[\rho(\mathbf{r}) - \rho_{\text{B}}\right]$$
$$= \frac{\beta}{2}\int d\mathbf{r}\int d\mathbf{r}' \left[\rho(\mathbf{r})\rho(\mathbf{r}') - \rho_{\text{B}}^2\right] u_1(|\mathbf{r} - \mathbf{r}'|) + 2\beta\rho_{\text{B}}a\int d\mathbf{r}\rho(\mathbf{r})$$
$$- 2\beta\rho_{\text{B}}a\int d\mathbf{r}\rho(\mathbf{r}) - 2\beta\int d\mathbf{r}a\rho_{\text{B}}^2$$
$$- \beta\int d\mathbf{r}\int d\mathbf{r}'\rho(\mathbf{r})\rho(\mathbf{r}')u_1(|\mathbf{r} - \mathbf{r}'|). \tag{H.5}$$

Inserting the explicit expression for a and grouping like terms, we arrive at

$$\beta\Omega_{\text{solv}}[\phi] - \beta\Omega_{\text{R,solv}}[\phi_{\text{R}}] = \frac{\beta}{2}\int d\mathbf{r}\int d\mathbf{r}' \left[\rho(\mathbf{r})\rho(\mathbf{r}') - \rho_{\text{B}}^2\right] u_1(|\mathbf{r} - \mathbf{r}'|)$$
$$- \beta\int d\mathbf{r}d\mathbf{r}' \left[\rho(\mathbf{r})\rho(\mathbf{r}') - \rho_{\text{B}}^2\right] u_1(|\mathbf{r} - \mathbf{r}'|)$$
$$= -\frac{\beta}{2}\int d\mathbf{r}\int d\mathbf{r}' \left[\rho(\mathbf{r})\rho(\mathbf{r}') - \rho_{\text{B}}^2\right] u_1(|\mathbf{r} - \mathbf{r}'|), \tag{H.6}$$

which is Equation 6.16. Although the desired result is obtained from MF approximations, making use of such expressions is not justified in general. The derivation of Equation 6.16 in Section 6.2 involved the use of the LMF equation, which is obtained independently and is accurate in its own right, with appropriate separation of the potential into rapidly- and slowly-varying parts. Therefore, the MF approximations used in this Appendix are only justified when the interaction potential $u_1(r)$ satisfies the conditions on the LMF equation.

I

Stable iteration of the LMF equation for systems with a net charge

We first separate the electrostatic LMF $\mathcal{V}_R(\mathbf{r})$ into its short and long ranged components,

$$\mathcal{V}_R(\mathbf{r}) = \mathcal{V}_0(\mathbf{r}) + \mathcal{V}_{R1}(\mathbf{r}), \tag{I.1}$$

such that $\mathcal{V}_{R1}(\mathbf{r})$ is the slowly-varying portion of the renormalized potential. This potential is given by

$$
\begin{aligned}
\mathcal{V}_{R1}(\mathbf{r}) &= \int d\mathbf{r}' \rho_R^q(\mathbf{r}') v_1(|\mathbf{r} - \mathbf{r}'|; \sigma) + \int d\mathbf{r}' \rho_{\text{ion}}^q(\mathbf{r}') v_1(|\mathbf{r} - \mathbf{r}'|; \sigma) \\
&= \int d\mathbf{r}' \rho_R^{q\sigma}(\mathbf{r}') \frac{1}{|\mathbf{r} - \mathbf{r}'|} + \int d\mathbf{r}' \rho_{\text{ion}}^{q\sigma}(\mathbf{r}') \frac{1}{|\mathbf{r} - \mathbf{r}'|},
\end{aligned} \tag{I.2}
$$

where $\rho_R^q(\mathbf{r})$ and $\rho_R^{q\sigma}(\mathbf{r})$ are the bare and Gaussian smoothed charge densities of the solvent, and $\rho_{\text{ion}}^q(\mathbf{r}) = Q\delta(\mathbf{r})$ and $\rho_{\text{ion}}^{q\sigma}(\mathbf{r}) = Q\rho_G(\mathbf{r}; \sigma)$ are the bare and Gaussian smoothed charge densities of the ion.

Equation I.2 can then be rewritten in the following form

$$\mathcal{V}_{R1}(\mathbf{r}) = \int d\mathbf{r}' \left[\rho_R^{q\sigma}(\mathbf{r}') + Q\rho_G(\mathbf{r}'; \sigma) \right] \frac{1}{|\mathbf{r} - \mathbf{r}'|}. \tag{I.3}$$

This illustrates that $\mathcal{V}_{R1}(\mathbf{r})$ is the electrostatic potential arising from a fixed Gaussian charge distribution of width σ placed at the origin and the charge density of the mobile solvent charges, after these mobile charges have been convoluted with Gaussian distributions of charge also of width σ. Therefore, we can consider $\rho_R^{q\sigma}(\mathbf{r})$ to be the "response" of the dielectric to the Gaussian charge $Q\rho_G(\mathbf{r}; \sigma)$.

To arrive at a stable iteration scheme, we can simply treat $\mathcal{V}_{R1}(\mathbf{r})$ as the total electrostatic potential in this new system, and employ LMF theory to map this system onto another mimic system with a smoothing length l. Separating $\mathcal{V}_{R1}(\mathbf{r})$ into its short and long ranged components yields $\mathcal{V}_{R1}(\mathbf{r}) = \mathcal{V}_{R1}^A(\mathbf{r}) + \mathcal{V}_{R1}^B(\mathbf{r})$. The new LMF potential, which is the long ranged component $\mathcal{V}_{R1}^B(\mathbf{r})$, is given by

$$
\begin{aligned}
\mathcal{V}_{R1}^B(\mathbf{r}) &= \int d\mathbf{r}' \rho_R^{q\sigma}(\mathbf{r}') v_1(|\mathbf{r} - \mathbf{r}'|; l) + \int d\mathbf{r}' Q\rho_G(\mathbf{r}'; \sigma) v_1(|\mathbf{r} - \mathbf{r}'|; l) \\
&\equiv \mathcal{V}_S^B(\mathbf{r}) + \mathcal{V}_1^B(\mathbf{r}).
\end{aligned}
\tag{I.4}
$$

The portion of $\mathcal{V}_{R1}^B(\mathbf{r})$ due to the fixed Gaussian charge distribution is readily evaluated using the convolution theorem, $\hat{\mathcal{V}}_1^B(\mathbf{k}) = 4\pi k^{-2} Q \exp(-k^2\gamma^2/4)$, which in real space is

$$
\mathcal{V}_1^B(\mathbf{r}) = Q v_1(r; \gamma),
\tag{I.5}
$$

such that the long ranged component of the potential arising from a Gaussian charge distribution of width σ is the potential of Gaussian with width

$$
\gamma \equiv \sqrt{l^2 + \sigma^2}.
\tag{I.6}
$$

We now turn our attention to the evaluation of the solvent component of the potential, $\mathcal{V}_S^B(\mathbf{r})$. In our analogy to a system comprised of Gaussian charges, $\rho_R^{q\sigma}(\mathbf{r})$ is the charge density *induced* by the Gaussian charge $Q\rho_G(\mathbf{r}; \sigma)$. Analytic approximations for this induced response were derived in Chapter 5, yielding

$$
\rho_R^{q\sigma}(\mathbf{r}) \approx -Q\left(1 - \frac{1}{\epsilon}\right) \frac{e^{-r^2/\sigma^2}}{\sigma^3 \pi^{3/2}}.
\tag{I.7}
$$

The corresponding solvent portion of the LMF is then given by

$$
\hat{V}_S^B(\mathbf{k}) \approx -\frac{4\pi}{k^2} Q\left(1 - \frac{1}{\epsilon}\right) \exp(-k^2\gamma^2/4),
\tag{I.8}
$$

or

$$
\mathcal{V}_S^B(\mathbf{r}) \approx -Q\left(1 - \frac{1}{\epsilon}\right) v_1(r; \gamma)
\tag{I.9}
$$

182

in real space. The total long ranged portion of the renormalized electrostatic potential is then obtained from the sum of the portions due to the fixed and mobile charges,

$$\mathcal{V}_{\text{R1}}^{B}(\mathbf{r}) = \mathcal{V}_{\text{S}}^{B}(\mathbf{r}) + \mathcal{V}_{1}^{B}(\mathbf{r}) \approx \frac{Q}{\epsilon} v_1(\mathbf{r}; \gamma), \tag{I.10}$$

such that $\mathcal{V}_{\text{R1}}^{B}(\mathbf{r}) \to Q/\epsilon r$ as $r \to \infty$, which is the desired asymptotic behavior.

This stable iteration scheme for systems with a net charge requires solution of the relatively short ranged portion of the renormalized field

$$\mathcal{V}_{\text{R1}}^{A}(\mathbf{r}) = \int d\mathbf{r}' \left[\rho_{\text{R}}^{q\sigma}(\mathbf{r}') + Q\rho_G(\mathbf{r}'; \sigma) \right] v_0(|\mathbf{r} - \mathbf{r}'|; l) \tag{I.11}$$

from simulation data, while the long ranged, slowly varying component $\mathcal{V}_{\text{R1}}^{B}(\mathbf{r})$ is approximated by Equation I.10 at each iteration. This method of self-consistently solving the LMF equation is employed when calculating the ion solvation free energies presented in Section 6.2.3.

J
LMF Free Energy Calculations with Multiple Equilibrium States

J.1 The Multi-State Bennett Acceptance Ratio in the Full System

We first review the MBAR method in this section before combining it with LMF theory. Following the work of Shirts and Chodera [68], and Varilly [144], we consider an equilibrium, Boltzmann ensemble with a configurational partition function

$$Z = \int d\overline{\mathbf{R}} e^{-\beta U(\overline{\mathbf{R}})} \tag{J.1}$$

and free energy $F = -\beta^{-1} \ln Z$, such that $U(\overline{\mathbf{R}})$ is the potential energy of the system in a configuration $\overline{\mathbf{R}}$. This will be referred to as the *unbiased* ensemble.

Now, consider a set of K biasing (umbrella) potentials $\{V_1, V_2, ..., V_K\}$. For each biasing potential V_k, N_k statistically independent samples, labeled $\overline{\mathbf{R}}_{k,n}$, are collected, which are Boltzmann-weighted with a potential $U(\overline{\mathbf{R}}) + V_k(\overline{\mathbf{R}})$. The partition function and free energy in the ensemble defined by the potential V_k are then

$$Z_k = \int d\overline{\mathbf{R}} e^{-\beta[U(\overline{\mathbf{R}}) + V_k(\overline{\mathbf{R}})]} \tag{J.2}$$

and $F_k = -\beta^{-1} \ln Z_k$, respectively.

We then define the free energy difference between the ensemble corresponding to the kth window and the unbiased ensemble as

$$\Delta F_k \equiv F_k - F = \beta^{-1} \ln\left(Z/Z_k\right). \tag{J.3}$$

Now, we construct a model of the probability density of the unbiased ensemble, $P(\overline{\mathbf{R}})$, constructed as a sum of Dirac δ-functions centered at each of the $N_1 + ... + N_K$ samples observed, with unknown weights $p_{j,n}$:

$$P(\overline{\mathbf{R}}) \approx \mathcal{Z}^{-1} \sum_{j=1}^{K} \sum_{n=1}^{N_j} p_{j,n} \delta(\overline{\mathbf{R}} - \overline{\mathbf{R}}_{j,n}). \tag{J.4}$$

Analogously, the probability density of the kth biased ensemble is

$$P_k(\overline{\mathbf{R}}) \approx \mathcal{Z}_k^{-1} \sum_{j=1}^{K} \sum_{n=1}^{N_j} p_{j,n} e^{-\beta V_k(\overline{\mathbf{R}})} \delta(\overline{\mathbf{R}} - \overline{\mathbf{R}}_{j,n}). \tag{J.5}$$

The normalization constants are given by

$$\mathcal{Z} = \sum_{j=1}^{K} \sum_{n=1}^{N_j} p_{j,n} \tag{J.6}$$

and

$$\mathcal{Z}_k = \sum_{j=1}^{K} \sum_{n=1}^{N_j} p_{j,n} e^{-\beta V_k(\overline{\mathbf{R}}_{j,n})}. \tag{J.7}$$

These are the best estimates to Z and Z_k, respectively, up to an undetermined measure factor, such that $\mathcal{Z}/\mathcal{Z}_k \approx Z/Z_k$.

An estimate of the free energy differences between biased ensembles and the unbiased ensemble is enough to estimate the probability of *every* observed sample in the unbiased ensemble (this statement will be key to using LMF theory to estimate averages using biased sampling, as described later). These free energy differences are obtained by self-consistent iteration using the multi-state Bennett acceptance ratio (MBAR) as

$$e^{-\beta \Delta F_i} = \sum_{j=1}^{K} \sum_{n=1}^{N_j} \frac{e^{-\beta V_i(\overline{\mathbf{R}}_{j,n})}}{\sum_{k=1}^{K} N_k e^{\beta \Delta F_k - \beta V_k(\overline{\mathbf{R}}_{j,n})}}. \tag{J.8}$$

185

Once the set of free energy differences $\{\Delta F_k\}$ are obtained, ensemble averages of an observable $A(\overline{\mathbf{R}})$ can then be estimated as

$$\langle A \rangle \approx \sum_{j=1}^{K} \sum_{n=1}^{N_j} \frac{A(\overline{\mathbf{R}}_{j,n})}{\sum_{k=1}^{K} N_k e^{\beta \Delta F_k - \beta V_k(\overline{\mathbf{R}}_{j,n})}}, \tag{J.9}$$

where the approximation only appears because we have a finite number of samples N_j in each simulation window j.

J.2 Ensemble Averages in the Full System from Biased Sampling Performed in the Mimic System

We now consider performing umbrella sampling in the mimic system. Each of the K biased ensembles will have an associated LMF. Therefore, we will have a set of renormalized fields $\{\phi_{\mathrm{R},k}(\mathbf{r})\}$ associated with each of the K windows. The partition function in the unbiased mimic ensemble is given by

$$Z_{\mathrm{R}} = \int d\overline{\mathbf{R}} e^{-\beta \left[U_0(\overline{\mathbf{R}}) + \Phi_{\mathrm{R1}}(\overline{\mathbf{R}}) \right]}, \tag{J.10}$$

and the partition function of the kth biased window is

$$Z_{\mathrm{R},k} = \int d\overline{\mathbf{R}} e^{-\beta \left[U_0(\overline{\mathbf{R}}) + \Phi_{\mathrm{R1},k}(\overline{\mathbf{R}}) + V_k(\overline{\mathbf{R}}) \right]}, \tag{J.11}$$

where $\Phi_{\mathrm{R1},k} = \sum_{i=1}^{N} \phi_{\mathrm{R1},k}(\mathbf{r}_i)$. The free energy difference between the kth window and the unbiased mimic ensemble is given by

$$\Delta F_{\mathrm{R},k} = F_{\mathrm{R},k} - F_{\mathrm{R}} = \beta^{-1} \ln \left(\frac{Z_{\mathrm{R}}}{Z_{\mathrm{R},k}} \right). \tag{J.12}$$

In analogy with the previous section, estimates for the normalization constants Z_{R} and $Z_{\mathrm{R},k}$ are given respectively by

$$\mathcal{Z}_{\mathrm{R}} \approx \sum_{j=1}^{K} \sum_{n=1}^{N_j} p_{j,n}^{(\mathrm{R})} \tag{J.13}$$

and

$$\mathcal{Z}_{\mathrm{R},k} \approx \sum_{j=1}^{K} \sum_{n=1}^{N_j} p_{j,n}^{(\mathrm{R})} e^{-\beta V_k(\overline{\mathbf{R}}_{j,n})} e^{-\beta \Delta \Phi_{\mathrm{R1},k}(\overline{\mathbf{R}}_{j,n})}, \tag{J.14}$$

where $\Delta\Phi_{R1,k} \equiv \Phi_{R1,k} - \Phi_{R1}$.

The set of free energy differences $\{\Delta F_{R,k}\}$ can then be obtained in analogy with those of the full system, Equation J.8, by replacing $V_k(\overline{\mathbf{R}})$ with $\tilde{V}_k(\overline{\mathbf{R}}) \equiv V_k(\overline{\mathbf{R}}) + \Delta\Phi_{R1,k}(\overline{\mathbf{R}})$ and $p_{j,n}$ with $p_{j,n}^{(R)}$:

$$e^{-\beta\Delta F_{R,i}} = \sum_{j=1}^{K} \sum_{n=1}^{N_j} \frac{e^{-\beta\tilde{V}_i(\overline{\mathbf{R}}_{j,n})}}{\sum_{k=1}^{K} N_k e^{\beta\Delta F_{R,k} - \beta\tilde{V}_k(\overline{\mathbf{R}}_{j,n})}}. \tag{J.15}$$

The $\Delta\Phi_{R1,k}$ term presents a problem, since we may not know $\phi_{R1}(\mathbf{r})$ of the unbiased ensemble in advance (if we could obtain this easily, we would not need to overcome sampling issues in the first place!). However, the free energy differences obtained from the MBAR calculation are known up to an undetermined constant. Therefore, we can choose this constant such that it exactly cancels the Φ_{R1} term in each window, and we can write

$$e^{-\beta\Delta F_{R,i}} = \sum_{j=1}^{K} \sum_{n=1}^{N_j} \frac{e^{-\beta\left[V_i(\overline{\mathbf{R}}_{j,n}) + \Phi_{R1,i}(\overline{\mathbf{R}}_{j,n})\right]}}{\sum_{k=1}^{K} N_k e^{\beta\left[\Delta F_{R,k} - V_k(\overline{\mathbf{R}}_{j,n}) - \Phi_{R1,k}(\overline{\mathbf{R}}_{j,n})\right]}}, \tag{J.16}$$

without any loss of generality. Ensemble averages in the mimic system can then be estimated following

$$\langle A \rangle_R \approx \sum_{j=1}^{K} \sum_{n=1}^{N_j} \frac{A_R(\overline{\mathbf{R}}_{j,n})}{\sum_{k=1}^{K} N_k e^{\beta\left[\Delta F_{R,k} - V_k(\overline{\mathbf{R}}_{j,n}) - \Phi_{R1,k}(\overline{\mathbf{R}}_{j,n})\right]}}, \tag{J.17}$$

where the notation A_R emphasizes that the observable A is evaluated over configurations in the mimic system.

However, averages in the mimic system are not of interest, and we want to calculate averages in the *full* system. As stated earlier, the free energy differences between the unbiased full ensemble and the K biased full ensembles is enough to estimate the probability of *every* sample in the unbiased ensemble of the *full* system. From the LMF theory-based framework for free energy calculations, we know that the free energy energy difference between the full and mimic systems is given by

$$F - F_R = F_{LMF} = -\frac{1}{2} \int d\mathbf{r} \left[\rho_R(\mathbf{r}) + \rho_B\right] \left[\phi_R(\mathbf{r}) - \phi(\mathbf{r})\right]. \tag{J.18}$$

Therefore, the free energy difference between the kth biased mimic ensemble and the kth biased full ensemble is given by an analogous expression,

$$F_k - F_{R,k} = F_{LMF,k} = -\frac{1}{2} \int d\mathbf{r} \left[\rho_{R,k}(\mathbf{r}) + \rho_B\right] \left[\phi_{R,k}(\mathbf{r}) - \phi_k(\mathbf{r})\right]. \tag{J.19}$$

Now, note that $\Delta F_k = F_k - F$ are the desired free energy differences, and we can define $\tilde{F}_k \equiv F_{\mathrm{R},k} + F_{\mathrm{LMF},k}$ to be the LMF theory based estimate of the free energy in the kth window of the full system. By again taking advantage of the fact that the free energies determined using MBAR have an undetermined constant, averages in the *full, unbiased* ensemble can be obtained from

$$\langle A \rangle \approx \sum_{j=1}^{K} \sum_{n=1}^{N_j} \frac{A_{\mathrm{R}}(\overline{\mathbf{R}}_{j,n})}{\sum_{k=1}^{K} N_k e^{\beta\left[\Delta F_{\mathrm{R},k} + F_{\mathrm{LMF},k} - V_k(\overline{\mathbf{R}}_{j,n})\right]}}. \tag{J.20}$$

Equation J.20 is the main result of this subsection, and states that averages in the unbiased, full ensemble can be obtained from calculations in the mimic system by simply *reweighting* the free energy differences between windows by a simple, analytic correction, $F_{\mathrm{LMF},k}$.

J.3 Ensemble Averages in the Full System from Biased Sampling Performed in the Strong Coupling System

Within the linear response regime, we can seek to evaluate the full free energy directly from the SCA system, as was done above in the case of HS solvation in water. We again consider K biasing potentials and the corresponding biased ensembles in the strong-coupling (SCA) system. The unbiased SCA ensemble has a partition function

$$Z_0 = \int d\overline{\mathbf{R}} e^{-\beta U_0(\overline{\mathbf{R}})}, \tag{J.21}$$

while the kth biased SCA ensemble has the partition function

$$Z_{0,k} = \int d\overline{\mathbf{R}} e^{-\beta\left[U_0(\overline{\mathbf{R}}) + V_k(\overline{\mathbf{R}})\right]}. \tag{J.22}$$

The free energy difference between the kth biased SCA ensemble and the unbiased SCA ensemble is

$$\Delta F_{0,k} = F_{0,k} - F = \beta^{-1} \ln\left(\frac{Z_0}{Z_{0,k}}\right). \tag{J.23}$$

This set of free energy differences can be obtained using MBAR, in analogy with the full system, as

$$e^{-\beta\Delta F_{0,i}} = \sum_{j=1}^{K} \sum_{n=1}^{N_j} \frac{e^{-\beta V_i(\overline{\mathbf{R}}_{j,n})}}{\sum_{k=1}^{K} N_k e^{\beta\Delta F_{0,k} - \beta V_k(\overline{\mathbf{R}}_{j,n})}}, \tag{J.24}$$

and averages in the SCA system can be obtained following

$$\langle A \rangle_0 \approx \sum_{j=1}^{K} \sum_{n=1}^{N_j} \frac{A_0(\overline{\mathbf{R}}_{j,n})}{\sum_{k=1}^{K} N_k e^{\beta \Delta F_{0,k} - \beta V_k(\overline{\mathbf{R}}_{j,n})}}. \tag{J.25}$$

where the notation A_0 is used to emphasize that the observable A is evaluated over configurations in the SCA system.

However, as stated above, we are really interested in averages in the full system. These averages can be calculated if we have an estimate for the set of free energy differences $\{\Delta F_k\}$. To obtain this set of free energy differences, we note that

$$\begin{aligned} \Delta F_k &= F_k - F \approx F_{\mathrm{R},k} + F_{\mathrm{LMF},k} - F \\ &= F_{0,k} + F_{\mathrm{R1},k} + F_{\mathrm{LMF},k} - F, \end{aligned} \tag{J.26}$$

where $F_{\mathrm{R1},k}$ is the free energy of turning on the LMF $\phi_{\mathrm{R1},k}(\mathbf{r})$ in the kth biased ensemble. Using LRT, we can estimate the set of renormalized fields $\{\phi_{\mathrm{R},k}(\mathbf{r})\}$, and the free energy of turning on each field in the corresponding biased ensemble is given by the Gaussian approximation,

$$F_{\mathrm{R1},k} \approx \frac{1}{2} \int d\mathbf{r} \left[\rho_{\mathrm{R},k}(\mathbf{r}) + \rho_{0,k}(\mathbf{r}) \right] \phi_{\mathrm{R1},k}(\mathbf{r}). \tag{J.27}$$

Once the renormalized potentials are determined using LRT, we can also calculate the LMF free energy term,

$$F_{\mathrm{LMF},k} = -\frac{1}{2} \int d\mathbf{r} \left[\rho_{\mathrm{R},k}(\mathbf{r}) + \rho_{\mathrm{B}} \right] \left[\phi_{\mathrm{R},k}(\mathbf{r}) - \phi_k(\mathbf{r}) \right]. \tag{J.28}$$

By again taking advantage of the fact that the free energy differences $\{\Delta F_{0,k}\}$ are determined up to some unknown constant, we can estimate averages in the full system from umbrella simulations of the SCA system through reweighting,

$$\langle A \rangle \approx \sum_{j=1}^{K} \sum_{n=1}^{N_j} \frac{A_0(\overline{\mathbf{R}}_{j,n})}{\sum_{k=1}^{K} N_k e^{\beta \left[\Delta F_{0,k} + F_{\mathrm{R1},k} + F_{\mathrm{LMF},k} - V_k(\overline{\mathbf{R}}_{j,n}) \right]}}. \tag{J.29}$$

If $F_{\mathrm{R1},k}$ can be obtained accurately with the Gaussian approximation for all k, this is the most efficient way to estimate $\langle A \rangle$. If not, then $\{\Delta F_{\mathrm{R},k}\}$ would need to be determined from biased simulations in the mimic system.

K
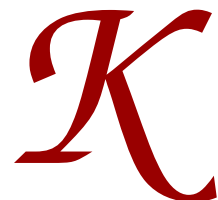
Liquid-Vapor Interfaces of Truncated Water Models

In this Appendix, we present details of the structure and height flucutations of the liquid-vapor interface of several truncated water models. We examine the structure of these interfaces using the instantaneous interface formalism developed by Willard and Chandler [145]. The instantaneous density field as function of the spatial coordinate $\mathbf{r}$ and time t is defined as

$$\rho(\mathbf{r}, t) = \sum_i \delta(\mathbf{r} - \mathbf{r}_i(t)), \tag{K.1}$$

where $\mathbf{r}_i(t)$ is the position of particle i at time t and the sum is over all particles of interest. This bare density field is then coarse-grained via convolution with a truncated and shifted Gaussian density function,

$$\rho_{\mathrm{G}}(\mathbf{r}; \xi) = (2\pi\xi^2)^{-d/2} \left[e^{-r^2/2\xi^2} - e^{-r_c^2/2\xi^2} \right], \tag{K.2}$$

where ξ is the width of the Gaussian, $|r_c|$ is the distance at which the Gaussian is truncated and shifted to zero, here chosen to be equal to 3ξ, and d is the dimensionality of the system.

Convolution of the bare density field yields the coarse-grained density field

$$\rho^\xi(\mathbf{r}, t) = \sum_i \rho_{\mathrm{G}}(|\mathbf{r} - \mathbf{r}_i(t)| ; \xi). \tag{K.3}$$
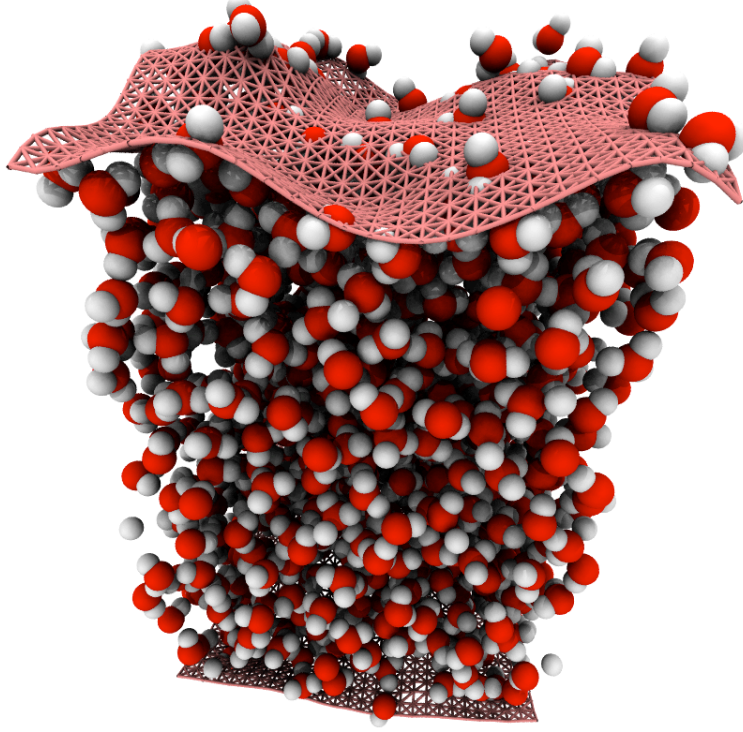
Figure K.1: Snapshot of a single configuration of the liquid-vapor slab of water (red oxygen sites and white hydrogen sites) with its instantaneous interface (pink). Note that there are two interfaces present in the system.

The interface at space-time point $(\mathbf{r}, t)$ is then defined as the $(d-1)$-dimensional manifold $\mathbf{r} = \mathbf{s}$ along which the coarse-grained density field is a specified constant, $\rho^{\xi}(\mathbf{s}, t) = \rho_c$. Note that $\mathbf{s} = \mathbf{s}(t)$ is a time-dependent quantity which varies with the set of coordinates of the particles. Following Willard and Chandler, we utilize a smoothing length of $\xi = 2.4$ Å and a density cutoff of approximately half the bulk number density, $\rho_c = 0.016$ Å^{-3}. A typical configuration of this interface for a slab of water in equilibrium with its vapor is illustrated in Figure K.1, where the non-planar, fluctuating nature of this interface is readily apparent.

The nonuniform density with respect to the instantaneous interface is given by

$$\rho_{\mathbf{s}}(z) = \frac{1}{L^2} \left\langle \sum_i \delta(a_i - z) \right\rangle, \tag{K.4}$$
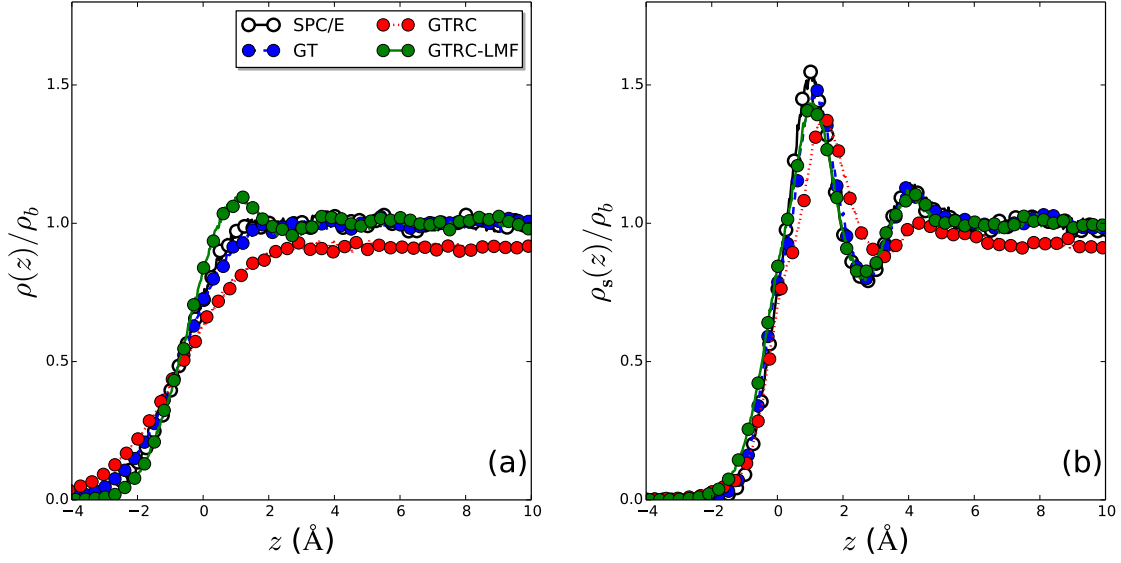
Figure K.2: Nonuniform density with respect to (a) the mean liquid-vapor interface and (b) the instantaneous liquid-vapor interface for the four systems under study.

where the proximity of particle i to the instantaneous interface is

$$a_i(t) = \left\{ [\mathbf{s}(t) - \mathbf{r}_i(t)] \cdot \hat{\mathbf{n}}(t) \right\} \Big|_{\mathbf{s}(t) = \mathbf{s}_i^*(t)}, \tag{K.5}$$

such that $\langle \cdot \rangle$ indicates an equilibrium average, $\hat{\mathbf{n}}(t)$ is the unit vector normal to interface at $\mathbf{s}(t)$, and $\mathbf{s}_i^*(t)$ is the point on $\mathbf{s}(t)$ nearest to $\mathbf{r}_i(t)$. Analogously, the density profile with respect to the mean interface can be written as

$$\rho(z) = \frac{1}{L^2} \left\langle \sum_i \delta(b_i - z) \right\rangle, \tag{K.6}$$

where

$$b_i(t) = [\langle \mathbf{s} \rangle - \mathbf{r}_i(t)] \cdot \langle \hat{\mathbf{n}} \rangle. \tag{K.7}$$

The nonuniform densities $\rho(z)$ and $\rho_\mathbf{s}(z)$ are shown in Figures K.2a and K.2b, respectively. The density $\rho(z)$ for SPC/E and GT is typical of that for a liquid-vapor interface; $\rho(z)$ monotonically decreases from the liquid to the vapor due to broadening by interfacial fluctuations. The $\rho(z)$ obtained for the GTRC model is qualitatively similar to that of the SPC/E and GT models, albeit that interfacial width is significantly larger. In addition, the bulk density of the GTRC is roughly 15 percent lower than that of the SPC/E model.

Mean-field theories, LMF theory included, cannot capture capillary wave fluctuations. Therefore, we would expect to observe layering at the liquid-vapor interface of the GTRC model in the presence of the LMF $\phi_R^{LJ}(z)$. Indeed, $\rho(z)$ obtained for the system (GTRC-LMF in Figure K.2a) displays a small peak at the interface, indicative of layering. However, there still exists some broadening of $\rho(z)$ due to the presence of small wavelength fluctuations in the system.

We now turn our attention to the nonuniform density with respect to the instantaneous interface, $\rho_s(z)$, shown in Figure K.2b. The profiles obtained for the SPC/E, GT, and GTRC-LMF systems are nearly identical, illustrating that layering at the interface is the same in all three systems and is independent of the amount of interfacial fluctuations present in the system. Analogous to the results obtained for $\rho(z)$, $\rho_s(z)$ for the GTRC model is qualitatively similar to that of the other systems. However, the features of $\rho_s(z)$ are broadened due to the more diffuse interface and lower bulk density.

Table K.1: Mean Squared Interfacial Height Fluctuations

System	$\langle(\delta h(\mathbf{x}))^2\rangle$ (Å^2)
SPC/E	1.14±0.09
GT	1.31±0.15
GTRC	3.1 ±0.7
GTRC-LMF	0.34±0.03

Finally, we conclude this Appendix by using the instantaneous interface to calculate the average fluctuations in the interfacial height, $\langle(\delta h(\mathbf{x}))^2\rangle$, where $\delta h(\mathbf{x}) = h(\mathbf{x}) - \langle h(\mathbf{x})\rangle$ is the deviation in the interfacial height from its mean. The mean squared height fluctuations are listed in Table K.1. The results for SPC/E and its truncated variants are consistent with their respective surface tensions, $\langle(\delta h(\mathbf{x}))^2\rangle^{GTRC} > \langle(\delta h(\mathbf{x}))^2\rangle^{GT} > \langle(\delta h(\mathbf{x}))^2\rangle^{SPC/E}$. In addition, the interfacial fluctuations of the GTRC model in the presence of the LJ-LMF $\phi_R^{LJ}(z)$ are significantly significantly damped, and $\langle(\delta h(\mathbf{x}))^2\rangle^{GTRC-LMF}$ is nearly 70 % smaller than that of the SPC/E model.

References

[1] J. M. Rodgers and J. D. Weeks. Local molecular field theory for the treatment of electrostatics. *J. Phys.: Condens. Matter*, 20:494206, 2008.

[2] J. M. Rodgers and J. D. Weeks. Interplay of local hydrogen-bonding and long-ranged dipolar forces in simulations of confined water. *Proc. Natl. Acad. Sci. USA*, 105:19136, 2008.

[3] J. D. Weeks. Connecting local structure to interface formation: A molecular scale van der waals theory of nonuniform liquids. *Annu. Rev. Phys. Chem.*, 53:533–562, 2002.

[4] Y. G. Chen and J. D. Weeks. Local molecular field theory for effective attractions between like charged objects in systems with strong coulomb interactions. *Proc. Natl. Acad. Sci. USA*, 103:7560, 2006.

[5] Y. G. Chen, C. Kaur, and J. D. Weeks. Connecting systems with short and long ranged interactions: Local molecular field theory for ionic fluids. *J. Phys. Chem. B*, 108:19874, 2004.

[6] J. D. Weeks, D. Chandler, and H. C. Andersen. Role of repulsive forces in determining the equilibrium structure of simple liquids. *J. Chem. Phys.*, 54:5237–5247, 1971.

[7] B. Widom. Intermolecular forces and the nature of the liquid state. *Science*, 157:375–382, 1967.

[8] J. S. Rowlinson and B. Widom. *Molecular Theory of Capillarity*. Dover Publications, Inc., 2002.

[9] H. C. Andersen, J. D. Weeks, and D. Chandler. Relationship between the hard-sphere fluid and fluids with realistic repulsive forces. *Phys. Rev. A*, 4:1597–1607, 1971.

[10] R. Evans. Density functionals in the theory of nonuniform fluids. In D. Henderson, editor, *Fundamentals of Inhomogenous Fluids*, chapter 3. Marcel Dekker, Inc., 1992.

[11] J. M. Rodgers, Z. Hu, and J. D. Weeks. On the efficient and accurate short-ranged simulations of uniform polar molecular liquids. *Mol. Phys.*, 109:1195–1211, 2011.

[12] L. R. Pratt, A. Pohorille, and D. Asthagiri. What is special about water as a matrix of life? arxiv:physics/0701282, Jan 2007.

[13] P. Ball. Water as an active constituent in cell biology. *Chem. Rev.*, 108:74–108, 2008.

[14] D. Chandler. Interfaces and the driving force of hydrophobic assembly. *Nature*, 437:640–647, 2005.

[15] H. J. C. Berendsen, J. R. Grigera, and T. P. Straatsma. The missing term in effective pair potentials. *J. Phys. Chem.*, 91:6269–6271, 1987.

[16] M. Chaplin. Water structure and science. http://www.lsbu.ac.uk/water/, July 2013.

[17] R. C. Remsing, J. M. Rodgers, and J. D. Weeks. Deconstructing classical water models at interfaces and in bulk. *J. Stat. Phys.*, 145:313–334, 2011.

[18] F. H. Stillinger. Structure in aqueous solutions of nonpolar solutes from the standpoint of scaled-particle theory. *J. Solution Chem.*, 2:141–158, 1973.

[19] K. Lum, D. Chandler, and J. D. Weeks. Hydrophobicity at small and large length scales. *J. Phys. Chem. B*, 103:4570–4577, 1999.

[20] R. C. Remsing and J. D. Weeks. Dissecting hydrophobic hydration and association. *J. Phys. Chem. B*, (in press), 2013.

[21] G. Guillot. A reappraisal of what we have learnt during three decades of computer simulations of water. *J. Mol. Liq.*, 101:219–260, 2002.

[22] C. Vega, J. L. F. Abascal, M. M. Conde, and J. L. Aragones. What ice can teach us about water interactions: A critical comparison of the performance of different water models. *Faraday Discuss.*, 141:251–276, 2009.

[23] L. Xu, S. V. Buldyrev, C. A. Angell, and H. E. Stanley. Thermodynamics and dynamics of the two-scale spherically symmetric jagla ramp model of anomalous liquids. *Phys. Rev. E*, 74:031108, 2006.

[24] Z. Yan, S. V. Buldyrev, N. Giovambattista, and H. E. Stanley. Structural order for one-scale and two-scale potentials. *Phys. Rev. Lett.*, 95:130604, 2005.

[25] S. V. Buldyrev, P. Kumar, P. G. Debenedetti, and P. J. Rossky. Water-like solvation thermodynamics in a spherically symmetric solvent model with two characteristic lengths. *Proc. Natl. Acad. Sci. USA*, 104:20177–20182, 2007.

[26] J. P. Hansen and I. R. McDonald. *Theory of Simple Liquids*. Elsevier Ltd., 2006.

[27] J. M. Rodgers and J. D. Weeks. Accurate thermodynamics for short-ranged truncations of coulomb interactions in site-site molecular models. *J. Chem. Phys.*, 131:244108, 2009.

[28] A. Ben-Naim and F. H. Stillinger. *Water and Aqueous Solutions: Structure, Thermodynamics, and Transport Processes*. Wiley-Interscience, New York, 1972.

[29] A. Luzar and D. Chandler. Effect of environment on hydrogen bond dynamics in liquid water. *Phys. Rev. Lett.*, 76:928–931, 1996.

[30] W. Smith, C. Yong, and P. Rodger. DL_POLY: Application to molecular simulation. *Mol. Simul.*, 28:385–471, 2002.

[31] M. P. Allen and D. J. Tildesley. *Computer Simulation of Liquids*. Oxford: New York, 1987.

[32] H. J. C. Berendsen, J. P. M Postma, W. F. van Gunsteren, A. DiNiola, and J. R. Haak. Molecular dynamics with coupling to an external bath. *J. Chem. Phys.*, 81:3684, 1984.

[33] S. H. Lee and P. J. Rossky. A comparison of the structure and dynamics of liquid water at hydrophobic and hydrophilic surfaces – a molecular dynamics simulation study. *J. Chem. Phys.*, 100:3334–3345, 1994.

[34] I. C. Yeh and M. L. Berkowitz. Ewald summation for systems with slab geometry. *J. Chem. Phys.*, 111:3155–3162, 1999.

[35] W. M. Haynes, editor. *CRC Handbook of Chemistry and Physics, 91st Edition (Internet Version 2011)*. CRC Press/Taylor and Francis, Boca Raton, FL, 2011.

[36] H. S. Ashbaugh, N. J. Collett, H. W. Hatch, and J. A. Staton. Assessing the thermodynamic signatures of hydrophobic hydration for several common water models. *J. Chem. Phys.*, 132:124504, 2010.

[37] J. Jirsák and I. Nezbeda. Molecular mechanisms underlying the thermodynamic properties of water. *J. Mol. Liq.*, 134:99–106, 2007.

[38] J. Schmidt, J. VandeVondele, I.-F. W. Kuo, D. Sebastiani, J. I. Siepmann, J. Hutter, and C. J. Mundy. Isobaric-isothermal molecular dynamics simulations utilizing density functional theory: An assessment of the structure and density of water at near-ambient conditions. *J. Phys. Chem. B*, 113:11959–11964, 2009.

[39] I-F. Kuo, C. J. Mundy, B. L. Eggimann, M. J. McGrath, J. I. Siepmann, B. Chen, J. Vieceli, and D. J. Tobias. Structure and dynamics of the aqueous liquid-vapor interface: A comprehensive particle-based simulation study. *J. Phys. Chem. B*, 110:3738–3746, 2006.

[40] J. Wang, G. Román-Pérez, J. M. Soler, E. Artacho, and M.-V. Fernández-Serra. Density, structure, and dynamics of water: The effect of van der waals interactions. *J. Chem. Phys.*, 134:024516, 2011.

[41] J. K. Shah, D. Asthagiri, L. R. Pratt, and M. E. Paulaitis. Balancing local order and long-ranged interactions in the molecular theory of liquid water. *J. Chem. Phys.*, 127:144508, 2007.

[42] E. K. Goharshadi, A. Morsali, and G. A. Mansoori. A molecular dynamics study on the role of attractive and repulsive forces in internal energy, internal pressure, and structure of dense fluids. *Chem. Phys.*, 331:332–338, 2007.

[43] J. R. Errington and P. G. Debenedetti. Relationship between structural order and the anomalies of liquid water. *Nature*, 409:318–321, 2001.

[44] N. A. Denesyuk and J. D. Weeks. A new approach for efficient simulation of coulomb interactions in ionic fluids. *J. Chem. Phys.*, 128:124109, 2008.

[45] C. Y. Lee, J. A. McCammon, and P. J. Rossky. The structure of liquid water at an extended hydrophobic surface. *J. Chem. Phys.*, 80:4448–4455, 1984.

[46] B. J. Berne, J. D. Weeks, and R. Zhou. Dewetting and hyrophobic interactions in physical and biological systems. *Annu. Rev. Phys. Chem.*, 60:85–103, 2009.

[47] P. Varilly, A. J. Patel, and D. Chandler. An improved coarse-grained model of solvation and the hydrophobic effect. *J. Chem. Phys.*, 134:074109, 2011.

[48] R. C. Remsing, J. M. Rodgers, and J. D. Weeks. (to be published).

[49] T. D. Iordanov, G. K. Schenter, and B. C. Garrett. Sensitivity analysis of thermodynamic properties of liquid water: A general approach to improve empirical potentials. *J. Phys. Chem. A*, 110:762–771, 2006.

[50] E. Marcotte, F. H. Stillinger, and S. Torquato. Optimized monotonic convex pair potentials stabilize low-coordinated crystals. *Soft Matter*, 7:2332–2335, 2011.

[51] S. B. Zhu and C. F. Wong. Sensitivity analysis of water thermodynamics. *J. Chem. Phys.*, 98:8892–8899, 1993.

[52] D. M. Huang and D. Chandler. Cavity formation and the drying transition in the lennard-jones fluid. *Phys. Rev. E*, 61:1501–1506, 2000.

[53] D. M. Huang, P. L. Geissler, and D. Chandler. Scaling of hydrophobic solvation free energies. *J. Phys. Chem. B*, 105:6704–6709, 2001.

[54] H. Acharya and S. Garde. (to be published).

[55] D. M. Huang and D. Chandler. The hydrophobic effect and the influence of solute-solvent attractions. *J. Phys. Chem. B*, 106:2047–2053, 2002.

[56] F. H. Stillinger and A. Ben-Naim. Liquid-vapor interface potential for water. *J. Chem. Phys.*, 47:4431–4437, 1967.

[57] C. H. Bennett. Efficient estimation of free energy differences from monte carlo data. *J. Comput. Phys.*, 22:245–268, 1976.

[58] A. Pohorille, C. Jarzynski, and C. Chipot. Good practices in free-energy calculations. *J. Phys. Chem. B*, 114:10235–10253, 2010.

[59] P. R. ten Wolde and D. Chandler. Drying-induced hydrophobic polymer collapse. *Proc. Natl. Acad. Sci. USA*, 99:6539–6543, 2002.

[60] S. Rajamani, T. M. Truskett, and S. Garde. Hydrophobic hydration from small to large lengthscales: Understanding and manipulating the crossover. *Proc. Natl. Acad. Sci. USA*, 102:9475–9480, 2005.

[61] P. A. Egelstaff and B. Widom. Liquid surface tension near the triple point. *J. Chem. Phys.*, 53:2667, 1970.

[62] F. Sedlmeier and R. R. Netz. The spontaneous curvature of the water-hydrophobe interface. *J. Chem. Phys.*, 137:135102, 2012.

[63] S. Garde, G. Hummer, A. E. García, M. E. Paulaitis, and L. R. Pratt. Origin of entropy convergence in hydrophobic hydration and protein folding. *Phys. Rev. Lett.*, 77:4966–4968, 1996.

[64] G. Hummer, S. Garde, A. E. García, M. E. Paulaitis, and L. R. Pratt. Hydrophobic effects on a molecular scale. *J. Phys. Chem. B*, 102:10469–10482, 1998.

[65] F. Sedlmeier, D. Horinek, and R. R. Netz. Entropy and enthalpy convergence of hydrophobic solvation beyond the hard-sphere limit. *J. Chem. Phys.*, 134:055105, 2011.

[66] G. Graziano. A van der waals approach to the entropy convergence phenomenon. *Phys. Chem. Chem. Phys.*, 6:406–410, 2004.

[67] G. Hummer, S. Garde, A. E. García, A. Pohorille, and L. R. Pratt. An information theory model of hydrophobic interactions. *Proc. Natl. Acad. Sci. USA*, 93:8951–8955, 1996.

[68] M. R. Shirts and J. D. Chodera. Statistically optimal analysis of samples from multiple equilibrium states. *J. Chem. Phys.*, 129:124105, 2008.

[69] W. D. Cornell, P. Cieplak, C. I. Bayly, I. R. Gould, K. M. Merz, D. M. Ferguson, D. C. Spellmeyer, T. Fox, J. W. Caldwell, and P. A. Kollman. A second generation force field for the simulation of proteins, nucleic acids, and organic molecules. *J. Am. Chem. Soc.*, 117:5179–5197, 1995.

[70] L. A. Girifalco. Molecular properties of c_{60} in the gas and solid phases. *J. Phys. Chem.*, 96:858–861, 1992.

[71] N. Choudhury. A molecular dynamics simulation study of buckyballs in water: atomistic versus coarse-grained models of c_{60}. *J. Chem. Phys.*, 125:034502, 2006.

[72] K. Lum and A. Luzar. Pathway to surface-induced phase transition of a confined fluid. *Phys. Rev. E*, 56:R6283, 1997.

[73] A. P. Willard and D. Chandler. The role of solvent fluctuations in hydrophobic assembly. *J. Phys. Chem. B*, 112:6187–6192, 2008.

[74] A. J. Patel, P. Varilly, D. Chandler, and S. Garde. Quantifying density fluctuations in volumes of all shapes and sizes using indirect umbrella sampling. *J. Stat. Phys.*, 145:265–275, 2011.

[75] L. Li, D. Bedrov, and G. D. Smith. A molecular-dynamics simulation study of solvent-induced repulsion between c_{60} fullerenes in water. *J. Chem. Phys.*, 123:204505, 2005.

[76] A. Chaimovich and M. S. Shell. Anomalous waterlike behavior in spherically-symmetric water models optimized with the relative entropy. *Phys. Chem. Chem. Phys.*, 11:1901–1915, 2009.

[77] M. U. Hammer, T. H. Anderson, A. Chaimovich, M. S. Shell, and J. Israelachvili. The search for the hydrophobic force law. *Faraday Discuss.*, 146:299–308, 2010.

[78] S. Rajamani, T. Ghosh, and S. Garde. Size dependent ion hydration, its asymmetry, and convergence to macroscopic behavior. *J. Chem. Phys.*, 120:4457, 2004.

[79] J. P. Bardhan, P. Jungwirth, and L. Makowski. Affine-response model of molecular solvation of ions: Accurate predictions of asymmetric charging free energies. *J. Chem. Phys.*, 137:124101, 2012.

[80] G. Hummer, L. R. Pratt, and A. E. García. Free energy of ionic hydration. *J. Phys. Chem.*, 100:1206–1215, 1996.

[81] G. Hummer, L. R. Pratt, and A. E. García. Molecular theories and simulation of ions and polar molecules in water. *J. Phys.Chem. A*, 102:7885–7895, 1998.

[82] T. L. Beck, M. E. Paulaitis, and L. R. Pratt. *The Potential Distirbution Theorem and Models of Molecular Solutions*. Cambridge University Press, 2006.

[83] N. Agmon. Liquid water: From symmetry distortions to diffusive motion. *Acc. Chem Res.*, 45:63–73, 2012.

[84] V. Molinero and E. B. Moore. Water modeled as an intermediate element between carbon and silicon. *J. Phys. Chem. B*, 113:4008–4016, 2009.

[85] D. T. Limmer and D. Chandler. Corresponding states for mesostructure and dynamics of supercooled water. DOI: 10.1039/C3FD00076A, 2013.

[86] P. Jedlovszsky, M. Predota, and I. Nezbeda. Hydration of apolar solutes of varying size: a systematic study. *Mol. Phys.*, 104:2465–2476, 2006.

[87] H. S. Ashbaugh. Convergence of molecular and macroscopic continuum descriptions of ion hydration. *J. Phys. Chem. B*, 104:7235–7238, 2000.

[88] E. Harder and B. Roux. On the origin of the electrostatic potential difference at a liquid-vacuum interface. *J. Chem. Phys.*, 129:234706, 2008.

[89] K. Leung, S. B. Rempe, and O. A. von Lilienfeld. Ab initio molecular dynamics calculations of ion hydration free energies. *J. Chem. Phys.*, 130:204507, 2009.

[90] K. Leung and M. Marsman. Energies of ions in water and nanopores within density functional theory. *J. Chem. Phys.*, 127:154722, 2007.

[91] M. D. Baer, A. C. Stern, Y. Levin, D. J. Tobias, and C. J. Mundy. Electrochemical surface potential due to classical point charge models drives anion adsorption to the air-water interface. *J. Phys. Chem. Lett.*, 3:1565–1570, 2012.

[92] E. V. Kholopov. Mean potential of bethe in the classical problem of calculating bulk electrostatic potentials in crystals. *phys. stat. sol. (b)*, 243:1165–1181, 2006.

[93] F. E. Harris. *"Hartee-Fock Studies of Electronic Structures of Crystalline Solids" in Theoretical Chemistry: Advances and Perspectives Volume 1*. Academic Press, 1975.

[94] S. M. Kathmann, I-F. W. Kuo, C. J. Mundy, and G. K. Schenter. Understanding the surface potential of water. *J. Phys. Chem. B*, 115:4369–4377, 2011.

[95] F. Figueirido, G. S. Del Buono, and R. M. Levy. On finite-size effects in computer simulations using the ewald potential. *J. Chem. Phys.*, 103:6133–6142, 1995.

[96] M. A. Wilson, A. Pohorille, and L. R. Pratt. Comment on "study on the liquid-vaport interface of water. i. simulation results of thermodynamics properties and orientational structure". *J. Chem. Phys.*, 90:5211–5213, 1989.

[97] L. R. Pratt. Contact potentials of solution interfaces: Phase equilibrium and interfacial electric fields. *J. Phys. Chem.*, 96:25–33, 1992.

[98] X. Song, D. Chandler, and R. A. Marcus. Gaussian field model of dielectric solvation dynamics. *J. Phys. Chem.*, 100:11954–11959, 1996.

[99] T. L. Beck. The influence of water interfacial potentials on ion hydration in bulk water and near interfaces. *Chem. Phys. Lett.*, 561-562:1–13, 2013.

[100] G. Schenter. (to be published).

[101] L. Horváth, T. Beu, M. Manghi, and J. Palmeri. The vapor-liquid interface potential of (multi)polar fluids and its influence on ion solvation. *J. Chem. Phys.*, 138:154702, 2013.

[102] Y. Shi and T. L. Beck. Length scales and interfacial potentials in ion hydration. *J. Chem. Phys.*, 139:044504, 2013.

[103] M. Born. Volumes and hydration warmth of ions. *Z. Phys.*, 1:45–48, 1920.

[104] A. Zangwill. *Modern Electrodynamics*. Cambridge University Press, 2013.

[105] J. D. Jackson. *Classical Electrodynamics*. John Wiley & Sons, 1999.

[106] Ph. A. Martin. Sum rules in charged fluids. *Rev. Mod. Phys.*, 60:1075–1127, 1988.

[107] F. H. Stillinger and R. Lovett. General restriction on the distribution of ions in electrolytes. *J. Chem. Phys.*, 49(5):1991–1994, 1968.

[108] F. H. Stillinger and R. Lovett. Ion-pair theory of concentrated electrolytes. i. basic concepts. *J. Chem. Phys.*, 48(9):3858–3868, 1968.

[109] R. Lovett and F. H. Stillinger. Ion-pair theory of concentrated electrolytes. ii. approximate dielectric response calculation. *J. Chem. Phys.*, 48(9):3869–3884, 1968.

[110] Z. Hu and J. D. Weeks. Efficient solutions of self-consistent mean field equations for dewetting and electrostatics in nonuniform liquids. *Phys. Rev. Lett.*, 105:140602, 2010.

[111] C. J. Fennell, L. Li, and K. A. Dill. Simple liquid models with corrected dielectric constants. *J. Phys. Chem. B*, 116:6936–6944, 2012.

[112] B. P. Lee and M. E. Fisher. Density fluctuations in an electrolyte from generalized debye-hückel theory. *Phys. Rev. Lett.*, 76(16):2906–2909, 1996.

[113] B. P. Lee and M. E. Fisher. Charge oscillations in debye-hückel theory. *Europhys. Lett.*, 39(6):611–616, 1997.

[114] S. K. Das, Y. C. Kim, and M. E. Fisher. Near critical electrolytes: Are the charge-charge sum rules obeyed? *J. Chem. Phys.*, 137:074902, 2012.

[115] R. W. Zwanzig. High-temperature equation of state by a perturbation method. i. nonpolar gases. *J. Chem. Phys.*, 22:1420, 1954.

[116] C. Chipot and A. Pohorille, editors. *Free Energy Calculations: Theory and Applications in Chemistry and Biology.* Springer, 2007.

[117] J. G. Kirkwood. Statistical mechanics of fluid mixtures. *J. Chem. Phys.*, 3:300–313, 1935.

[118] G. M. Torrie and J. P. Valleau. Nonphysical sampling distributions in monte carlo free-energy estimation: Umbrella sampling. *J. Comput. Phys.*, 23:187–199, 1977.

[119] C. Jarzynski. Nonequilibrium equality for free energy differences. *Phys. Rev. Lett.*, 78:2690–2693, 1997.

[120] G. E. Crooks. Entropy production fluctuation theorem and the nonequilibrium work relation for free energy differences. *Phys. Rev. E*, 60:2721–2726, 1999.

[121] P. G. Bolhuis, D. Chandler, C. Dellago, and P. L. Geissler. Transition path sampling: Throwing ropes over rough mountain passes, in the dark. *Annu. Rev. Phys. Chem.*, 53:291–318, 2002.

[122] R. Schulz, B. Lindner, L. Petridis, and J. C. Smith. Scaling of multimillion-atom biological molecular dynamics simulation on a petascale supercomputer. *J. Chem. Theory Comput.*, 5:2798–2808, 2009.

[123] P. H. Hünenberger and J. A. McCammon. Effect of artificial periodicity in simulations of biomolecular under ewald boundary conditions: a continuum electrostatics study. *Biophys. Chem.*, 78:69–88, 1999.

[124] J. Lekner. Summation of coulomb fields in computer-simulated disordered systems. *Physica A*, 176:485–498, 1991.

[125] T. L. Beck. Hydration free energies by energetic partitioning of the potential distribution theorem. *J. Stat. Phys.*, 145:335–354, 2011.

[126] J. D. Weeks. External fields, density functionals, and the gibbs inequality. *J. Stat. Phys.*, 110:1209–1217, 2003.

[127] J. D. Weeks, D. Bedeaux, and B. J. A. Zielinska. Anisotropic van der waals model of the liquid-vapor interface. *J. Chem. Phys.*, 80:3790–3800, 1984.

[128] G. E. Crooks and D. Chandler. Gaussian statistics of the hard-sphere fluid. *Phys. Rev. E*, 56:4217–4221, 1997.

[129] J. Adams, P. Swarztrauber, and R. Sweet. Fishpack - efficient fortran subprograms for the solution of separable elliptic partial differential equations. http://www2.cisl.ucar.edu/resources/legacy/fishpack, 2011.

[130] N. A. Denesyuk and J. D. Weeks. in preparation.

[131] O. Mishima and H. E. Stanley. The relationship between liquid, supercooled, and glassy water. *Nature*, 396:329–335, 1998.

[132] P. H. Poole, R. K. Bowles, I. Saika-Voivod, and F. Sciortino. Free energy surface of st2 water near the liquid-liquid phase transition. *J. Chem. Phys.*, 138:034505, 2013.

[133] Y. Liu, A. Z. Panagiotopoulos, and P. G. Debenedetti. Low-temperature fluid-phase behavior of st2 water. *J. Chem. Phys.*, 131:104508, 2009.

[134] Y. Liu, J. C. Palmer, A. Z. Panagiotopoulos, and P. G. Debenedetti. Liquid-liquid transition in st2 water. *J. Chem. Phys.*, 137:214505, 2012.

[135] D. T. Limmer and D. Chandler. The putative liquid-liquid transition is a liquid-solid transition in atomistic models of water. *J. Chem. Phys.*, 135:134503, 2011.

[136] D. T. Limmer and D. Chandler. The putative liquid-liquid transition is a liquid-solid transition in atomistic models of water. ii. *J. Chem. Phys.*, 138:214504, 2013.

[137] S. D. Overduin and G. N. Patey. An analysis of fluctuations in supercooled tip4p/2005 water. *J. Chem. Phys.*, 138:184502, 2013.

[138] D. E. Otten, P. R. Shaffer, P. L. Geissler, and R. J. Saykally. Elucidating the mechanism of selective ion adsorption to the liquid water surface. *Proc. Natl. Acad. Sci. USA*, 109:701–705, 2012.

[139] P. L. Geissler. Water interfaces, solvation, and spectroscopy. *Annu. Rev. Phys. Chem.*, 64:317–337, 2013.

[140] A. C. Stern, M. D. Baer, C. J. Mundy, and D. J. Tobias. Thermodynamics of iodide adsorption at the instantaneous air-water interface. *J. Chem. Phys.*, 138:114709, 2013.

[141] S. Toxvaerd and J. C. Dyre. Role of the first coordination shell in determing the equilibrium structure and dynamics of simple liquids. *J. Chem. Phys.*, 135:134501, 2011.

[142] J. D. Weeks. (unpublished).

[143] Y. G. Chen. *General Theory of Nonuniform Fluids: From Hard Spheres to Ionic Fluids*. PhD thesis, University of Maryland, 2004.

[144] P. S. Varilly. *Fluctuations in Water and their Relation to the Hydrophobic Effect*. PhD thesis, University of California, Berkeley, 2011.

[145] A. P. Willard and D. Chandler. Instantaneous liquid interfaces. *J. Phys. Chem. B*, 114:1954–1958, 2010.